DISSERTATION

MULTIFRACTAL ANALYSIS OF THE EFFECTS OF RAINFALL AND K_s ON SURFACE INFILTRATION AND RUNOFF

Submitted by

Huan Meng

Department of Civil Engineering

In partial fulfillment of the requirements

For the Degree of Doctor of Philosophy

Colorado State University

Fort Collins, Colorado

Spring 2004

COLORADO STATE UNIVERSITY

April 6th, 2004

WE HEREBY RECOMMEND THAT THE DISSERTATION PREPARED UNDER OUR SUPERVISION BY HUAN MENG ENTITLED MULTIFRACTAL ANALYSIS OF THE EFFECTS OF RAINFALL AND K_s ON SURFACE INFILTRATION AND RUNOFF BE ACCEPTED AS FULLFILING IN PART REQUIREMENTS FOR THE DEGREE OF DOCTOR OF PHILOSOPHY.

Committee on Graduate Work

(Please print name under signature)

Duane C Boes
DUANE C BOES

TR Green
TIMOTHY R. GREEN

Freeman M Smith
FREEMAN M SMITH

Jorge Ramirez
JORGE A RAMIREZ

Jose D. Salas
Adviser JOSE D. SALAS

L. R. Ahuja
Co-Adviser (L. R. AHUJA)

Sandra Woods
Department Head SANDRA WOODS

ABSTRACT OF DISSERTATION

MULTIFRACTAL ANALYSIS OF THE EFFECTS OF RAINFALL AND K_s ON SURFACE INFILTRATION AND RUNOFF

This research analyzes the effects of rainfall and saturated hydraulic conductivity (K_s) on surface infiltration and runoff using numerical experiments in the framework of universal multifractal (UM) model.

A set of criteria is first defined based on radial power spectrum of a physical field for its scaling in general and for fitting the UM model in particular. Then a technique is developed to estimate the UM model parameters of non-conservative multifractal fields. The estimation approaches for both conservative and non-conservative fields are evaluated and demonstrated to produce estimates with good to excellent accuracy.

A physically based, distributed rainfall-runoff model, named DIMBRR, was developed for the study on surface infiltration and runoff. The event-based DIMBRR model employs the Green-Ampt model for infiltration and the kinematic wave model for routing. The routing hierarchy of a watershed is defined based on the D-infinity flow direction model. DIMBRR model is calibrated using data collected from the sub-watershed 11 of the USDA-ARS Walnut Gulch experimental watershed.

To analyze the effects of driving fields (rain and K_s) on surface infiltration and runoff, a series of rainfall and K_s fields are generated including both random, non-scaling fields and multifractal fields produced using the UM model. By varying the UM model parameters based on physical considerations, rain and K_s fields with various characteristics are obtained. These rain and K_s data are then fed into the DIMBRR model to produce space-time infiltration and runoff processes. The scaling properties of these watershed processes are then analyzed to find the impact from the rain and K_s fields mainly in terms of the connections among the UM model parameters from the input and the output fields. Some of the major findings from this research are: 1) K_s, rather than rain, determines if the resulting infiltration field is scaling after an adjusting period; 2) some model parameters from both rain and K_s fields have a strong impact on infiltration while only rain parameters have a significant influence on runoff; 3) infiltration fields are usually non-homogeneous while runoff fields are usually homogeneous; 4) if an infiltration field becomes more singular (localized large infiltration rates) in time, it usually also becomes more sparse on average and more homogeneous; 5) a runoff field always becomes more singular in time, yet it also becomes more space-filling on average.

Huan Meng
Department of Civil Engineering
Colorado State University
Fort Collins, CO 80523
Spring, 2004

ACKNOWLEDGEMENTS

Many people have offered assistance during this research. I would like to thank Dr. José Salas, who is my adviser, and Dr. Timothy Green for their technical and practical guidance. I would also like to thank my committee members for their encouragement and patience. I am deeply grateful for the theoretical assistance I received from Dr. Daniel Lavallée, Dr. Shaun Lovejoy, Dr. David Marsan, Dr. Hui-Hai Liu, and Dr. Thomas Over. Special thanks are given to Dr. Rose Shillito and Dr. David Goodrich for providing various data from the Walnut Gulch Experimental Watershed. This project was supported through an USDA-ARS/CSU Specific Cooperative Agreement. I gratefully acknowledge the assistance and support from Dr. Laj Ahuja of USDA-ARS. This research would not have been possible without his initiation.

DEDICATED TO MY FAMILY AND BOMU

TABLE OF CONTENTS

Chapter 1

INTRODUCTION

1.1 Problem Descriptions

The observed variability of rainfall, landscape topography, soil properties, infiltration, soil moisture, erosion, and crop yield has been of great interest to the agriculture community for many years. Generally, research has been focused on: 1) incorporating spatial-temporal variability, and uncertainty of soil, plant, weather, and management parameters in models of production and environmental impact, ranging from field to farm ecosystem scales; and 2) developing models of surface and subsurface water and mass flow networks appropriate for various landscape types and scales. A significant amount research has been done on these subjects at the USDA Agriculture Research Service (ARS), *e.g.* Green *et al.* (2001), as well as other organizations worldwide. In accordance with the aforementioned research themes, this work will focus on the space-time properties of two specific watershed processes in the hydrological cycle: surface infiltration rate and surface runoff. In addition to applications in agriculture, surface infiltration and runoff during rainfall events are also vital components in studies such as watershed modeling, groundwater and surface water quality, land-atmosphere feedback for global climate study, and sub-grid scale parameterization of general circulation model for numerical weather prediction, to name but a few.

The importance of surface infiltration has been realized for many years and numerous studies have been devoted to the subject. Previous research on infiltration, however, has contributed primarily to our understanding of point infiltration process. As stochastic process both in space and in time, surface infiltration is characterized by considerable spatial and temporal variations. This feature leads to large variations in model parameters. Attempts to incorporate such variability into so-called equivalent parameters, and to replace point infiltration parameters with these equivalent parameters have largely proved fruitless. In general, such approaches are inadequate to describe the complexity of the processes under study, due to the lack of parameter variability at field or even larger scales. To improve modeling capability and accuracy of various processes related to infiltration, there is clearly a great need for better understanding of the complex patterns of infiltration both in space and in time, and a need for the development of new methods to model infiltration at field scales.

Surface runoff is also a stochastic process marked by great spatial and temporal variability. In the literature, runoff studies are generally confined to streamflow in channel network, or are a by-product of research on other related processes such as erosion and solute transport. Unfortunately, the space-time properties of surface runoff are rarely a primary study objective, even though they are an important component of the water cycle and play a vital role in the re-distribution of excess rainfall. It is thus highly desirable to dedicate research to surface runoff and methodically explore its space-time structure.

Scaling theory is an excellent approach to dealing with stochastic processes across scales, provided the processes are scaling. The development and application of scaling techniques in geophysical research has become increasingly popular over the last two decades. Some of the main driving fields of infiltration and runoff processes have been found to possess scaling behavior, including rainfall, hydraulic conductivity, channel network, and topography (Over and Gupta 1996, Tessier *et al.* 1996, Marson *et al.* 1996, Liu and Molz 1997, Lavallée *et al.* 1993). Moreover, some fields that are subject to a significant influence from infiltration, such as soil moisture, have also been shown to have scaling properties (Rodriguez-Iturbe *et al.*, 1995, Peters-Lidard *et al.*, 2001). Since surface infiltration and runoff are the combined result of the non-linear interactions among some scaling fields, it is logical to hypothesize the scaling nature of infiltration and runoff processes. Thus, this research will be conducted on the basis of scaling theory.

1.2 Research Objectives

The overarching objective of this study is to acquire a more clear understanding of the spatial and temporal structures of surface infiltration and runoff processes through the exploration of the effects of driving fields, namely rainfall and saturated hydraulic conductivity, on infiltration and runoff using numerical experiments in the framework of scaling. More specifically, this research will proceed as follow:

(1) a scaling model will be chosen for the generation of scaling rainfall and saturated hydraulic conductivity fields;

(2) parameters for the scaling model will be determined for simulating the rainfall and saturated hydraulic conductivity fields based on literature and physical considerations; these model parameters will be systematically varied to represent rainfall and saturated hydraulic conductivity fields with various combinations of characteristics;

(3) a series of non-scaling rainfall and non-scaling saturated hydraulic conductivity fields will be generated;

(4) a series of scaling steady rainfall and scaling saturated hydraulic conductivity fields will be generated using the model chosen in (1) above, and the parameters set in (2) above;

(5) a series of space-time scaling rainfall processes will be generated using the same model and model parameters as used in (4) above; these space-time rainfall fields will essentially be the combinations of steady rain and advection;

(6) a physically based distributed rainfall-runoff model will be developed which will produce space-time surface infiltration rate and runoff processes;

(7) the rainfall-runoff model developed in (6) above will be calibrated and verified using rainfall and runoff data collected from a chosen watershed;

(8) the non-scaling rainfall and saturated hydraulic conductivity fields generated in (3) above are inputted to the rainfall-runoff model to produce infiltration and runoff processes; these two watershed processes are analyzed for the effect of non-scaling forcing on the processes;

(9) the scaling steady rain fields and the scaling saturated hydraulic conductivity fields generated in (4) above are inputted to the rainfall-runoff model, and the resulting infiltration and runoff processes are analyzed for their space-time scaling properties and the effect of scaling steady rain and scaling saturated hydraulic conductivity on the output processes;

(10) the scaling space-time rainfall generated in (5) above are input to the rainfall-runoff model, and the resulting infiltration and runoff processes are analyzed for their space-time scaling properties and the effect of the input fields with the added dynamics.

1.3 Expected Contributions

A physically based, distributed rainfall-runoff model will be developed in this research for the study of surface infiltration and runoff. This model will employ one of the best algorithms available for determining flow path, have functionality to define the routing hierarchy throughout a watershed or any study area, take in rainfall that varies both in space and in time, compute infiltration and excess rainfall dynamically, route the excess rainfall as overland flow, and finally route channel streamflow to the outlet of the watershed or to the boundary of the study area. This model will be calibrated and verified using separate sets of data collected from a watershed.

This study will also improve the understanding of the spatial and temporal structures of the surface infiltration and runoff processes from the scaling perspective. The rainfall-runoff model will output infiltration and runoff as space-time processes. The scaling properties of these processes will then be quantified and analyzed, revealing the 3D (2D in space, 1D in time) structure of the processes.

By definition, a scaling process is scale invariant. For stochastic processes such as infiltration and runoff, scale invariance is represented in probabilistic terms, as elaborated in the following chapter. Thus, if infiltration and runoff are shown to be scaling, their scaling properties as described in the following chapters will not only be valid for the scale adopted in this study, but will also apply to the processes at a range of scales, although work beyond this research is needed to quantify such range.

Another important contribution expected from this research is the elucidation of connections between infiltration and runoff and their driving forces in the framework of scaling. By analyzing the two watershed processes as the outcome of rainfall and soil inputs that have various scaling characteristics, the scaling properties of the watershed processes could be linked to those of the input fields in a systematic way. The significance of each aspect of the driving fields will be identified in terms of their impact on infiltration and runoff processes. Additionally, non-scaling input fields will be used to drive watershed responses. The analyses of the output fields will reveal the effects of such non-scaling fields on infiltration and runoff as compared to the effects of scaling input fields.

Chapter 2

LITERATURE REVIEW

This chapter consists of a literature review of the four topics pertaining to this study: scaling theory, rainfall-runoff models, surface infiltration, and surface runoff.

2.1 Scaling Theory Review

The most fundamental characteristic of a scaling system is its scale invariance, *i.e.* its small and large-scale (statistical) properties are related by a scale-changing operation involving only the scale ratio (Tessier *et al.*, 1993). Two types of scaling processes are observed in the physical world: simple scaling, and its generalization, multiscaling. Generally, if a complex geophysical process or field is scaling, it will most likely obey multiscaling rules.

2.1.1 Simple Scaling

The notion of simple scaling has its origin in the characterization of stable distributions, and was generalized to its present form by Lamperti (1962). Gupta and Waymire (1990) presented a detailed account of the theory of simple scaling, as well as some examples of simple scaling processes. They (Gupta and Waymire, 1990) defined a random field $\{Y(\underline{x})\}$, indexed by $\underline{x} \in D$, as being simple scaling if its joint distribution functions have the following property:

$$P[\lambda^{-\theta}Y_\lambda(\underline{x}_1) < y_1, ..., \lambda^{-\theta}Y_\lambda(\underline{x}_n) < y_n] = P[Y(\underline{x}_1) < y_1, ..., Y(\underline{x}_n) < y_n], \quad \forall\, y_1,...,y_n \quad (2.1)$$

and $\lambda > 0$, where $\underline{x}_1, ..., \underline{x}_n$ is an arbitrary set of index points, λ is a scaling parameter, θ is the scaling exponent, and $Y_\lambda(\underline{x}) = Y(\lambda \underline{x})$. Note that $Y_1(\underline{x}) = Y(\underline{x})$. The distributional equalities of eq. (2.1) are often denoted (Boes, personal communication)

$$\{\lambda^{-\theta}Y_\lambda(\underline{x})\} \stackrel{d}{=} \{Y(\underline{x})\} \quad (2.2)$$

or

$$\{Y_\lambda(\underline{x})\} \stackrel{d}{=} \{\lambda^{\theta}Y(\underline{x})\} \quad (2.3)$$

which says that the random field $\{\lambda^{-\theta}Y_\lambda(\underline{x})\}$ has the same distribution as the random field $\{Y(\underline{x})\}$. An even more compact notation, suppressing the index, is

$$Y_\lambda \stackrel{d}{=} \lambda^{\theta} Y_1$$

In this study, the index set will be space and two-dimensional. This definition of simple scaling is often too restrictive to be applied in practice. Rather, two more practical scaling relations are often applied. They are moment scaling

$$E[Y_\lambda^q] = \lambda^{q\theta} E[Y_1^q] \quad (2.4)$$

which is equivalent to

$$\log E[Y_\lambda^q] = q\theta \log\lambda + \log E[Y_1^q] \quad (2.5)$$

and power spectrum scaling for isotropic fields

$$\hat{E}(k) \sim k^{-\beta} \quad (2.6)$$

where $\hat{E}(\,)$ indicates power spectrum, which is the modulus squared of the Fourier amplitudes in the Fourier space of the field, k represents a wave vector modulus and β is power spectral exponent. In the time domain, the spectrum becomes a function of frequency with the same form. Note that eq. (2.6) holds true for all scaling fields whether they are simple scaling or multiscaling (introduced in the next section). As indicated by eq. (2.5), the q-th moment of a simple scaling field has a log-log linear relationship with scale. The slope of the fitted regression line will be a linear function of the order of moment, q. In the language of fractal, a simple scaling field is defined by one fractal set and corresponds to a single fractal dimension, *i.e.* a simple scaling field is monofractal.

Efforts have been made to apply simple scaling models to various fields in hydrology since the early 1980's (Lovejoy 1981). However, the contradiction between such models and observed data have made it clear that simple scaling is too restrictive to hold for complex geophysical processes. In fact, multiscaling is a more general framework for scale-invariant nonlinear dynamics.

2.1.2 Multiscaling

Instead of simple scaling, real-world dynamic systems are sometimes observed to be multiscaling, a notion first introduced by Grassberger (1983), Hentschel and Procaccia (1983) in their work on turbulent cascade. The following relationship holds for some geophysical processes

$$E[Y_\lambda^q] = \lambda^{K(q)} E[Y_1^q] \tag{2.7}$$

which is equivalent to

$$\log E[Y_\lambda^q] = K(q)\log\lambda + \log E[Y_1^q] \tag{2.8}$$

where Y_λ is the λ-scaled random field $\{Y(\underline{x})\}$, $K(q)$ is a non-linear function of the order of moment, q. As displayed in the above equation, the moments are still log-log linear with scale, but the slope of the moments versus order of moments is no longer linear.

A multiscaling field corresponds to a series of random scale functions rather than a single deterministic function as in the case of simple scaling. Each of these scale functions is defined by a fractal subset which has its often unique fractal dimension or rather codimension (the difference between the dimension of space and the fractal dimension) (Schertzer and Lovejoy, 1987). Therefore, a multiscaling field is also called a multifractal field (Parisi and Frisch, 1985).

2.1.3 Random Cascade – Multiplicative Process

Multiscaling, or multifractals, provide the appropriate theoretical framework for scaling nonlinear dynamical systems. By using stable multifractal generators in multiscaling models (Chapter 3), for instance, many of the details of the dynamics become irrelevant (Tessier *et al.*, 1993). This quality makes multiscaling models an attractive tool to study complicated geophysical processes such as rainfall, infiltration and runoff. Unlike some other natural processes such as fully developed turbulence, there are no governing equations for these geophysical processes.

A popular class of multiscaling models is the set of multiplicative cascade models, which originated from the statistical theory of turbulence (Kolmogorov, 1941). Turbulent eddies of larger scale break up into smaller eddies and transfer their kinetic energy to the new eddies. This process proceeds in turbulence and creates a cascade that is scale invariant and conserves energy from scale to scale. The construction of the random cascade model is based on the phenomena observed in turbulence. Through a multiplicative process, a random cascade generates new 'pieces' at each scale, which are products of some multipliers associated with its predecessors at all previous scales. Yaglom (1966) was the first researcher to develop a three-dimensional discrete random cascade. Mandelbrot (1974) introduced what is termed as a 'canonical' cascade, which is a variant of Yaglom's model. A canonical cascade conserves energy on average. By contrast, a 'microcanonical' cascades conserves energy everywhere in space and at each scale.

The development and applications of random cascade theory have been very active in many fields including hydrology, especially in rain-related fields. Schertzer and Lovejoy (1987) first proposed that rain variability could be directly modeled as a turbulent cascade process. As noted by Over and Gupta (1994), the application of random cascade theory to rainfall is based on two observations: first, that rainfall fields appear to have scaling structure that can be described by random cascades; secondly, rainfall fields are clustered in space. It is observed in mesoscale rainfall that a rainfall intensity hierarchy exists where rain cells with high intensity are embedded in areas with medium rainfall intensity, which are embedded in larger areas with low intensity, and so on. An unknown conserved property is taken as the analogy of energy flux when a random cascade is used to model rainfall. As the underlying process for rainfall, this conserved property concentrates into smaller regions of space as the cascade proceeds to higher resolution, yielding the observed high spatial variability in rain field.

One type of widely used cascade models is discrete random cascade. It is reviewed here briefly as an introduction to the construction of a random cascade. The multiscaling model adopted in this study - universal multifractal model - will be elaborated upon in Chapter 3. The presentation of discrete random cascade models herein will closely follow Gupta and Waymire (1993).

The mathematical construction begins with a given mass density, W_0, distributed uniformly over some bounded domain (Fig. 2.1), for example, a unit square $J = [0, 1]^2$. J is subdivided into $b = N^2$ sub-squares of side length 1/N where b is called the branching number. Now distribute the mass density W_0 over each of the b sub-squares, $J(\sigma_1)$ ($\sigma_1 = 1, 2, ..., b$), as $W_0W_1(1), W_0W_1(2), ..., W_0W_1(b)$, respectively, where the W_1's are mutually independent, identically distributed random variables, denoting W. W is called generator.

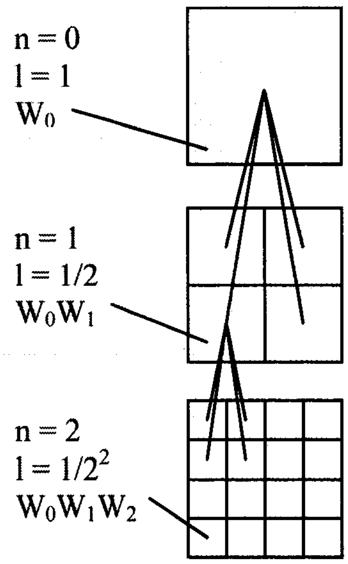

Figure 2.1 *Schematic of two-dimensional cascade with branching number b = 4 (reproduced from Gupta and Waymire, 1993)*

In addition, it is required that E[W] = 1, which means that the ensemble average of the mass density W_0 is conserved after this redistribution. This constraint is set in order to respect the energy-flux conservation requirement in turbulence. At the next step of the cascade construction, each of the sub-squares $J(\sigma_1)$ is further subdivided into b sub-squares of side lengths $1/N^2$, say $J(\sigma_1, \sigma_2)$, $\sigma_1, \sigma_2 = 1, 2, \ldots, b$. The mass density $W_0W_1(\sigma_1)$ is redistributed as $W_0W_1(\sigma_1)W_2(\sigma_2)$, where the W_2's are independent of the W_1's and W_0 and are independently and identically distributed (iid) random variables as W with mean one. This construction is shown schematically in Fig. 2.1 for N = 2. The cascade construction continues iteratively, such that at the n-th generation, the unit square J is divided into $N^{2n} = b^n$ sub-squares of side length or spatial scale $l = 1/N^n$. Each of these sub-squares is denoted by $J_n = J(\sigma_1, \sigma_2, \ldots, \sigma_n)$, $\sigma_i = 1, 2, \ldots, b$; $i = 1, 2, \ldots, n$. The random mass density in J_n is denoted by the product $W(\sigma_1, \sigma_2, \ldots, \sigma_n) = W_0W_1(\sigma_1)W_2(\sigma_2)\ldots W_n(\sigma_n)$. The path leading to J_n through the n generations is denoted by $(\sigma_1), (\sigma_1, \sigma_2), \ldots, (\sigma_1, \sigma_2, \ldots, \sigma_n)$. The total mass (measure) $\varepsilon_n(J_n)$ in the sub-square J_n is

$$\varepsilon_n(J_n) = \int_{J_n} \psi_n(x)dx \tag{2.9}$$

where the mass density $\psi_n(x)$ is given by

$$\psi_n(x) = \prod_{j \in path\ to\ J_n} W_j, \qquad W_j \geq 0; \quad x \in J_n \tag{2.10}$$

with the constraint $E[W_j] = 1$.

If the cascading process continues, it can be shown that ε_n will converge to a limit mass ε_∞. If the limiting mass is degenerate, the mass distribution will be almost surely zero throughout the bounded area. Otherwise, the limiting cascade distribution will show highly singular behavior, *i.e.* the mass field goes to infinity at some points and goes to zero over most of the area.

2.2 Rainfall-Runoff Model Review

A vast number of rainfall-runoff models have been reported in the literature. Only a few distributed rainfall-runoff models will be mentioned here. Woolhiser *et al.* (1990) and Smith *et al.* (1995) introduced an event-oriented kinematic runoff and erosion model called KINEROS. Instead of being in a grid format, the watershed in this model is divided into a cascade of planes and channels so it qualifies as a distributed model. The KINEROS infiltration sub model is based on the work by Smith and Parlange (1978), and excess rainfall is routed using the kinematic wave model. James and Kim (1990) proposed a two-dimensional hydrodynamic model to simulate uncoupled overland and channel flow routing for a single storm event. Excess rainfall calculated by the Green-Ampt infiltration equation is routed as overland flow using a two-dimensional diffusion wave implicit scheme. Scoging (1993) built a distributed overland flow model that adopts a one-dimensional kinematic wave equation for the spatial and temporal prediction of flow depth. A flowline sub component determines the character of flowline through vector analysis. No splitting in flowline in a pixel is allowed. Ogden and Julien (2002) developed a raster-based, two-dimensional rainfall-runoff model, CASC2D. It is a physically based distributed parameter model that calculates surface runoff as the result of the Hortonian runoff production mechanism. CASC2D uses the Green-Ampt equation to determine infiltration rate, a two-dimensional diffusion wave model to rout overland flow with an explicit finite difference scheme, and a one-dimensional explicit diffusion wave model or implicit dynamic model for channel routing. This model requires significantly more input data than traditional approaches. Yoo (2002) proposed an event-based rainfall-runoff model which combines four sub models to describe the surface rainfall runoff, subsurface flow with infiltration, river discharge, and groundwater flow. Its major algorithms are based on the theoretical description of the physical processes, but it also incorporates some conceptual approaches to evaluate the individual or joint effects on the whole processes. Its hydrograph is developed based on the assumption of linear superposition and has a shape represented by a double triangle. Equations are given for peak discharge and peak time, which are functions of hydrograph shape, infiltration depth, and time of concentration among other factors. The infiltration component of the model is a combination of several existing infiltration models such as Green & Ampt. All the relevant equations are solved using finite difference scheme.

2.3 Surface Infiltration-Related Review

It has long been realized that infiltration at the soil surface is a stochastic process with spatial heterogeneity because, like many other geophysical fields, infiltration is a combined result of several heterogeneous processes or fields including rainfall, soil properties, vegetation, and topography, *etc.* Various stochastic approaches have been employed to deal with the problem of infiltration. Among them, Maller and Sharma (1981) assumed lognormal distributions for the parameters in the Philip's two-parameter infiltration model and analyzed the corresponding distribution of infiltration flux. Dagan and Bresler (1983) took advantage of Green and Ampt's moving front concept and the assumption of effective parameters to derive the expectation and variance of the water flux as function of depth and time. Sivapalan and Wood (1986) derived cumulative distribution of ponding time from lognormally distributed saturated hydraulic conductivity (K_s) by using derived distribution theory. Based on this distribution, they obtained some quasi-analytical expressions for the statistics of surface infiltration. The mean and variance of infiltration appeared to be functions of rainfall and statistics of K_s, especially mean and coefficient of variation. Govindaraju, *et al.* (2001) provided expressions for describing the ensemble-averaged field-scale infiltration as well as for predicting the time it took for a given areal depth of water to infiltrate into soil. These expressions were valid if the saturated hydraulic conductivity was represented by a homogeneous correlated lognormal random field, and infiltration followed the Green-Ampt model. Olsson *et al.* (2002) conducted a scaling study on spatial variability of infiltration in field soils based on digitized images of dye infiltration from experiments carried out on three sites. Their research showed that infiltration in field soils were of multiscaling type. They also fitted the universal multifractal model, which is used extensively in this study, to the dye infiltration data and found that the simulated fields reproduced key features of the observed data. This work is actually outside the realm of surface infiltration, but is included here because of its close connection with the subject and the analytical approach it took, which is very relevant to this study.

As described above, the majority of the work done in the area of spatial distribution of infiltration is based on the traditional statistical or stochastic approaches. The outcomes of the studies are usually expressed as the general statistics of the infiltration fields that are only suitable to the scale at which the studies were conducted. The only research that was conducted in the framework of scaling (Olsson *et al.*, 2002) was about infiltration in the soils. While the underground process is closely related to the water flux at the surface, the research by Olsson *et al.* (2002) ultimately deals with a different problem, although its analytical framework is rather similar to that of this study.

2.4 Surface Runoff-Related Review

Many studies on runoff are confined to the spatial or temporal variations of channel or river flow. Even research designed to inspect the spatial and/or temporal variations of the hydrological responses of a watershed to various factors usually use runoff at single points, usually outlets of watersheds, to evaluate such effects. This observation also holds true for scaling studies on runoff. The following literature review will reflect this fact.

Gupta *et al.* (1996) studied the scaling properties of spatial peak flows as a result of simulated rainfall at a real basin. In one experiment, a random, spatially uniform rainfall was instantaneously applied to the basin. The magnitudes of the resulting peak flows in different sub-basins were found to be simple scaling. In another experiment the rain field was generated using a random cascade model (Section 2.1.3) and was applied instantaneously to the basin, showing that the resulting peak flows are multiscaling. In a study of flood quantiles, Gupta and Dawdy (1995) explored the regional flood frequency relations and their underlying physical generation mechanisms. Using data from three states in the USA, they computed the scaling exponents of the power law relationship between flood quantiles and drainage areas and found clear variations in the exponents from different regions in each state. These variations suggested that floods generated by melting snow are simple scaling, whereas floods generated by rainfall are multiscaling. These conclusions were also supported by their (Gupta and Dawdy, 1995) rainfall-runoff experiment and research on the spatial scaling structure of mesoscale rainfall. Tessier *et al.* (1996) worked with time series of daily rainfall and river runoff from 30 catchments with basin sizes of 40 to 200 km^2 and used spectral analysis to identify the types and extents of the scaling regimes of the data. A scale break at about 16 days was found in both river flow and rainfall time series. Tessier *et al.* (1996) associated this break with the 'synoptic maximum', the time scale of processes of planetary spatial scale. The universal multifractal (Chapter 3) parameters were then estimated for the two scaling regimes. Causal simulations of rain and river flow time series were performed based on the scaling properties obtained from the data. Finally, the researchers showed that the low-frequency rainfall series and the corresponding river flow series could be linked by a linear scaling transfer function, and such connection in the high-frequency regime required nonlinear transforms. The work by Pandey *et al.* (1998) on daily river flow also found the data being multifractal and supported the basic findings by Tessier *et al.* (1996). The universal multifractal parameters they (Pandey *et al.*, 1998) derived for daily river flow data from 19 river basins showed no systematic basin-to-basin variation. Pandey *et al.* (1998) presumed that this reflected the space-time multiscaling of both the rainfall and the runoff processes. Merz and Bardossy (1998) applied a quasi-three-dimensional, event-based model to a small catchment to explore the influence of spatial variability on the runoff. They compared the model outputs from soil parameters that were randomly distributed, and that had structured spatial variability, and found that the two cases yielded very different runoff. It was also showed that spatial variability in soil moisture could have a dominant influence on the rainfall runoff behavior. Canton *et al.* (2002) carried out both field and model studies on the overall runoff from three small catchments in a desert area that was characterized by a high variability in surface cover, soil properties, and topography. The catchments, each with different surface type, were monitored for three years and the data were used to find out the effect of different soil surface on the catchment runoff. Analyses on the data proved that the soil surface units (defined as terrain units with the same cover, soil type, and landform) within the study area responded differently to natural rainfalls. Canton *et al.* (2002) explained the observed responses by the types of cover, topographical characteristics and soil properties. A simple distributed model was built in this study and the model results also showed the influence of the spatial distribution of soil surfaces on the overall runoff. Joel *et al.* (2002) studied the scale effect on the runoff process under natural field and rainfall conditions. The cumulative rainfall and runoff were sampled every 5 minutes at 3 plots of size 50 m^2 and 12 plots of size 0.25 m^2. The scale effect on runoff was found to be significant. On average, large plots yielded only 40% of the total runoff produced on small plots per unit area.

Two main points stand out from the above review: (1) hydrological processes related to surface runoff are shown scaling on various spatial and temporal scales; (2) spatial and temporal variation in rain, and spatial variability in watershed properties (soil, topography, scale, *etc.*) play a vital role in determining the characteristics of surface runoff. Both of these points serve as the basis for this study.

Chapter 3

UNIVERSAL MULTIFRACTAL MODEL AND ESTIMATION OF PARAMETERS

The scaling model used in this study for generating rainfall and saturated hydraulic conductivity fields is the universal multifractal model developed by Schertzer and Lovejoy (1987). This model also sets the framework for the scaling analyses performed on surface infiltration and runoff in Chapters 5 and 6. As this model plays such a central role in this research, it will be introduced first in Section 3.1. Section 3.2 describes the criteria used in this study for determining a scaling field in general, and a universal multifractal field in particular. The chapter concludes by examining the approaches for estimating universal multifractal model parameters in Section 3.3, including a new estimation technique developed here, as well as an analysis of the estimation accuracy.

3.1 Universal Multifractal Model

As introduced in Section 2.1.2, a multifractal field is characterized by a fractal dimension function (Feder, 1988) rather than a single fractal dimension. It is not easy to fully describe a multifractal field because of the infinite number of fractal dimensions associated with it. However, Schertzer and Lovejoy (1987) proposed a universal multifractal (UM) model which completely defines a multifractal field by only three parameters. What follows is an overview of the UM model from the perspective of model application.

To build a discrete random cascade, multiplication of mutually independent and identically distributed (iid) random variables is required on progressively smaller scale (Section 2.1.3). In the UM model, however, these random variables are replaced by iid random variables on the same predefined scale. Schertzer and Lovejoy (1987) showed that by transforming of these iid variables, the final field converges to a Lévy stable distribution. This is elaborated as follow. Denote the iid variables as $\varepsilon_\lambda^{(i)}$ (λ is resolution, i = 1, 2, ..., N, where N is a positive integer) and their logarithms as $\Gamma_\lambda^{(i)}$, then the multiplication of the iid variables corresponds to the addition of their logarithms, *i.e.*

$$\varepsilon_{N,\lambda} = \prod_{i=1}^{N} \varepsilon_\lambda^{(i)} \tag{3.1}$$

yields

$$\Gamma_{N,\lambda} = \sum_{i=1}^{N} \Gamma_\lambda^{(i)} \tag{3.2}$$

where $\Gamma_{N,\lambda}$ is called the generator of the multifractal field. Equation (3.2) is normalized by $N^{1/\alpha}$ so that

$$S_\alpha = \frac{1}{N^{1/\alpha}} \sum_{i=1}^{N} \Gamma_\lambda^{(i)} \tag{3.3}$$

then the re-centered S_α (so its expectation is zero) will converge towards a member of the Lévy stable distributions (Feller, 1971). This class of distributions has the property that the distribution is preserved under convolution, *e.g.* the re-centered S_α has the same distribution as $\Gamma_\lambda^{(i)}$ in eq. (3.3). The characteristic function of Lévy stable distribution is (Samorodnitsky and Taqqu, 1994, Section 1)

$$E\exp(i\theta S)=\begin{cases}\exp\{-\sigma^{\alpha}\mid\theta\mid^{\alpha}[1-i\beta(sign\theta)\tan(\pi\alpha/2)]+i\mu\theta\} & if\ \alpha\neq 1\\ \\ \exp\{-\sigma\mid\theta\mid[1+i\beta(2/\pi)(sign\theta)\ln\mid\theta\mid]+i\mu\theta\} & if\ \alpha=1\end{cases}\tag{3.4}$$

where

$$sign\theta=\begin{cases}1 & if\ \theta>0\\ 0 & if\ \theta=0\\ -1 & if\ \theta<0\end{cases}\tag{3.5}$$

and α ($0 < \alpha \leq 2$) is the Lévy index or the characteristic exponent; μ ($-\infty < \mu < \infty$) is the shift parameter; σ ($\sigma > 0$) is the scale parameter; and β ($-1 \leq \beta \leq 1$) is the skewness parameter. It is noted that Cauchy and Gaussian distributions are two special cases of Lévy distributions with α equal to 1 and 2, respectively. In the UM model, Lévy index α is an important parameter that defines the multifractality (degree of multifractal in comparison with monofractal) of a field. Other parameters of the Lévy distribution are set as $\mu = 0$, $\sigma = 1$, $\beta = -1$. Thus, exponentiation of a generator that has a Lévy or Gaussian distribution will in effect be equivalent to the multiplication of iid random variables after some mathematical operations as described below.

It can be proved (Appendix 3.1) that the energy spectrum of the generator (eq. (3.2)) as proposed by Schertzer and Lovejoy (1987) must be a '1/f noise' (having a wavenumber spectrum $E(k) \propto k^{-1}$ where k is wavenumber vector modulus) for the generated field to be multifractal. This requires an appropriate weighting factor being applied to the generator in the Fourier space. The generator also needs to be filtered for wave number greater than λ so the physical field will be smooth at scales smaller than λ^{-1} as λ^{-1} is the resolution of the field. The formulas for generating a conservative (or homogeneous) physical field, ε_λ, using UM model are (Pecknold *et al.*, 1993)

$$\varepsilon_\lambda = e^{\Gamma_\lambda} \tag{3.6}$$

$$\widetilde{\Gamma}_\lambda = \Im^{-1}\left\{\left(\frac{C_1}{\alpha-1}\right)^{1/\alpha} \widetilde{S}(\alpha) k^{-d/\alpha'} f(\lambda,\vec{k}) \kappa_d(\lambda)\right\} \tag{3.7}$$

where $\widetilde{\Gamma}_\lambda$ is the Fourier transform of generator Γ_λ; $\Im^{-1}$ represents inverse Fourier transform; α is Lévy index ; C_1 is another UM model parameter, it is called codimension of the mean process and defines the sparseness of the average level of the field (Lavallée *et al.*, 1993); $\vec{k}$ is wavenumber vector and k is wavenumber vector modulus; $\widetilde{S}$ is Lévy noise in Fourier space; d is the dimension of the underlying space; α' is related to α through $1/\alpha + 1/\alpha' = 1$; and κ is a factor that makes up the difference between a continuous Fourier transform and the discrete fast Fourier transform (FFT). The multiplication of term $k^{-d/\alpha'}$ is for achieving a '1/f noise'. The function $f(\lambda,\vec{k})$ is 1 for $k \leq \lambda$ and decays exponentially for $k > \lambda$ to filter out wave numbers greater than λ. The equations for generating a Lévy white noise are given by Chambers *et al.* (1976):

$$S(\alpha) = \begin{cases} \dfrac{\sin\alpha(\Phi-\Phi_0)}{(\cos\Phi)^{1/\alpha}}\left[\dfrac{\cos(\Phi-\alpha(\Phi-\Phi_0))}{W}\right]^{(1-\alpha)/\alpha}, & \alpha \neq 1 \\ \dfrac{2}{\pi}\left[(\dfrac{\pi}{2}-\Phi)\tan\Phi + \ln(\dfrac{\pi W \cos\Phi}{\pi - 2\Phi})\right], & \alpha = 1 \end{cases} \tag{3.8}$$

$$\Phi_0 = \frac{2}{\pi}(1-|1-\alpha|)/\alpha \tag{3.9}$$

where Φ is a uniform random variable on ($-\pi/2$, $\pi/2$), and W is a standard exponential deviate, with Φ and W mutually independent. The process described above is actually a fractional integration of order d/α'. Finally, the weighted noise is transformed back into real space and is exponentiated to give the conservative physical field ε_λ.

UM model draws a parallel between a non-conservative (or non-homogeneous) physical field and the velocity field in turbulence (Schertzer and Lovejoy, 1987). The non-conservative velocity field, v, is linked to the conservative energy flux from large to small scales through dimensional analysis as

$$\Delta v_{\lambda} \approx \phi_{\lambda}^{1/3} \lambda^{1/3} \tag{3.10}$$

where Δv is the velocity fluctuation; ϕ is the conservative energy flux; and λ is scale. In analogy with eq. (3.10), a non-conservative physical field, R, is linked to a conservative quantity, ε, through

$$\Delta R_{\lambda} = \varepsilon_{\lambda}^{a} \lambda^{H} \tag{3.11}$$

where ΔR is the fluctuations of the R field; H is the non-conservation parameter and measures the degree of (scale by scale) non-conservation of the R field (Pecknold *et al.*, 1993). H is the last of the three fundamental UM model parameters (the other two are α and C_1). In Fourier space, the relation expressed by eq. (3.11) translates to

$$\Delta \widetilde{R}_{k} = \widetilde{\varepsilon}_{k}^{a} k^{-H} \tag{3.12}$$

or

$$\Delta R_{\lambda} = \Im^{-1} \left\{ \widetilde{\varepsilon}_{k}^{a} k^{-H} \right\} \tag{3.13}$$

where the tilde sign represents Fourier transform. Thus, the fluctuation of a non-conservative field can be derived from the underlying conservative field by filtering it with k^{-H} in the Fourier space. This operation is called fractional integration of order H (H > 0). It has the effect of scale-invariant smoothing of the conservative field (Schertzer and Lovejoy, 1987). The inverse operation, fractional differentiation where a non-conservative field is filtered by k^{H} (H > 0), can be used to get the underlying conservative field of the non-conservative field (Lavallée *et al.*, 1993). In practice, parameter a in eq. (3.11) is almost always taken to be *1*.

In summary, Schertzer and Lovejoy (1987) turned the multiplicative process in a discrete cascade into the addition of generators in the UM model by working with the logarithm of a multifractal field. They further showed that the addition of the generators will converge to Gaussian or Lévy stable distributions, and a multifractal field can be built from a generator that is based on a Gaussian or Lévy noise. Since a stable distribution only has a few parameters, the multifractal fields generated using UM model in turn only depend on a few fundamental parameters. Specifically, the fundamental parameters are Lévy index, α; codimension for the mean process, C_1; and non-conservation parameter, H. Lévy index characterizes the degree of multifractality. As $\alpha \to 0$, simple scaling field results; $\alpha = 2$ corresponds to lognormal multifractals. C_1 measures the sparseness of the average intensity of the field. $C_1 = 0$ represents a space-filling field. If $C_1 > d$ (dimension of the underlying space), then the intensity of the field almost surely vanishes everywhere. H indicates the deviation of the observed field from the underlying conservative (or statistically homogeneous) field. H = 0 represents a conservative field (Lavallée *et al.*, 1993). Appendix 3.2 shows how these three parameters determine the two functions that completely describe a multiscaling field, *i.e.* the moment scaling function (moment slope), K(q), and the codimension function, $c(\gamma)$. Figure 3.1 shows 6 multifractal fields that have different parameter combinations to demonstrate the effects of each parameter.

3.2 Scaling Criteria

This section is divided into two parts. The first part introduces the methods used in literature, including the method adopted in this study, for checking whether a given field

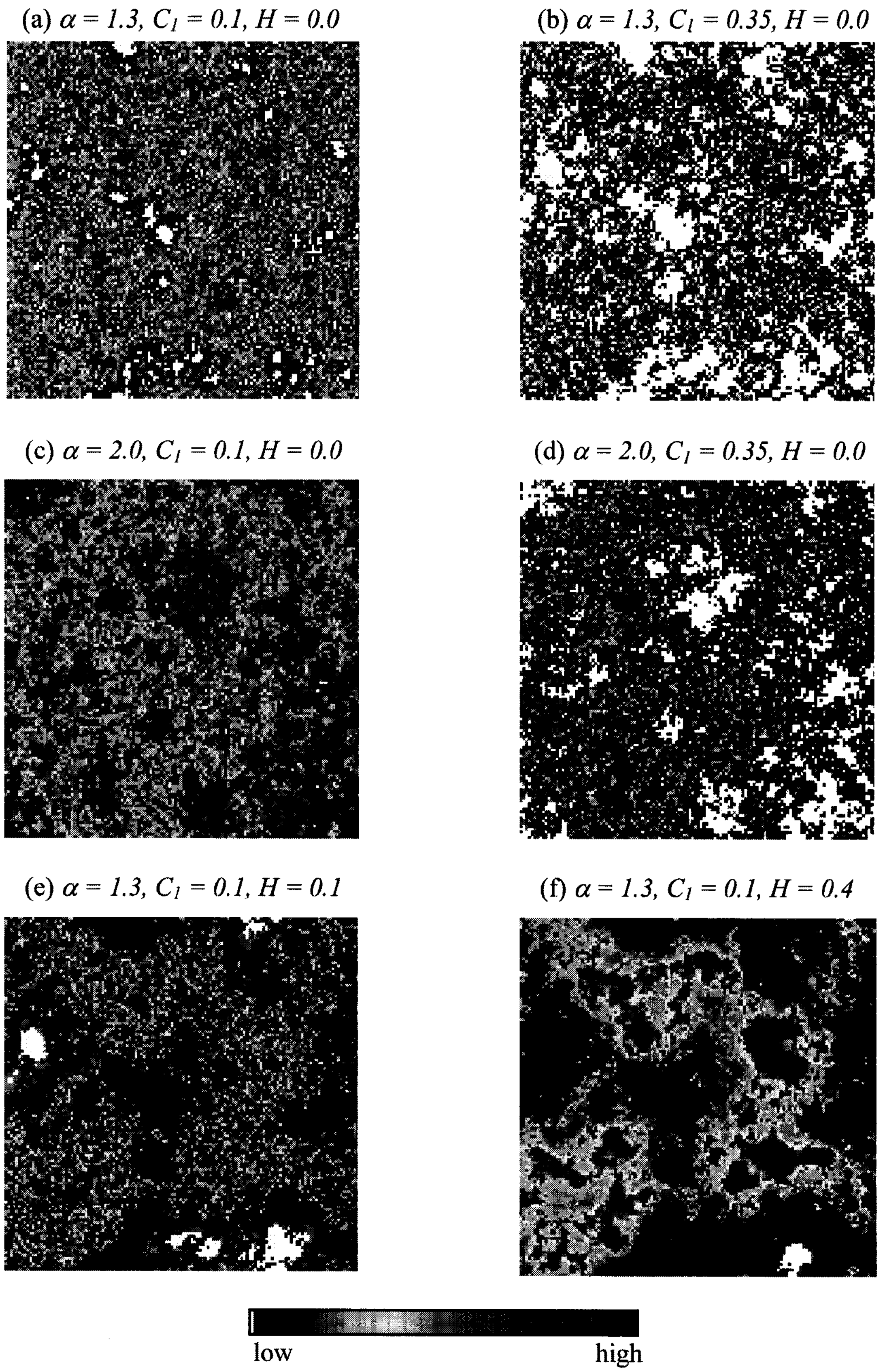

Figure 3.1 Multifractal fields with different UM model parameters

is scaling. A detailed analysis is conducted in an effort to quantitatively define a scaling criterion for this research. The second part of the section concerns the criteria for evaluating the fitness of the UM model to a scaling field.

3.2.1 General Scaling Criteria

A few approaches have been reported in the literature to assess the scaling behavior of a given field or process by exploring their moment, structure function, and power spectrum, *etc.* A brief description of these methods follows.

A conservative scaling field has the following property by definition (Schertzer and Lovejoy, 1987; Gupta and Waymire, 1990)

$$E[\varepsilon_\lambda^{\ q}] \approx \lambda^{\ K(q)} \tag{3.14}$$

where ε is field intensity; λ is resolution; q is the order of moment; and $K(q)$ is the moment scaling function. Thus, the moments of a conservative scaling field will have a logarithm linear relation with scales. The slopes of the regression line for each order, q, is the moment scaling function, $K(q)$, which is linear for a simple scaling field and convex for a multiscaling field. This approach is only appropriate for checking the scaling of conservative fields.

The q^{th} order structure function of a field Q is

$$E[\Delta Q_h^{\ q}] = E[| Q_{r+h} - Q_r |^q] \tag{3.15}$$

where r is distance; and h is distance increment. If Q is a scaling field, the following relation holds with a scale invariant structure function exponent, $\zeta(q)$ (Monin and Yaglom, 1975; Schmitt *et al.*, 1995; Liu and Molz, 1997)

$$E[\Delta Q_h^{\ q}] \approx A h^{\zeta(q)} \tag{3.16}$$

where A may be a function of q but not h. Equation (3.16) shows that the structure function of a scaling field has a log-log linear relation with the distance increment. Since the structure function is defined on the basis of the increment of a field or process (eq. (3.15)), this approach is especially well suited for assessing the scaling of non-conservative fields.

The popular power spectrum method is chosen in this study for checking whether a field is scaling. Equation (3.17) is the formula for computing power spectrum of a 2D field (derived from an IDL program for computing radial power spectrum at http://www.astro.washington.edu/deutsch-bin/getpro/library28.html?PSD). Note the symbol $E()$ in eq. (3.17) represents power spectrum, not moment.

$$E(k) = 2\pi k \,|\, \widetilde{R}(k) \,|^2 \tag{3.17}$$

where $\widetilde{R}$ is the Fourier transform of a physical field under study, $|\widetilde{R}|$ is the Fourier amplitude; and k is wavenumber modulus

$$k = \sqrt{k_x^{\ 2} + k_y^{\ 2}} \tag{3.18}$$

where

$$k_x = \begin{cases} \dfrac{i-1}{n_x/2}, & 1 < i \le \dfrac{n_x}{2} \\ \dfrac{i-n_x-1}{n_x/2}, & \dfrac{n_x}{2} < i \le n_x \end{cases} \tag{3.19}$$

and

$$k_y = \begin{cases} \dfrac{j-1}{n_y/2}, & 1 < j \le \dfrac{n_y}{2} \\ \dfrac{j-n_y-1}{n_y/2}, & \dfrac{n_y}{2} < j \le n_y \end{cases} \tag{3.20}$$

where n_x and n_y are the numbers of pixels in the X and Y directions, respectively. Power spectrum has the following property if the field is scaling.

$$E(k) \approx k^{-\beta} \tag{3.21}$$

Figure 3.2 shows the power spectrum of a climate proxy temperature time series from Greenland ice-core records (Schmitt *et al.*, 1995). Since a 1D time series is the study subject in this particular case, the independent variable is frequency, *f*, rather than wavenumber, *k*.

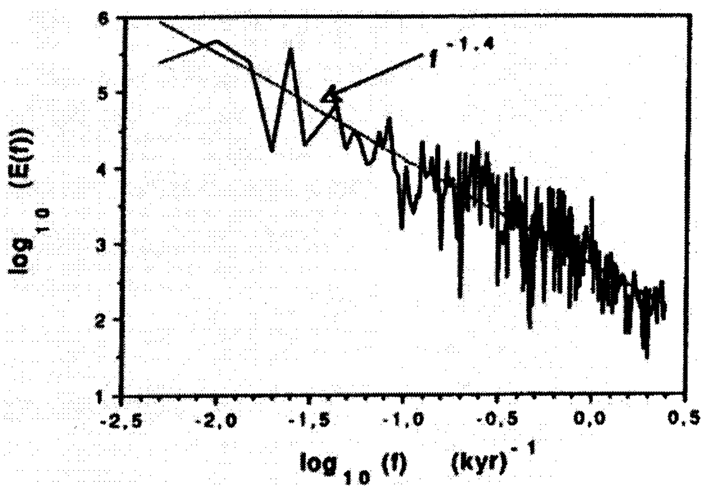

Figure 3.2 Power spectrum of climate proxy temperature time series (from Schmitt et al., 1995). Symbol f represents frequency.

Radial power spectrum is used in this research because the studied fields are embedded in a 2D space. Radial power spectrum is obtained by angular integration in Fourier space. When using the power spectrum approach, an intrinsic assumption is made that the field being examined is isotropic. However, radial power spectrum will largely average out the effect of spectral anisotropy (Falco *et al.*, 1996). Another issue about power spectrum is the sample size. The relation expressed by eq. (3.21), like other power law relations in the scaling theory, only holds on average, *i.e.* a large sample size is required for the equations to be accurate (Lavallée *et al.*, 1993). The equation will be broken on a single realization (sample size = 1). For instance, large variation is always observed in the spectrum of a single field (Figure 3.2). The power spectrum method can be applied to both conservative and non-conservative fields directly. This is because the fluctuation of a non-conservative field has the same power spectrum slope, $-\beta$, and linearity as the non-conservative field itself. It is these two characteristics rather than the power spectrum itself that are relevant in scaling analysis.

The applications of power spectrum method in literature are mostly qualitative. An effort was made in this study to use the approach in a quantitative manner so certain criteria are set for evaluating whether a given field is scaling. For a field to be scaling, two conditions must be met:

1) The logarithm of the power spectrum is a linear function of the logarithm of the wavenumber, *i.e.* the power spectrum is a straight line in a log-log scale.
2) The slope of the straight line in the log-log domain ($-\beta$) is less than 0, *i.e.* $\beta > 0$. This states that more prominent features of a field (corresponding to smaller wavenumber) contribute more to the power than finer features (corresponding to larger wavenumber) do. This is the usual case for scaling physical fields. It is noted here that white noise in 2D space has $\beta = -1$ (slope = 1). This can be derived from eq. (3.17).

To quantify the linearity of power spectrum, a modified R^2 variable is employed which is based on the conventional R^2 ($0 \leq R^2 \leq. 1$). The equation for computing the conventional R^2 is given below.

$$R^2 = \frac{\left[n\sum_{i=1}^{n}(x_i y_i) - (\sum_{i=1}^{n} x_i)(\sum_{i=1}^{n} y_i) \right]^2}{\left[n\sum_{i=1}^{n} x_i^{\,2} - (\sum_{i=1}^{n} x_i)^2 \right]\left[n\sum_{i=1}^{n} y_i^{\,2} - (\sum_{i=1}^{n} y_i)^2 \right]} \qquad (3.22)$$

where y_i is the corresponding value of a real data point x_i (i = 1, ..., n) on the regression line. This definition of R^2 is not an ideal measure for accessing linearity because it is angle (of regression line) dependent. Figure 3.3 illustrates this point with the power spectrum of a runoff field (Chapter 6) and its replica with an angle shift, *i.e.* the two lines have the same variations around their respective regression lines. The figure shows that the R^2 values of the two lines are drastically different.

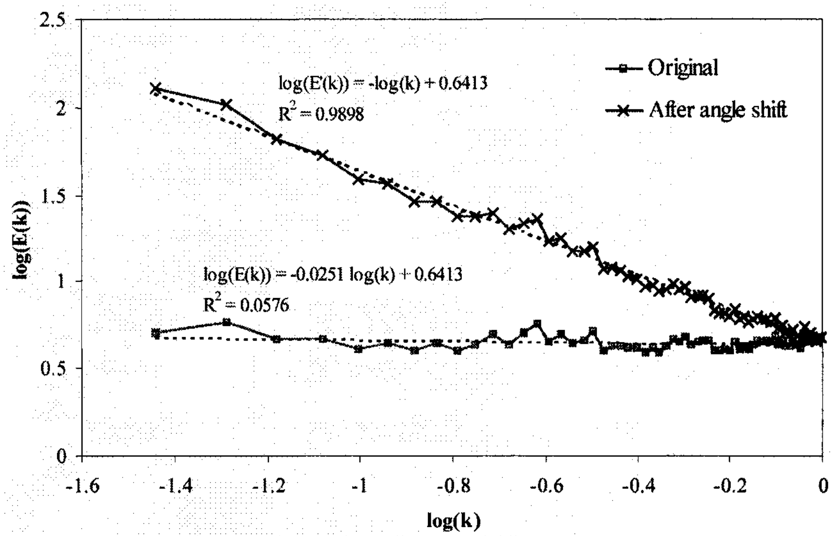

Figure 3.3 Radial power spectrum of runoff field from steady scaling rain field (α_R = 1.2, C_{1R} = 0.1, and H_R = 0.2) and scaling K_s field (α_{Ks} = 2.0, C_{1Ks} = 0.01, and H_{Ks} = 0.2) at 150 min, and its replica with an angle shift.

To overcome the above-mentioned problem, all power spectrums are transformed to slope = -1 using the following equation before their R^2 values are calculated.

$$\log(E'(k)) = \log(E(k)) - (1+s)\log(k) \tag{3.23}$$

where $E'(k)$ is the power spectrum after the angle shift; and s is the slope of the original power spectrum. This modified R^2 instead of the conventional R^2 is used throughout the rest of the study. To determine a threshold modified R^2 (the word 'modified' is dropped hereafter for brevity) that can be used as an indication of a linear spectrum in the log-log domain, an experiment is conducted whereby a number of multifractal fields is generated using the UM model and the R^2 values of their logarithm power spectrums are calculated. Table 3.1 lists the UM model parameters (α, C_1, and H) of the 108 cases tested.

Table 3.1 UM Model Parameters of the 108 Cases for Determining R^2 Threshold

Case #	α	C_1	H	R^2	Case #	α	C_1	H	R^2	Case #	α	C_1	H	R^2
1	1.2	0.1	0.0	0.94	37	1.4	0.5	0.2	0.94	73	1.8	0.4	0.0	0.94
2	1.4	0.1	0.0	0.96	38	1.6	0.5	0.2	0.94	74	1.8	0.01	0.2	0.97
3	1.6	0.1	0.0	0.96	39	1.8	0.5	0.2	0.94	75	1.8	0.05	0.2	0.97
4	1.8	0.1	0.0	0.96	40	2.0	0.5	0.2	0.94	76	1.8	0.2	0.2	0.95
5	2.0	0.1	0.0	0.96	41	1.2	0.5	0.4	0.92	77	1.8	0.4	0.2	0.94
6	1.2	0.1	0.2	0.94	42	1.4	0.5	0.4	0.94	78	1.8	0.01	0.4	0.97
7	1.4	0.1	0.2	0.96	43	1.6	0.5	0.4	0.94	79	1.8	0.05	0.4	0.97
8	1.6	0.1	0.2	0.96	44	1.8	0.5	0.4	0.94	80	1.8	0.2	0.4	0.95
9	1.8	0.1	0.2	0.96	45	2.0	0.5	0.4	0.94	81	1.8	0.4	0.4	0.94
10	2.0	0.1	0.2	0.96	46	1.2	0.01	0.0	0.94	82	1.2	0.1	0.1	0.94
11	1.2	0.1	0.4	0.94	47	1.2	0.05	0.0	0.94	83	1.2	0.1	0.3	0.94
12	1.4	0.1	0.4	0.96	48	1.2	0.2	0.0	0.93	84	1.2	0.1	0.5	0.94
13	1.6	0.1	0.4	0.96	49	1.2	0.4	0.0	0.92	85	1.2	0.3	0.1	0.93
14	1.8	0.1	0.4	0.96	50	1.2	0.01	0.2	0.94	86	1.2	0.3	0.3	0.93
15	2.0	0.1	0.4	0.96	51	1.2	0.05	0.2	0.94	87	1.2	0.3	0.5	0.93
16	1.2	0.3	0.0	0.93	52	1.2	0.2	0.2	0.93	88	1.2	0.5	0.1	0.92
17	1.4	0.3	0.0	0.94	53	1.2	0.4	0.2	0.92	89	1.2	0.5	0.3	0.92
18	1.6	0.3	0.0	0.95	54	1.2	0.01	0.4	0.94	90	1.2	0.5	0.5	0.92
19	1.8	0.3	0.0	0.94	55	1.2	0.05	0.4	0.94	91	1.4	0.1	0.1	0.96
20	2.0	0.3	0.0	0.94	56	1.2	0.2	0.4	0.93	92	1.4	0.1	0.3	0.96
21	1.2	0.3	0.2	0.93	57	1.2	0.4	0.4	0.92	93	1.4	0.1	0.5	0.96
22	1.4	0.3	0.2	0.94	58	1.4	0.01	0.0	0.96	94	1.4	0.3	0.1	0.94
23	1.6	0.3	0.2	0.95	59	1.4	0.05	0.0	0.96	95	1.4	0.3	0.3	0.94
24	1.8	0.3	0.2	0.94	60	1.4	0.2	0.0	0.95	96	1.4	0.3	0.5	0.94
25	2.0	0.3	0.2	0.94	61	1.4	0.4	0.0	0.94	97	1.4	0.5	0.1	0.94
26	1.2	0.3	0.4	0.93	62	1.4	0.01	0.2	0.96	98	1.4	0.5	0.3	0.94
27	1.4	0.3	0.4	0.94	63	1.4	0.05	0.2	0.96	99	1.4	0.5	0.5	0.94
28	1.6	0.3	0.4	0.95	64	1.4	0.2	0.2	0.95	100	1.8	0.1	0.1	0.96
29	1.8	0.3	0.4	0.94	65	1.4	0.4	0.2	0.94	101	1.8	0.1	0.3	0.96
30	2.0	0.3	0.4	0.94	66	1.4	0.01	0.4	0.96	102	1.8	0.1	0.5	0.96
31	1.2	0.5	0.0	0.92	67	1.4	0.05	0.4	0.96	103	1.8	0.3	0.1	0.94
32	1.4	0.5	0.0	0.94	68	1.4	0.2	0.4	0.95	104	1.8	0.3	0.3	0.94
33	1.6	0.5	0.0	0.94	69	1.4	0.4	0.4	0.94	105	1.8	0.3	0.5	0.94
34	1.8	0.5	0.0	0.94	70	1.8	0.01	0.0	0.97	106	1.8	0.5	0.1	0.94
35	2.0	0.5	0.0	0.94	71	1.8	0.05	0.0	0.97	107	1.8	0.5	0.3	0.94
36	1.2	0.5	0.2	0.92	72	1.8	0.2	0.0	0.95	108	1.8	0.5	0.5	0.94

The parameters shown in Table 3.1 cover a wide range of parameter combinations. They are chosen in such a manner that the first 45 cases examine the effect of α under different C_1 and H, cases 46 to 81 explores the effect of C_1, while cases 82 to 108 check the effect of H. For statistical accuracy and to be consistent with the numerical studies later on, 25 experiments are carried out for each of the 108 cases and the average of the 25 R^2 values is used in analysis. Figure 3.4(a) shows the average power spectrums of the first 10 cases listed in Table 3.1; the histogram of the 25 R^2 from the first case (a = 1.2, C1 = 0.1, H = 0.0) is shown in Figure 3.4 (b); and the average R^2 values of all the cases are displayed in Figure 3.4 (c). The large R^2 variation observed in Figure 3.4 (b) demonstrates the necessity of performing multiple experiments. Figure 3.4 (c) reveals that the R^2 values of the 108 cases are fairly high with an average of 0.945 and indicate good linearity in all the cases tested. The pattern present in this figure also indicates that R^2 is dependant of input scaling parameters, especially α and C_1 (refer to Table 3.1). Based on the above analysis, a value of 0.9 is set in this study to be the reference R^2 threshold for assessing the logarithm linearity of power spectrum. More specifically, the following factors are taken into consideration in choosing this reference value:

i) As indicated in Figure 3.4 (c), the average R^2 value from the 108 cases is 0.945. This average value is derived from the multifractal fields generated using UM model. These fields supposedly have better defined scaling properties than real data which are plagued with uncertainties involved in the processes of obtaining the data. For instance, Figure 3.2 demonstrates the level of noise that might be present in the power spectrum of a real physical field. Even in the case of numerical simulations such as in this study, the data fields (infiltration and runoff) are also under the influences of uncertainties introduced by model assumptions and by numerical approximations of the real watershed processes, *etc.* Such uncertainties could lower the R^2 of the data fields significantly. Therefore it is reasonable to relax the R^2 threshold to a lower value than the average R^2 from the 108 cases.

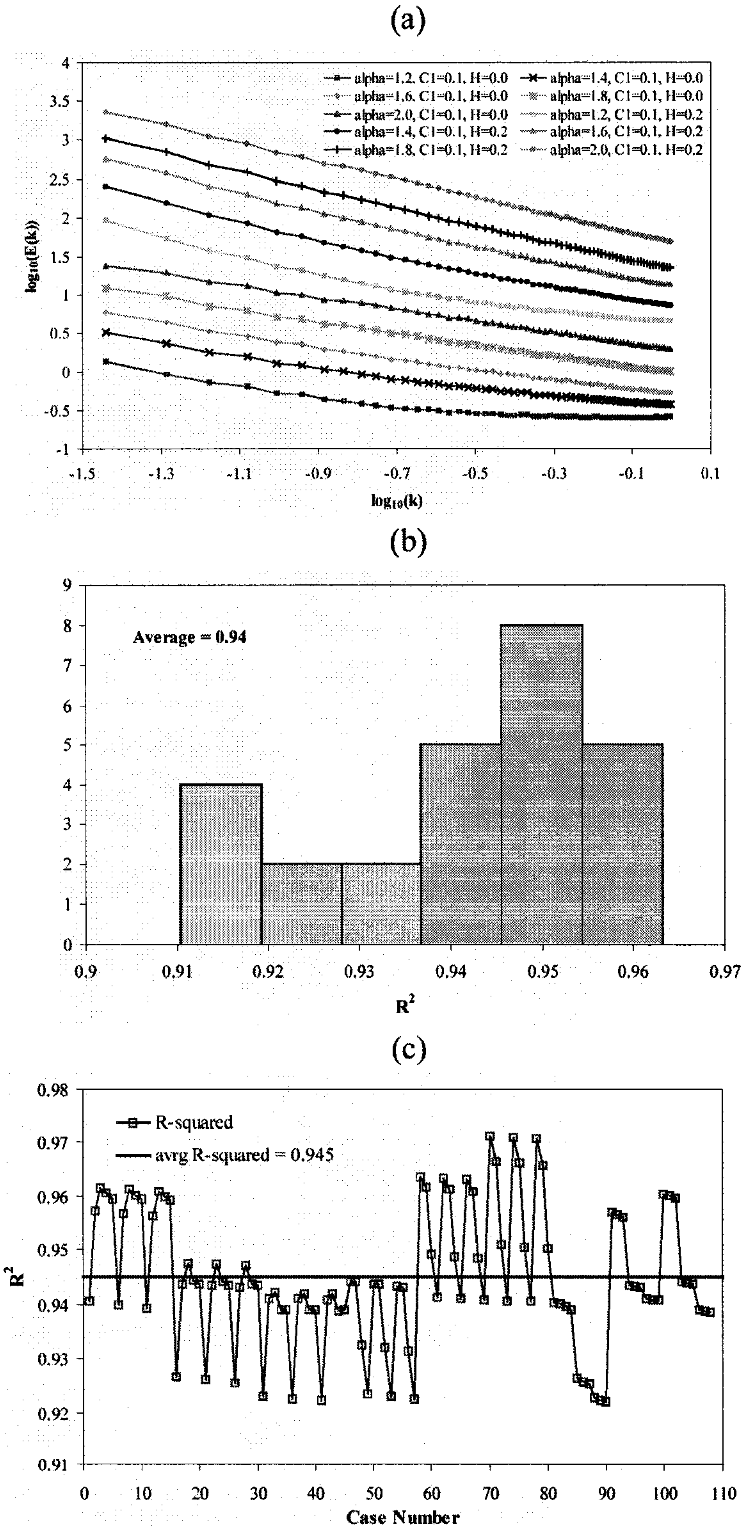

Figure 3.4 (a) Log-log plot of power spectrums of multifractal fields (the lines have been offset for clarity), each line represents the average power spectrum from 100 fields with the same UM model parameters; (b) R^2 histogram of the first case in Table 3.1; (c) R^2 values of the108 average power spectrums.

ii) A generated scaling field such as rainfall usually has smoother power spectrum than a derived field such as infiltration. The latter is subject to the influences from rainfall, soil (K_s) and topography (especially channels) among some other factors, and the complex interactions of these driving factors. It is conceivable that such derived fields will have noisier power spectrum and thus lower R^2 than the generated fields. Figure 3.5 illustrates this point by comparing three pairs of rain and the corresponding infiltration power spectrums from one of the cases cited in Chapter 5.

iii) A wide range of R^2 values are observed in the above analysis. Figure 3.4(a) shows that even a generated scaling field may have non-linear power spectrum at the high end of the wavenumber (*e.g.* cases with $\alpha = 1.2$). Since the rainfall and the K_s fields used in this research are generated using the UM model, the influence of their power spectrums is expected to propagate to some of the output fields. Hence, such variation in the R^2 should be taken into consideration when choosing the R^2 threshold for judging the scaling of the output fields.

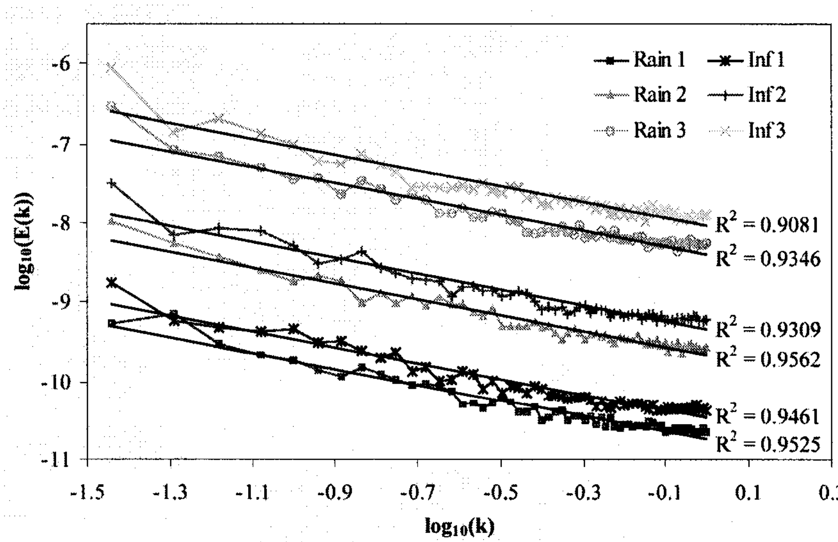

Figure 3.5 Comparison of three sets of power spectrums of steady rains ($\alpha = 1.2$, $C_1 = 0.1$, and $H = 0.0$) and their corresponding infiltration fields at 150 min. after rain starts.

It is noted that $R^2 = 0.9$ is intended to be an indicator of scaling behavior rather than a cutoff value for scaling field. It will be physically unrealistic to impose such a strict cutoff value. Thus, two terms are used in this study to describe a field as "strongly scaling" or "weakly scaling" depending on if its R^2 is above or below but close to 0.9. Only fields with R^2 values much smaller than 0.9 can be determined to be non-scaling.

3.2.2 Criteria for Fitting UM Model

For a conservative multifractal field that fits in the UM model framework, its moment scaling function K(q) (eq. (3.14)) can be predicted from its UM model parameters (eqs. (A3.17) and (A3.19) in Appendix 3.2). The agreement between the predicted and the estimated K(q) has been used in literature as evidence of various physical fields and processes being described by the UM model. However, this approach suffers from two constraints. The first one is the divergence of the moments for order $q > q_D$, where q_D is the critical moment, due to a phenomenon called the first-order multifractal phase transition (Schertzer *et al.*, 1993). This critical moment is equal to the slope of the algebraic tails of the probability density distribution, *i.e.* (Pandey *et al.*, 1998)

$$\Pr(\varepsilon_\lambda \geq s) \approx s^{-q_D} \qquad for\ s >> 1 \tag{3.24}$$

Secondly, for any finite number of samples, there is also a maximum order moment that can be reliably estimated. This maximum order is denoted as q_s and can be determined by UM model parameters and the spatial and sample dimensions. The second-order multifractal phase transition is responsible for the existence of the maximum order moment (Schertzer *et al.*, 1993; Pandey *et al.*, 1998). Besides the above two constraints, the determination of the theoretical moment scaling function is only for conservative field, *i.e.* it involves only two UM model parameters, α and C_1.

The UM model also links the slope of the logarithm of power spectrum, $-\beta$, to its parameters through the following equation (the same as eq. (A3.24) in Appendix 3.2)

$$H = \frac{\beta - 1}{2} + \frac{C_1(2^\alpha - 2)}{2(\alpha - 1)} \qquad (3.25)$$

or

$$\beta = 2H - \frac{C_1(2^\alpha - 2)}{\alpha - 1} + 1 \qquad (3.26)$$

As shown in Appendix 3.2, the derivation of eq. (3.25) involves the theoretical formula for computing moment scaling function (eq. (A3.17)). Thus, using eq. (3.26) to examine the fitness of the UM model to a scaling field is equivalent to using the moment scaling function technique. Besides keeping in line with the general scaling criteria adopted in this study, eq. (3.26) also has the advantage of being a function of all three UM model parameters. This feature is important for this research because most of the scaling fields included in later chapters are non-conservative. However, this technique (hereafter denoted as β-technique) also has its own shortcomings. As shown in Figure 3.4 (a), for instance, the power spectrum of a scaling field may not be a straight line as wavenumber increases. Therefore in such cases, the value of β is very sensitive to the portion of a log-log power spectrum line used for deriving the slope.

To form a general guideline for using the β-technique in later chapters, the slopes of the 108 average power spectrums in the last section are calculated and analyzed below. It was found through experiments that the estimated β are generally closest to the theoretical β if the portion of a power spectrum corresponding to the lowest 10 or fewer wavenumbers is used in estimation. Thus, the slope of the log-log power spectrum is usually estimated using the first 5 to 10 points in the rest of the study. Figure 3.6 shows the average power spectrums of the first 5 cases in Table 3.1 along with their respective regression lines.

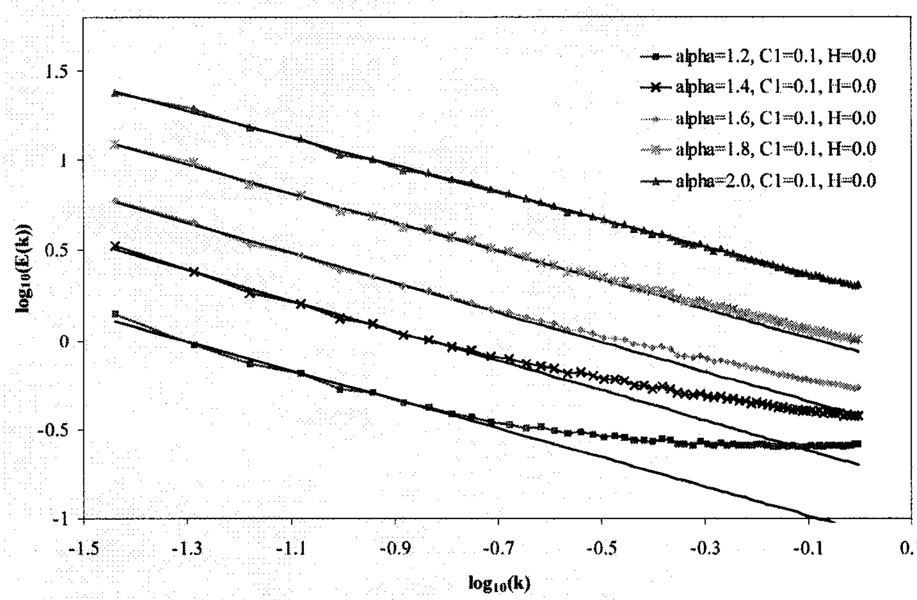

Figure 3.6 Average power spectrums of the first 5 cases in Table 3.1 and their respective regression lines (the lines have been offset for clarity).

Figure 3.7 compares the estimated β of the 108 cases in Table 3.1 with the theoretical β values predicted using eq. (3.26). Parameters α and C_1 used for the theoretical predictions are estimated from the generated (underlying) conservative fields (Section 3.3.1 and 3.3.4). Parameter H is taken to be the input H as this parameter is generally accurately reproduced (Section 3.3.4). It is noted that the 108 cases include both conservative and non-conservative multifractal fields. The pattern observed in Figure 3.7 reveals the sensitivity of β to the scaling parameters (refer to Table 3.1). Compared with the theoretical predictions, it is clear that β is generally overestimated if both α and C_1 are large, and underestimated if both parameters are small. The overall root mean square difference (RMSD) between the theoretical β and the estimated β of the108 cases is 0.0427. This is a very small RMSD considering the sensitivity of β to the estimation method.

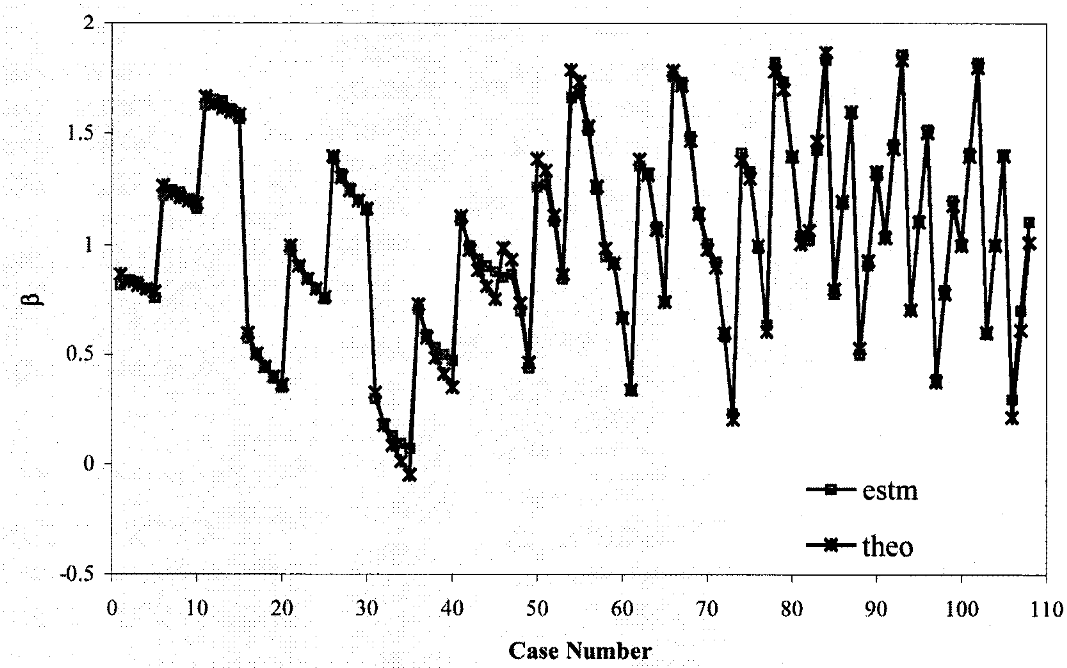

Figure 3.7 Comparison of theoretical and estimated β of 108 multifractal cases

The β-technique is employed in Chapter 5 for evaluating the suitability of fitting UM model to the various scaling infiltration fields. Compared to the above 108 cases, a much larger degree of uncertainty is involved in the application of the technique to the infiltration fields as elaborated in Section 5.3.4. Thus, no attempt is made herein to set a general quantitative criterion for fitting UM model to a scaling field.

3.3 Estimation of Model Parameters

Needless to say, an accurate estimation of model parameters is essential to the success of the numerical studies carried out in this research effort. This section introduces some of the methods used in the literature for estimating the three UM model parameters, followed by a technique developed in this study for refined estimation of the parameters. The last part of this section evaluates the estimation approaches by comparing the input and the estimated model parameters of a series of multifractal fields.

3.3.1 Estimation of α and C_1

The most effective method for estimating α and C_1 of a conservative scaling field was the Double Trace Moment (DTM) technique developed by Lavallée (1991). The basic idea of the technique is to introduce a second moment η by transforming the highest resolution scaling field $\varepsilon_{\lambda'}$ into its η-th power $\varepsilon_{\lambda'}^{\eta}$ where resolution λ' is the ratio of the scale of the field (*i.e.* the largest scale) to the smallest scale of homogeneity. The relation between the moment of this new field and the scale yields the 'double' moment exponent $K(q, \eta)$ (Lavallée, 1991; Lavallée *et al.*, 1993):

$$\overline{E}\left[\sum_{i_\lambda}\left(\sum_{j_{\lambda'}}\varepsilon_{\lambda'}{}^{\eta}\right)^{q}\right] \approx \lambda^{K(q,\eta)-(q-1)d} \tag{3.27}$$

where the first summation (i) is over all disjoint sets covering the field at resolution λ ($\lambda \leq \lambda'$); the second summation (j) is over all pixels of the largest resolution λ' in each set of resolution λ; the ensemble average $\overline{E}[\ ]$ is over all the realizations; η and q are the powers of the moment; and d is the dimension of the physical field. For the slope of the double trace moment, following relationships hold

$$K(q, \eta) = \begin{cases} \dfrac{C_1}{\alpha - 1}\eta^{\alpha}(q^{\alpha} - q), & \alpha \neq 1 \\ C_1 \eta q \log(q), & \alpha = 1 \end{cases} \tag{3.28}$$

That is

$$\log|K(q,\eta)| \propto \alpha \log(\eta) \qquad \alpha \neq 1 \tag{3.29}$$

and

$$C_1 = \frac{(\alpha - 1)\, 10^{\log|K(q,1)|}}{q^{\alpha} - q} \qquad \eta = 1 \tag{3.30}$$

Thus, α can be estimated from a simple plot of $\log|K(q, \eta)|$ versus $\log(\eta)$ for fixed q. C_1 is then obtained using eq. (3.30). Figure 3.8 shows a sample log-log plot of $|K(q, \eta)|$ against η. Two values of q are used in this case: q = 1.1 and q = 2.0. They give consistent estimations of α and C_1. Logarithm of $|K(q, \eta)|$ will deviate from the straight line at too low or too high values of η, so the range of η used in this study is usually from 0.1 to 0.5. Parameter α and C_1 of any conservative fields are estimated using the DTM technique throughout this study.

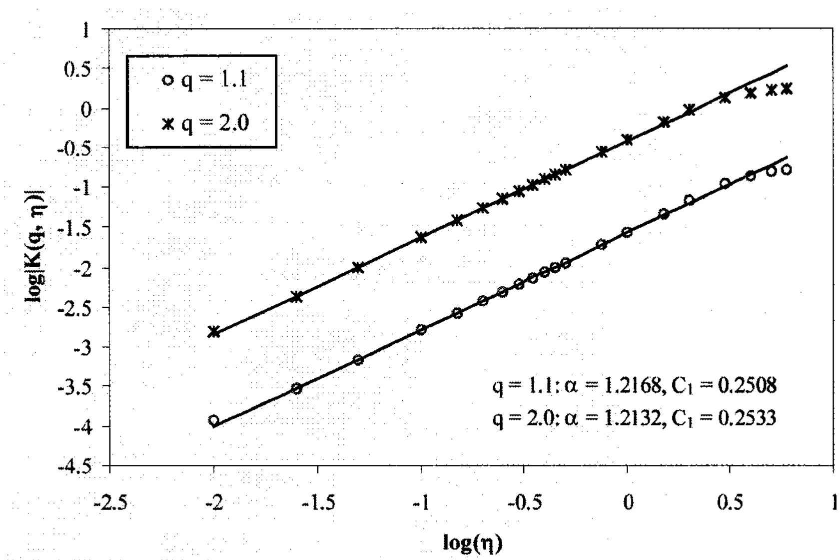

Figure 3.8 Log $|K(q, \eta)|$ versus $\log(\eta)$ of a conservative scaling field with $q = 1.1$ and $q = 2.0$. The input parameters of the scaling field are: $\alpha = 1.2$, and $C_1 = 0.3$.

3.3.2 Initial Estimation of H

Schmitt *et al.* (1995) and Liu and Molz (1997) introduced a method for estimating UM model parameter H of a non-conservative scaling field using structure functions. The following equation defines the q^{th} order structure function

$$E[(\Delta R_h)^q] = E[|R(z+h) - R(z)|^q] \tag{3.31}$$

where E[ ] is moment, R is a multifractal process, z is distance, and h is distance increment. If q = 2, the above equation defines variogram. For scaling processes, the scale invariant structure function exponent, $\xi(q)$, (Monin and Yaglom, 1975) is defined by

$$E[(\Delta R_h)^q] = Ah^{\xi(q)} \tag{3.32}$$

where A may be a function of q but not of h, or

$$\log\{E[(\Delta R_h)^q]\} \propto \xi(q)\log(h) \tag{3.33}$$

The structure function exponent, ξ, has the following relation with the three UM model parameters (Wilson *et al.*, 1991)

$$\xi(q) = qH - \frac{C_1}{\alpha - 1}(q^\alpha - q), \qquad \alpha \neq 1 \tag{3.34}$$

Thus H = $\xi(1)$. Figure 3.9 shows a sample log-log plot of the first order structure function versus distance increment of two generated non-conservative fields. The slopes of the straight lines are the estimated H.

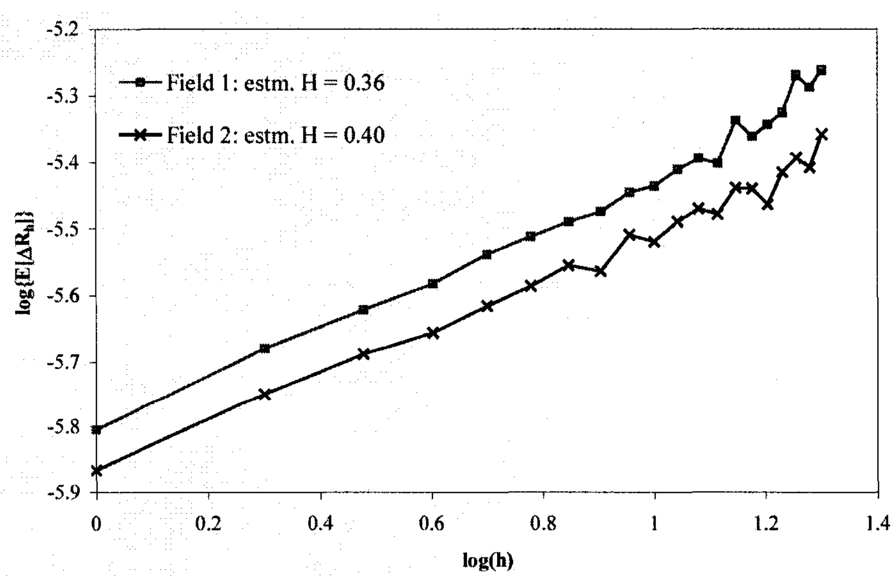

Figure 3.9 Log-log plot of the first-order structure function versus distance increment of two non-conservative scaling fields with parameters α = 1.2, C_1 = 0.1 and H = 0.4.

This approach is adopted in this study to estimate 'initial' H. As explained in the next section, the 'initial' H estimate as well as the 'initial' α and C_1 estimates need to be further refined for more accurate results.

3.3.3 Refined Estimation of UM Model Parameters

Values of the parameter H estimated using the approach as described in the last section inevitably would have some inaccuracy. Since H is needed for the fractional differentiation that yields the underlying conservative field from a non-conservative field (Section 3.1), and parameters α and C_1 are estimated from the conservative field, estimated α and C_1 become functions of estimated H. It is found that the α estimate is very sensitive to H. Figure 3.10 shows an example of such sensitivity from a simulated (non-conservative) infiltration field which corresponds to a steady rain with input parameters $\alpha = 1.2$, $C_1 = 0.2$, and $H = 0.5$ (Chapter 5). It is observed that the estimated α value decreases rapidly when the estimated H falls into a tiny range around the true H. This characteristic is exploited in this study to find more accurate parameter estimates. The procedure for refined parameter estimation is summarized below.

i) An initial H estimate is obtained using structure function (Section 3.3.2)

ii) A search range is decided based on the initial H value.

iii) A series of H values within the search range are determined with a small increment between any two consecutive values. For each trial H, a fractional differentiation of order H is applied to the (non-conservative) field with its minimum value removed throughout the field to achieve a 'fluctuation' field, and α and C_1 are calculated from the derived conservative field using DTM.

(a)

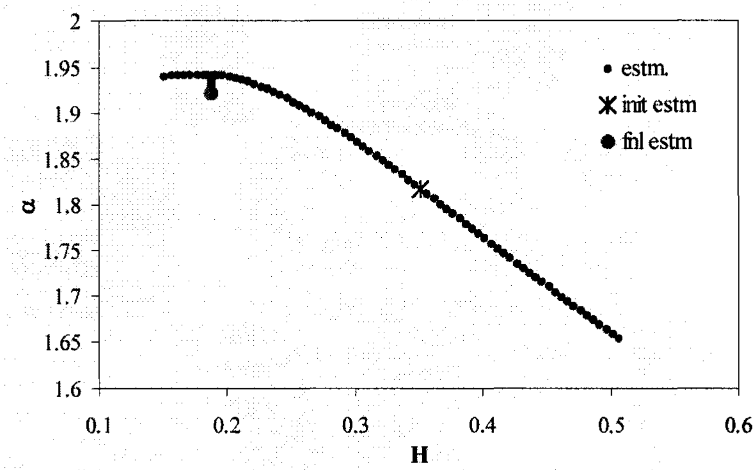

(b)

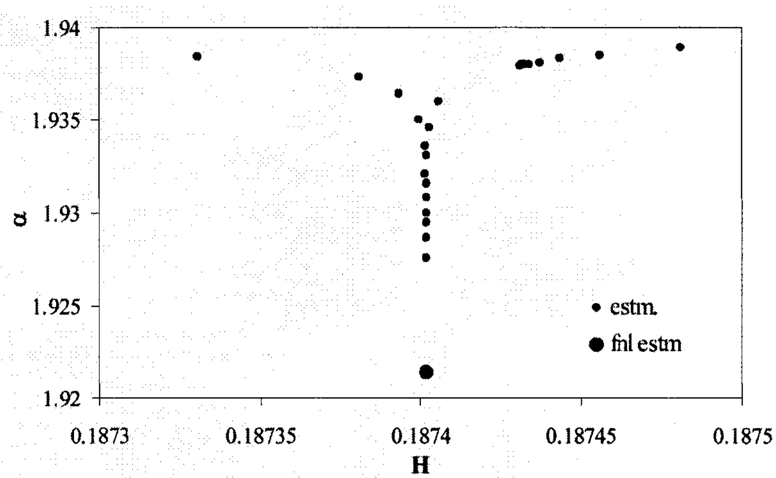

Figure 3.10 Sensitivity of estimated α to estimated H, (a) α versus H in the initial search range for H, (b) α versus H in the refined search range for H.

iv) If a 'trough' exists in a plot of α versus H (Figure 3.10), a smaller search range is determined around the "trough", and more trial-and-error is performed until the difference between two consecutive estimated $\alpha < 10^{-4}$ and/or H $< 10^{-7}$. The last set of α, C_1 and H are the final estimated multifractal parameters. Figure 3.11 displays the estimated C_1 versus estimated H from the same field as the one used for Figure 3.10.

Besides the sensitivity of the estimated α to the estimated H, computer limitations also make it impossible to precisely recover the extremely small values (on the order of 10^{-6} or smaller) in the original underlying conservative fields when a fractional differentiation is performed. This is another source of the inaccuracy observed in the estimations of α and C_1. Because of these reasons, the above procedure tends to over- or under-estimate α and C_1 to a certain degree, but produces a remarkably accurate H estimate. This is demonstrated in detail in the next section.

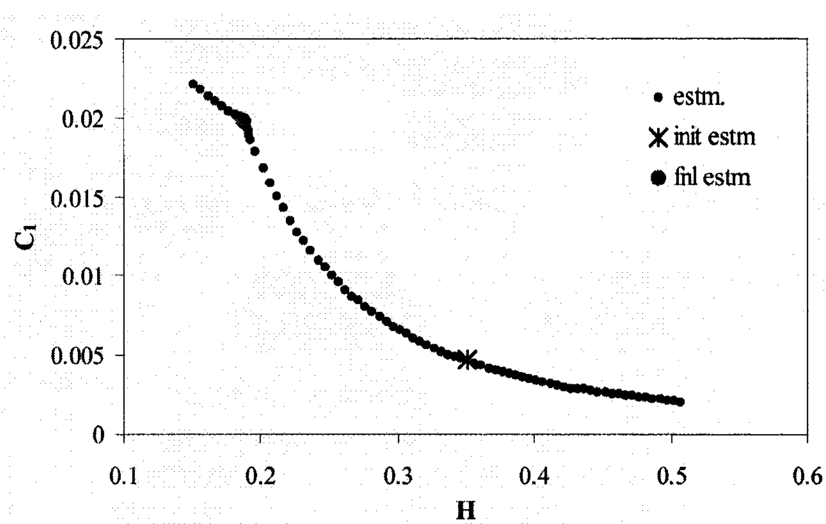

Figure 3.11 Estimated C_1 versus estimated H

3.3.4 Evaluation of Estimated Parameters

The estimated parameters are evaluated in this section to show the effectiveness of the estimation techniques. The estimated parameters of some conservative fields are first examined before the evaluation of the estimated parameters of non-conservative fields. Since non-conservative fields are generated from their underlying conservative fields, the estimated parameters of the conservative fields serve as input parameters to the non-conservative fields and are essential to the statistical analysis of the estimated parameters of the latter.

A conservative UM multifractal field is defined by two parameters: α and C_1. Nine pairs of α and C_1 are used to generate conservative fields as shown in Table 3.2. With each pair of the input parameters, 100 conservative fields are generated and the two parameters of each field are estimated using the DTM technique. Figure 3.12 (a) compares the input α and the average α estimates from the 100 fields. Figure 3.12 (b) shows the relative bias and the relative RMSE of the estimated α. These figures reveal that the estimated α do not always agree with the input parameter. The discrepancy is the largest with small input C_1 and small to medium α. On average (100 experiments), the relative biases of the 9 cases range from –0.01 to 0.07, and the maximum relative RMSE is 0.09.

Table 3.2 Input Parameters of Conservative Fields

α	C_1
1.2	0.02
1.2	0.1
1.2	0.4
1.5	0.02
1.5	0.1
1.5	0.4
2	0.02
2	0.1
2	0.4

The estimated C_1 of the 9 cases are compared to their corresponding input parameters in Figure 3.13 (a). The statistics of the estimated C_1 are shown in Figure 3.13 (b). The difference between the estimated and the input C_1 increases with C_1. However, the discrepancies between the two sets of values are also small with relative bias ranging from –0.12 to 0.06 and the maximum relative RMSE is 0.307 with most RMSE less than 0.15. As with estimated α, the largest relative RMSE is associated with small

C_1 and small to medium α. The above results indicate that the input UM model parameters are reproduced with good accuracy in the generated conservative fields.

To evaluate the estimated parameters of non-conservative fields, 27 sets of parameters (α, C_1, and H) (Table 3.3) are selected and 100 conservative and then non-conservative

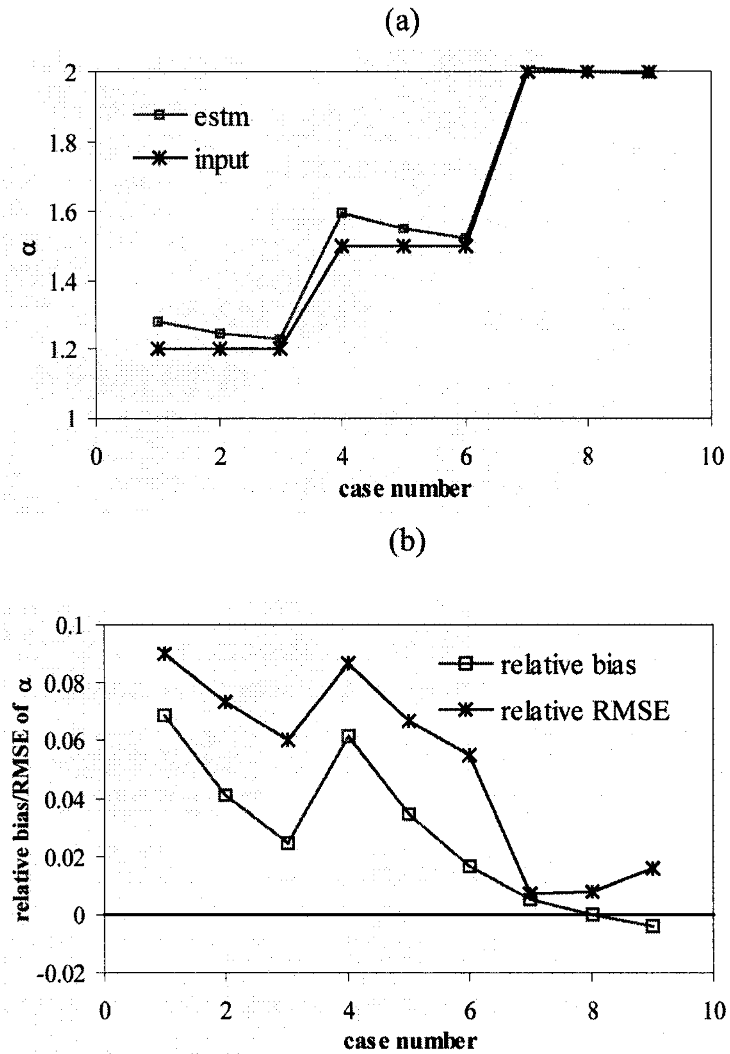

Figure 3.12 Parameter α of conservative fields, (a) comparison of the input α and the average α estimates from 100 fields; (b) bias and RMSE of the estimated α of 100 fields.

fields are generated for each set of parameters. The parameter sets cover a wide range of parameter combinations. The DTM technique is used to first estimate α and C_1 from the conservative fields, which then serve as the input parameters for the corresponding non-conservative fields. The procedure outlined in Section 3.3.3 is followed to derive the estimated parameters of the non-conservative fields. Figure 3.14 (a) compares the average initial α estimates, the average final α estimates, and the input α. The initial α estimates are from the fields that are derived from fractionally differentiating the non-conservative fields by order of the initial H estimates. Again, the input α are the estimated α of the conservative fields. Figure 3.14 shows the statistics of the estimated α from the 100 fields. The following conclusions can be drawn from Figure 3.14 about the estimated α of non-conservative fields:

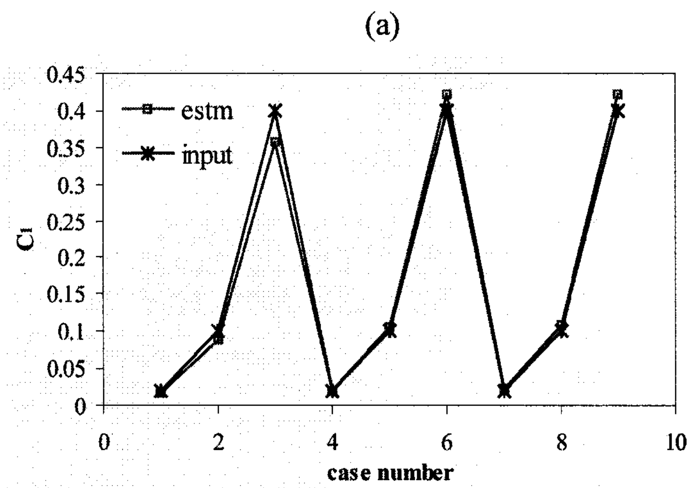

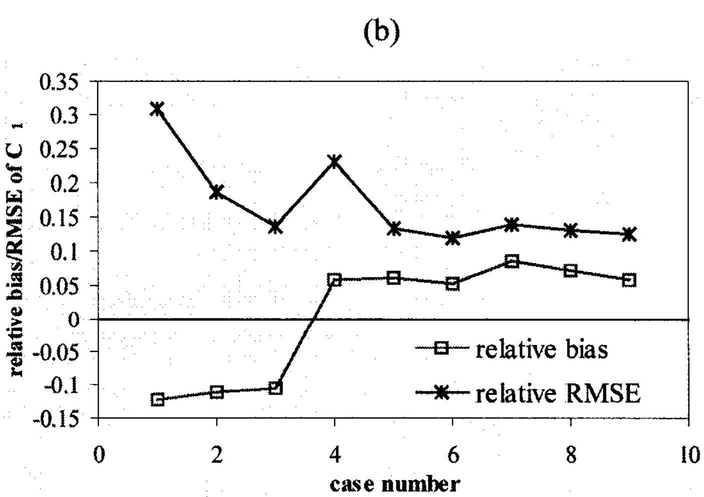

Figure 3.13 Parameter C_1 of conservative fields, (a) comparison of the input C_1 and the average C_1 estimates from 100 fields; (b) bias and RMSE of the estimated C_1 of 100 fields.

Table 3.3 Input Parameters of Non-conservative Fields

Case #	α	C_1	H
1	1.2	0.02	0.1
2	1.2	0.02	0.3
3	1.2	0.02	0.5
4	1.2	0.1	0.1
5	1.2	0.1	0.3
6	1.2	0.1	0.5
7	1.2	0.4	0.1
8	1.2	0.4	0.3
9	1.2	0.4	0.5
10	1.5	0.02	0.1
11	1.5	0.02	0.3
12	1.5	0.02	0.5
13	1.5	0.1	0.1
14	1.5	0.1	0.3
15	1.5	0.1	0.5
16	1.5	0.4	0.1
17	1.5	0.4	0.3
18	1.5	0.4	0.5
19	2.0	0.02	0.1
20	2.0	0.02	0.3
21	2.0	0.02	0.5
22	2.0	0.1	0.1
23	2.0	0.1	0.3
24	2.0	0.1	0.5
25	2.0	0.4	0.1
26	2.0	0.4	0.3
27	2.0	0.4	0.5

i) It is crucial to perform the refined parameter estimation for more accurate α estimate of a non-conservative field.

ii) Parameter α is overestimated with small and medium input α and especially with large input C_1.

iii) Parameter α is underestimated with large input α and especially with small input C_1.

(a)

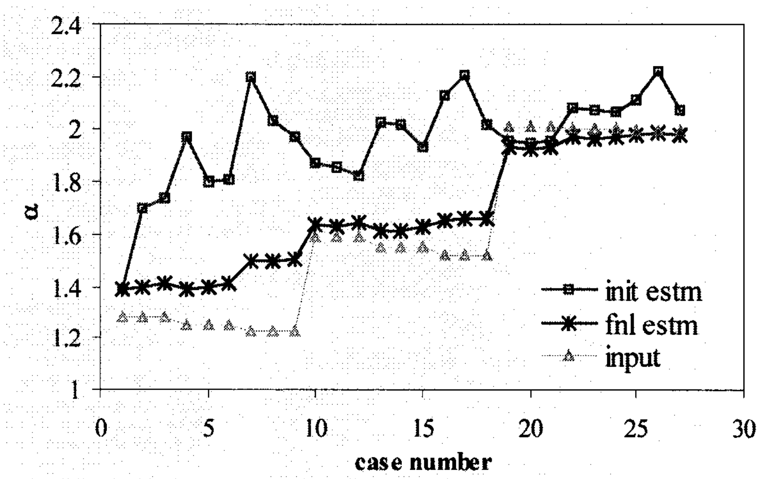

(b)

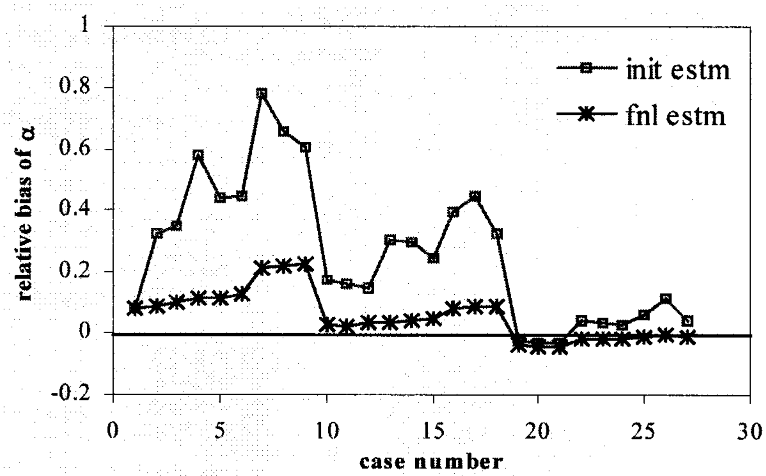

(c)

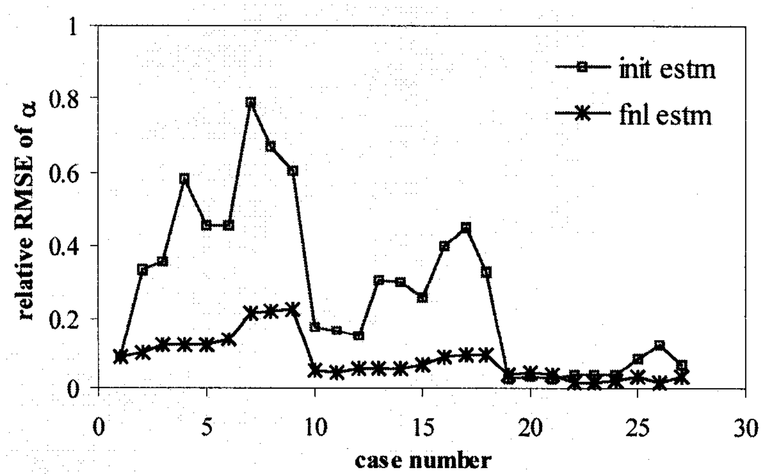

Figure 3.14 Parameter α of non-conservative fields, (a) comparison of the input α and the initial and the final α estimates; (b) bias of the initial and the final α estimates; (c) RMSE of the initial and the final α estimates.

iv) The relative biases of the final α estimates range from -0.04 to 0.23. The maximum bias is with small input α and large input C_1.

v) The relative RMSE of the final α estimates is less than 0.23. The maximum RMSE is, as with the bias, with small input α and large input C_1.

Figure 3.15 (a) compares the average initial C_1 estimates, the average final C_1 estimates, and the input C_1. Figure 3.15 (b) and (c) respectively show the relative bias and the relative RMSE of the estimated C_1 from the 100 fields. The conclusions drawn from this set of figures are as follows:

i) It is crucial to perform the refined parameter estimation for more accurate C_1 estimate of a non-conservative field.

ii) Parameter C_1 is overestimated with small to medium input α and large input C_1.

iii) The relative biases of the final C_1 estimates range from -0.05 to 0.49. The maximum relative bias is with large input α and small input C_1.

iv) The relative RMSE of the final C_1 estimates is less than 0.51. The maximum relative RMSE is, as with the bias, with large input α and small input C_1.

Figure 3.16 (a) compares the average initial H estimates, the average final H estimates, and the input H. Figure 3.16 (b) and (c) respectively show the bias and the RMSE of the estimated H from the 100 fields. The following conclusions can be obtained from this set of figures:

i) It is crucial to perform the refined parameter estimation for more accurate H estimate of a non-conservative field. In fact, the errors in the initial H

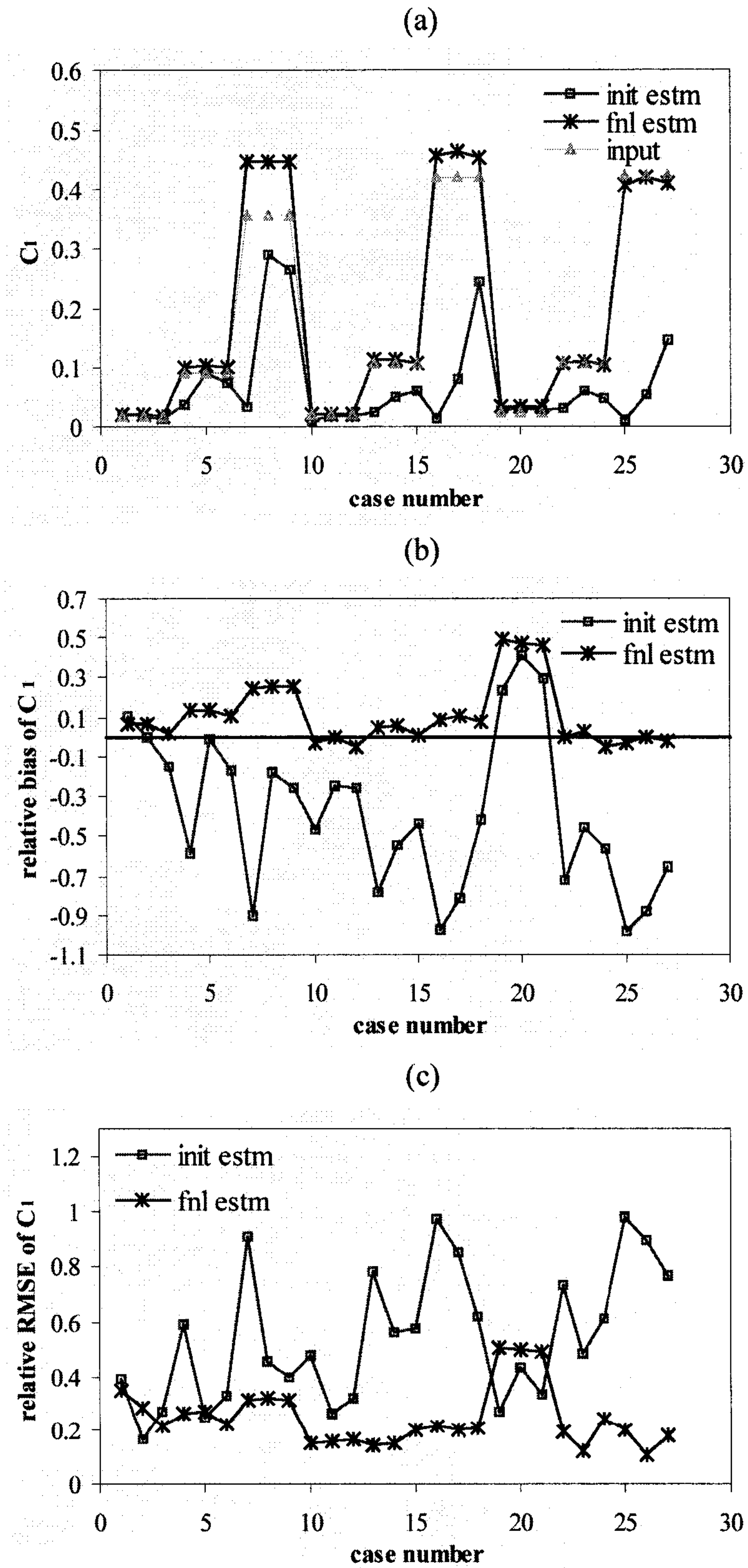

Figure 3.15 Parameter C_l of non-conservative fields, (a) comparison of the input C_l and the initial and the final C_l estimates; (b) bias of the initial and the final C_l estimates; (c) RMSE of the initial and the final C_l estimates.

estimates are the direct reason for the gross errors in the initial α and C_1 estimates observed in Figures 3.14 and 3.15.

ii) The final H estimates have excellent agreement with the input H. The only noticeably differences are with large α ($\alpha \cong 2.0$), especially with small C_1 ($C_1 \cong 0.02$). However, the discrepancies in H in these cases do not cause serious errors in the estimated α and C_1 as shown in Figures 3.14(a) and 3.15(a).

iii) The majority of the relative biases of the final H estimates range from –0.02 to 0.14 with one exception of 0.76 when input $\alpha \cong 2.0$, $C_1 \cong 0.02$ and $H = 0.1$.

iv) The relative RMSE of the final H estimates is mostly less than 0.47 with one exception of 0.91 which, again, is when input $\alpha \cong 2.0$, $C_1 \cong 0.02$ and $H = 0.1$.

In summary, the refined parameter estimation technique developed in this study can produce accurate H estimates for most non-conservative fields, which in turn lead to generally good C_1 and α estimates. The cases with the maximum estimation errors are associated with either small α and large C_1 or large α and small C_1.

3.3.5 Parameter Estimation using Quasi-Monte Carlo Technique

As introduced in Section 3.1, the scaling fields generated using the UM model are based on Lévy noise, *i.e.* the fields have a random nature. Therefore, a number of fields with the same UM model parameters are generated for every multifractal case presented in this Chapter. The averages of the estimated parameters and other relevant values of these fields are used in various analyses. This practice follows the concept of Monte Carlo technique. The same procedure is applied in Chapter 5 and 6 for estimating scaling parameters and other variables of the infiltration and runoff processes. A series of simulations is run in each case studied and the average quantities are analyzed for scaling

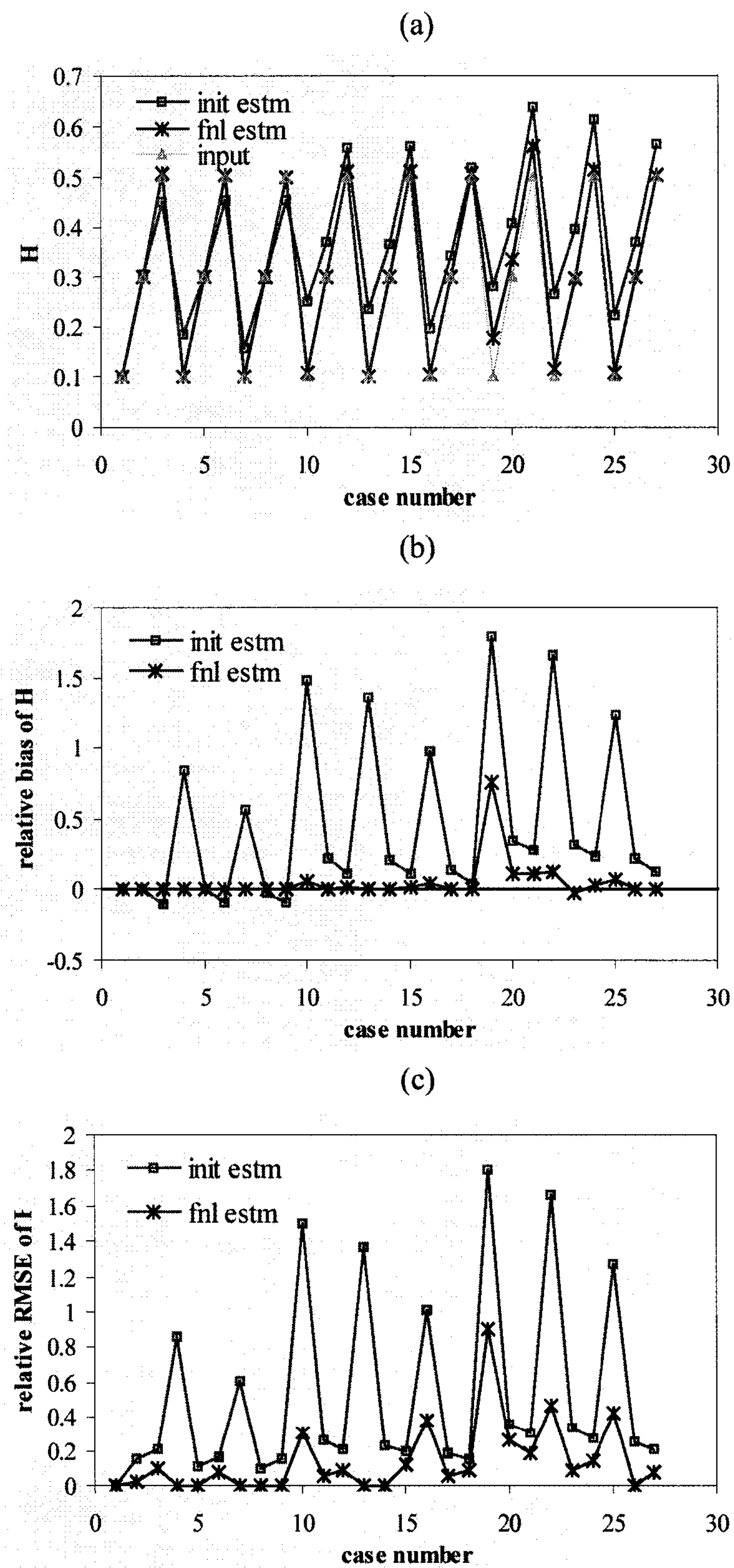

Figure 3.16 Parameter H of non-conservative fields, (a) comparison of the input H and the initial and the final H estimates; (b) bias of the initial and the final H estimates; (c) RMSE of the initial and the final H estimates.

behavior. This approach is labeled a quasi-Monte Carlo method because only 25 experiments are conducted in most cases. The number of 'samples' in this study is limited by the vast amount of time it takes to more accurately estimate the scaling parameters of non-conservative scaling fields and to perform any data analysis in the space-time rainfall cases because of the large size of the original rain fields (Section 5.4).

Chapter 4

DIMBRR RAINFALL-RUNOFF MODEL AND ITS CALIBRATION AND VERIFICATION

A physically based, distributed rainfall-runoff model, called the D-Infinity Model Based Rainfall-Runoff (DIMBRR) model, has been developed in this work for the study of watershed processes. It consists of the following basic elements: flow path scheme, ponding time computation, infiltration computation, over-land flow routing, and channel flow routing. The first part of this chapter describes the DIMBRR rainfall-runoff model, and the second part is devoted to the calibration and verification of this model.

4.1 Rainfall–Runoff Model

4.1.1 Flow Path Scheme

There have been a few methods developed in the past two decades or so to determine flow directions on hillslopes based on grid digital elevation models (DEM). The earliest and simplest method is the single flow direction (SFD) algorithm, or D8, (O'Callaghan and Mark 1984) which assigns flow from each pixel to one of its eight neighbors, either adjacent or diagonal, in the direction with steepest downward slope. The shortcoming of this model is the limitation of flow direction to only eight possible directions. To overcome the problems of the single flow direction algorithm, multiple flow direction

(MFD) methods were suggested by Quinn *et al.* (1991) and Freeman (1991) which distribute flow fractionally to each lower neighbor in proportion to the slope toward the neighbor. The disadvantage of this approach arises from the dispersion of flow from a pixel to all its neighboring pixels with lower elevation. Lea (1992) and Coasta-Cabral and Burges (1994) proposed two relatively more complicated models for specifying flow direction. While these models overcome the problems of SFD and MFD models, they are hindered by the requirement of fitting a plane to four pixel corners that are usually not on a plane. This problematic requirement can lead to inconsistent or counterintuitive flow directions. The model finally chosen for this study is a method proposed by Tarboton (1997), D∞ (stands for infinite direction) model, which represents flow direction as a single angle (anywhere between 0 and 2π) based on the steepest downward slopes. It compared favorably to most other schemes available (Tarboton, 1997).

The basic concept of this procedure is to first define eight facets for each pixel (Figure 4.1). In Figure 4.1 (a), there are nine pixels depicted in dotted lines and eight triangular facets centered at the central pixel. Figure 4.1 (b) shows a single facet and the symbols used in the computation of slope and flow direction in that facet where d_i ($i = 1, 2$) is distance between two pixels and e_i ($i = 1, 2, 3$) symbolizes the elevation of a pixel. Downward slope is represented by the vector (s_1, s_2) where

$$s_1 = \frac{e_0 - e_1}{d_1} \tag{4.1}$$

$$s_2 = \frac{e_1 - e_2}{d_2} \tag{4.2}$$

The slope direction and magnitude for this facet are

$$r = \tan^{-1}\left(\frac{s_1}{s_2}\right) \tag{4.3}$$

$$s = (s_1^{\ 2} + s_2^{\ 2})^{1/2} \tag{4.4}$$

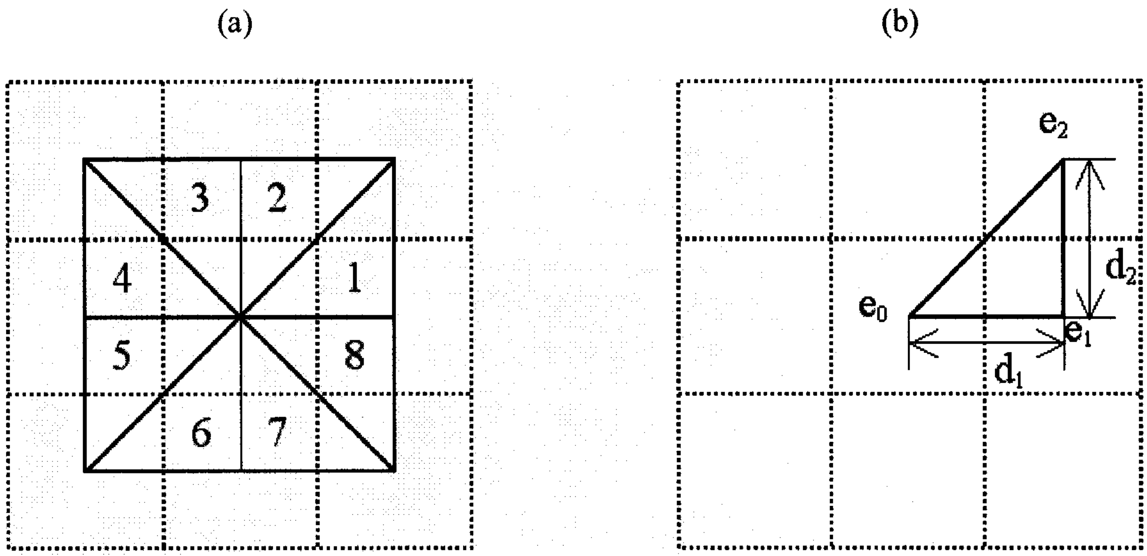

Fig. 4.1 Layout of grid for calculation of slope in D∞ model (reproduced from Tarboton, 1997)

The eight slopes for each pixel are compared and the maximum downward slope is chosen to be the slope for the pixel and the corresponding slope direction is the direction of flow of this pixel. If this angle follows one of the cardinal (0, $\pi/2$, π, and $3\pi/2$) or diagonal ($\pi/4$, $3\pi/4$, $5\pi/4$, and $7\pi/4$) directions, flow from this pixel directs to only one downslope pixel. Otherwise, flow is apportioned into two downslope pixels according to how close the flow angle is to the direct angle to this pixel center. The watershed area contributing to each pixel can then be calculated based on flow directions of all its upslope pixels. A threshold contributing area can be defined and any pixels with contributing area larger than the threshold value will be taken as channel pixels, *i.e.* pixels being part of a channel.

Since a one-dimensional routing scheme and an implicit finite difference method will be employed for DIMBRR model, it is essential to determine the flow path and the routing sequence pixel by pixel. This is accomplished with the aid of flow direction at each pixel, which is obtained using Tarboton's (1997) flow direction model. After flow paths are determined, routing can proceed in order. At each time step, the first set of pixels where infiltration and excess runoff are calculated is the pixels that do not take any inflows from their neighboring pixels. The next set of pixels handled is the pixels that only receive inflows from the first set of pixels, *i.e.* pixels that have already been operated. This cascading procedure proceeds until all pixels are dealt with. Then time advances one step and the same computation procedure is repeated. This routing process lasts until the end of the time period of interest.

4.1.2 Ponding Time Computation

DIMBRR model assumes variable rainfall both in space and time. Such an assumption requires a ponding time formula that can handle variable rainfall rate. Smith and Parlange (1978) have developed a formula based on theoretical considerations which in principle suit any rainfall pattern. Broadbridge and White (1987) slightly improved this formula by changing its coefficient M from 0.5 to the range $0.5 \leq M \leq 0.66$ with an average value of 0.55. The final form of the formula for calculating ponding time with variable rainfall rate is

$$\int_0^{t_p} R(t)dt = M\left[\frac{S^2(\theta_i)}{K_e}\right]\ln\left[\frac{K_e}{R(t_p)-K_e}\right] \tag{4.5}$$

where R(t) is rainfall rate at time t; t_p is ponding time; $S(\theta_i)$ is soil sorptivity at initial soil moisture content, θ_i, $S(\theta_i) = [2(\phi - \theta_i)K_e\psi]^{1/2}$, ϕ is soil porosity, K_e is effective hydraulic conductivity which is assumed to equal saturated hydraulic conductivity K_s in this study, ψ is wetting front suction. It should be noted that R(t) in this formula represents rainfall rate only when there is no inflow or run-on from adjacent pixels. Should there be run-on before ponding occurs at a pixel, R(t) has to incorporate both rainfall and run-on. This feature is included in the DIMBRR model.

The required input data for the computation of ponding time includes following fields: saturated hydraulic conductivity, rainfall rate, initial soil moisture content, porosity and wetting front suction for the computation of sorptivity.

4.1.3 Infiltration Component

Infiltration excess runoff or Hortonian runoff is taken to be the mechanism for runoff generation in this study where overland flow occurs when rainfall intensity exceeds infiltration rate.

The Green-Ampt model is adopted for the computation of infiltration capacity,

$$i_c(t) = \begin{cases} R(t), & \text{for } t \le t_p \\ K_e + \dfrac{K_e[h(t) + R(t)/2 + \psi](\phi - \theta_i)}{I(t)}, & \text{for } t > t_p \end{cases} \tag{4.6}$$

where $i_c(t)$ is infiltration capacity rate at time t; h(t) is surface water depth; I(t) is cumulative infiltration. Before the time to ponding, infiltration at each pixel is equal to the rainfall rate. At each time step after the time to ponding, rainfall rate is added to surface water depth and infiltration capacity is computed from eq. (4.6). The actual infiltration rate is taken as the minimum of the infiltration capacity and the available water supply rate, *i.e.*

$$i(t) = \min\left[i_c(t),\ R(t) + \frac{h(t)}{\Delta t} \right] \tag{4.7}$$

It is also noted that infiltration rate equals surface water supply rate if the latter is less than K_e.

The required data for infiltration computation includes the following fields: rainfall rate, saturated hydraulic conductivity, wetting front suction, porosity, and initial soil moisture content.

4.1.4 Overland Flow Routing

The average slope over the chosen study area (discussed in Chapter 5) is larger than 3%. Slope of this magnitude is steep enough to satisfy the assumption of a kinematic wave model, *i.e.* the friction and gravity forces balance each other and the acceleration terms and pressure terms can be neglected (Chow, *et al.*, Chapter 9, 1988). The continuity equation for one-dimensional flow is

$$\frac{\partial A}{\partial t}+\frac{\partial Q}{\partial x}=q \tag{4.8}$$

where A is area of cross section of control volume, Q is discharge, and q is lateral inflow per unit length. The momentum equation for kinematic wave is

$$S_0 = S_f \tag{4.9}$$

where S_0 is slope; and S_f is friction slope. Manning's equation (Chow, *et al.*, Chapter 9, 1988) in SI units is

$$Q=\frac{S_f^{\frac{1}{2}}}{nP^{\frac{2}{3}}}A^{\frac{5}{3}} \tag{4.10}$$

or

$$A=\left(\frac{nP^{\frac{2}{3}}}{S_f^{\frac{1}{2}}}\right)^{\frac{3}{5}}Q^{\frac{3}{5}} \tag{4.11}$$

where n is Manning roughness coefficient, and P is wetted perimeter. Taking the derivative of A with respect to t in eq. (4.11) and combining the result with eq. (4.8) and (4.9), an equation with Q(t) as the only dependent variable can be derived (Chow, *et al.*, Chapter 9, 1988)

$$\frac{\partial Q}{\partial t}+\frac{5}{3}\left(\frac{S_0^{\frac{1}{2}}}{nP^{\frac{2}{3}}}\right)^{\frac{3}{5}}Q^{\frac{2}{5}}\frac{\partial Q}{\partial x}-\frac{5}{3}\left(\frac{S_0^{\frac{1}{2}}}{nP^{\frac{2}{3}}}\right)^{\frac{3}{5}}Q^{\frac{2}{5}}q=0 \qquad (4.12)$$

For overland flow,

$$P=B \qquad (4.13)$$

and

$$h=\frac{A}{B} \qquad (4.14)$$

where B is pixel width, and h is surface water depth.

To numerically solve eq. (4.12) and (4.14), an implicit finite difference scheme will be adopted because of its well-known stability and capability to handle relatively large time step. The following approximations are made for ∂Q/∂t, ∂Q/∂x, Q, and q

$$\frac{\partial Q}{\partial t}\approx\frac{Q_i^{\,j}-Q_i^{\,j-1}}{\Delta t} \qquad (4.15)$$

$$\frac{\partial Q}{\partial x}\approx\frac{Q_i^{\,j}-Q_{i-1}^{\,j}}{\Delta x} \qquad (4.16)$$

$$Q\approx\frac{Q_{i-1}^{\,j}+Q_i^{\,j-1}}{2} \qquad (4.17)$$

$$q\approx\frac{q_i^{\,j}+q_i^{\,j-1}}{2} \qquad (4.18)$$

where Q_i^j and Q_i^{j-1} are respectively the discharge of pixel i at time step j and j-1, $Q_i^{\ j}$ is unknown, Q_{i-1}^j is the summation of inflows from all immediate upslope pixels to pixel i at time step j. Δx_i^j is the weighted average of the distances between the center of pixel i and the centers of all immediate upslope pixels depending on their contributing inflows. q_i^j and q_i^{j-1} are respectively the excess rainfall rate of pixel i at time step j and j-1. Substituting eqs. (4.15) - (4.18) into eq. (4.12) and manipulating the result yields the equation for the unknown Q_i^j

$$Q_i^j = \frac{\frac{\Delta t}{\Delta x} Q_{i-1}^j + \frac{3}{5}\left(\frac{nB^{\frac{2}{3}}}{S_0^{\frac{1}{2}}}\right)^{\frac{3}{5}} \left(\frac{Q_{i-1}^j + Q_i^{j-1}}{2}\right)^{-\frac{2}{5}} Q_i^{j-1} + \Delta t\left(\frac{q_i^j + q_i^{j-1}}{2}\right)}{\frac{\Delta t}{\Delta x} + \frac{3}{5}\left(\frac{nB^{\frac{2}{3}}}{S_0^{\frac{1}{2}}}\right)^{\frac{3}{5}} \left(\frac{Q_{i-1}^j + Q_i^{j-1}}{2}\right)^{-\frac{2}{5}}} \tag{4.19}$$

The water depth h_i^j can then be determined from eqs. (4.11) and (4.14)

$$h_i^j = \left[\frac{n}{\sqrt{S_0}B}\right]^{\frac{3}{5}} \left(Q_i^j\right)^{\frac{3}{5}} \tag{4.20}$$

The initial condition is $Q_i^0 = 0$ for all pixels in the study area. The boundary condition for a watershed is that inflow from outside the watersheds remains zero.

The required input data for overland flow routing includes the following fields: slope, and Manning roughness coefficient.

4.1.5 Channel Flow Routing

Channel pixels should first be carefully defined based on certain criteria. The same kinematic wave model used for overland flow is applied to channel flow routing. In this study, the channels are assumed to have trapezoidal shape. It is assumed that channel bottom width is B, the slope for channel left bank is S_L and for right bank S_R. Then

$$C = \frac{1}{S_L} + \frac{1}{S_R} \tag{4.21}$$

$$h = -\frac{B}{C} + \sqrt{\left(\frac{B}{C}\right)^2 + \frac{2A}{C}} \tag{4.22}$$

$$P = B + h\left(\sqrt{1 + \frac{1}{S_L^{\,2}}} + \sqrt{1 + \frac{1}{S_R^{\,2}}}\right) \tag{4.23}$$

The numerical solutions for channel flow are

$$Q_i^j = \frac{\frac{\Delta t}{\Delta x} Q_{i-1}^j + \frac{3}{5}\left(\frac{nP_i^{j\frac{2}{3}}}{S_0^{\frac{1}{2}}}\right)^{\frac{3}{5}} \left(\frac{Q_{i-1}^j + Q_i^{j-1}}{2}\right)^{-\frac{2}{5}} Q_i^{j-1} + \Delta t\left(\frac{q_i^j + q_i^{j-1}}{2}\right)}{\frac{\Delta t}{\Delta x} + \frac{3}{5}\left(\frac{nP_i^{j\frac{2}{3}}}{S_0^{\frac{1}{2}}}\right)^{\frac{3}{5}} \left(\frac{Q_{i-1}^j + Q_i^{j-1}}{2}\right)^{-\frac{2}{5}}} \tag{4.24}$$

and

$$h_i^j = -\frac{B}{C} + \sqrt{\left(\frac{B}{C}\right)^2 + \frac{2A_i^j}{C}} \tag{4.25}$$

where

$$A_i^j = \left[\frac{n\left(P_i^j\right)^{\frac{2}{3}}}{\sqrt{S_0}}\right]^{\frac{3}{5}} \left(Q_i^j\right)^{\frac{3}{5}} \tag{4.26}$$

$$P_i^j = B + h_i^{j-1}\left(\sqrt{1 + \frac{1}{S_L^{\,2}}} + \sqrt{1 + \frac{1}{S_R^{\,2}}}\right) \tag{4.27}$$

The main difference between channel routing and overland flow routing lies in the Q_{i-1}^j and q_i terms in eq. (4.24). For channel routing, Q_{i-1}^j becomes the inflow from the immediate upstream channel pixel(s) instead of the summation of inflows from all the immediate upslope pixels. All inflows to pixel i from pixels other than channel pixels are added to the excess rainfall rate of pixel *i* as lateral inflow q_i.

Since the channel flow in the study area (Chapter 5) is of intermittent nature, no base flow is assumed in the channels. Channel flow routing starts as soon as excess runoff occurs. Similar to overland flow routing, the requirements for channel routing include slope and Manning roughness coefficient data for all channel pixels.

Appendices 4.1 and 4.2 give the flowcharts of routing schemes for overland flow and channel flow, respectively.

4.2 Model Calibration – Theoretical Calibration

The DIMBRR model was first tested on idealized overland flow over a uniform plane catchment whose overall length in the direction of flow is L. The surface roughness, slope, and flow regime are assumed invariant in space and time. In all the numerical experiments in this section, Manning's n is set to be 0.01, and slope of the plane is 0.01. Analytical solutions exist for hydrographs in such an idealized watershed based on the kinematic wave assumption (*e.g.* Eagleson, 1970, Chapter 15).

Figure 4.2 (a) and (b) show the hydrographs at x = L both from theoretical prediction and from the numerical solution using the DIMBRR model. R denotes constant rainfall rate. Figure 4. 2 (a) represents the case of $t_r > t_c$, where t_r is storm duration and t_c is the time of concentration, *i.e.* the time when flow from the farthest point in the watershed reaches outlet. Figure 4.2 (b) shows the case of $t_r < t_c$. In both cases, the agreement between the theoretical and numerical solutions is very good with slight numerical dispersions at the beginning or ending parts of steady runoff. Figure 4.3 displays the hydrographs when constant infiltration (i) is present. Figure 4.3 (a) and (b) show the cases of $t_r > t_c$ and $t_r < t_c$, respectively. Again, a good agreement between the theoretical and the numerical results is observed. Such agreements validate the overland flow routing part of the rainfall-runoff model.

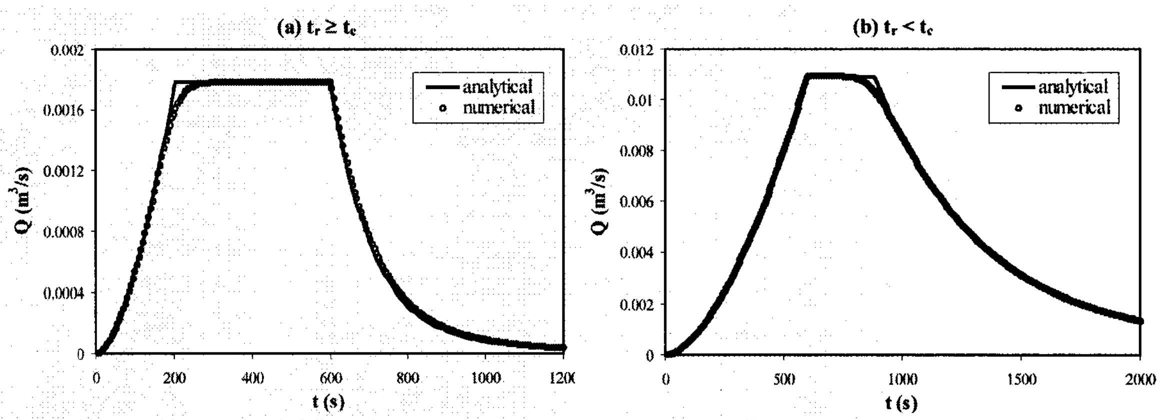

Figure 4.2 Kinematic Wave Hydrograph, R = 10 cm/hr
(a) t_r = 600 s, t_c = 202 s, L = 64 m, analytical hydrograph obtained using eq. (A4.4)
(b) t_r = 600 s, t_c = 850 s, L = 700 m, analytical hydrograph obtained using eq. (A4.6)

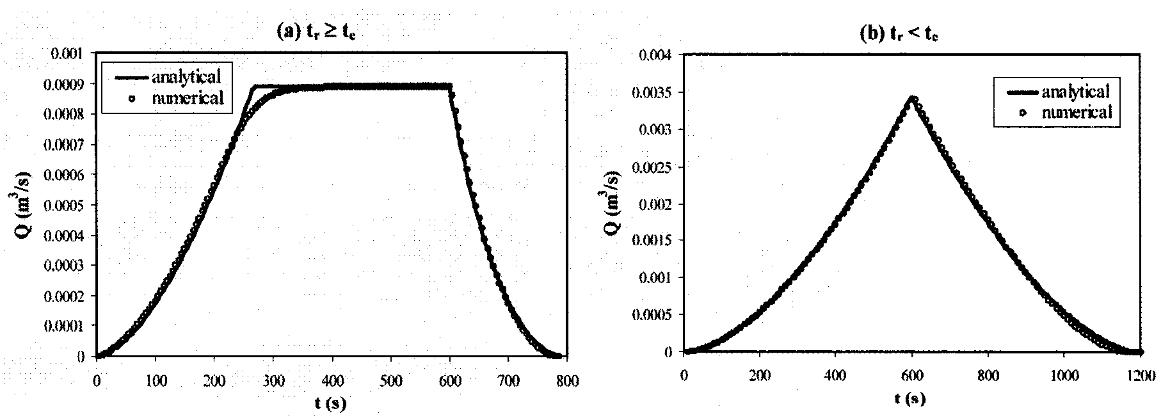

Figure 4.3 Kinematic Wave Hydrograph with Infiltration, R = 10 cm/hr, i = 5 cm/hr
(a) t_r = 600 s, t_c = 267 s, L = 64 m, analytical hydrograph obtained using eqs. (A4.10) to (A4.12), (b) t_r = 600 s, t_c = 872 s, L = 460 m, analytical hydrograph obtained using eqs. (A4.14) to (A4.19)

4.3 Model Calibration – Calibration on Watershed

It should be emphasized that the ultimate purpose of the calibration and verification of DIMBRR model on an actual watershed is to prove the acceptability of the model as the rainfall-runoff model for the study on scaling properties of watershed processes in the next chapter.

The watershed used for the DIMBRR model calibration is subwatershed 11 of the Walnut Gulch Experimental Watershed near Tombstone, Arizona. The reason for this choice is (a) the extensive data availability from this watershed, and (b) the hydrological and climatological similarity between this watershed and the chosen study area in Colorado.

Research on rangeland hydrology was initiated on the Walnut Gulch Experimental Watershed in 1953. This watershed is currently under the management of the Southwest Watershed Research Center of USDA-ARS, with its headquarters in Tucson, Arizona. Over the years, scientists from the center have collected a massive amount of rainfall, runoff, and other hydrological data on the watershed, making it a valuable data source for studying hydrological processes in arid and semi-arid watersheds.

4.3.1 Watershed Description

Walnut Gulch is a semiarid ephemeral stream joining the San Pedro River at Fairbank in the southeastern Arizona. The watershed is representative of approximately 60 million ha of brush and grass covered rangeland found throughout the semiarid southwest (Renard, *et al.*, 1993).

Subwatershed 11 (WG11) (30°44′32″N, 109°59′35″W) (Figure 4.4) is one of 15 major subwatersheds of the Walnut Gulch Watershed. It includes two stock ponds, 216 and

218. The area of the subwatershed is 786 ha including the pond contributing areas and 635 ha excluding the pond contributing areas. There are 9 weighing-type recording rain gages on this subwatershed and one supercritical flume with a capacity of 170 m^3/s at the outlet of the subwatershed (Figure 4.5). The major soil type on WG11 is sandy loam.

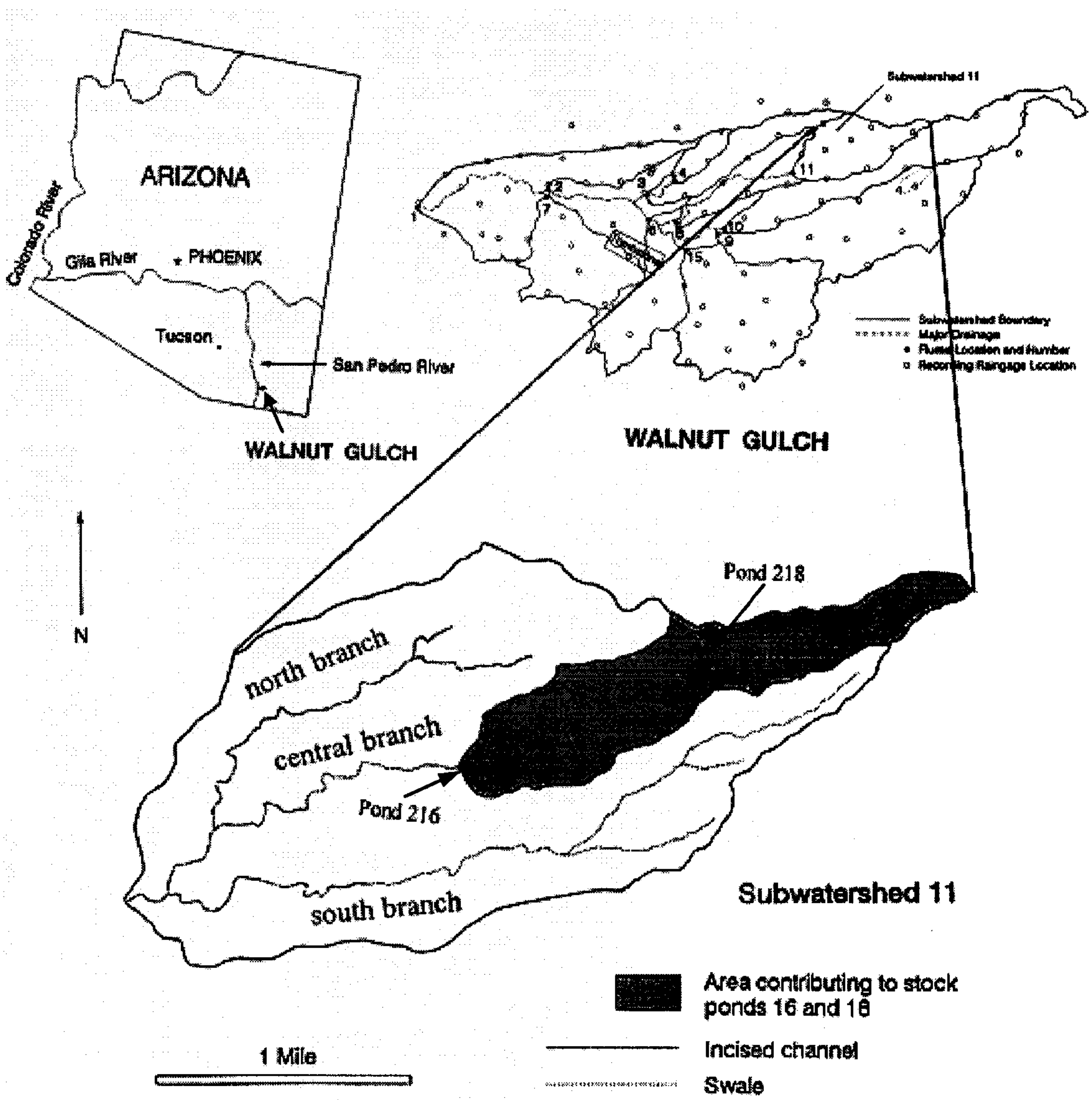

Figure 4.4 Walnut Gulch Experimental Watershed and sub-watershed 11

The vegetation of the lower 20% of the watershed is mainly desert shrub while the rest of the watershed is covered with grass (SWRC, 1993). The drainage network on the watershed is composed of 3 major channel branches. The north branch is incised with sandy bottom. The central branch is largely intercepted by the two stock ponds. The lower half of the south branch is incised and the upper part is swale (Woolhiser, *et al.*, 1990).

4.3.2 Data Preparation

DEM Data

The delineation of WG11 is based on a set of 7.5-minute digital elevation model (DEM) data (http://edc.usgs.gov/products/elevation/dem.html). The data files are produced by the U.S. Geological Survey (USGS). The data has 30-meter resolution with the Universal Transverse Mercator (UTM) projection. Ninety percent of the DEM data have a vertical accuracy of 7-meter RMSE or better and 10 percent are in the 8 to 15 meter range. These relatively large values of RMSE are likely caused by a bias (incorrect reference elevation, so the relative elevations within the study area provide reasonable topographic attributes (Timothy Green, personal communication).

Delineation of Watershed

Recall that the watershed area contributing to each pixel can be calculated based on flow directions of all its upslope pixels (Section 4.1.1). Thus, the WG11 watershed is delineated by specifying its outlet pixel. The measured coordinate of the WG11 outlet in the UTM projection is converted to a Cartesian coordinate that is set on the watershed (Figure 4.5). All the pixels directly and indirectly draining to the outlet pixel make up the entire WG11 watershed. As shown in Figure 4.5, the agreement between the delineated boundary and the measured boundary is good.

The stock pond 218 at the upper end of WG11 drains to stock pond 216. Because of the significant transmission losses within the WG11 channels, the spillage from the stock pond 216 is insignificant to be taken into consideration in the watershed runoff (SWRC, 1993). So the area contributing to the stock ponds is excluded from the contributing area of the WG11 throughout this study.

Channel Definition

Channels can be defined by giving a threshold contributing area. Any pixel that has contributing area larger than the threshold will be a channel pixel. The threshold for defining the channel network on WG11 is set to be 250 pixels (22.5 ha). This results in the channel network shown in Figure 4.5 – a network that resembles well the measured channel network (Figure 4.4).

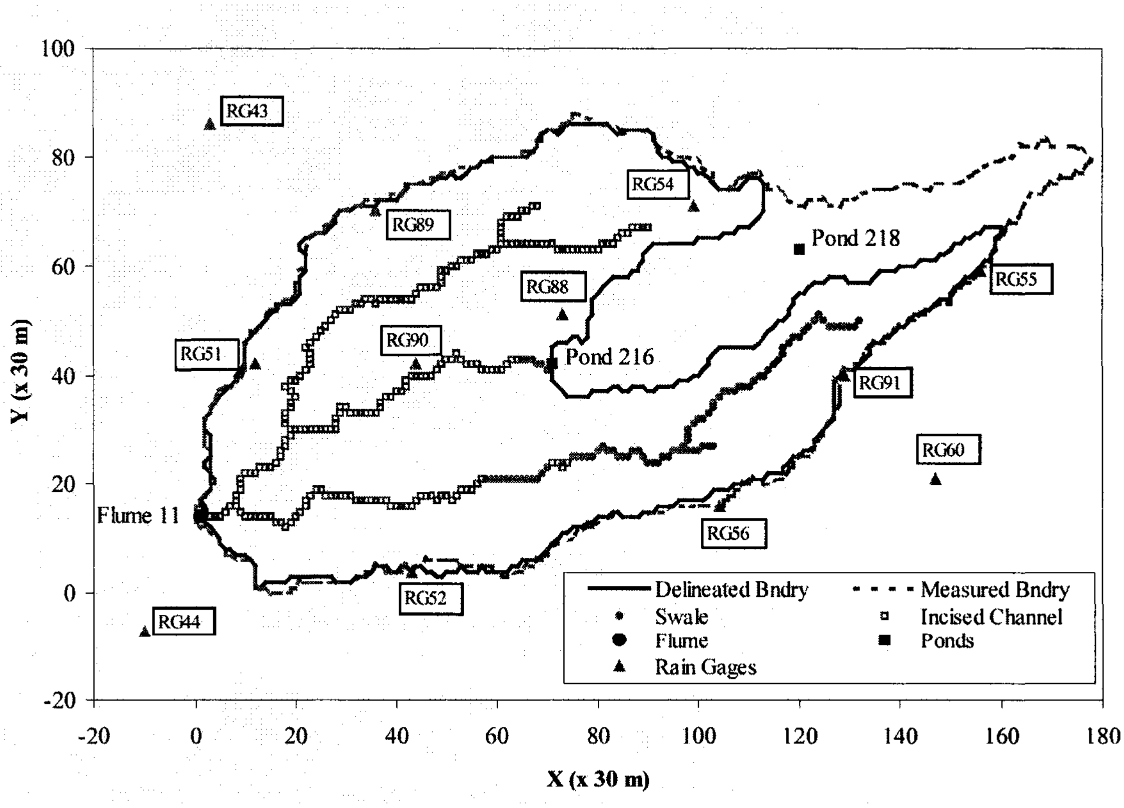

Figure 4.5 Walnut Gulch Subwatershed 11

Precipitation and Runoff Data

There are 12 rain gages on or near WG11 (Figure 4.5). To achieve better accuracy in rain rate estimations at all grid points, more rain measurements are desirable. Thus, rain records from rain gages on or near a larger watershed, Walnut Gulch subwatershed 8 (WG8), are used for rain rate estimation (next section). WG8 covers an area of 1326 ha. Figure 4.6 shows WG8, which includes WG11 and has 31 rain gages on the watershed or nearby. Breakpoint rainfall records for most of these rain gages are available from 1961 to 1990 at the ARS Water Data Center database web site (ftp://hydrolab.arsusda.gov/pub/arswater/163/).

Runoff data measured by Flume 11 at the outlet of WG11 can also be downloaded from the ARS Water Data Center database. Data is available from August 1968 to October 1977. This relatively short record becomes a limiting factor in the choice of rainfall-runoff events for calibration and verification as shown in later sections.

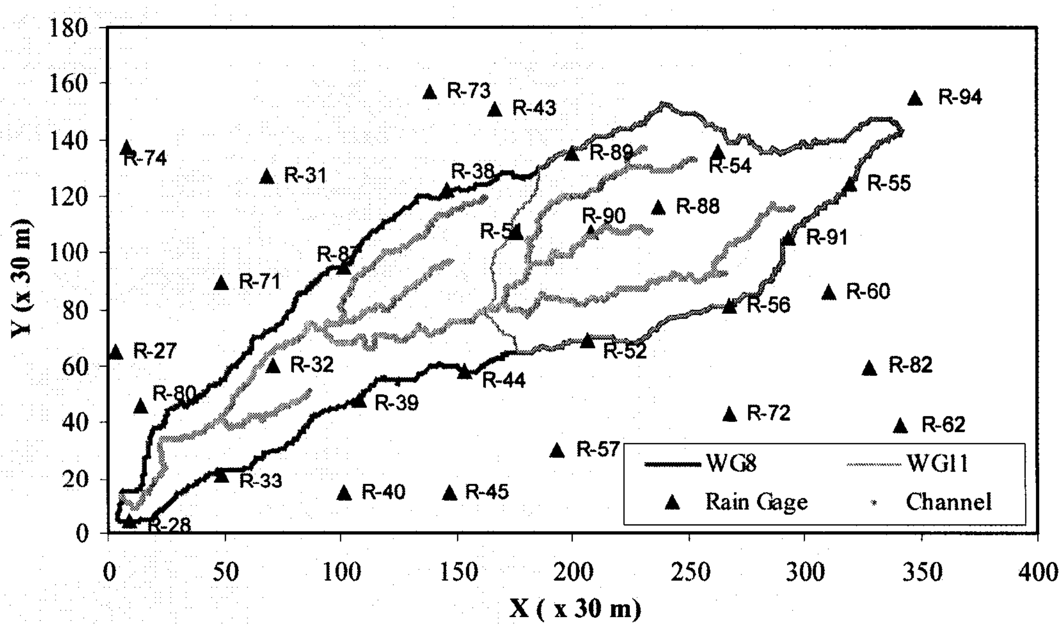

Figure 4.6 Walnut Gulch Subwatershed 8

Kriging of Rain Fields

Spatial interpolation is required to obtain rain rate field at each time step on a regular grid from the measurements at the 31 rain gage stations. This work is accomplished by using ordinary kriging. Kriging is widely used in environmental sciences for data interpolation in space. It relies on the spatial dependence structure among the measurements in the form of variogram to determine the estimated values of unsampled points. Since rain rate usually has rather strong spatial dependency at small scale, ordinary kriging is a good method to use here for rain rate estimation.

A variogram of the rain rate field is estimated using the following equation (ASCE Task Committee, 1990) and data are grouped together based on the distance between data pairs.

$$\gamma(|\vec{h}|) = \frac{1}{2N(|\vec{h}|)} \sum_{i=1}^{N(|\vec{h}|)} \left[R(\vec{x}_i + \vec{h}') - R(\vec{x}_i)\right]^2 \qquad (4.28)$$

where $^{\rightarrow}$ denotes a vector; R($\vec{x}_i$) is measured rain rate at point $\vec{x}_i$; $|\vec{h}|$ is the average distance between pairs of data points belonging to a distance group; N($|\vec{h}|$) is the number of pairs of data points belonging to the distance group represented by $\vec{h}$. Since there are 31 rain gage stations, 31 x 30 / 2 = 465 pairs of stations can be obtained. The corresponding distances are binned into 12 groups. Table 4.1 gives the information about the grouped distances.

The full variogram model is (Marsily, 1986)

$$\gamma(h) = C[1-\delta(h)] + \omega h^{\lambda} \qquad \lambda \in (0, 2) \qquad (4.29)$$

where h is distance, C is nugget effect, ω and λ are constants, and δ (h) is the Kronecker δ which has the form

$$\delta(h) = \begin{cases} 1, & \text{if } h = 0 \\ 0, & \text{if } h \neq 0 \end{cases} \tag{4.30}$$

A linear variogram model is adopted in this study where $\lambda = 1$ and there is no nugget effect, *i.e.* the variogram model used in this study for rain field kriging is

$$\gamma(h) = \omega h \tag{4.31}$$

where ω is the slope at the origin.

Table 4.1 Information about Distance Groups for Variogram Estimation

Group #	Group Lower Limit (x 30 m)	Group Upper Limit (x 30 m)	Average Distance (x 30m)	Number of Points
1	0	47	37.51	37
2	47	65	57.22	40
3	65	85	74.54	37
4	85	99	92.35	41
5	99	116	107.66	39
6	116	135	125.14	41
7	135	153	143.81	42
8	153	175	163.82	39
9	175	202	187.11	38
10	202	230	213.72	37
11	230	280	253.19	38
12	280	400	312.20	36

There are two reasons for choosing linear variogram model. One is the support of some rain measurements (Figure 4.7), and the other is to be in accordance with the multifractal rain assumption that is used extensively in the next chapter. A process with linear variogram has an unlimited capacity for spatial dispersion, which is a characteristic of multifractal field. Figure 4.7 shows the variograms of rain fields at five different times from the rain event on September 13, 1975. They display reasonably well-defined linear trend for h < 100. Thus, h < 100 is used in the estimation of ω for each rain field. As an example, Appendix 4.6 gives the ω time series for the rain event on August 12, 1971.

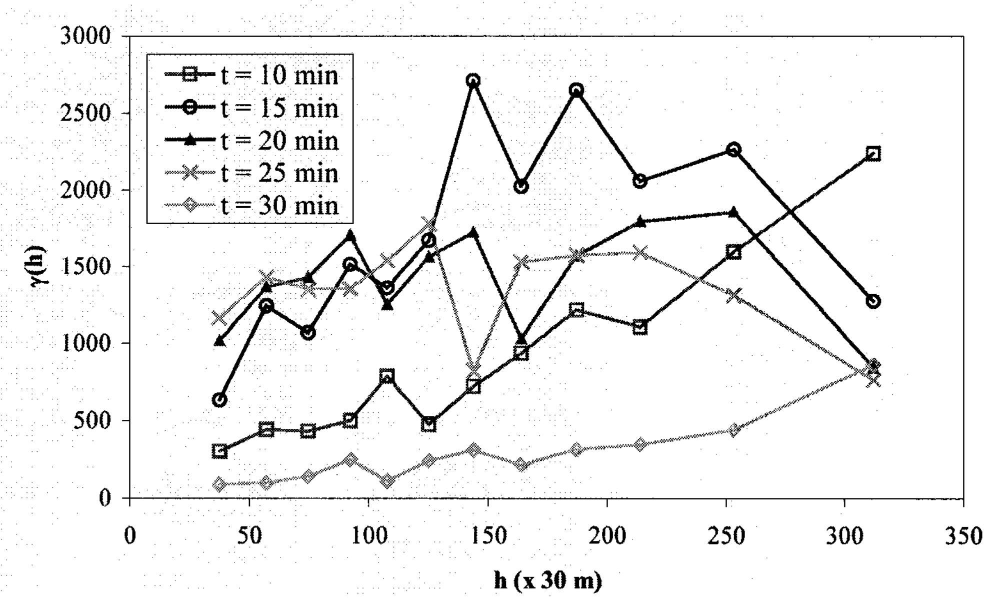

Figure 4.7 Variograms of rain fields from the rain event on Sept. 13, 1975

<u>*Saturated Hydraulic Conductivity Field*</u>

Goodrich (1990) carried out an extensive study on WG11 and divided the saturated hydraulic conductivity, K_s, into six categories based on soil composition and vegetation. Table 4.2 shows the categories and their K_s values. Figure 4.8 gives a visual account of the layout of the six K_s categories in WG11.

Table 4.2 Ks sub-categories at WG11 (Goodrich, 1990)

Category	Soil	Vegetation	K_s (cm/hr)
A	very gravely sandy loam	Bush	0.757
B	extremely gravely sandy loam	Bush	0.838
C	extremely gravely sandy loam	Grass	0.884
D	very gravely sandy loam	Grass	0.798
E (swale)	very gravely sandy loam		0.831
F (incised channel)	sand		21.082

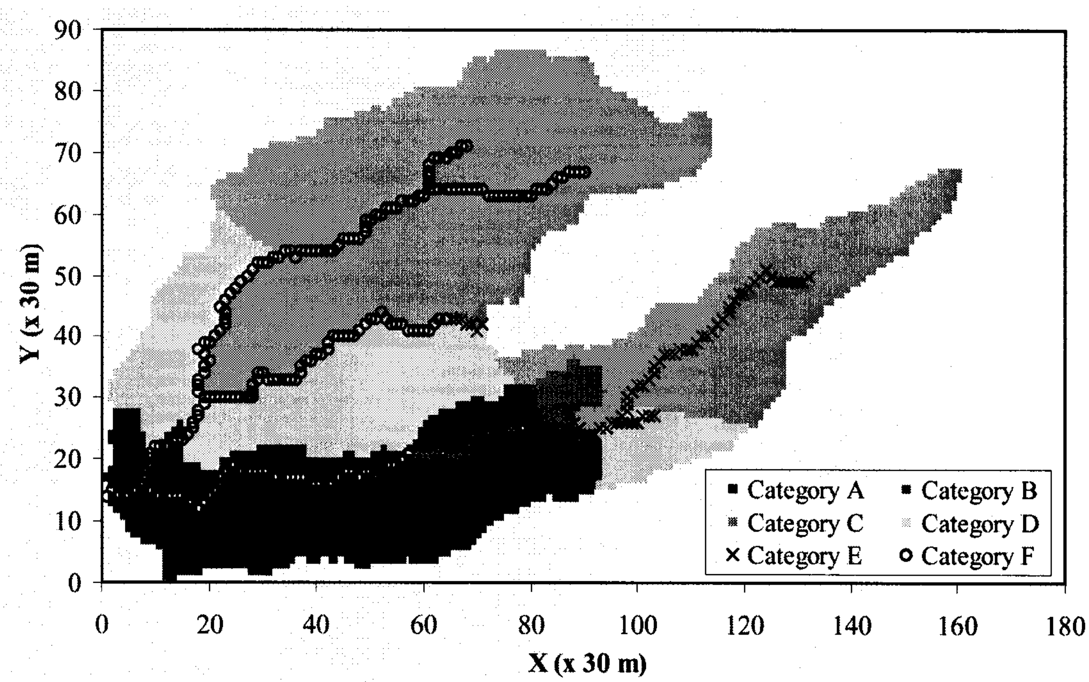

Figure 4.8 K_s Regions for WG11 basin classified according to soil type and vegetation (after Goodrich, 1990)

To represent the spatial variability of K_s, a lognormal distribution is assumed for the four regions corresponding to the K_s categories A, B, C, and D. The channels, corresponding to categories E and F, are assumed to have constant K_s. If K_s is lognormally distributed, then $Y = \ln(K_s)$ is normal distributed. Denote the mean of K_s by

μ_{Ks}, and the coefficient of variation by η_{Ks}. Then the standard deviation and the mean of Y are

$$\sigma_Y = \sqrt{\ln(\eta_{Ks}{}^2 + 1)} \tag{4.32}$$

and

$$\mu_Y = \ln(\mu_{Ks}) - \sigma_Y{}^2 / 2 \tag{4.33}$$

Field Y can be generated from a standard normal distribution. If Z ~ N(0, 1), then

$$Y = \mu_Y + \sigma_Y Z \tag{4.34}$$

and

$$K_s = e^Y \tag{4.35}$$

A pair of standard normal random numbers can be generated as (Salas *et al.*, 1993).

$$Z_1 = \sin(2\pi U_1)\sqrt{-2\ln(U_2)} \tag{4.36}$$

$$Z_2 = \cos(2\pi U_1)\sqrt{-2\ln(U_2)} \tag{4.37}$$

where U_1 and U_2 are (0, 1) uniform random numbers. A pseudorandom number generator, Mersenne Twister (MT), is used to generate the (0, 1) uniform random variables. MT was developed by Matsumoto and Nishimura during 1996-1997 (http://www.math.keio.ac.jp/~matumoto/emt.html). It generates high quality random numbers with a period of 2^{19937}-1.

The K_s value for each overland plane sub-region of WG11 given by Goodrich (1990) is taken as the mean of the K_s for that sub-region. The coefficient of variation is assumed to be 1.0 – the same as used by Goodrich (1990). The lognormal K_s field generated using these parameters and the approach described above is used in the calibration and validation procedures in later sections. In the actual application, the generated K_s values are assigned to the pixels in each K_s region one after another. Since the effect of ground cover is already incorporated in Goodrich's (1990) research, the saturated hydraulic conductivity, K_s, is assumed to be equal to the effective hydraulic conductivity, K_e, in this study.

Manning's Roughness Coefficient n

The lower 20% of the area (Category A and B in Figure 4.8) on WG11 is dominated by light to medium desert brush while the rest of the area supports a grass cover (SWRC, 1993). According to Chow *et al.* (1988, Chapter 2), Manning's n for grass flood plains is 0.035, for light brush 0.05, and for dense brush 0.07. Therefore, Manning's n for the grassland is taken as 0.035 and for the brush area is taken as 0.06. The channels on WG11 are mostly clean and straight natural stream channels. Manning's n for the channel pixels is taken from a data set provided by Goodrich (personal communication). These data were collected in the field for each channel stretch all through WG11. The minimum n for channel is 0.025, the maximum is 0.04, and the average value is 0.033.

Porosity

Porosity is an important parameter in the computation of infiltration. It is determined by soil texture. WG11 is dominated by sandy loam soil type with wide sand bed incised channels (Goodrich, 1990). From Rawls and Brakensiek's study (1985), the porosity for sandy loam is 0.453 and for sand is 0.437. Therefore, the porosity for all overland and swale pixels is 0.453 and for incised channels is 0.437.

Other Hydrological Parameters

Field capacity, residual soil moisture content and wetting front suction are some of the parameters used in the computation of infiltration. They are closely related to saturated hydraulic conductivity. Because of the lack of field measurements for these parameters, they are assumed to be functions of K_s and can be derived from K_s through regression relations. The infiltration parameters for 10 soil textures (Rawls and Brakensiek, 1983, 1985) (Appendix 4.4) are used to obtain the regression relations. Sand is not included in the regression because: 1) its properties have the tendency to deviate away from the logarithmic linear relation that other soil types follow; and 2) the only sand-covered regions in WG11 are channels for which it is assumed that hydrological parameters are constant. Figure 4.9 (a), (b), and (c) show the regression relations between K_s and field capacity, θ_f, between K_s and residual soil moisture content, θ_r, and between K_s and wetting front suction, ψ. It is assumed that θ_f is equal to soil moisture content at –33 kPa, and θ_r equal to soil moisture content at –1500 kPa. The following relations are obtained through regression.

$$\theta_f = 0.2510 - 0.1210 \log(K_s) \tag{4.38}$$

$$\theta_r = 0.1276 - 0.1095 \log(K_s) \tag{4.39}$$

$$\psi = 14.5035 - 13.1294 \log(K_s) \tag{4.40}$$

Parameters θ_f, θ_r, and ψ will be derived in the field from these regression relations and the lognormally distributed K_s. This approach ensures the spatial variability of these parameters.

<u>*Channel Geometry*</u>

The channels on WG11 are assumed to have trapezoidal shape – a reasonable assumption for channels at Walnut Gulch. In general, the swales have small bank slopes, which lead to broad channels. Incised channels usually have relatively steep bank slopes. It is assumed that the following relations govern channel geometry at WG11 (Woolhiser, *et al.*, 1990).

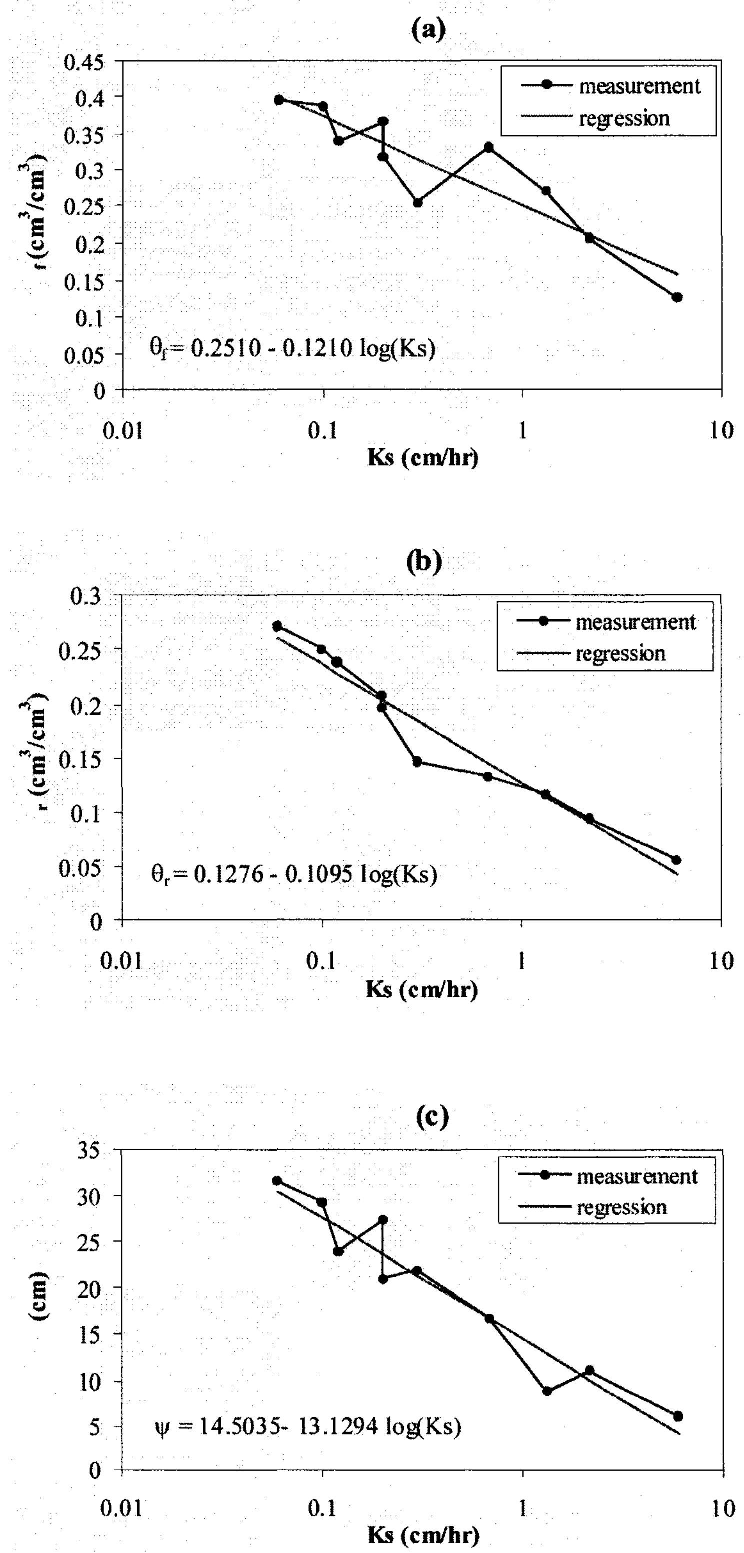

Figure 4.9Regression relations (a) between K_s and field capacity, θ_f; (b)between K_s and residual soil moisture θ_r; and (c) between K_s and wetting front suction, ψ.

$$P = B + h\left(\sqrt{1+\frac{1}{S_L^{\,2}}} + \sqrt{1+\frac{1}{S_R^{\,2}}}\right) \tag{4.41}$$

and

$$P_e = \begin{cases} B/5, & h \le h_0 = 0.03\ m \\ P\min\left(\dfrac{h}{0.0828\sqrt{B}},\ 1\right), & h > h_0 \end{cases} \tag{4.42}$$

where P is wetted perimeter, P_e is effective wetted perimeter which is used in channel routing, B is channel bottom width in *m*, h is flow depth in *m*, S_L and S_R are respectively the channel left bank slope and right bank slope. The initial perimeter is set to be 1/5 of the channel bottom width before flow depth reaches 0.03 m. The values were set arbitrarily after testing proved that small values at the beginning of a runoff event have insignificant effect on hydrograph. It is necessary, however, to set an initial perimeter to ensure smooth operation of the runoff model. The empirical expression for P_e after h reaches 0.03 m is adopted from Woolhiser *et al.* (1990). It states that the effective perimeter remains smaller than the channel perimeter until the flow depth reaches a critical value, $h_c = 0.0828\sqrt{B}\,(m)$. This modification on perimeter was introduced to correct the error at low flow rate caused by the simplification of trapezoidal channel. Goodrich (1990) took detailed measurements of channel geometries on WG11, which included channel bottom width and bank slopes. This set of data is used in this study for channel routing.

<u>*Selection of Rainfall-Runoff Events*</u>

The selection of rainfall-runoff events for calibration and verification is limited by two major factors: data quality and data availability. High quality measurements are absolutely essential to successful calibration and verification of rainfall-runoff models.

Because of the lack of means to check and correct precipitation and runoff data from WG11, the rainfall-runoff events selected in previous studies by other researchers are chosen for this study. These events were chosen for the time period when no changes were made to the measuring instrumentation and no major watershed management changes occurred (Goodrich, 1990; SWRC, 1993). All the data were carefully checked using strict criteria and only the best events with the minimum errors were selected. Other considerations for choosing the events were the diversifications of event sizes, initial conditions, and number of peaks in hydrographs. Even though the available precipitation records from the WG11 rain gages are fairly long, from about 1960 to 1990, the available runoff record from flume 11 is very short, only from 1968 to 1977. Among all the rainfall-runoff events used by Goodrich (1990) and SWRC (1993), only 14 are from the period of 1968 to 1977. Table 4.3 lists the rainfall-runoff events used in this study for calibration and verification with some detailed information.

Table 4.3 Rainfall-Runoff Events for Calibration and Verification

Event Date	Rain Starting	Rain Ending	Runoff Starting	Runoff Ending	Rain Duration (min)	Runoff Volume (mm)	Peak Flow (m^3/s)	Peak Time (min)
08/05/68*	17:59	21:43	19:46	22:30	225	4.60	24.81	74
08/12/71*	20:15	23:46	21:22	1:38	226	3.41	6.74	97
08/24/71	13:45	15:51	14:46	17:01	127	1.30	9.26	49
07/12/73	12:36	13:53	13:24	16:05	77	2.08	10.51	56
07/16/73	23:37	1:36	1:59	4:59	119	1.72	6.54	67
08/21/73*	18:15	20:17	20:23	23:16	122	5.37	14.22	99
09/24/74*	16:13	19:30	17:21	20:19	197	0.59	4.98	51
09/03/75	23:00	2:44	0:33	5:45	224	2.31	4.56	112
09/05/75	12:32	15:54	13:33	17:45	202	8.92	33.30	100
09/07/75	14:13	17:58	15:42	18:57	225	1.94	4.47	118
09/13/75	15:56	18:35	16:04	21:15	159	7.75	19.77	49
07/27/76	19:28	21:48	20:45	2:26	141	4.89	14.67	46
09/06/76*	14:59	17:08	15:38	20:53	128	2.41	5.18	92
06/22/77	11:00	13:52	14:18	17:59	173	3.34	9.83	154

* Calibration event

Five events are used for calibration (event dates marked by asterisk in Table 4.2) and nine for verification. Calibration events are selected so they cover a good range of runoff volumes and peak flow rates.

Initial Soil Moisture Content

Initial soil moisture content, θ_i, is estimated from information on soil properties, rain and runoff history prior to the rain event. Because WG11 is a semiarid rangeland where the average soil condition is fairly dry, field capacity θ_f, which is assumed to be the soil moisture content held at –33 kPa in this study, is taken as the moisture content under wet condition. The residual soil moisture content θ_r, which is assumed to be the soil moisture content held at –1500 kPa here, represents the moisture content under dry condition. The initial soil moisture content is assumed to be

$$\theta_i = \theta_r + \frac{\theta_f - \theta_r}{d} \tag{4.43}$$

where $d \geq 1$ is a factor estimated based on rain history. Thus it is subjective to a certain degree. This factor is proportional to the dryness of the soil with $d = 1$ corresponding to $\theta_i = \theta_f$, and $d = \infty$ corresponding to $\theta_i = \theta_r$. Figure 4.10 (a) - (e) show the 10-day rain histories prior to the calibration rain events.

The incised channels on WG11 usually have sandy bottoms while the overland plane and swales have sandy loam soil type. So incised channels are typically drier than other parts of the watershed. This phenomenon is reflected in the estimated values of factor d as given in Table 4.4.

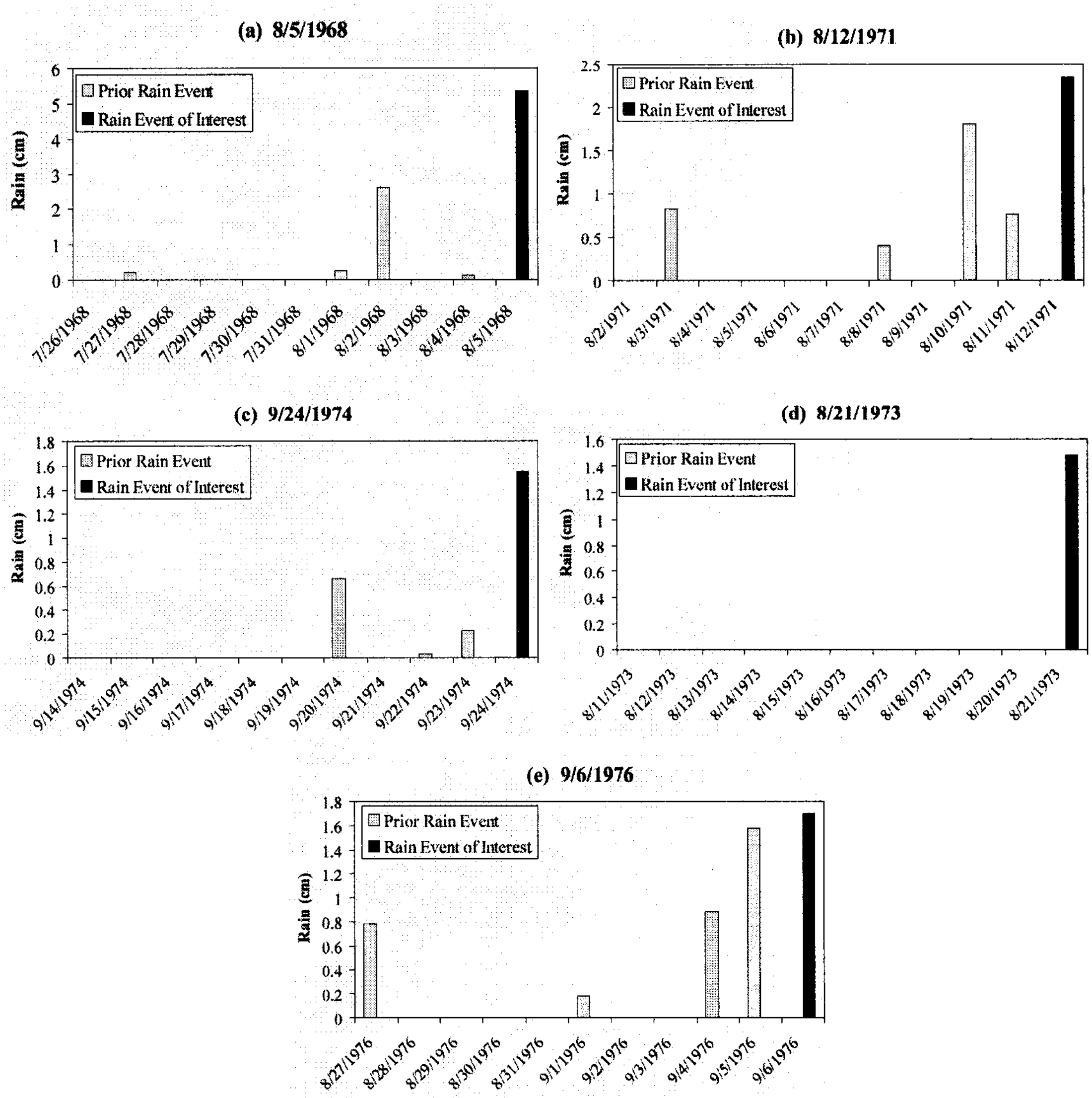

Figure 4.10 Ten-day rain event history at rain gage 90 prior to calibration rain event (a) 8/5/1968; (b) 8/12/1971; (c) 9/24/1974; (d) 8/21/1973; and (e) 9/6/1976.

Table 4.4 Factor d for Rainfall-Runoff Events in Calibration Set

	8/5/1968	8/12/1971	9/24/1974	8/21/1973	9/6/1976
Overland	3	2	3.5	∞	1.5
Swale	3	2	3.5	∞	1.5
Incised Channel	∞*	4	∞	∞	2.5

* Dry condition corresponds to $d = \infty$.

4.3.3 Sensitivity Analysis

The rain event on Aug. 12, 1971 is used to derive a set of initial parameters for the sensitivity analysis that follows. The rainfall data from all rain gages for this rain event are given in Appendix 4.5. The ω (eq. 4.31) time series estimated for this rain event is listed in Appendix 4.6. This event is chosen because it has medium runoff volume and peak flow (Table 4.3). Upon checking its rain pattern, it is found that the most intense rainfall during this event distributed fairly evenly over the subwatershed – making it a good candidate for studying watershed response. Figure 11 shows three rain fields from this event after spatial interpolation using kriging. The model results are fitted to the measurements by adjusting the saturated hydraulic conductivity, K_s. The K_s values for the 6 categories as given in Goodrich (1990) are applied to the WG11 watershed along with a uniform multiplier M_k. This multiplier is adjusted during fitting to achieve a reasonably good fit between the measured hydrograph at the outlet and the simulated hydrograph. Since the goal of this analysis is to obtain a set of initial parameters for further sensitivity analysis, a good fit rather than a best fit between the runoff measurement and runoff simulation will serve the purpose well enough. Table 4.5 shows the final K_s used for a good fit and Figure 4.12 exhibits the hydrographs at the outlet.

Table 4.5 K_s Parameters

	Cat. A	Cat. B	Cat. C	Cat. D	Cat. E	Cat. F
Orig. K_s (cm/hr)	0.757	0.838	0.884	0.798	0.831	21.082
K_s multiplier	0.5	0.5	0.5	0.5	0.5	0.5
K_s (cm/hr)	0.3785	0.4190	0.4420	0.3990	0.4155	10.5410

Note: C_v for categories A, B, C, and D is 1.0.

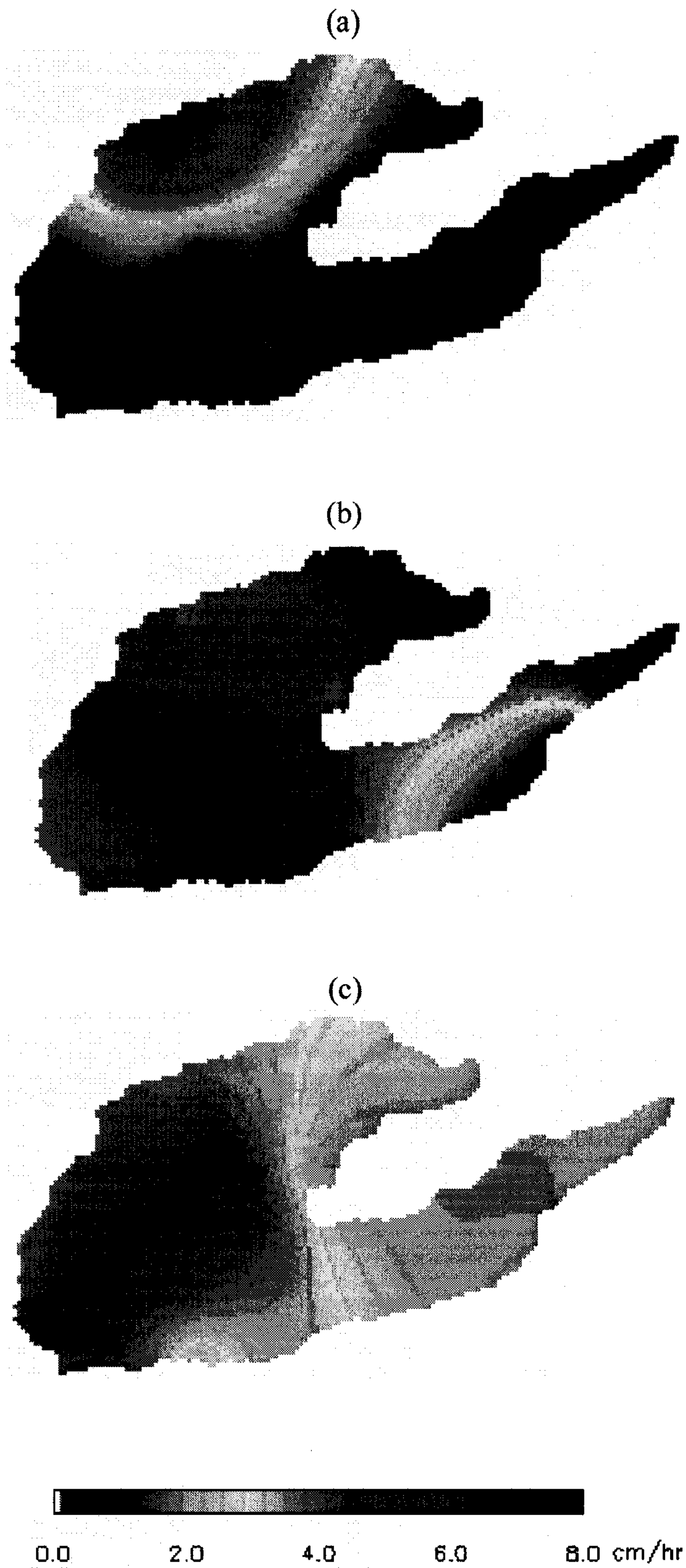

Figure 4.11 Interpolated rain fields from WG11 during the rain event on August 12, 1971 at (a) t = 60 min, (b) t = 70 min, and (c) t = 80 min after rain starts.

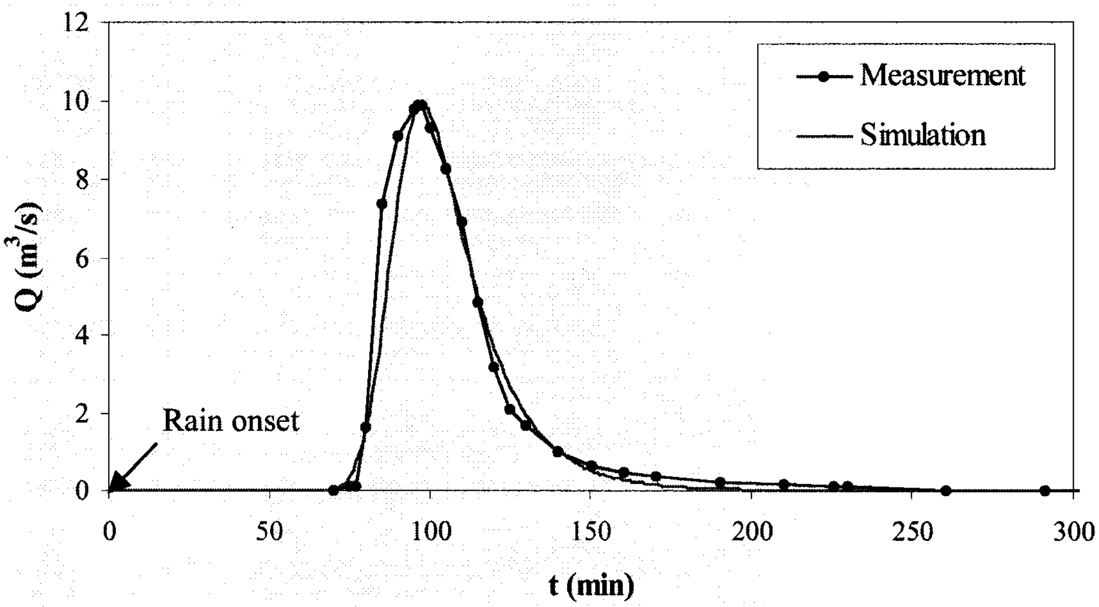

Figure 4.12 Measured and simulated hydrographs at WG11 outlet for rain event on Aug. 12, 1971. Rainfall started at 20:15.

The other model parameters used in the simulation above, such as porosity and Manning's n, take values as introduced in Section 4.3.2. Table 4.6 summarizes the parameters used for the simulation of this rainfall-runoff event.

Table 4.6 Parameter Summarization for Simulation of Event 8/12/1971

Paramters	Value or method used
K_S	See Table 4.5
Manning's n for grassland	0.035
Manning's n for brush area	0.06
Manning's n for channels	Field measurements
Porosity for overland and swale (cm^3/cm^3)	0.453
Porosity for incised channel (cm^3/cm^3)	0.437
Field capacity (cm^3/cm^3)	See eq. (4.38)
Residual soil moisture content (cm^3/cm^3)	See eq. (4.39)
Wetting front suction (cm)	See eq. (4.40)

The five rainfall-runoff events for calibration are used for sensitivity analysis. The same set of model parameters as used in the study above is applied to the DIMBRR model for each of the five calibration events. The resulting runoff volumes (V), peak flows (Qp), and times to peak flows (Tp), are taken as the base values for sensitivity analysis. The model parameters being tested for sensitivity analysis are

i) porosity

ii) K_s

iii) coefficient of variation of K_s, *i.e.* Cv of K_s

iv) Manning's n

v) wetting front suction

vi) initial soil moisture content

vii) field capacity

viii) residual soil moisture content

Apply the model parameters as used in the above rain event with ±20% perturbation respectively to the five calibration events and compare the model results with the base values in terms of V, Qp, and Tp. The 20% is chosen to keep the parameters in their physical ranges and still produce enough changes in the three runoff-related variables for sensitivity analysis. Figure 4.13 gives a visual account of the results of sensitivity analysis. The five rainfall-runoff events used for sensitivity analysis are 1) 08/05/1968, 2) 08/12/1971, 3) 09/24/1974, 4) 08/21/1973, and 5) 09/06/1976. Table 4.7 gives the Root Mean Squared Differences (RMSD) between the base values and the model results with ±20% perturbations in each model parameter. RMSD is defined as

$$RMSD = \sqrt{\frac{1}{n}\sum_{i=1}^{n}(x_i - y_i)^2} \tag{4.44}$$

where X and Y are two variables being compared, n is the number of samples. In this case, n = 5. In hydrological practice, V has the highest significance and Tp has the least among the three variables being analyzed. Table 4.7 is thus given in the order of RMSD of the total runoff volume.

Table 4.7 Results of Sensitivity Analysis

Model Parameter	Change In Value	RMSD of V (mm)	RMSD of Qp (m^3/s)	RMSD of Tp (min)
Porosity	+20%	1.21	3.79	2.28
	-20%	0.76	2.59	2.90
K_s	+20%	0.72	2.41	0.45
	-20%	0.58	1.98	1.84
Initial Soil Moisture Content	+20%	0.44	1.37	1.90
	-20%	0.63	1.80	1.00
Manning's n	+20%	0.46	2.79	3.55
	-20%	0.39	2.30	3.85
Wetting Front Suction	+20%	0.41	1.49	0.00
	-20%	0.35	1.26	1.41
Cv of K_s	+20%	0.17	0.61	1.00
	-20%	0.16	0.60	0.0 0
Residual Soil Moisture Content	+20%	0.12	0.39	0.63
	-20%	0.14	0.44	0.00
Field Capacityl Moisture Content	+20%	0.12	0.30	0.63
	-20%	0.13	0.34	0.45

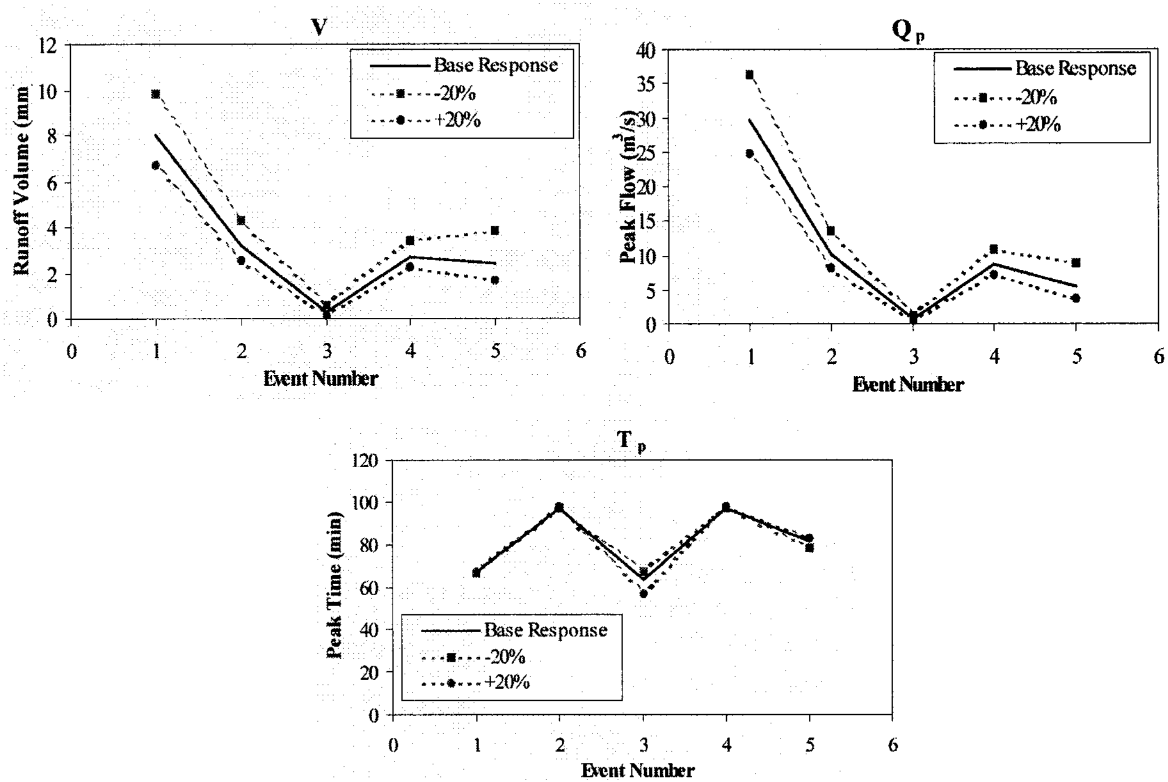

Figure 4.13 (a) Sensitivity of V, Qp and Tp to porosity

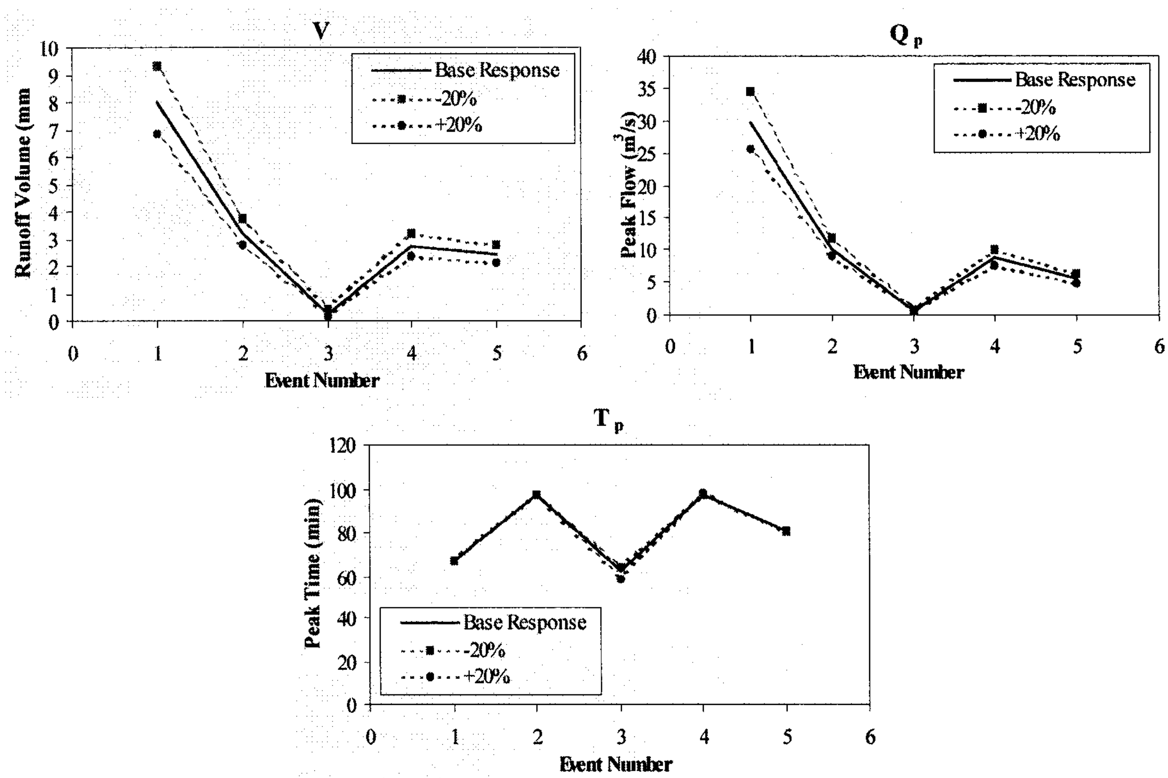

Figure 4.13 (b) Sensitivity of V, Qp and Tp to K_s

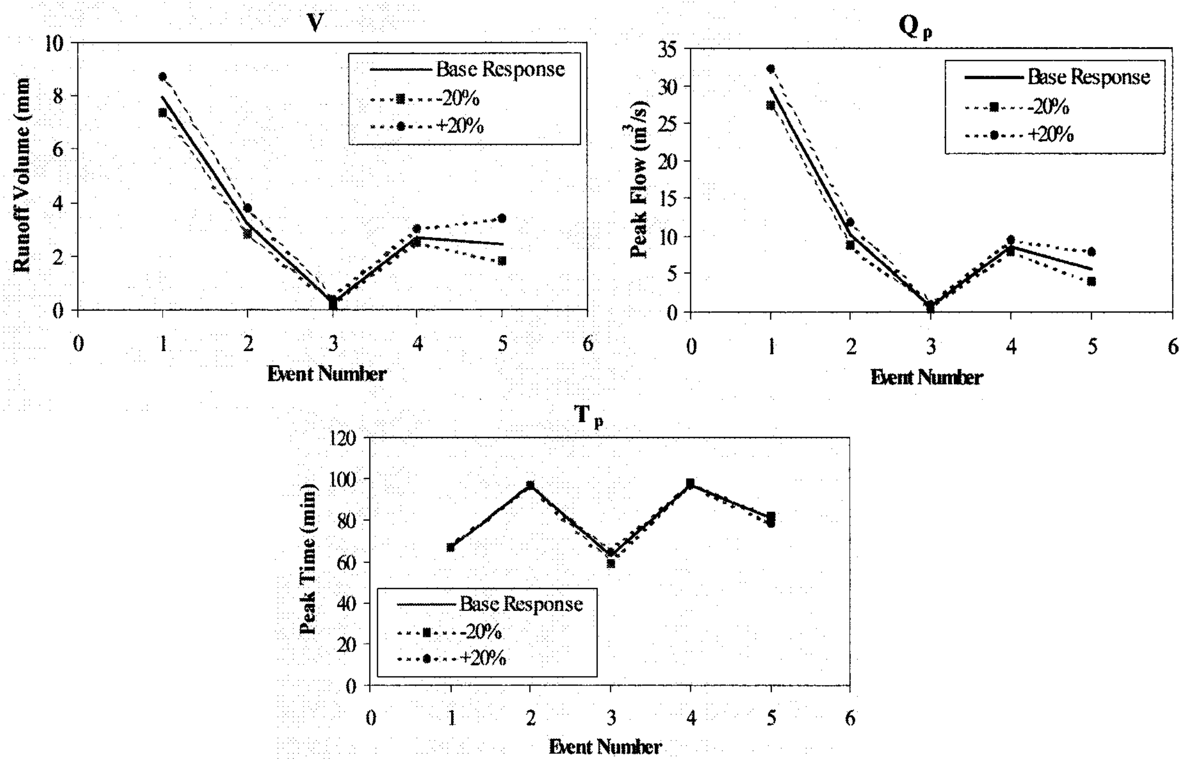

Figure 4.13 (c) Sensitivity of V, Qp and Tp to initial soil moisture content

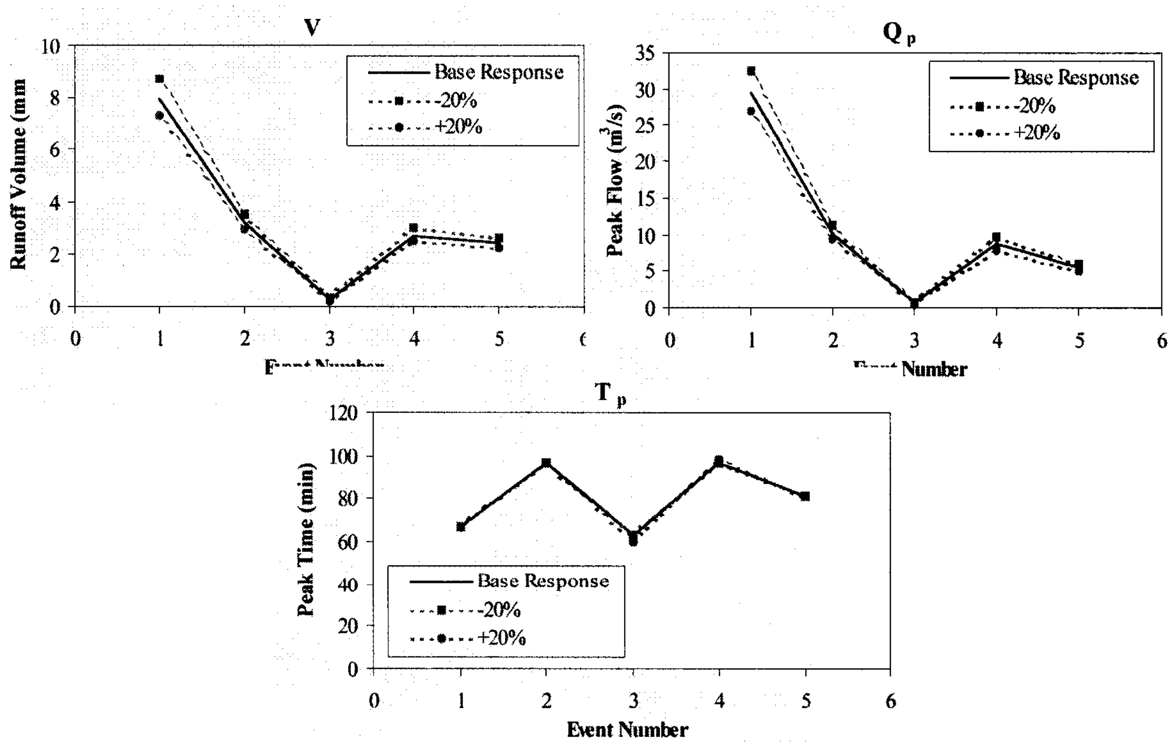

Figure 4.13 (d) Sensitivity of V, Qp and Tp to wetting front suction

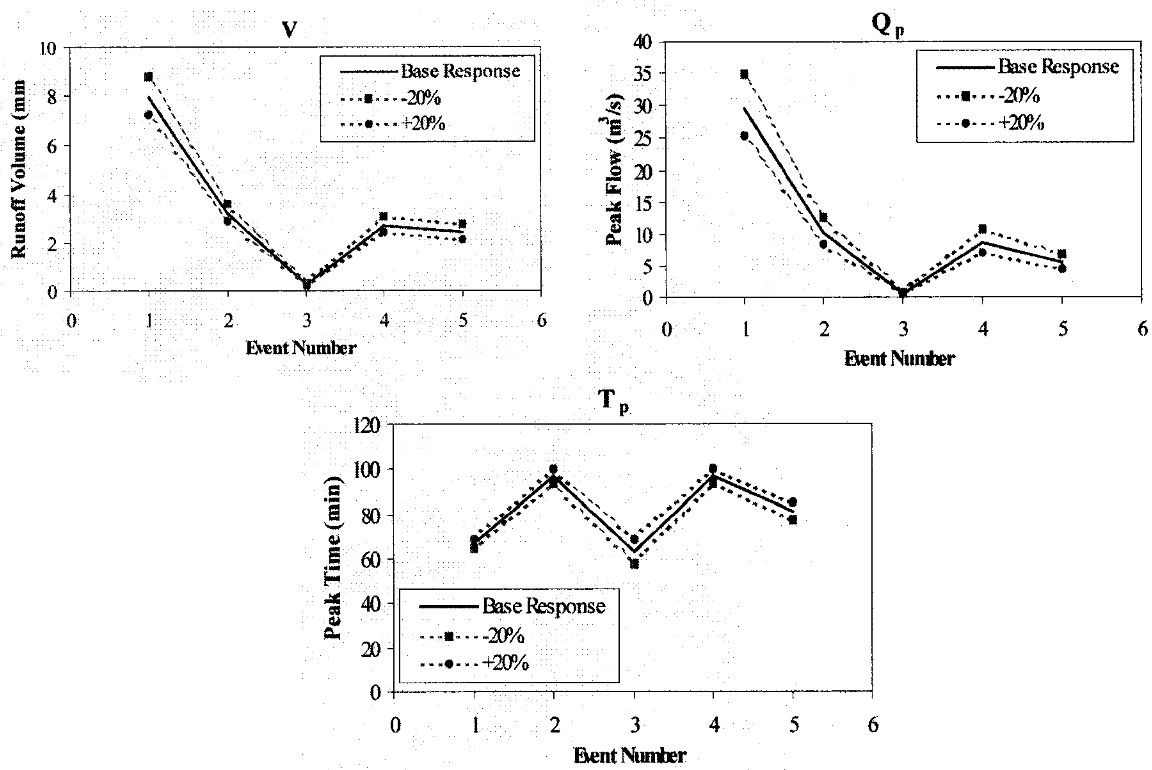

Figure 4.13 (e) Sensitivity of V, Qp and Tp to Manning's n

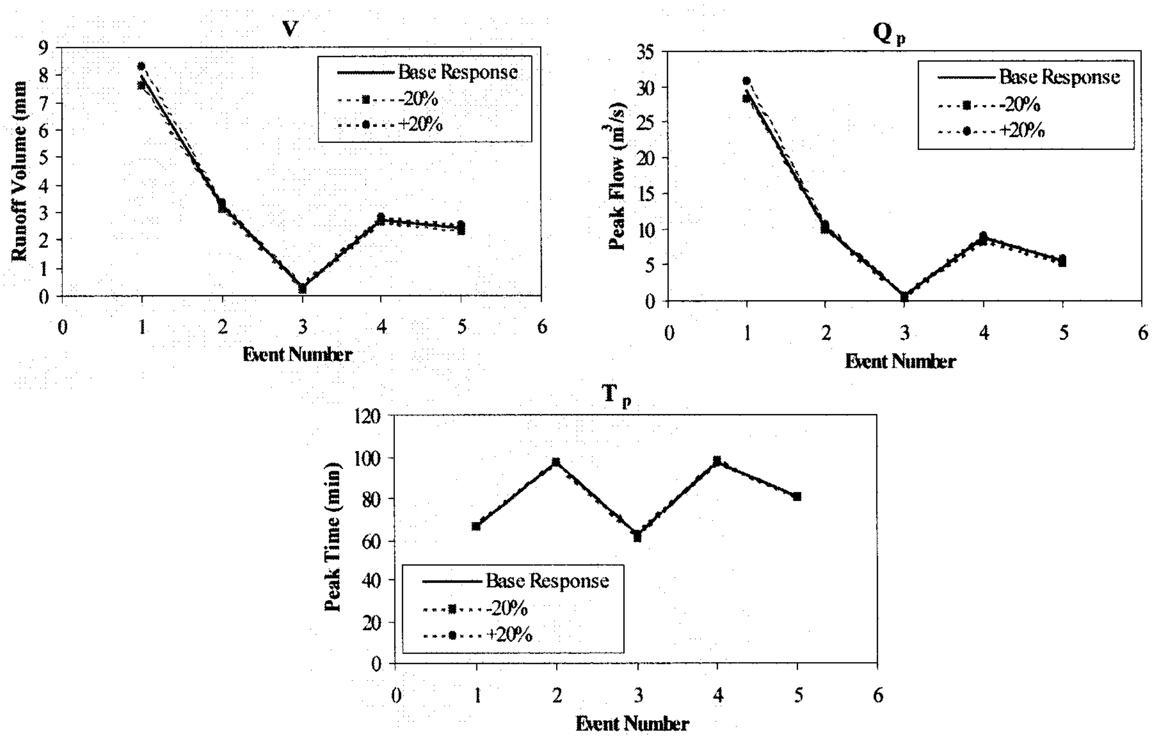

Figure 4.13 (f) Sensitivity of V, Qp and Tp to Cv of K_s

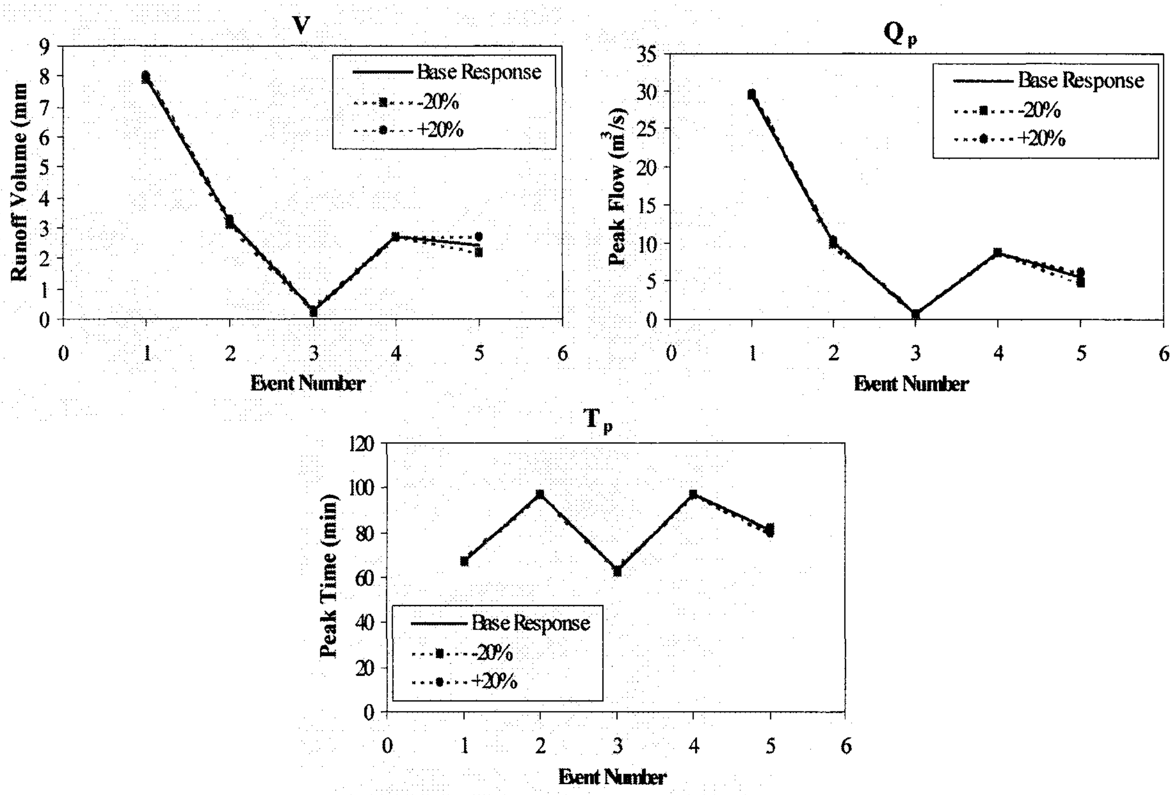

Figure 4.13 (g) Sensitivity of V, Qp and Tp to field capacity

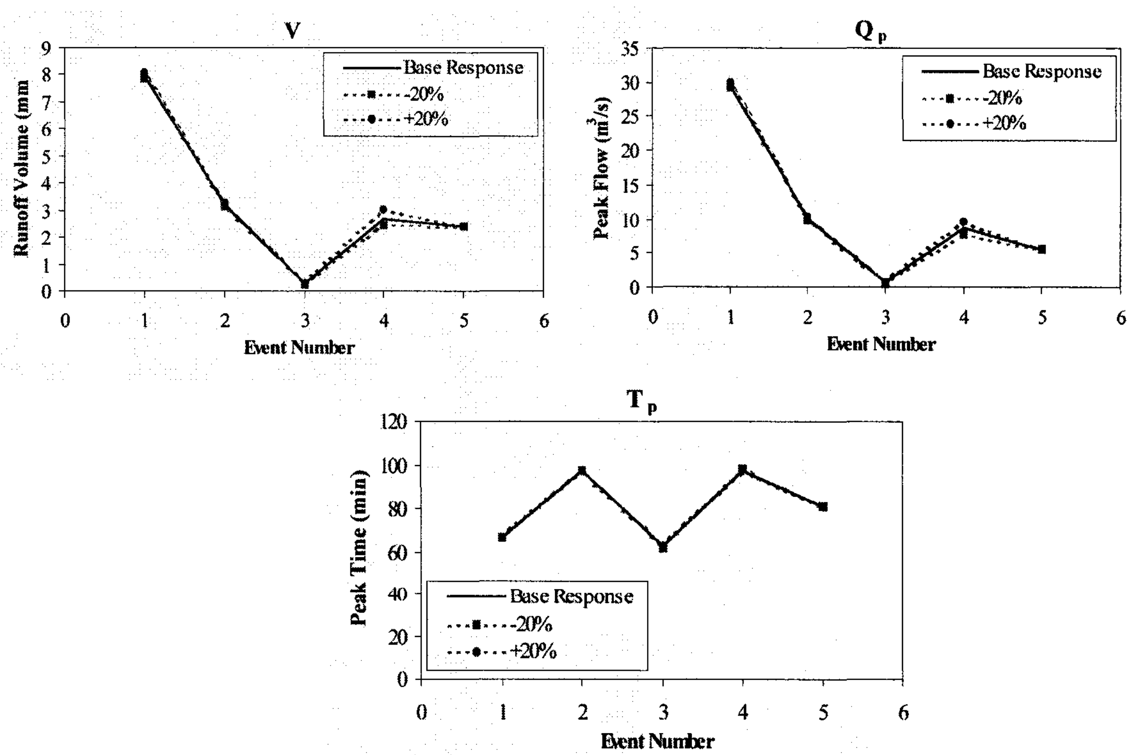

Figure 4.13 (h) Sensitivity of V, Qp and Tp to residual soil moisture content

As shown in Table 4.7 and Figure 4.13, the impact of perturbations in porosity and effective hydraulic conductivity on runoff volume is most significant (RMSD > 0.7 mm) except in the case of K_s with –20% perturbation which has RMSD = 0.58, a value that is still quite large. The impact of initial soil moisture content, Manning's n, and wetting front suction is moderate (0.35 mm ≤ RMSD ≤ 0.63 mm), while impact of the rest of the parameters is negligible (RMSD < 0.2 mm). Perturbations in porosity, Manning's n, and effective hydraulic conductivity lead to the most significant changes in the peak flow (RMSD > 1.9 m^3/s). The most important parameters for the time to peak flow are Manning's n and porosity (RMSD > 2.0 min).

4.3.4 Calibration

Choosing Calibration Parameters

A very crucial part of model calibration is to choose appropriate calibration parameters. Efforts need to be made to strike a balance between over-parameterization and under-parameterization. Over-parameterization refers to the situation when calibration parameters are highly correlated or redundant parameters are used in calibration. Under-parameterization occurs when there are not enough calibration parameters to represent the various aspects of the model (Goodrich, 1990).

It is learned from the sensitivity analysis that the coefficient of variation of effective hydraulic conductivity, field capacity, and residual soil moisture content are insignificant parameters to watershed response. These three parameters are thus removed from the list of calibration parameters to avoid over-parameterization. Instead, the coefficient of variation of K_s is fixed as 1 in all calibration and verification cases in the rest of this chapter, and field capacity and residual soil moisture content are determined from K_s by using eqs. (4.38) and (4.39).

Wetting front suction is highly correlated to effective hydraulic conductivity. In fact, it is derived from K_e through a regression relation in this study. It will lead to identifiable problem and over-parameterization if both K_e and wetting front suction are included as calibration parameters. Since K_s is a more important parameter compared to wetting front suction and will be taken as a calibration parameter, the latter will be determined from K_s by using eq. (4.40).

Initial soil moisture content has a moderate impact on watershed response in the DIMBRR model. It is a combined result of residual soil moisture content, field capacity, and K_s. It is also partially estimated from the 10-day rain history prior to the rain event of interest. Because of its complicated nature and the concern of parameter interaction, it is decided to exclude initial soil moisture from calibration.

Manning's n is an important parameter for peak flow and time to peak, but has a minor effect on runoff volume. Since runoff volume is the main target for calibration, decision is made that Manning's n is not included in the calibration process.

Porosity and K_s play dominant roles in determining runoff volume. A regression analysis on K_s and porosity values of the USDA 11 soil classes yields an R^2 value of 0.0678, *i.e.*, the two parameters are essentially uncorrelated. Thus the pair is chosen to be calibration parameters.

Porosity is assumed to be constant for each soil type (sandy loam or sand). A uniform multiplier is applied to porosity throughout the watershed during calibration. The calibration of effective hydraulic conductivity, however, is somewhat more complicated.

As introduced in Section 4.3.2, there are six K_s categories at WG11. Each category has a unique K_s value as given by Goodrich (1990) (Table 4.2). When these "default" values are applied to the DIMBRR model as the mean of the lognormally distributed K_s in each region, some interesting phenomena are observed. For instance, intense rain in certain areas always results in serious overestimates of runoff volume while heavy rain in some other areas will lead to underestimates of runoff volume. This sensitivity of runoff volume to intense rain on different regions calls for the individual adjustment of K_s value for each sub-region. Therefore, a new approach is adopted where the six K_s categories are tested individually to determine their relative magnitude. Then a uniform multiplier is applied in calibration with the fixed relative magnitudes among the K_s regions. With the knowledge about the soil characters and vegetation (Table 4.2) that determine the K_s values of the six categories, combined with a detailed study on the interaction between runoff and rainfall pattern, a set of K_s modifiers are chosen for the six categories: 0.4, 1.0, 3.5, 0.4, 1.0, 1.0. The first and the forth categories correspond to very gravely sandy loam soil and either bush or grass covered land while the third category has extremely gravely sandy loam and grassy land. Compared with the first and the forth categories, both the soil and the vegetation in the third category render larger effective hydraulic conductivity. Thus it is physically reasonable to assume a set of K_s modifiers as given above.

Evaluation Methods

A few measures are adopted in this study to evaluate model performance. The most important one is the coefficient of efficiency, E. The concept was first introduced by Nash and Sutcliffe (1970). The definition of coefficient of efficiency is

$$E = 1 - \left[\frac{\sum_{i=1}^{n} (\hat{Q}_i - Q_i)^2}{\sum_{i=1}^{n} (Q_i - \overline{Q})^2} \right] \tag{4.43}$$

where $\hat{Q}_i$ is simulated model variable, Q_i is observed variable, and $\overline{Q}$ is mean of Q_i for all events (i = 1 to n). If a model predicts observed variables with perfection, E = 1. If E < 0, the model's predictive power is worse than simply using the average of observed values. It should be pointed out that when E is used to evaluate discharge from a single event, a slight shift in the timing of simulated hydrograph from the observed one would lead to un-proportionally large E.

The second measure is the mass conservation between rainfall, runoff and infiltration. The relative error that reflects mass conservation is defined as

$$e(\%) = \frac{\sum_{D,t} rain - \sum_{D,t} runoff - \sum_{D,t} infiltration}{\sum_{D,t} rain} \text{ x } 100 \tag{4.44}$$

where $\sum_{D,t}$ represents the summation over space and time. Note that evaporation and transpiration are not considered in the DIMBRR model. A small relative error indicates that the model is able to follow the principal of mass conservation.

Another statistics included in the analysis is Root Mean Squared Error (RMSE)

$$RMSE = \sqrt{\frac{1}{n} \sum_{i=1}^{n} (Q_i - \hat{Q}_i)^2} \tag{4.45}$$

where Q_i is simulated flow and $\hat{Q}_i$ is observed flow, n is the number of observations. RMSE measures the fitness between the observed and the simulated hydrographs. It also suffers the same inherent weakness as coefficient of efficiency when there is a slight shift in the timing between the simulated hydrograph and the observed one.

The common mean and standard deviation are also used to judge the calibration results. In addition, visual inspections of the simulated hydrographs and the comparisons of the calibration quantities in the form of scatter plots are provided.

Calibration Results

The final calibration parameters are porosity and K_s. The K_s modifiers for the six sub-categories are 0.4, 1.0, 3.5, 0.4, 1.0, and 1.0. Two uniform multipliers M_{psi} and M_{Ks} are then applied to the porosity and K_s field respectively. The multipliers are varied systematically to test the watershed responses in each calibration event. Figure 4.14 shows the contour plots of the coefficient of efficiency for the three calibration variables, *i.e.* runoff volume, peak flow, and time to peak flow, in the dual-multiplier space. The search ranges of the multipliers are set so the calibration parameters will have physically meaningful values. The criteria for choosing multipliers are for the calibration parameters to produce the best possible coefficient of efficiency ($E = 1$ for perfect simulation) for runoff volume, and good coefficients of efficiency for peak flow and time to peak flow within the search ranges. Based on the above considerations, a pair of multipliers is chosen:

$$M_{psi} = 0.80$$

$$M_{Ks} = 0.96$$

The porosity multiplier corresponds to the following parameters.

$$\psi_{sandy\_loam} = 0.36$$

$$\psi_{sand} = 0.35$$

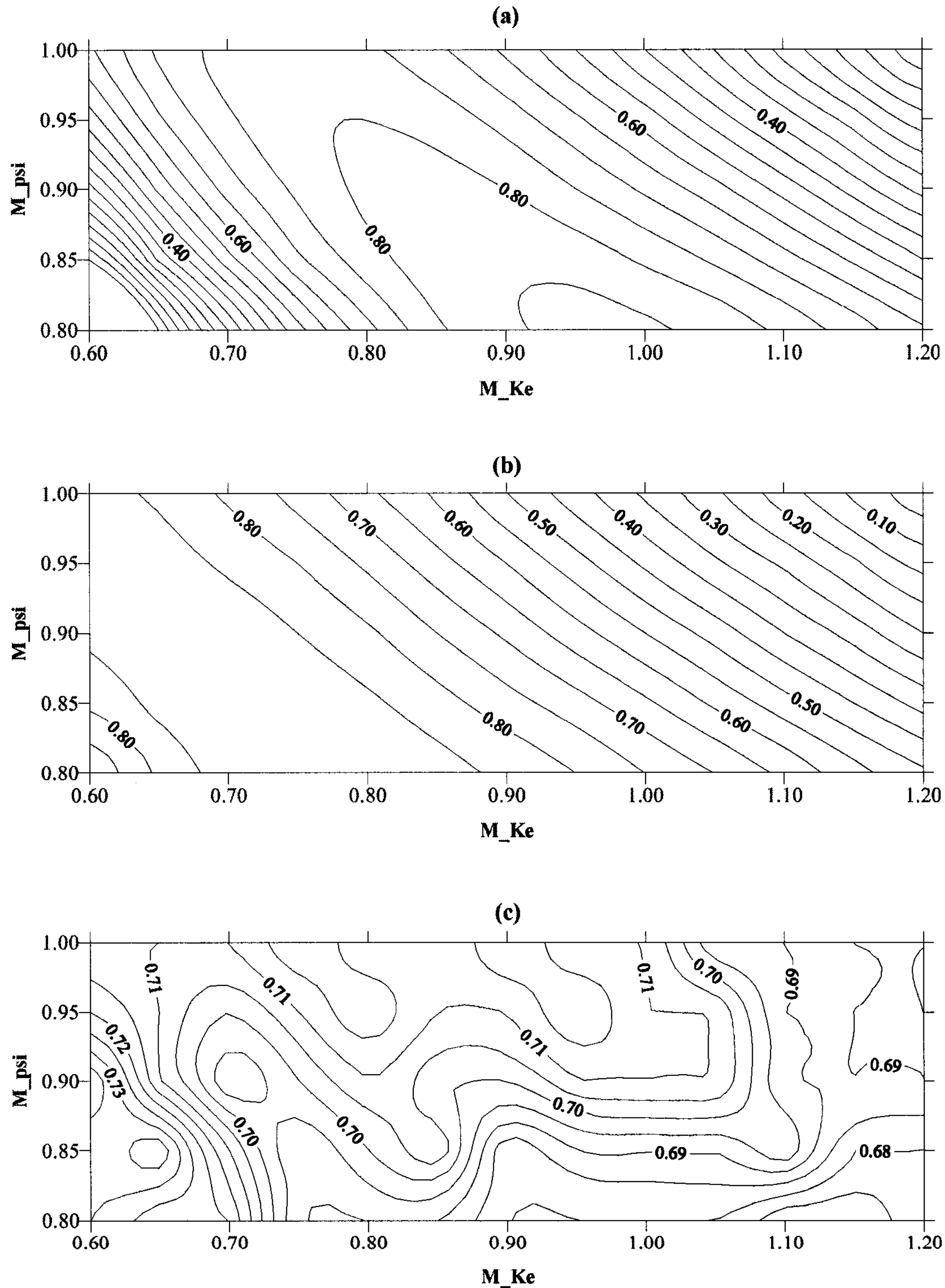

Figure 4.14 Contour plots of the coefficient of efficiency for (a) runoff volume, (b) peak flow, and (c) time to peak flow. M_{Ks} and M_{psi} are multipliers for effective hydraulic conductivity and porosity, respectively.

The mean K_s values corresponding to the K_s multiplier are given in Table 4.8.

Table 4.8 Effective Hydraulic Conductivities for the Six Categories

	Cat. A	Cat. B	Cat. C	Cat. D	Cat. E	Cat. F
Orig. K_s (cm/hr)	0.757	0.838	0.884	0.798	0.831	21.082
K_s category modifier	0.4	1.0	3.5	0.4	1.0	1.0
K_s uniform multiplier	0.96	0.96	0.96	0.96	0.96	0.96
K_s (cm/hr)	0.2907	0.8045	2.9702	0.3065	0.7978	20.2387

From Rawls and Brakensiek (1985), the mean porosity for sand is 0.437 with the ± one standard deviation about the mean being 0.374 ~ 0.500. The mean porosity for sandy loam is 0.453 and the ± one standard deviation about the mean is 0.351 ~ 0.555. The porosity for sandy loam used in this study is within one standard deviation range of the mean porosity given by Rawls and Brakensiek (1985). While the porosity of sand falls just outside the one standard deviation range of the mean as given in literature, its value, however, is close enough to the lower range to be considered physically acceptable. The saturated hydraulic conductivity given by Rawls and Brakensiek (1983) is 23.56 cm/hr for sand and 2.18 cm/hr for sandy loam. The latter is much larger than the effective hydraulic conductivities obtained by Goodrich (1990) for the sandy loam category at WG11. Goodrich's (1990) K_s values are first derived from a regression equation based on soil information and the K_s values from Rawls and Brakensiek (1983), and then corrected for rock and vegetation cover. Since this study employs Goodrich's K_s data as base line, the K_s values tend to be much smaller than the K_s values reported by Rawls and Brakensiek (1983). With the physical considerations going into the procedure to derive K_s in Goodrich's (1990) study, the K_s values used here are assumed to be acceptable.

Applying the above multiplier pair to DIMBRR model and the five calibration rainfall-runoff events, the following statistics can be drawn from the model results.

i) Coefficient of efficiency

The following coefficients of efficiency are obtained for the five calibration events.

Runoff volume: $E_v = 0.87$

Peak flow rate: $E_{Qp} = 0.79$

Time to peak: $E_{Tp} = 0.68$

Table 4.9 lists the coefficient of efficiency for discharge from each event.

Table 4.9 Coefficient of Efficiency for Discharge

Event #	E of Discharge
1	0.81
2	0.92
3	0.08
4	0.65
5	0.88

The runoff volumes of the calibration set have a coefficient of efficiency of 0.87 which is good considering all the uncertainties involved in the field data collections on a watershed of this magnitude. The coefficient of efficiency for peak flow is 0.79 and for time to peak flow is 0.68. These numbers are also acceptable for calibration variables with less importance. Of the five coefficients of efficient for discharge shown in Table 4.9, three are larger than 0.8 which are considered good given that E = 1 represents the perfect model simulation. The E of discharge for Event 4 (8/21/1973) is 0.65. This is primarily caused by a slight shift in the timing of simulated hydrograph from the observed one (Figure 15). Among all the calibration events, event 3 (9/24/1974) suffers the worst E of discharge. This event has the smallest runoff volume among all the 14 rainfall-runoff events that are used for calibration and verification (Table 4.3). The less than satisfactory simulation results for this runoff event could be caused by one or both of the following reasons: 1) too large an uncertainty in the calibration data, 2) the model's inability to capture runoff dynamics when there is little rainfall. Fortunately, it is the large rainfall-runoff events that are most important from the point of view of watershed management. Overall, the above coefficients of efficiency are considered satisfactory for the calibration set.

ii) Mass conservation

Table 4.10 Mass Relative Error of Calibration Set

Event #	*e(%)*
1	3.7
2	2.2
3	-0.2
4	3.4
5	5.5

The mass relative errors for the five rainfall-runoff events are all less than or equal to 5.5%. Such small errors indicate that the DIMBRR model preserves mass balance well.

iii) Root mean squared error (RMSE)

Table 4.11 RMSE of Calibration Set

Event #	*RMSE* (m^3/s)
1	4.43
2	1.35
3	1.94
4	3.75
5	0.99
Mean	2.49

RMSE measures the agreement between the observed and the simulated hydrographs. The large RMSE for Event 1 and 4 are mainly caused by a slight shift between the timing of the observed and simulated hydrographs (Figure 4.15) and the relatively high flows from these events. As explained in earlier text, this is an inherent weakness of RMSE as a measure of goodness of fit.

iv) Mean and standard deviation

Table 4.12 Mean and Standard Deviation of Calibration Set

	Obs. V (mm)	Sim. V (mm)	Obs. Qp (m^3/s)	Sim. Qp (m^3/s)	Obs. Tp (min)	Sim. Tp (min)
Mean	3.27	3.04	11.82	9.28	83.00	76.40
St. Dev.	1.88	2.32	8.20	7.64	20.80	14.29

The mean and standard deviation of the three calibration variables are comparable between the observation set and the simulation set. This further confirms that the choices of the uniform multipliers are suitable to the model and the watershed.

v) Hydrographs and Hyetographs at Rain Gage 90

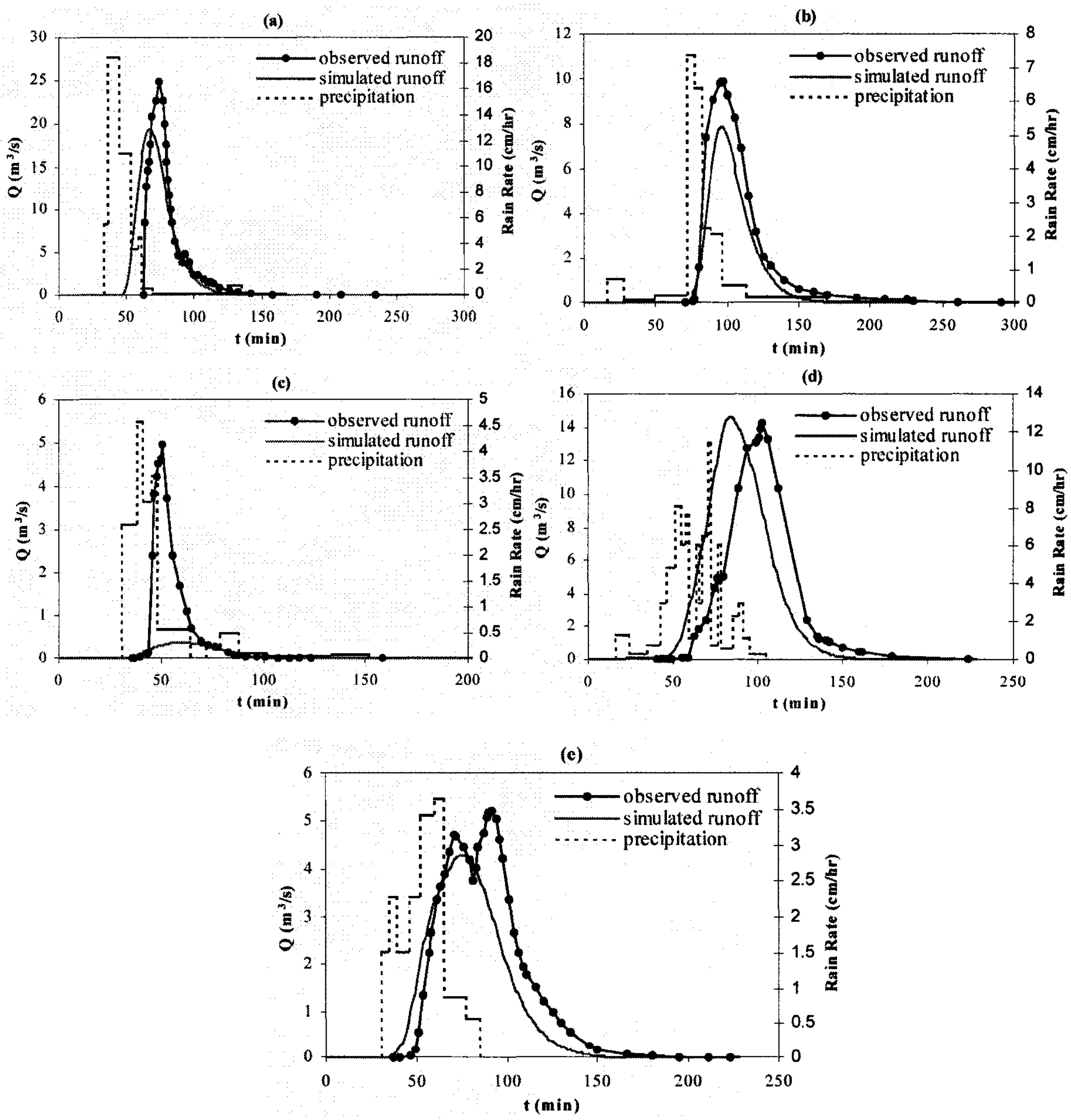

Figure 4.15 Observed and simulated hydrographs of calibration set: (a) event 1, 8/5/1968, (b) event 2, 8/12/1971, (c) event 3, 9/24/1974, (d) event 4, 8/21/1973, and (e) event 5, 9/6/1976. Time t = 0 in all graphs correspond to the time when rainfall starts.

vi) Scatter plots

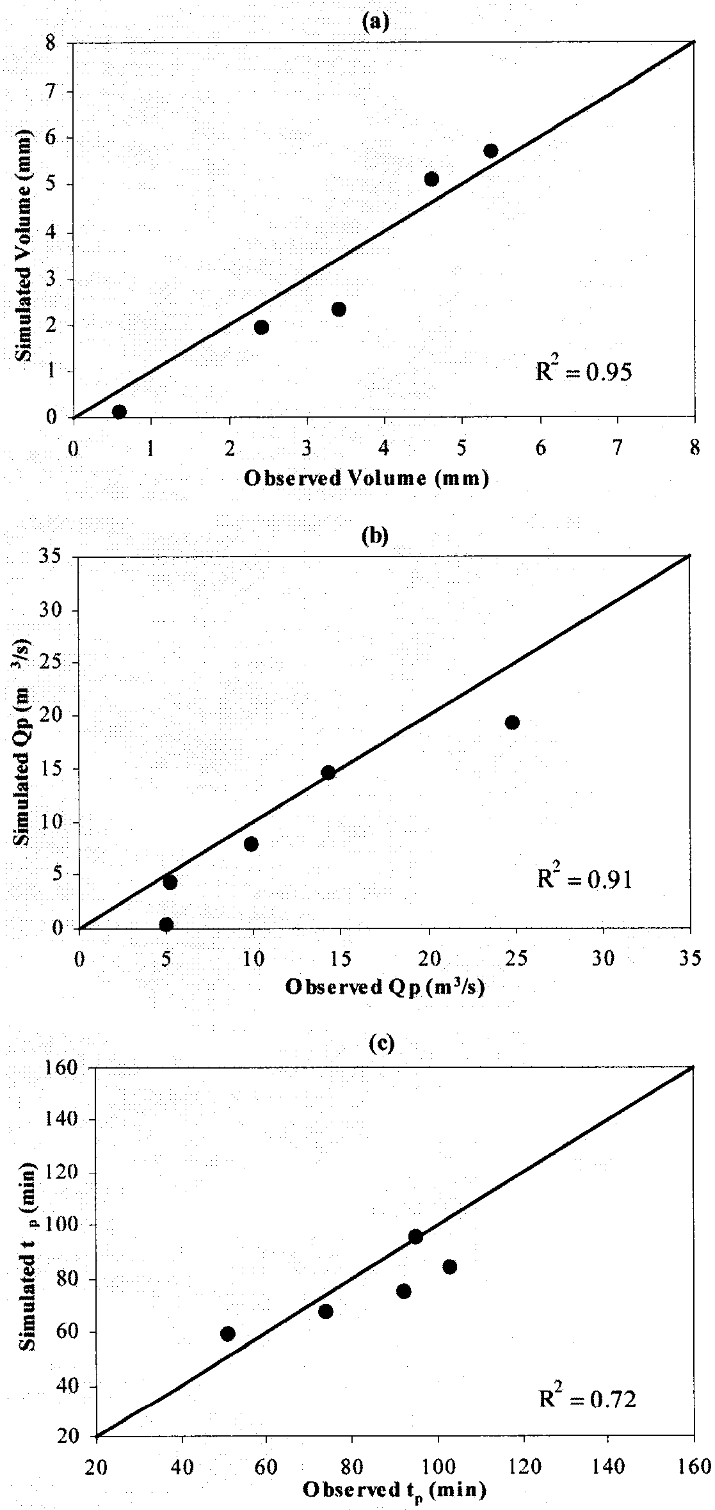

Figure 4.16 Scatter plots of observed and simulated variables of calibration events: (a) runoff volume, (b) peak flow, and (c) time to peak.

The R^2 values in Figure 4.16 are computed using the 45° line as a "regression line". The values indicate how well the model simulates the observed variables. If $R^2 = 1$, the data points will fall on the 45° line, indicating a perfect simulation. Based on R^2 values, runoff volume and peak flow exhibit better simulation results than the time to peak flow while the latter is still acceptable with an $R^2 = 0.72$.

In summary, the analysis of the calibration results show that choosing the uniform multipliers to be $M_{psi} = 0.8$ and $M_{Ks} = 0.96$ can lead to satisfactory model results that reasonably replicate watershed responses for the calibration rainfall-runoff events with the exception of the very small event on September 24, 1974 (Event 3). The model simulates runoff volume with the highest accuracy, peak flow the next and time to peak the least. To further prove the acceptance of the model as the rainfall-runoff model for later study on scaling properties of watershed processes, a complete verification procedure needs to be performed.

4.4 Model Verification

As listed in Table 4.3, the verification set is composed of nine rainfall-runoff events between 1971 and 1977. The set covers a wide range of event sizes, initial conditions, and hydrograph types. Even though the number of events makes it impossible to include all the possible rainfall patterns and to excite all runoff dynamics on a large watershed like WG11, the coverage is descent enough to capture the general behavior of the model under given conditions and helps with the understanding of how well the model can reproduce real events.

4.4.1 Data Preparation

Most of the data used for verification are the same as for calibration with the exception of rainfall data and initial soil moisture content. As explained in Section 4.3.2, initial soil moisture content is determined by soil properties and rainfall history. Soil properties include residual soil moisture and field capacity. They are derived from saturated hydraulic conductivity via regression relationships (Section 4.3.2). Figure 4.17 shows the 10-day rain history prior to the nine verification events. Factor *d*, which is estimated based on rain history (eq. (4.43) and the text that follows), represents the dryness of the soil. Table 4.13 lists the factor *d* set for the verification events.

Table 4.13 Factor d for Verification Rainfall-Runoff Events

	8/24/ 1971	7/12/ 1973	7/16/ 1973	9/13/ 1975	9/3/ 1975	9/5/ 1975	9/7/ 1975	7/27/ 1976	6/22/ 1977
Overland	4	3	3	3.5	4	1	1.5	4	∞
Swale	4	3	3	3.5	4	1	1.5	4	∞
Incised Channel	∞*	∞	4	∞	∞	1.5	3	∞	∞

* Dry condition corresponds to $d = \infty$.

4.4.2 Verification Results

Applying the uniform parameter multipliers obtained from calibration to the verification events, the following statistics can be derived from the model results for the verification set.

Runoff volume: $E_v = 0.66$

Peak flow rate: $E_{Qp} = 0.53$

Time to peak: $E_{Tp} = 0.97$

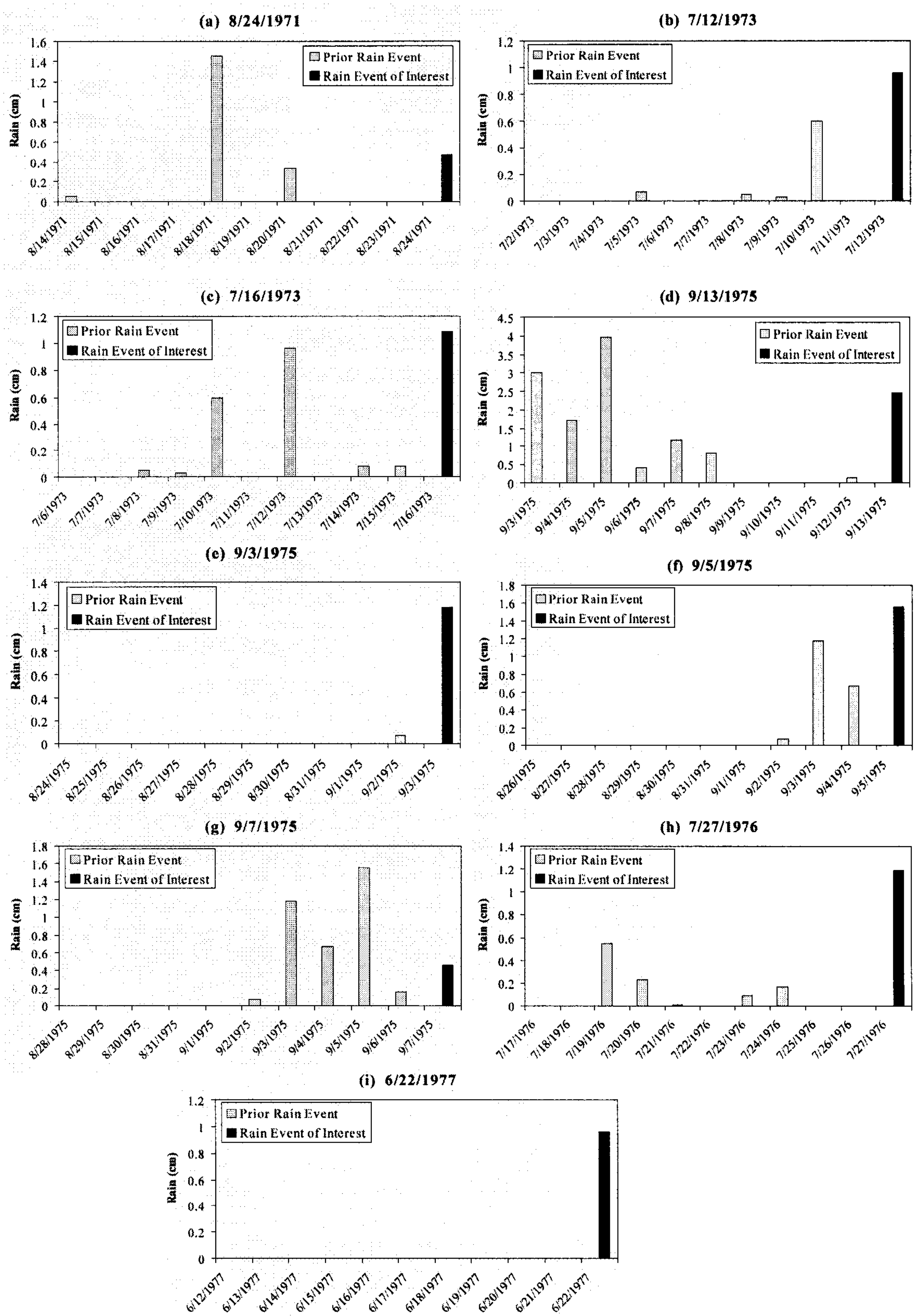

Figure 4.17 Ten-day rain event history at RG90 prior to verification rain event: (a) 8/24/1971, (b) 7/12/1973, (c) 7/16/1973, (d) 9/13/1975, (e) 9/3/1975, (f) 9/5/1975, (g) 9/7/1975, (h) 7/27/1976, and (i) 6/22/1977.

Table 4.14 lists the coefficient of efficiency for discharge from each verification event.

Table 4.14 Coefficient of Efficiency for Discharge

Event #	E of Discharge
1	0.44
2	0.26
3	0.74
4	0.71
5	0.50
6	0.82
7	0.66
8	0.92
9	0.73

Recall that the coefficients of efficiency for calibration set are: E_v = 87, E_{Qp} = 0.79, and E_{Tp} = 0.68. The runoff volumes and the peak flows from the nine verification events have smaller coefficients of efficiency than the calibration set while the times to peak show much better simulation results. The coefficients of efficiency for discharge from most verification events are well above 0.5, showing fairly good results for verification cases. To have a reference for the model performance, Table 4.15 compares the calibration and verification results described here and those by Goodrich (1990). *KINEROS* model (*Woolhiser et al.*, 1990) was calibrated and verified using data from Walnut Gulch including data from WG11 in Goodrich's (1990) work. While there is some overlapping in the runoff events used between the two works, Goodrich (1990) used more events along with some other difference in various aspects of his work. So this comparison is meant to be a general reference rather than precise assessment of the differences between the two studies. Compared to Goodrich's (1990) results, the coefficients of efficiency from this study prove that DIMBRR model performs well enough to be applied to scaling studies of watershed processes.

Table 4.15 Comparison of Calibration and Verification Results from Two Models

	KINEROS	DIMBRR
Calibration parameters	K_s, Manning's n, coeff. Of variation of K_s,	K_s, porosity
Variables used in calibration & verification	volume, peak flow	volume, peak flow, time to peak flow
Calibration E_v	0.86	0.87
Calibration E_{Qp}	0.84	0.79
Calibration T_p	--	0.68
Verification E_v	0.49	0.66
Verification E_{Qp}	0.16	0.53
Verification T_p	--	0.97

ii) Mass conservation

The mass relative errors of the verification events are given in Table 4.16. Similar to the calibration events, the verification set also has very small mass relative errors except event 6 which has the largest runoff volume and peak flow among all the calibration and verification events (Table 4.3). This signals that the model might not be able to uphold the principle of mass conservation very well for exceptionally large runoff events.

Table 4.16 Mass Relative Error of Verification Set

Event #	*e(%)*
1	2.3
2	2.9
3	2.2
4	3.6
5	1.5
6	6.6
7	1.3
8	3.0
9	2.4

Similar to the calibration events, the verification set also has very small mass relative errors except event 6 which has the largest runoff volume and peak flow among all the calibration and verification events (Table 4.3). This signals that the model might not be able to uphold the principle of mass conservation very well for exceptionally large runoff events.

iii) Root mean squared error (RMSE)

The RMSE of the flow rate of the verification events are given in Table 4.17. Caution needs to be taken when interpreting the value of RMSE. Both low peak flow and good agreement between observed and simulated hydrographs can lead to small RMSE. For instance, event 5 has a small RMSE that is caused by low flow while the small RMSE for event 7 reflects a relatively good fit between the hydrographs. It is also noted that large RMSE may be a result of large discrepancy in the hydrographs either in magnitude or in timing.

Table 4.17 RMSE of Verification Set

Event #	RMSE (m^3/s)
1	2.44
2	4.04
3	1.46
4	4.30
5	1.01
6	4.85
7	1.24
8	1.91
9	2.33
Mean	2.62

iv) Mean and standard deviation

Table 4.18 Mean and Standard Deviation of Verification Set

	Obs. V (mm)	Sim. V (mm)	Obs. Qp (m^3/s)	Sim. Qp (m^3/s)	Obs. Tp (min)	Sim. Tp (min)
Mean	3.81	2.81	12.56	8.86	82.56	81.67
St. Dev.	2.79	2.01	9.19	6.50	38.74	37.91

From Table 4.18, the discrepancies between the means and the standard deviations of the simulated runoff volumes and peak flows and those of the observed ones are noticeably larger than the discrepancies in times to peak. Nevertheless, the agreement between the simulations and the observations is still acceptable as far as verification result is concerned.

v) Hydrographs

Figure 4.18 compares the observed and simulated hydrographs of all the nine verification events under the watershed conditions either set by calibration or by the events' unique circumstances. The hyetographs at Rain Gage 90 are also shown in Figure 4.18. It is worth noting that the fifth event has a multi-peak hydrograph. This pattern is generally followed by simulated hydrograph with the exception of very small peaks and the magnitude of the peaks, possibly due to low flow. It proves that the model is capable of simulating multi-peak hydrographs for moderate runoff events.

vi) Scatter plots

Figure 4.19 displays the scatter plots of the verification events. The R^2 values in Figure 4.19 represent how well the model simulations fit the observed verification events. The best fit is for time to peak with $R^2 = 0.97$, followed by the runoff volume with $R^2 =$ 84, and then by peak flow with $R^2 = 0.74$. The order of the goodness of fit among the three variables is consistent with the findings from other evaluation methods used above. The scatter plots for runoff volume and peak flow reveal that the multipliers for porosity and K_s as chosen from the calibration will generally lead to underestimations of runoff volume and peak flow even though the overall statistics remain acceptable.

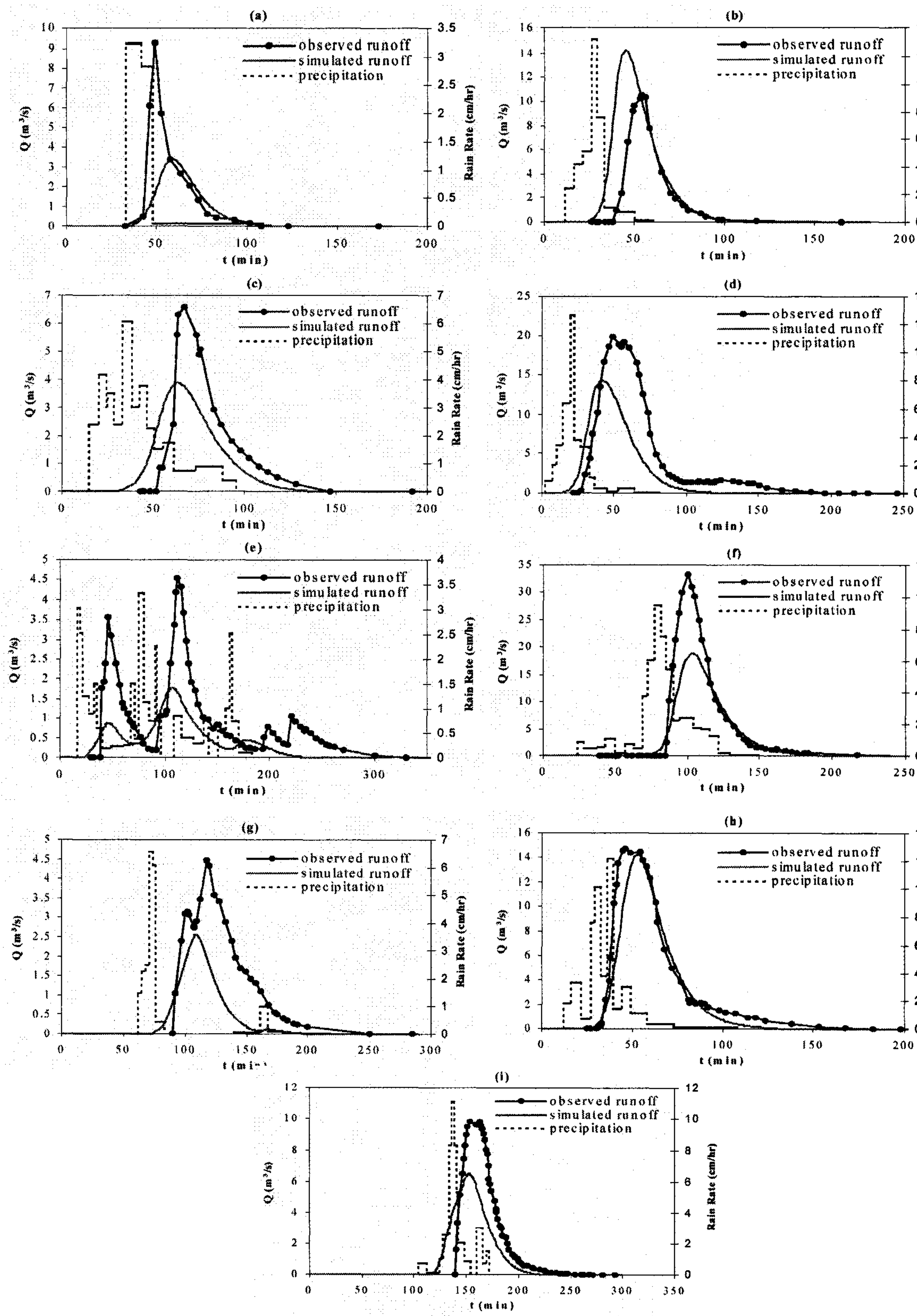

Figure 4.18 Observed and simulated hydrographs of verification set: (a) event 1, 8/24/1971, (b) event 2, 7/12/1973, (c) event 3, 7/16/1973, (d) event 4, 9/13/1975, (e) event 5, 9/3/1975, (f) event 6, 9/5/1975, (g) event 7, 9/7/1975, (h) event 8, 7/27/1976, and (i) event 9, 6/22/1977.

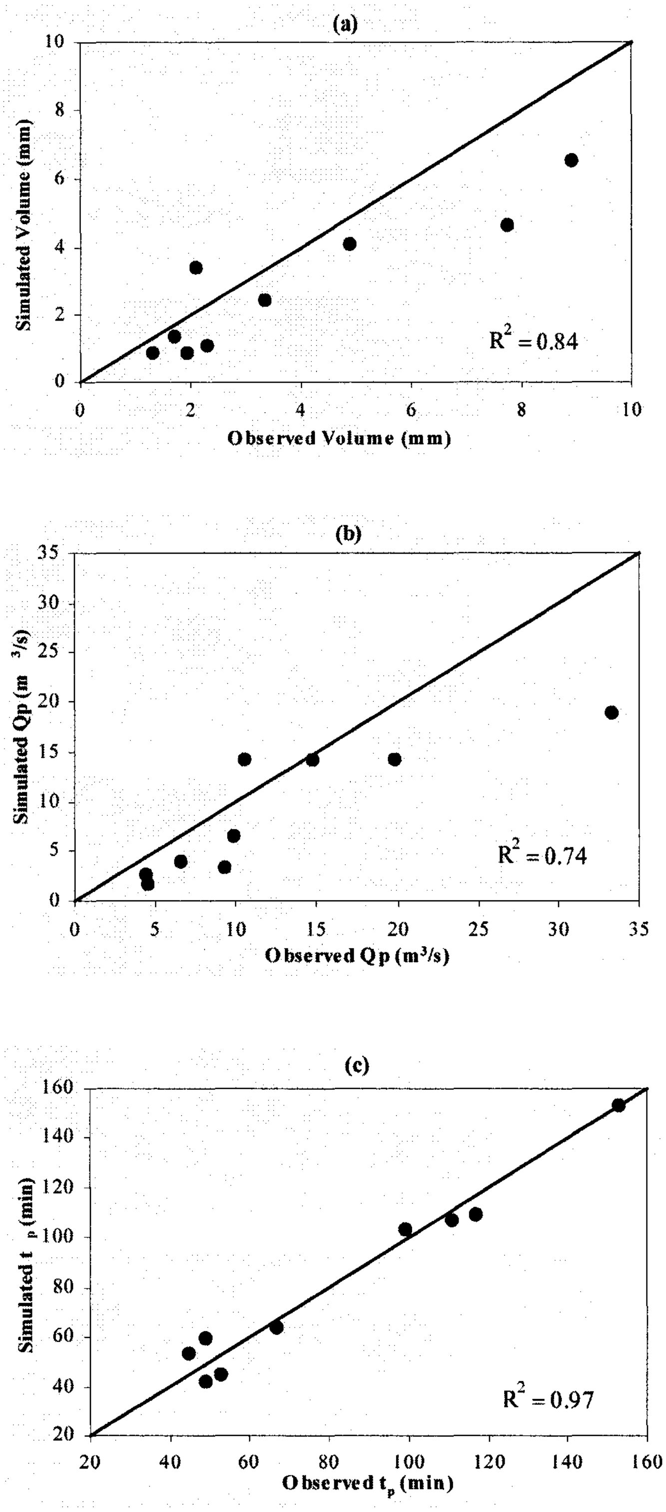

Figure 4.19 Scatter plots of observed and simulated variables of the verification events: (a) runoff volume, (b) peak flow, and (c) time to peak.

As mentioned at the beginning of the calibration section, the goal of the calibration and verification of DIMBRR model is to test the suitability of the model for application in the scaling studies in the next chapter. The above analyses on the verification results have shown that the DIMBRR model can reproduce the time to peak of runoff events with a high degree of accuracy and the runoff volume and peak flow with acceptable accuracy. This result instills a sense of confidence that the model can reasonably replicate the distributed watershed processes such as infiltration and runoff over a watershed – making it an acceptable rainfall-runoff model for the scaling studies that follow.

Chapter 5

EFFECTS OF MULTIFRACTAL RAINFALL AND SATURATED HYDRAULIC CONDUCTIVITY ON INFILTRATION

This chapter presents the research carried out on the infiltration processes in the framework of universal multifractal. Rainfall and soil fields with various characteristics, either scaling or non-scaling, are fed to the DIMBRR model and the resulting space-time surface infiltration rates are analyzed. The impacts of rainfall and soil fields on the watershed process are thus revealed through these numerical experiments, and the results are shown in two main parts: steady rainfall field (Section 5.3) and space-time multifractal rainfall field (Section 5.4). A brief discussion about the impact of average rain rate on infiltration is also given at the end of the chapter.

5.1 Study Area

A 15 km^2 square area on the Lindstrom Farm near Sterling, Colorado is chosen to be the study area for the numerical experiments (Figure 5.1). The choice of the area was made based on the following factors:

i. Climate similarities between the study area and the Walnut Gulch subwatershed 11 (WG11), which was used for the model calibration and verification in Chapter 4; both areas are semi-arid with high-intensity summer thunderstorms.

ii. Hydrological similarities between the study area and WG11 subwatershed; both watersheds have ephemeral streams where Hortonian overland flow is the predominant mechanism for runoff generation.

iii. Consistency with the locations of USDA-ARS experimental sites; Fig. 5.1 shows the relative location of the study area to USDA-ARS experimental sites near Sterling, Colorado.

iv. Requirement of the universal multifractal framework; both the generation of scaling fields and the estimation of universal multifractal parameters require the use of fast Fourier transform (FFT). This constrains the study area to be 2^n x 2^n pixels, where n is an integer and should be at least 7 (corresponding to 128 x 128 pixels) for meaningful analysis.

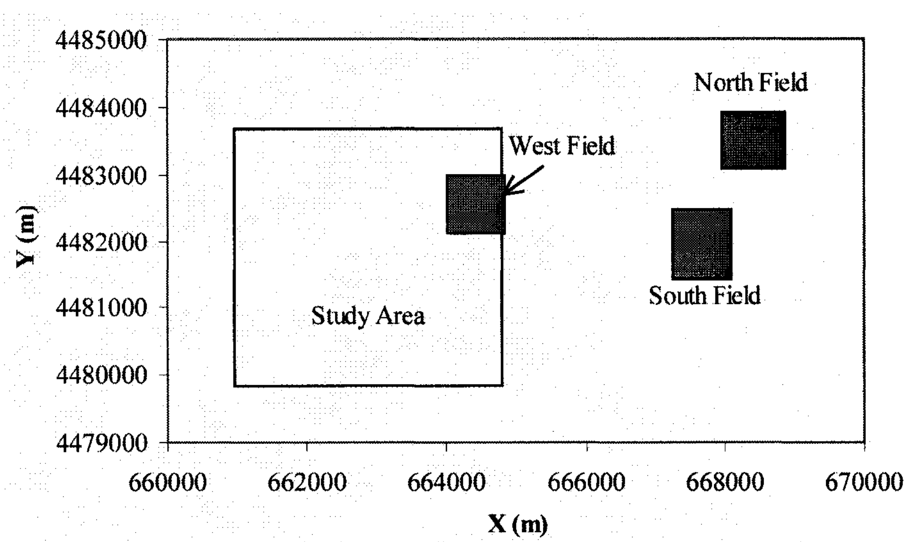

Figure 5.1 Locations of the study area and the USDA – ARS experimental sites on the Lindstrom Farm near Sterling, CO

A set of 7.5-minute DEM data named Buffalo Ranch NE was downloaded from USGS online data source (http://edc.usgs.gov/products/elevation/dem.html) which corresponds to latitude 40°22′30″ ~ 40°30′00″, longitude 103°00′00″ ~ 103°7′30″. It includes approximately 338 x 453 pixels, each with a size of 30 m x 30 m. Because of computational limitations with respect to rainfall simulation, and the constraint of FFT, a partial area 128 x 128 pixels is used as the study area. The size of the study area is thus about 1475 ha. The main soil type in the area is loam.

As stated in Chapter 4, channels in a watershed can be defined based on contributing area and a contributing area threshold. The channels in the study area are determined using a contributing area threshold of 110 pixels for optimal fittings of the defined channels to the observed ones. Figure 5.2 (a) displays the channels and the subwatershed used in the study area. Some corrections were made to conform the defined channels to the observed channels including minor changes to the DEM data and the removals of a few non-existent channels. There are 514 channel pixels and 15870 overland pixels in this area. Figure 5.2 (b) shows the channels in the study area obtained from a county survey (USDA Soil Conservation Service, 1974). The agreement between the two sets of channels is fairly good.

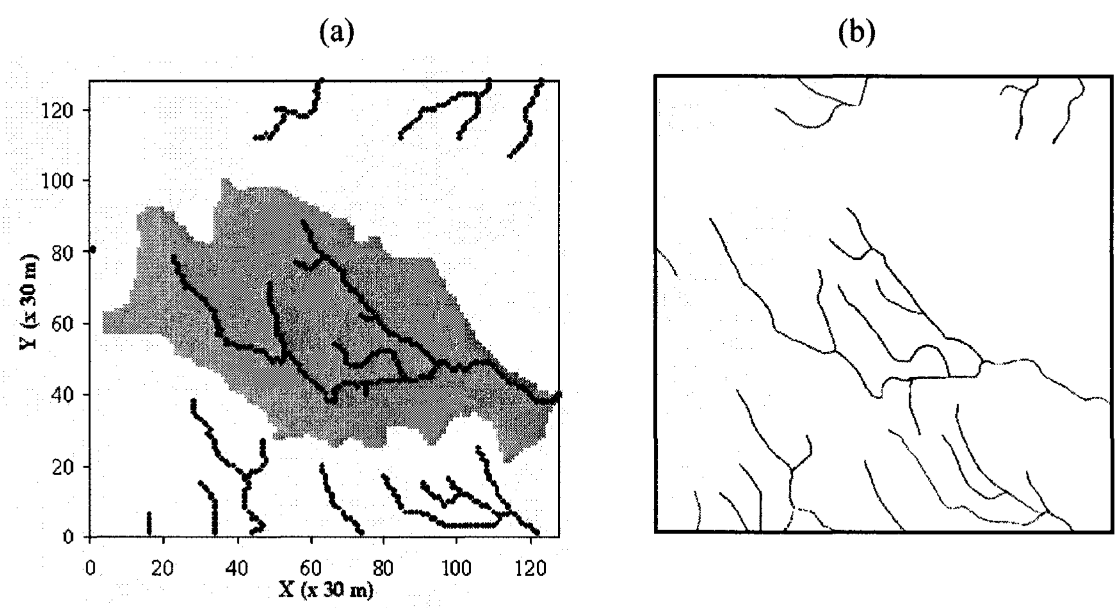

Figure 5.2 (a) Defined channels in the Sterling study area; (b) Channels in the Sterling study area from county survey (reproduced from USDA Soil Conservation Service, 1974)

5.2 Choosing Model Parameters

The choice of model parameters is an important issue for producing realistic infiltration fields. Two models are utilized in this study: the UM model for generating most rain rate and K_s fields, and the DIMBRR model for simulating the watershed responses (infiltration and runoff) to the rainfall. Sections 5.2.1 and 5.2.2 respectively introduce the UM model parameters chosen for generating the rainfall and the K_s fields used in this study. Section 5.2.3 describes the various DIMBRR model parameters adopted for the Sterling study area.

5.2.1 Rain Rate Model Parameters

Both conservative and non-conservative rain fields have been observed in nature (*e.g.* Tessier *et al.* 1993, Pecknold *et al.* 1993, Harris *et al.* 1996). Tessier and coworkers (1993) reported that the scaling parameters for radar rain fields are α = 1.35, C_1 = 0.3, and H = 0 (*i.e.* homogeneous); and the parameters from raingauge data are α = 1.35, C_1 = 0.2, and H = 0. Based on this information, the rain rate model parameters are chosen to be α = 1.2 – 1.8, C_1 = 0.2 – 0.4, and H = 0 – 0.5, where non-zero H is used to simulate non-conservative (non-homogeneous) rain field.

Typical spatial resolution for rain rate measurements are on the order of a few hundred meters to a few kilometers or even larger. Because of the constraint of the DEM data used here, the resolution of the study area for this research is 30 m. This is a very high resolution for rain fields. However, some radar rain data have shown that rain rate fields could be multiscaling at a resolution of 30 m to 120 m (Tessier *et al.*, 1993; Menabde *et al.*, 1997). This observation serves as the justification for the high resolution used in this study.

5.2.2 K_s Model Parameters

Some studies report that K_s and $\ln(K_s)$ data are multifractal in the horizontal and/or the vertical directions (*e.g.* Liu and Molz, 1997; Tennekoon, 2003). It is also known that some geophysical fields and processes closely related to K_s, such as soil moisture and topography, are multifractal (Rodriguez-Iturbe *et al.*, 1995; Lavallée *et al.*, 1993). It is thus reasonable to speculate the multifractal nature of K_s field. In this study, the horizontal K_s field is assumed to be multifractal and conforms to the universal multifractal concept. The following parameters are used in the numerical experiments: $\alpha = 1.5 - 2.0$, $C_1 = 0.01 - 0.05$, and $H = 0 - 0.5$ where $\alpha = 2.0$ corresponds to the lognormal multifractal case. The small C_1 values are taken because usually natural K_s field is known to have very little sparseness except in cases such as many rock outcrops.

5.2.3 DIMBRR Model Parameters

Since the dominant soil type at the Sterling study site is loam, the porosity for loam, 0.463 cm^3/cm^3 (Maidment, 1992, Chapter 5), is applied throughout the study area. Factor *d* (Section 4.3.2) for computing the initial soil moisture content is set to be 3 for overland and ∞ for channels. These correspond to the following initial soil moisture contents

$$\theta_i = \begin{cases} \theta_r + \frac{1}{3}(\theta_f - \theta_r), & \text{overland} \\ \theta_r, & \text{channel} \end{cases}$$

where θ_f is field capacity, and θ_r is residual soil moisture content. These two parameters and the wetting front suction are computed at each overland pixel from K_s using the regression equations (4.38) to (4.40). The three parameters are set to be constants at all channel pixels as follows: $\theta_f = 0.27$ cm^3/cm^3, $\theta_r = 0.117$ cm^3/cm^3, and ψ = 8.89 cm. These are the typical parameter values for loam (Maidment, 1992, Chapter 5). For the computation of perimeter, the cross-section of the channels is assumed to have trapezoidal shape and both banks have a uniform slope of 30°. Channels bottom width is assumed to be proportional to the contributing area at the channel pixel with the minimum width being 2 m and the maximum 6 m. Manning's n is set to be 0.035 overland (field crops) and 0.033 in channels (natural, clean, basically straight channels) (Chow *et al.*, 1988, Chapter 2).

The above settings are employed for all the rainfall-runoff experiments carried out in Chapters 5 and 6 so that the effect of rainfall and K_s on the watershed responses can be examined without the complications from other hydrological factors. It should be stressed that different choices on the parameters, such as the factor *d* for determining the initial soil moisture content, will result in different behavior of the infiltration processes and thus possibly different scaling features. It would be interesting to study the effects of these parameters on the scaling properties of the various watershed processes, but this topic is beyond the scope of this research effort.

5.3 Analysis of Infiltration Under Steady Rain

The first group of rainfall-runoff experiments is performed under the assumption of steady rainfall, that is, rain rate field that is variable in space but constant in time. Both scaling and non-scaling rain and K_s fields are tested for their effect on infiltration processes.

In the remaining study, the input parameters of the scaling rain and K_s fields are taken to be the real parameters of the generated fields. This assumption is made based on two considerations:

1) The studies carried out in Section 3.3.4 show that the input parameters α and C_1 of the conservative fields are reproduced with fairly high accuracy (Figures 3.12 and 3.13). It is also shown there (Figure 3.16) that the input parameter H of the non-conservative fields can be estimated precisely in most cases. A non-conservative field is generated from its underlying conservative field through a fractional differentiation of order H. This process does not change α and C_1. Hence, all the three input parameters are well reproduced in the non-conservative field.
2) The conclusions about the influence of the rain and the K_s scaling parameters on infiltration is largely in qualitative rather than quantitative terms. Therefore, the small discrepancy between the input and the actual parameters of the rain and the K_s fields does not pose a serious problem to the conclusions reached in this study.

To be consistent with the notations adopted in Chapter 4, the following symbols are used hereafter: α_R, C_{1R}, and H_R represent the input and the actual scaling parameters of the rain fields; α_{Ks}, C_{1Ks}, and H_{Ks} indicate the input and the actual scaling parameters of the K_s fields; and α_i, C_{1i}, and H_i are the *estimated* scaling parameters of the infiltration fields. Furthermore, R_R^2, R_{Ks}^2, and R_i^2 represent R^2 of log-power spectrums of rain, K_s and infiltration fields, respectively.

5.3.1 Experimental Set-up

Unless otherwise noted, the following set-ups are applied in the experiments carried out in this chapter.

i) Average rain rate is 3 cm/hr. This is a fairly large value for average rain rate in the field. However, as shown at the end of this chapter, rain with higher intensity will essentially lead to the same behavior in infiltration as with low intensity rain except such behavior is more stable in the former case. Such large average rain intensity is used to make clear the characteristics of the watershed processes.

ii) Average K_s is 1.32 cm/hr. This is the K_s value for loam as given by Rawls and Brakensiek (1983). This number is taken because the dominant soil type at the Sterling study area is loam.

iii) Rain duration is set to be 150 min. for the cases where both rain and K_s are scaling fields because, combined with the large rain rate used, it is long enough for infiltration and runoff processes to become well developed and exhibit their characteristics. Rain duration is set to be 1000 min. if either rain or K_s is non-scaling field because it could take longer time for the infiltration fields to manifest scaling behavior under these cases.

iv) Twenty-five runs (or samples) are used for each case studied and the average statistics are used for analysis (Section 3.3.5). This quasi-Monte Carlo approach is adopted to ensure more accurate representations of the processes being studied as a large degree of uncertainty is involved in such numerical experiments.

5.3.2 Effects of Non-Scaling Rain and Scaling K_s

In this set of experiments, non-scaling rain and scaling K_s fields are used to examine the effect the driving fields have on watershed infiltration processes. Twenty-five lognormally distributed random rain fields with 128 x 128 pixels are generated with a mean of 3 cm/hr and a standard deviation of 3 cm/hr. The random fields are generated by assigning a lognormally distributed random number series of 16384 values to a square area of 128 x 128 pixels row by row. The rain fields are white noises and have an average radial power spectrum with β = -1.02 (Figure 5.3). A scaling K_s field is generated using the UM model for the experiments with a mean of 1.32 cm/hr and the following scaling parameters: $\alpha_{Ks} = 2.0$, $C_{1Ks} = 0.01$, and $H_{Ks} = 0.2$. Its power spectrum has a $\beta = 1.32$ and $R_{Ks}^2 = 0.97$ (Figure 5.3). Therefore the K_s field is indeed a scaling field. Each of the 25 (steady) rain fields and the scaling K_s field are input to the DIMBRR model to derive the corresponding space-time infiltration processes. The rain duration for this set of runs is 1000 min so that there is enough time for the infiltration processes to develop. The rainfall-runoff model is run for 1050 min so the behavior of the infiltration field after the rain stops can be examined.

Figure 5.3 shows the offset average power spectrum of the infiltration fields at several points in time, along with the average power spectrum of the steady rain fields and the power spectrum of the K_s field. It is observed in Figure 5.3 that the power spectrum of the infiltration field resembles that of the steady rain field at the beginning of the infiltration process, and gradually becomes more similar to that of the K_s field (before rain stops) especially at lower wavenumbers. This observation is in agreement with the known fact that rain field has a dominant effect on surface infiltration in the early stage of an infiltration process, and K_s (soil) becomes a more important factor than rain in determining the properties of infiltration field as rainfall continues. The slopes and the (modified) R_i^2 of the average infiltration power spectrums are plotted in Figure 5.4 (note the dual Y-axes). The slopes are computed using the full length of the power spectrums. Recall that the two criteria for a scaling field are: 1) linear log-log power spectrum (reference $R^2 \geq 0.9$ for this study); and 2) slope of the power spectrum is less than 0

(Section 3.2.1). Even though R_i^2 is quite large in the first 50 min or so in Figure 5.4, the slope of the power spectrum is greater than 0 and thus the infiltration field is non-scaling in this period. As time progresses, the value of R_i^2 decreases to just around the 0.9 reference value and stays stable until rain stops. The slope of the power spectrums stays negative during this time and, combined with the high R_i^2, indicates that the infiltration fields are scaling. The slope increases rapidly and becomes greater than zero soon after rain stops – revealing that the infiltration fields are no longer scaling after rain stops.

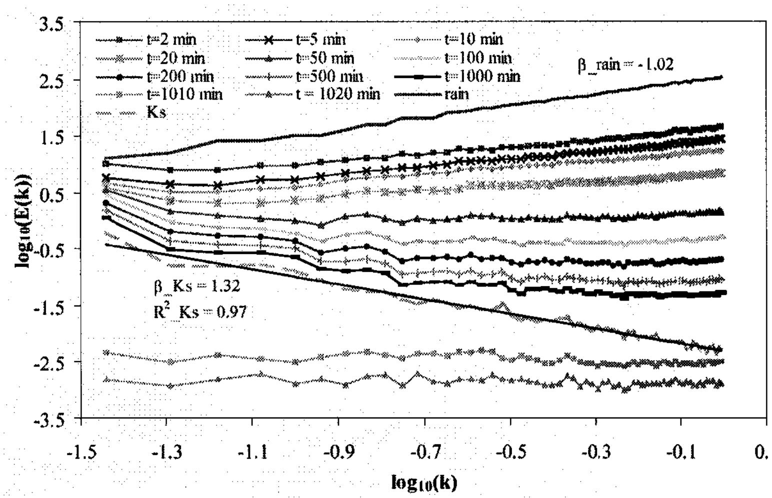

Figure 5.3 Average power spectrums of infiltration fields under non-scaling rainfall and scaling K_s field (the lines have been offset for clarity).

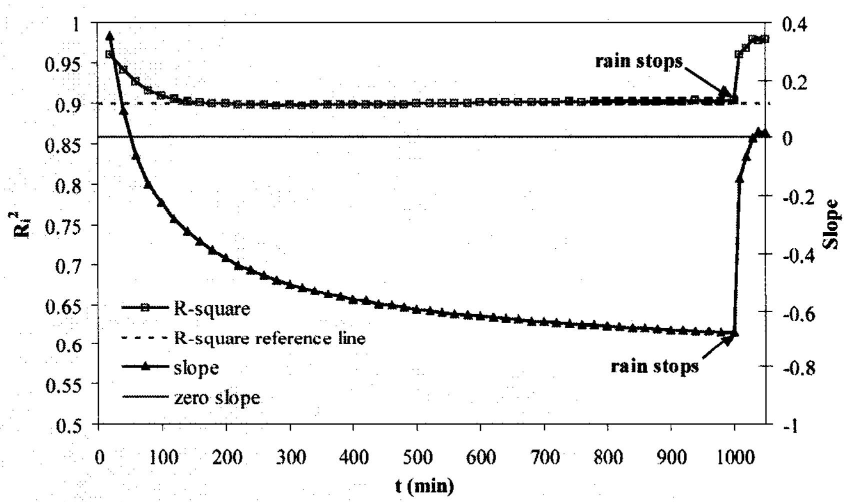

Figure 5.4 Slopes and R_i^2 of the average power spectrums of infiltration fields under non-scaling rainfall and scaling K_s field.

It is concluded from this set of experiments that a non-scaling rain field determines the non-scaling nature of its corresponding infiltration field in the early stage of the process. This 'early' stage may actually last for a long period of time. However, such an infiltration field may eventually become scaling if the K_s field is scaling.

5.3.3 Effect of Scaling Rain and Non-Scaling K_s

To test the effect of scaling rain and non-scaling K_s on infiltration, 25 lognormally distributed random K_s fields are generated with a mean of 1.32 cm/hr and a standard deviation of 0.7 cm/hr. The average power spectrum of the K_s fields has β = -1 (Figure 5.5), *i.e.* the K_s fields are realizations of white noise. The scaling rain field used in these experiments is generated using the UM model. It has a mean of 3 cm/hr and the following parameters: $\alpha_R = 1.5$, $C_{1R} = 0.2$, and $H_R = 0.5$. Its power spectrum has a β = 1.59 with $R_R^2 = 0.97$ (Figure 5.5) which confirms that the simulated rain -is a scaling field. The duration of the steady rain is 1000 min for this set of experiments. Each of the 25 K_s fields and the rain field are fed into the DIMBRR model and the average power spectrums of the 25 resulting infiltration processes at a few time points are shown in Figure 5.5. The time series of the slopes and the R_i^2 of the average power spectrums are presented in Figure 5.6. The power spectrums of the infiltration fields show a dominant effect from the rain field at the very early stage and a gradually stronger influence from the K_s field as time progresses especially at the high wavenumbers (Figure 5.5). The R_i^2 (= 0.76 at 20 min.) and the slopes of the power spectrums show that the infiltration field is scaling then close to be scaling for a short period of time at the beginning of the infiltration process because of the influence from the scaling rain, and rapidly becomes non-scaling as time increases (Figure 5.6). These results show that an infiltration process will be scaling at the early stage if the rainfall field is scaling, but will become non-scaling in time as long as the K_s field is non-scaling.

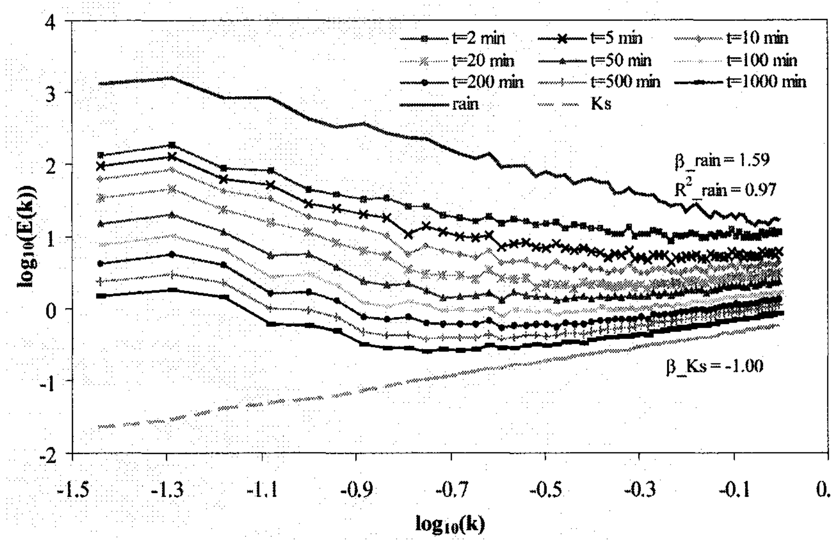

Figure 5.5 Average power spectrums of infiltration fields under scaling rainfall and non-scaling K_s field (the lines have been offset for clarity).

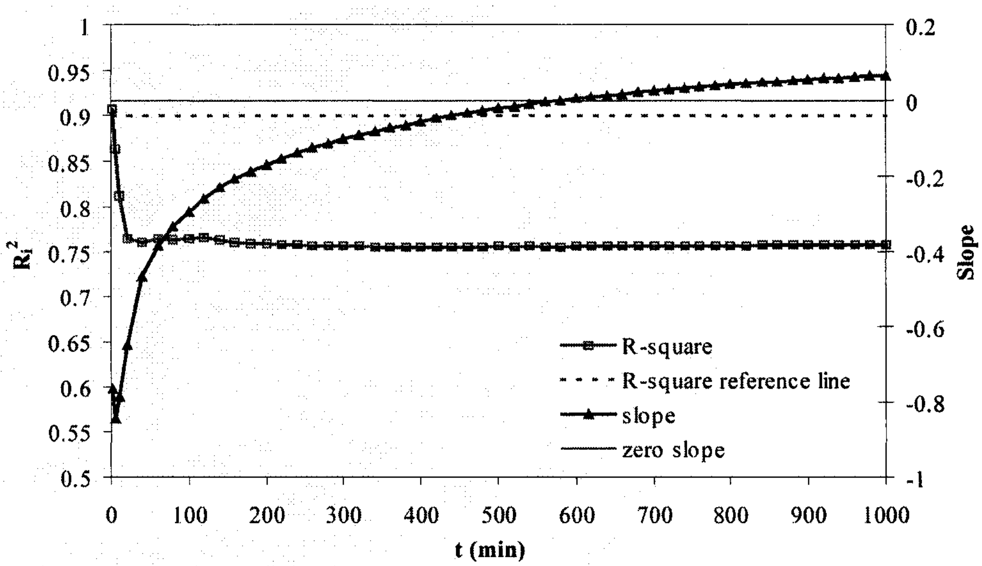

Figure 5.6 Slopes and R_i^2 of the average power spectrums of infiltration fields under scaling rainfall and non-scaling K_s field.

5.3.4 Effects of Scaling Steady Rain and Scaling K_s on Infiltration

The last two sections examined the general influences that either non-scaling rain or non-scaling K_s has on infiltration process. This section will be devoted to more in-depth studies of the impacts of steady scaling rain and scaling K_s fields on infiltration.

5.3.4.1 Effects of Rain α

To examine the effect of model parameter α_R of multifractal rain field on infiltration, three sets of experiments are executed. Each set includes three α_R: 1.2, 1.5 and 1.8, and different rain parameters C_{1R} and H_R as listed below.

Set 1: $C_{1R} = 0.1,\ H_R = 0.2$

Set 2: $C_{1R} = 0.2,\ H_R = 0.2$

Set 3: $C_{1R} = 0.2,\ H_R = 0.35$

The rain parameters are so chosen in the three sets that not only α_R covers a wide range for the study of impact of α_R, but there are also two values for each of C_{1R} and H_R to ensure that only the common phenomena among all the sets are analyzed and the conclusions drawn from the experiments are applicable for at least the ranges of rain parameters that are used here. Twenty-five experiments are carried out for each combination of the rain parameters. The average results of the 25 experiments, such as the average infiltration rate and average estimated scaling parameters, are used in the following analysis. The scaling K_s field used in the experiments is generated using the UM model with parameters $\alpha_{Ks} = 2.0$, $C_{1Ks} = 0.01$, and $H_{Ks} = 0.2$. For a visual inspection, Figure 5.7 shows the infiltration field in one of the experiments in Set 2 at 10 min and 150 min after rain starts. The white spot at the upper-right corner of the study area has little infiltration as a result of very low rain intensity in the region. However, infiltration in the channels in this area is still noticeable because 1) excess rainfall concentrates into the channels throughout the region; and 2) excess rainfall originated from areas outside the low rain intensity region is transported into the region through the channels.

(a) (b)

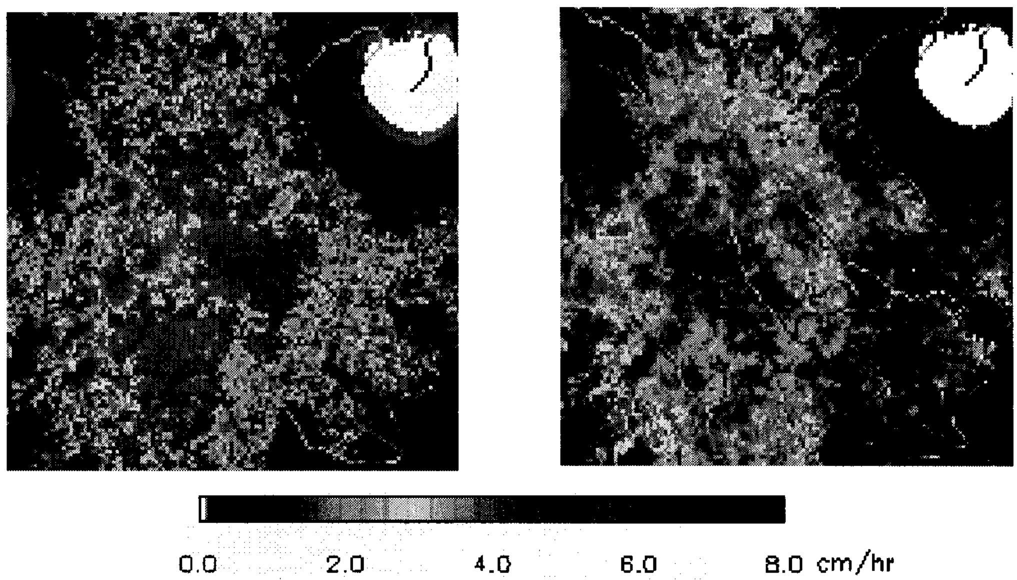

Figure 5.7 Infiltration fields at (a) 10 min, and (b) 150 min after rain starts. Rain field parameters are $\alpha_R = 1.2$, $C_{IR} = 0.2$, and $H_R = 0.2$; and K_s parameters are $\alpha_{Ks} = 2.0$, $C_{IKs} = 0.01$, and $H_{Ks} = 0.2$.

While the average rain rate remains the same in all the cases, the spatial structures of the rain fields can be quite different depending on the scaling parameters. Figure 5.8 compares the average relative frequencies of the rain fields from Set 2. Figure 5.9 shows some of the corresponding rain images. As expected, rain field with larger α_R has stronger singularity, *i.e.* rain is more concentrated in smaller areas and leaves most of the region with lower rain intensity. This is not a very effective rain structure for generating large field average infiltration. Thus, a rain field with lower α_R will lead to more infiltration than a rain field with higher α_R does, provided all other aspects of the rain fields are the same. Figure 5.10 compares the time series of the average infiltration rate in the study area with three rain scenarios from Set 2. Rain field with smaller parameter α_R clearly produces larger average infiltration. Figure 5.11 shows the average power

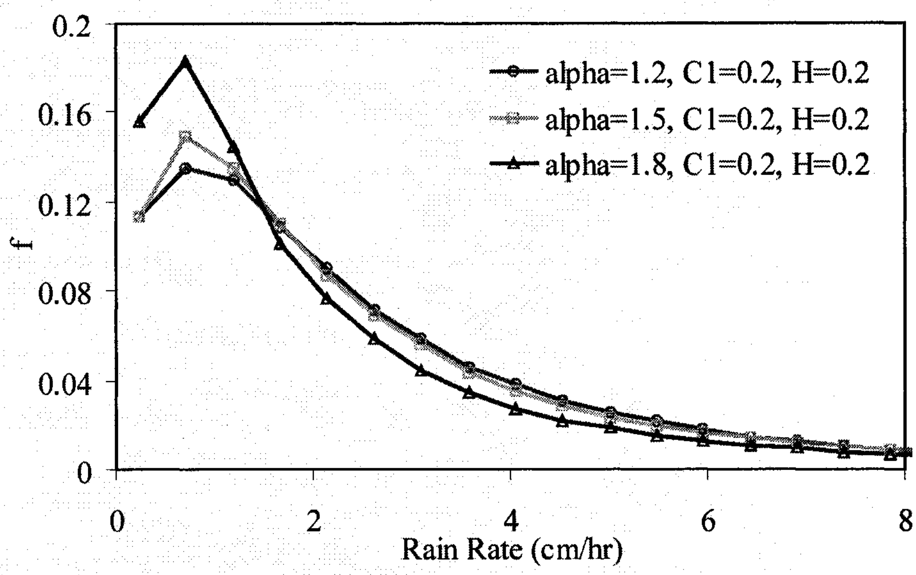

Figure 5.8 Average relative frequencies of steady rain fields

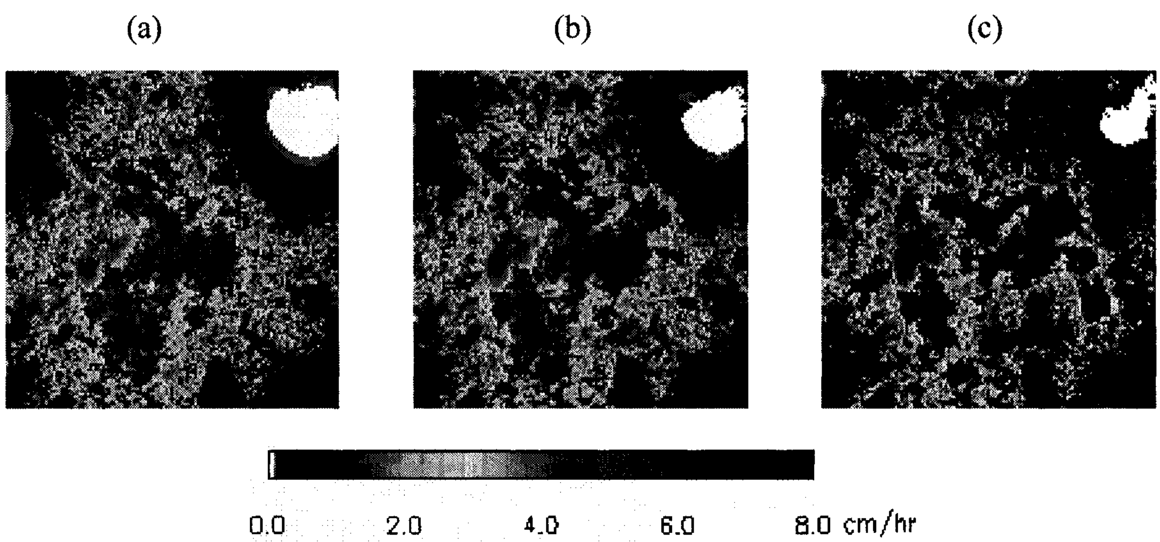

Figure 5.9 Steady rain fields with parameters (a) $\alpha = 1.2$, $C_1 = 0.2$, and $H = 0.2$; (b) $\alpha = 1.5$, $C_1 = 0.2$, and $H = 0.2$; and (c) $\alpha = 1.8$, $C_1 = 0.2$, and $H = 0.2$.

spectrums of the infiltration fields at a few points in time under the three rain fields from Set 2. Also shown in the figure are the average power spectrum of the steady rain field and the power spectrum of the K_s field. Under the influence of two scaling fields – rain and K_s, the power spectrums of infiltration fields show good linearity throughout the process. Figure 5.12 shows the R_i^2 time series of the power spectrums.

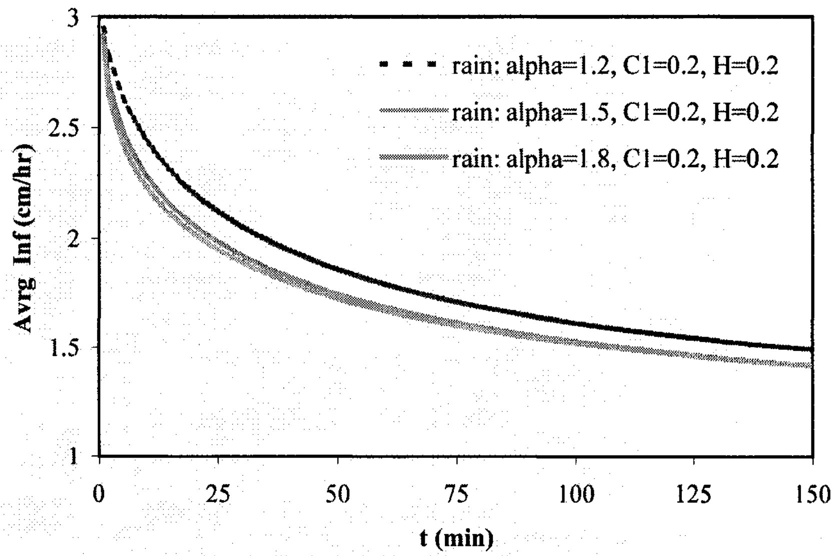

Figure 5.10 Effect of α_R on the field average surface infiltration rates under steady scaling rain fields and scaling K_s field (α_{Ks} = 2.0, C_{1Ks} = 0.01, and H_{Ks} = 0.2)

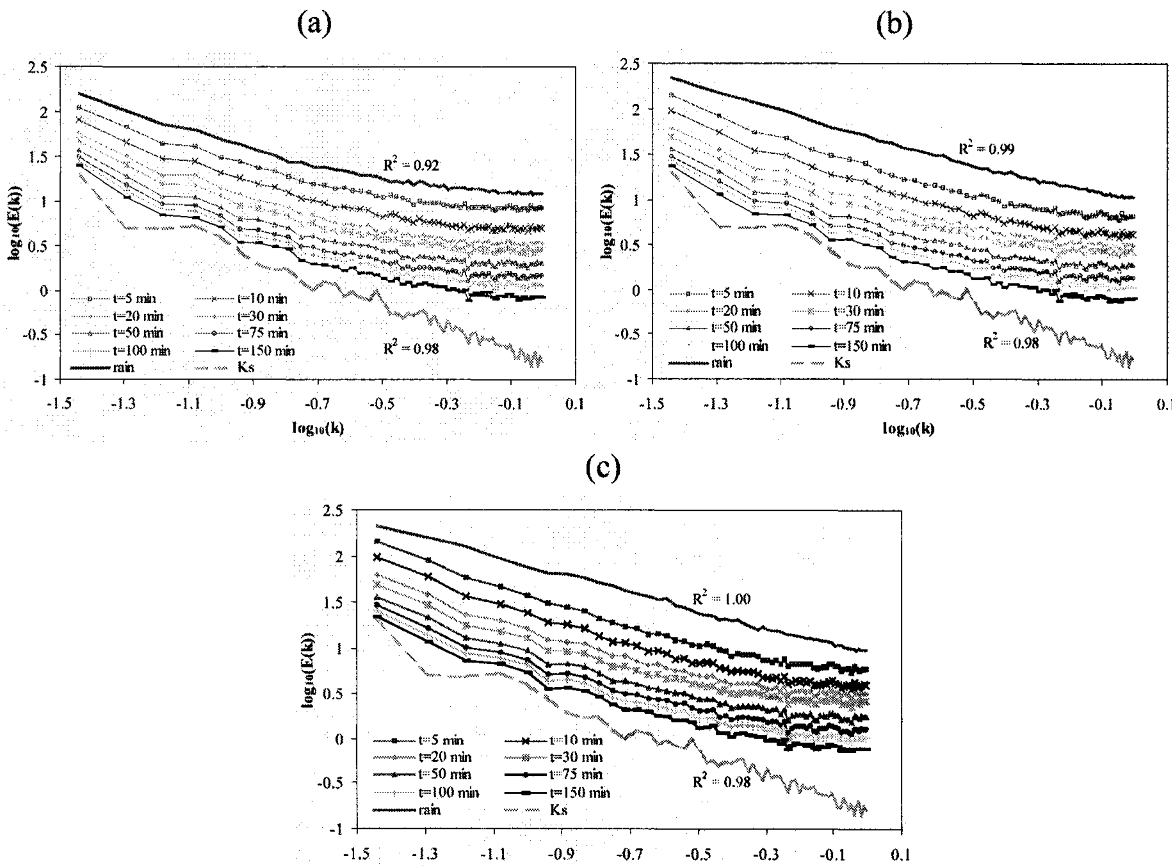

Figure 5.11 Power spectrums of infiltration fields under steady scaling rain fields: C_R = 0.2, H_R = 0.2 and (a) α_R = 1.2, (b) α_R = 1.5, and (c) α_R = 1.8; and scaling K_s field: α_{Ks} = 2.0, C_{1Ks} = 0.01, and H_{Ks} = 0.2.

Combined with the scaling K_s field, all three scaling rain fields yield scaling infiltration fields as the high values of the R_i^2 of the power spectrums indicate good log-linearity of the power spectrums. The three R_i^2 time series in Figure 5.12 are all well above the R^2 reference line – showing that the infiltration fields resulted from the three steady scaling rain fields are strongly scaling. The infiltration fields from the other two sets of experiments are also strongly scaling. Specifically, the minimum R_i^2 is 0.92 for the first set and 0.91 for the third set.

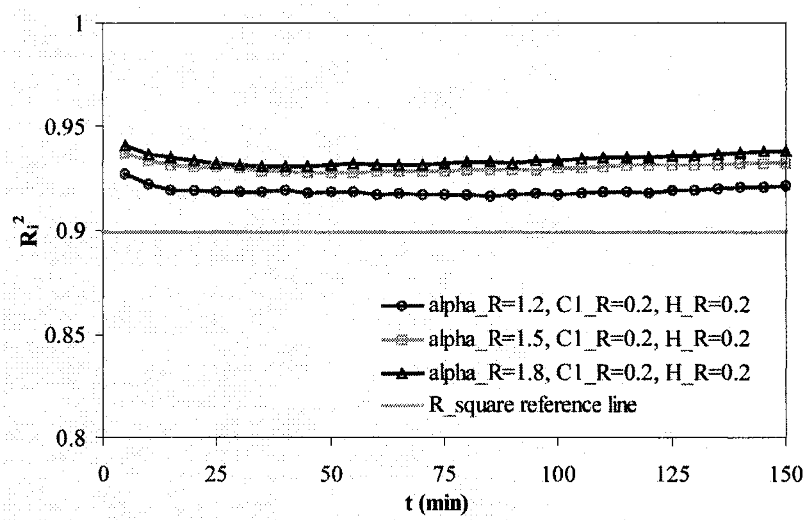

Figure 5.12 Effect of α_R on R_i^2 of the infiltration fields under steady scaling rain and scaling K_s fields (α_{Ks} = 2.0, C_{1Ks} = 0.01, and H_{Ks} = 0.2)

The β-technique (Section 3.2.2) is employed to check for the fitness of the UM model to the infiltration fields. Figure 5.13 compares the estimated β of the infiltration power spectrums with the 'theoretical' β of the three rain fields from Set 2. The 'theoretical' β is calculated using eq. (3.25) and the parameters (α_i, C_{1i}, and H_i) estimated from the non-conservative infiltration fields. As illustrated in Section 3.3.4, the estimation of parameters from a non-conservative field introduces some error. Therefore, the 'theoretical' β is essentially an estimate itself. Moreover, the estimated β is very sensitive to the range of wavenumbers used to derive the parameter. The power spectrum corresponding to the 10 lowest wavenumbers are used here to estimate β.

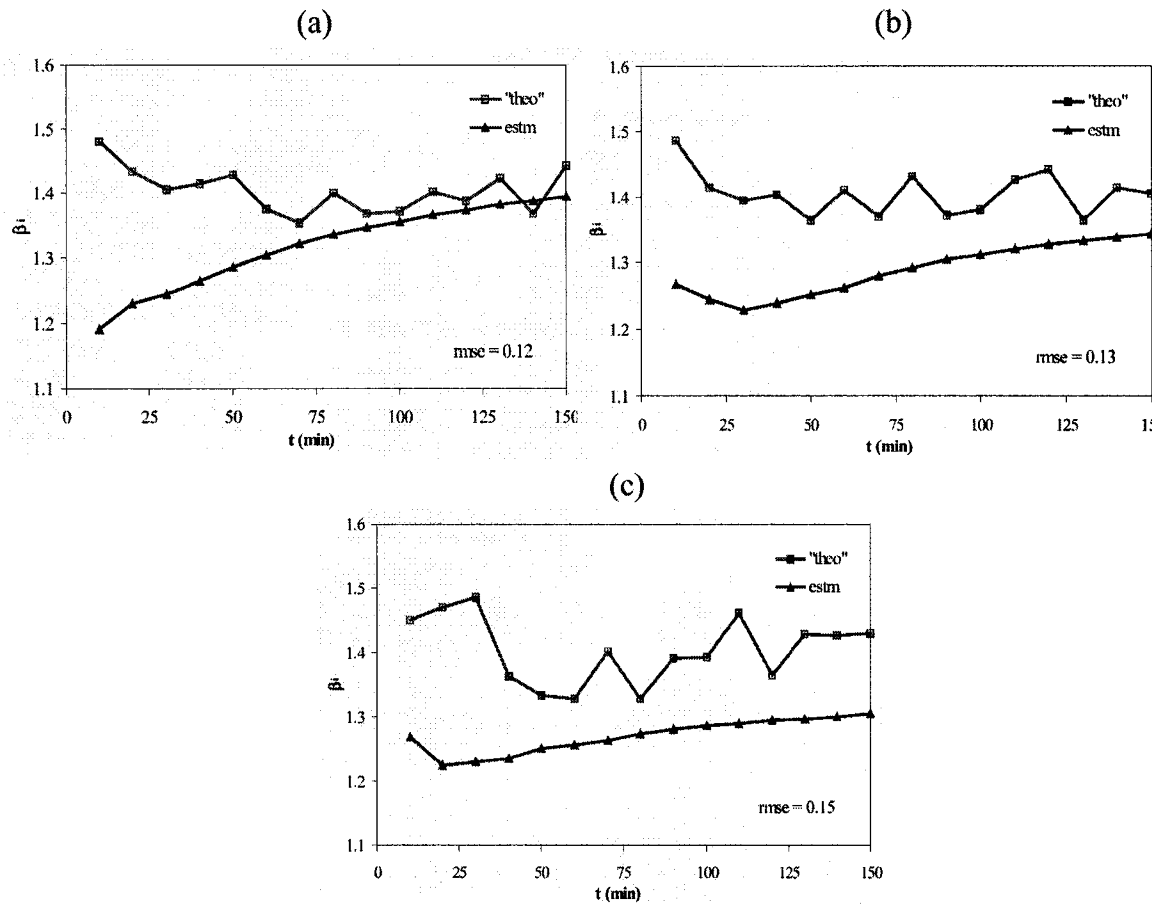

Figure 5.13 Comparisons of the theoretical and the estimated β_i of the infiltration fields under steady scaling rain fields: $C_{1R} = 0.2$, $H_R = 0.2$ and (a) $\alpha_R = 1.2$, (b) $\alpha_R = 1.5$, and (c) $\alpha_R = 1.8$; and scaling K_s field: $\alpha_{Ks} = 2.0$, $C_{1Ks} = 0.01$, and $H_{Ks} = 0.2$.

No criterion is given here for fitting the UM model because of the above-mentioned uncertainties. However, a measure of the 'goodness-of-fit' is given in Figure 5.13 – RMSE of the estimated β (taking the 'theoretical' β as the true value) of the infiltration fields at 10 min interval (hereafter denoted as rmse_β_i where β_i stands for β of infiltration field). This value gives a general idea of how close the two β's are. Figure 5.14 shows the estimated β time series of the three infiltration processes and their respective rmse_β_i. The rmse_β_i of the infiltration processes are 0.12, 0.13, and 0.15, respectively. Figure

5.14 reveals that rain field with lower α_R leads to larger β_i for the three cases tested. It is also observed that β_i generally increases in time. It is noted that large β_i indicates that large-scale structures, rather than fine features, dominate the infiltration fields. From eq. (3.25), β is proportional to H and inversely proportional to α and C_1. Thus, in the language of universal multifractal, large β_i means one or more of the following: increased H_i (homogeneity), decreased α_i (singularity), and decreased C_{1i} (sparseness). The effect of β_i is illustrated in Figure 5.15 with two infiltration fields from the same process but at two different points in time.

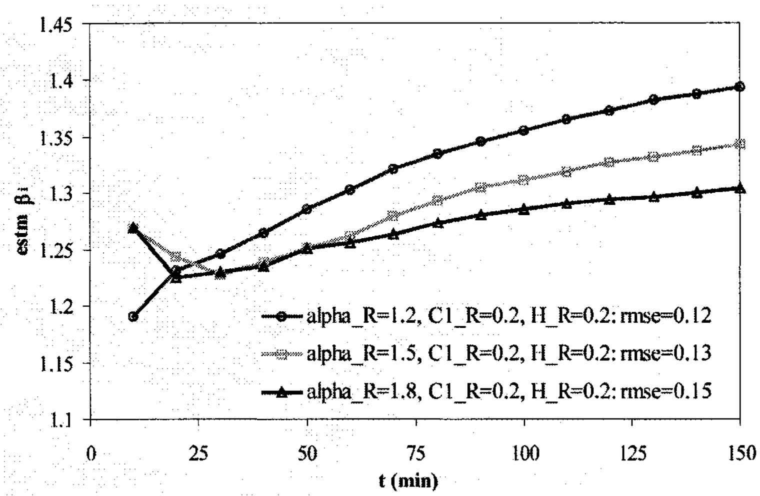

Figure 5.14 Effect of α_R on β_i of the infiltration processes under steady scaling rain and scaling K_s fields (α_{Ks} = 2.0, C_{1Ks} = 0.01, and H_{Ks} = 0.2).

The analysis shown above is based on the results of the Set 2 experiments. Similar conclusions can be drawn from the results of the Set 1 and Set 3 experiments. For instance, the rmse_β_i from the three rain fields of Set 1 are 0.16, 0.16, and 0.18; and from the rain fields of Set 3 are 0.08, 0.09, and 0.08.

Figures 5.16 – 5.18 present the estimated infiltration scaling parameters from the three sets of experiments. The following conclusions are drawn based on the figures.

(a) (b)

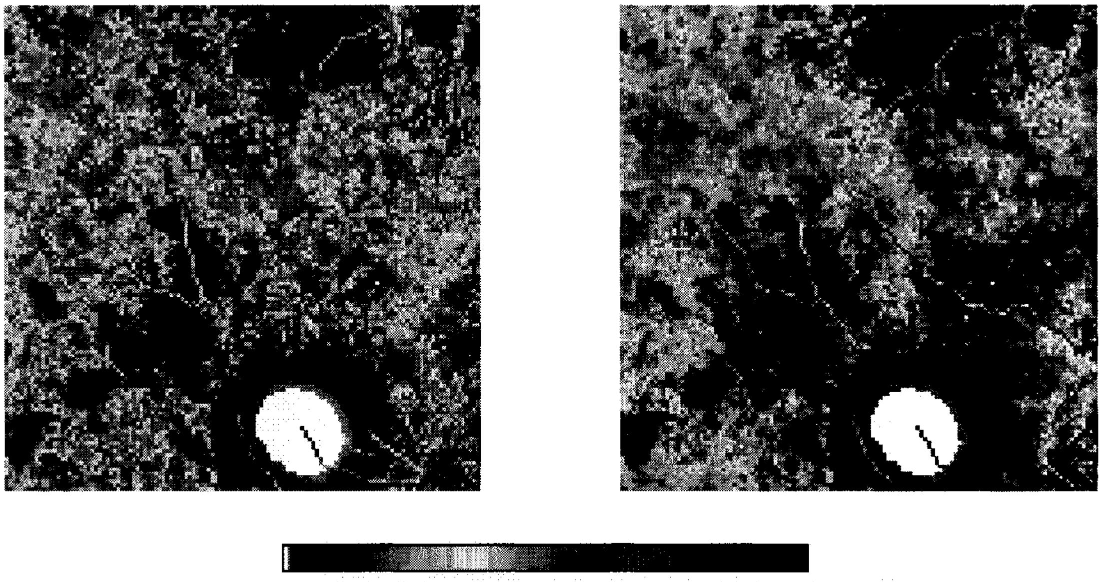

Figure 5.15 Infiltration fields at (a) 20 min; and (b) 150 min under steady scaling rain (α_R = 1.2, C_{1R} = 0.2, and H_R = 0.2) and scaling K_s fields (α_{Ks} = 2.0, C_{1Ks} = 0.01, and H_{Ks} = 0.2).

i) The impact of α_R on infiltration α_i is weak (Figure 5.16). It is observed in Figure 5.16 that the change of α_i is not always unidirectional with α_R. This is an indication of non-linearity in the relation between α_R and α_i.

ii) The impact of α_R on infiltration C_{1i} is also weak (Figure 5.17). The variation of C_{1i} with α_R is unclear.

iii) The impact of α_R on H_i is weak (Figure 5.18). The variation of H_i with α_R is also associated with non-linearity.

In general, the impact of α_R on infiltration parameters is weak.

5.3.4.2 Effects of Rain C_1

To explore the influences of rain model parameter C_{1R} on the scaling parameters of infiltration process, three sets of experiments are designed with the following rain parameters.

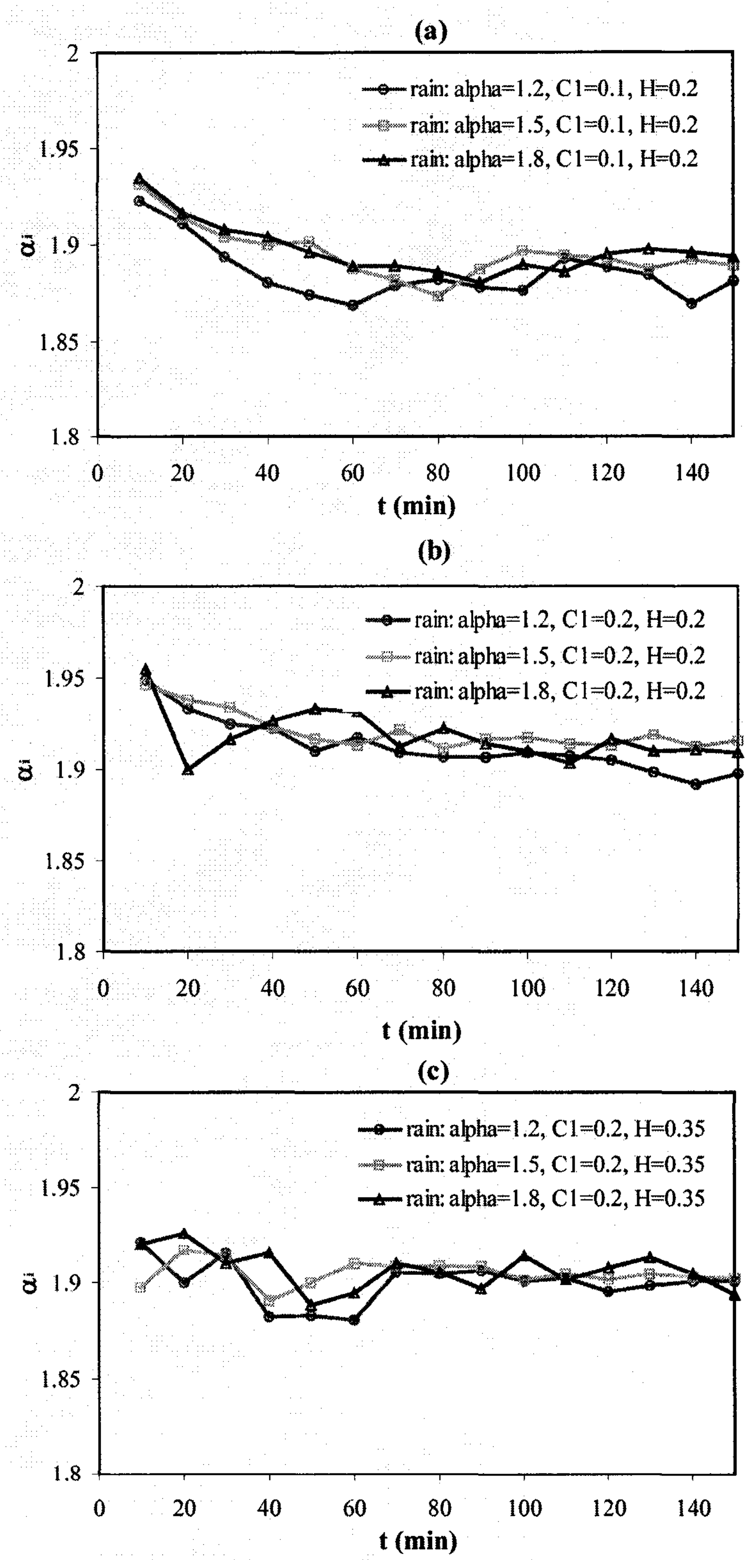

Figure 5.16 Effect of α_R on α_i under scaling K_s field: $\alpha_{Ks} = 2.0$, $C_{1Ks} = 0.01$, and $H_{Ks} = 0.2$; and steady scaling rain fields with $\alpha_R = 1.2/1.5/1.8$ and (a) $C_{1R} = 0.1$, $H_R = 0.2$; (b) $C_{1R} = 0.2$, $H_R = 0.2$; and (c) $C_{1R} = 0.2$, $H_R = 0.35$.

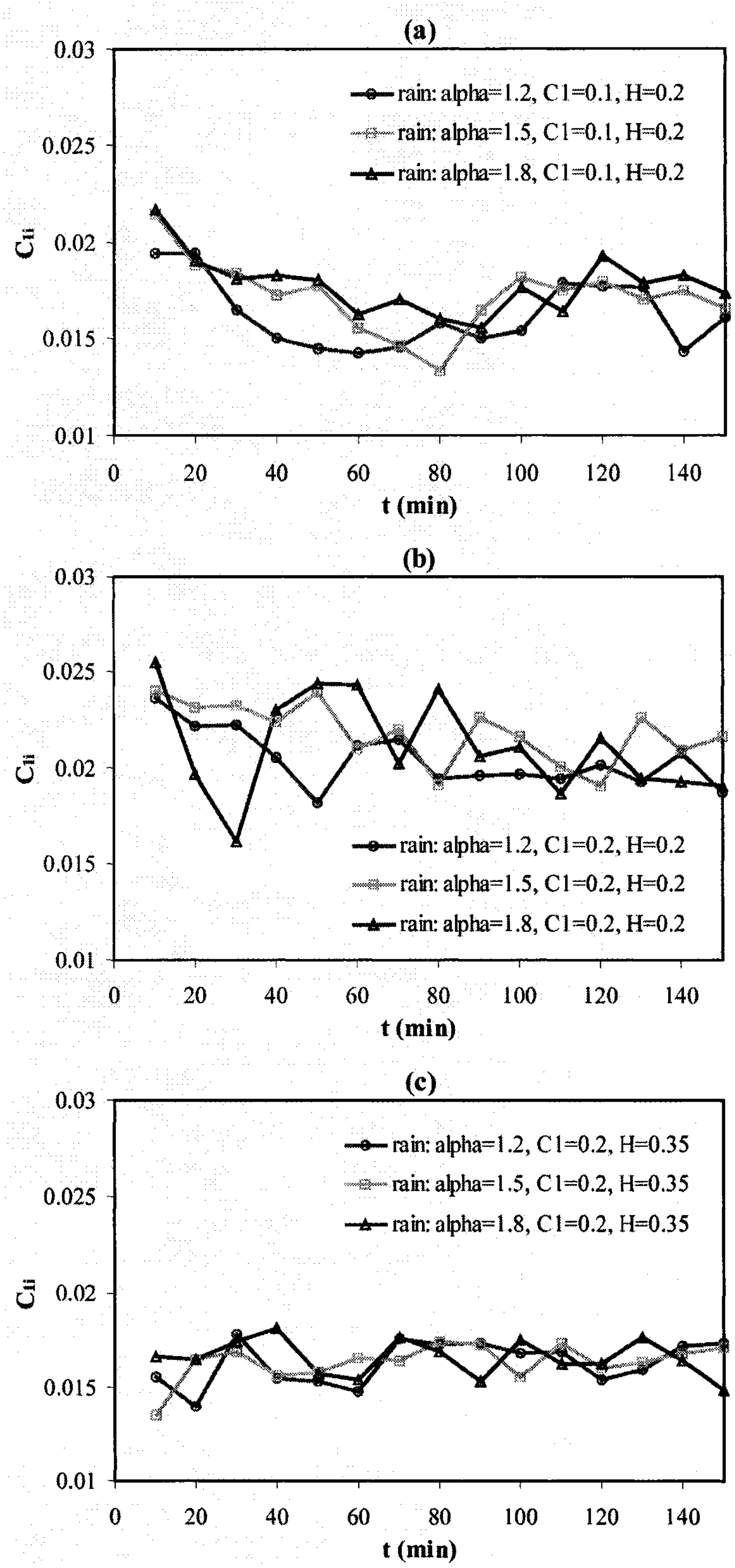

Figure 5.17 Effect of α_R on C_{1i} under scaling K_s field: $\alpha_{Ks} = 2.0$, $C_{1Ks} = 0.01$, and $H_{Ks} = 0.2$; and steady scaling rain fields with $\alpha_R = 1.2/1.5/1.8$ and (a) $C_{1R} = 0.1$, $H_R = 0.2$; (b) $C_{1R} = 0.2$, $H_R = 0.2$; and (c) $C_{1R} = 0.2$, $H_R = 0.35$.

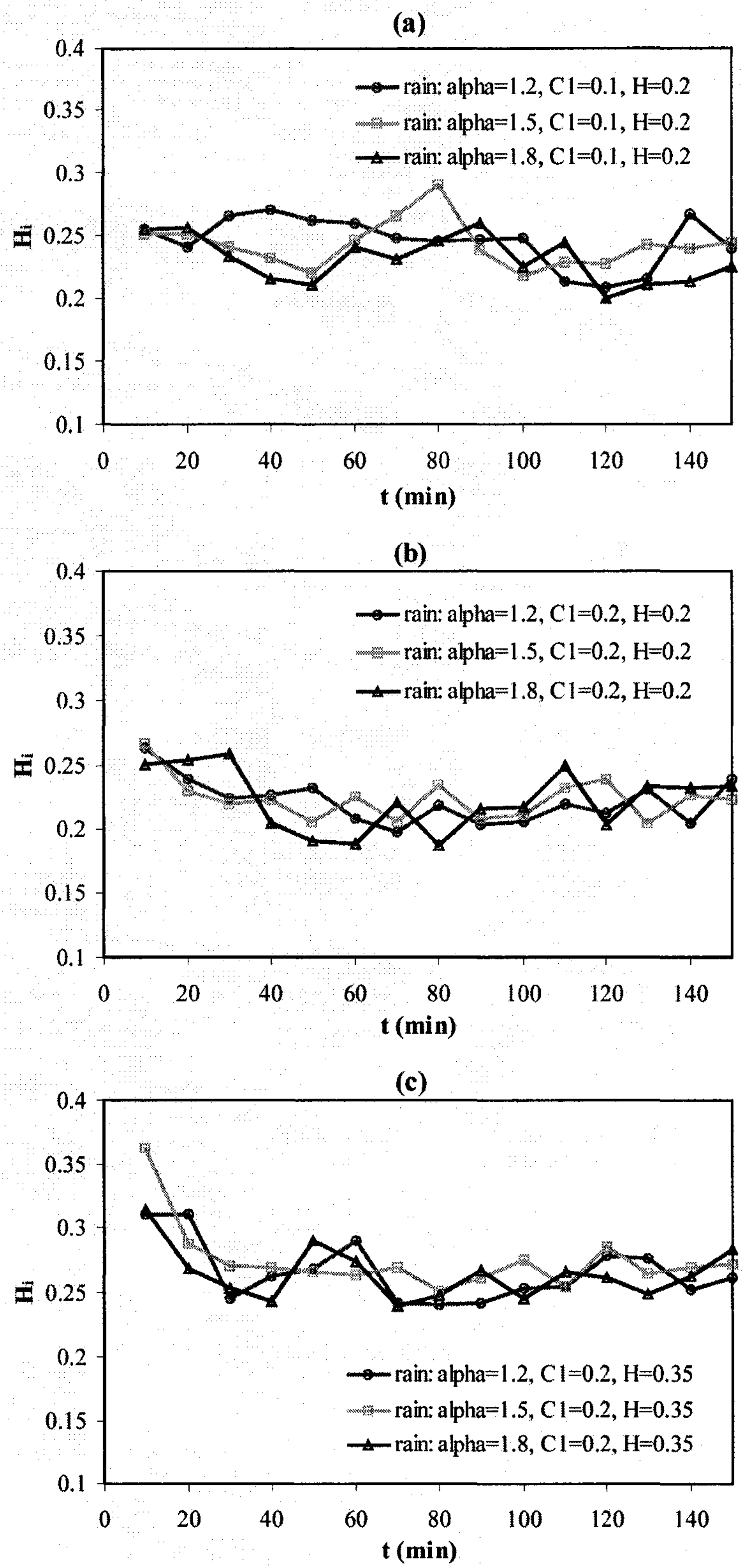

Figure 5.18 Effect of α_R on H_i under scaling K_s field: $\alpha_{Ks} = 2.0$, $C_{1Ks} = 0.01$, and $H_{Ks} = 0.2$; and steady scaling rain fields with $\alpha_R = 1.2/1.5/1.8$ and (a) $C_{1R} = 0.1$, $H_R = 0.2$; (b) $C_{1R} = 0.2$, $H_R = 0.2$; and (c) $C_{1R} = 0.2$, $H_R = 0.35$.

Set 1: $\alpha_R = 1.2$, $H_R = 0.2$

Set 2: $\alpha_R = 1.2$, $H_R = 0.35$

Set 3: $\alpha_R = 1.5$, $H_R = 0.35$

Parameter C_{1R} compared in all the experiments are $C_{1R} = 0.1$, 0.2, and 0.3. Twenty-five experiments are conducted for each combination of the three rain parameters. Figure 5.19 compares the average relative frequencies of the rain fields used in the first set, and Figure 5.20 shows some of the corresponding rain images.

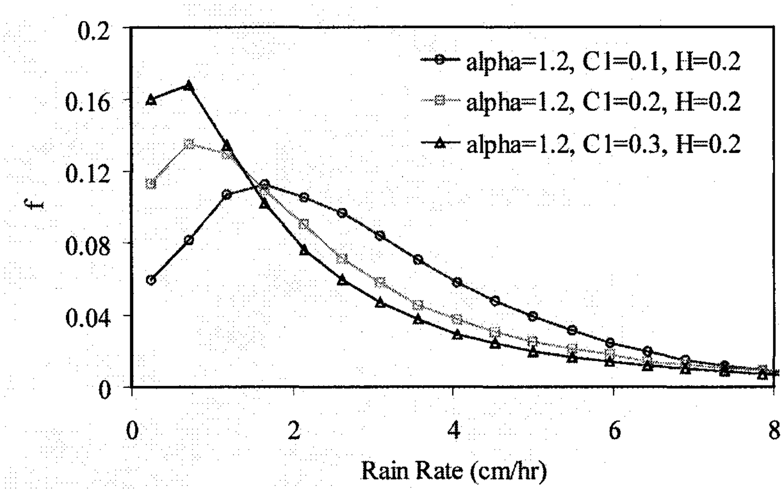

Figure 5.19 Average relative frequency of steady rain fields

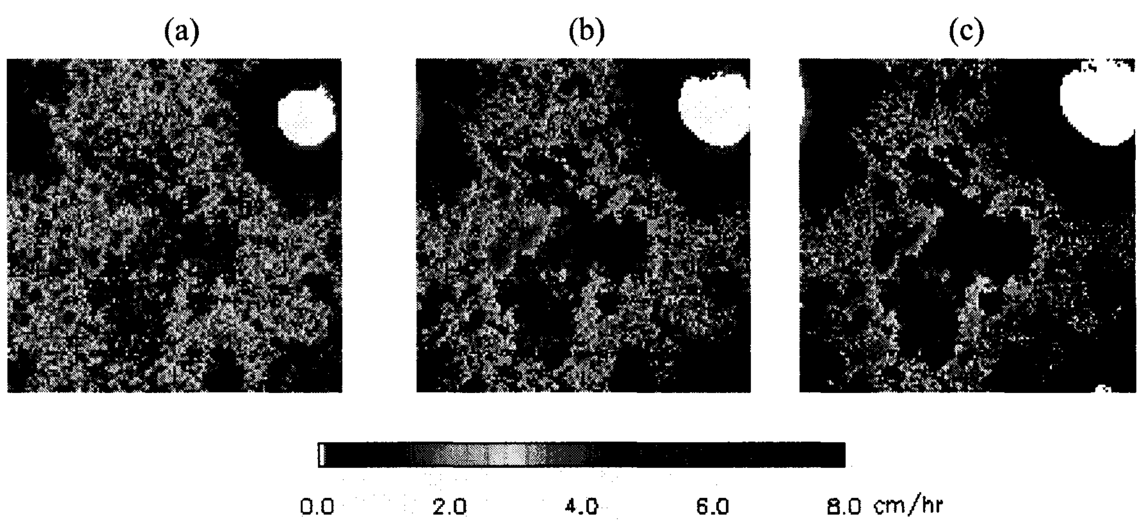

Figure 5.20 Steady rain fields with parameters (a) $\alpha_R = 1.2$, $C_{1R} = 0.1$, and $H_R = 0.2$; (b) $\alpha_R = 1.2$, $C_{1R} = 0.2$, and $H_R = 0.2$; and (c) $\alpha_R = 1.2$, $C_{1R} = 0.3$, and $H_R = 0.2$.

As illustrated in Figures 5.19 and 5.20, a rain field with smaller C_{1R} has a larger area covered with high rain intensity (*i.e.* less sparseness) than a rain field with larger C_{1R}. In other words, the former case is more evenly spread out in space than the latter one. Thus, a rain field with smaller C_{1R} will have more available water for infiltration and lead to more developed infiltration process. This is demonstrated in Figure 5.21 with the average infiltration rates of the infiltration processes under the three rain scenarios from Set 1.

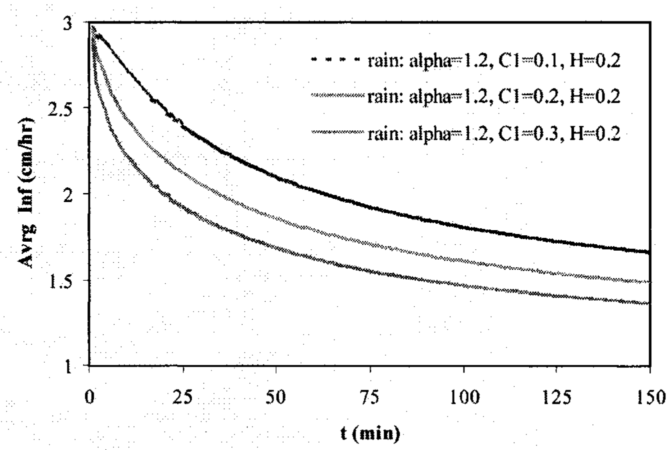

Figure 5.21 Effect of C_R on the field average surface infiltration rates under steady scaling rain and scaling K_s (α_{Ks} = 2.0, C_{1Ks} = 0.01, and H_{Ks} = 0.2)

Figures 5.22 and 5.23 respectively show the average R_i^2 and the β_i time series of the infiltration processes from the Set 1 experiments. The large R_i^2 values signify that the infiltration fields in the three rain cases are strongly scaling. The minimum R_i^2 is 0.91 for both the Set 2 and the Set 3, *i.e.* the infiltration fields from the other two sets are also strongly scaling. The rmse_β_i of the three cases are respectively 0.16, 0.12, and 0.18. The values indicate (to a certain degree) how well the UM model fits to the infiltration fields. The rmse_β_i of the three cases from Set 2 and 3 are respectively 0.11, 0.08, 0.08; and 0.08, 0.09, 0.09 (figures not included). Figure 5.23 also demonstrates that: 1) smaller C_{1R} leads to larger β_i; and 2) β_i increases in time. Large β_i means that the infiltration field is dominated by large-scale features.

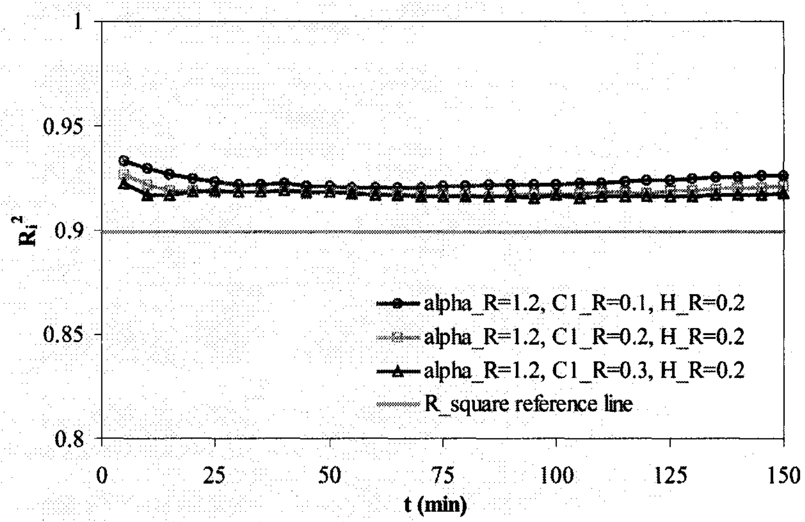

Figure 5.22 Effect of C_{1R} on R_i^2 of the infiltration fields under steady scaling rain and scaling K_s fields (α_{Ks} = 2.0, C_{1Ks} = 0.01, and H_{Ks} = 0.2)

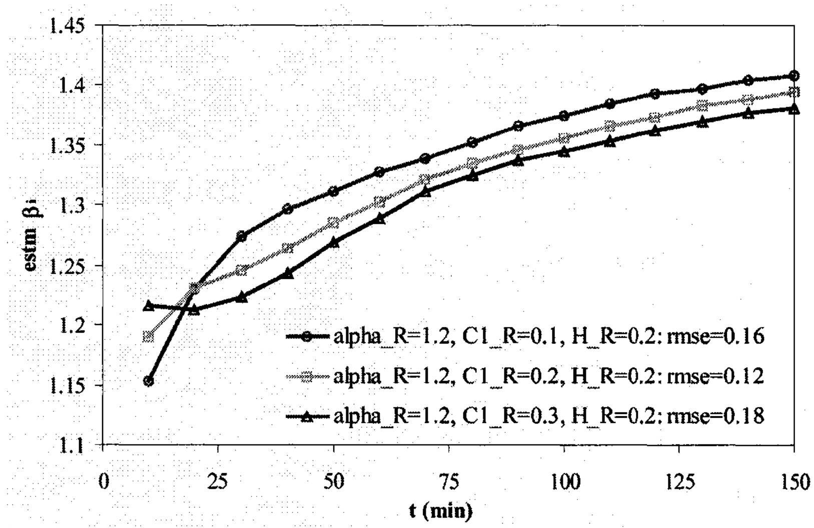

Figure 5.23 Effect of C_{1R} on β_i of the infiltration processes under steady scaling rain and scaling K_s fields (α_{Ks} = 2.0, C_{1Ks} = 0.01, and H_{Ks} = 0.2)

Figures 5.24 – 5.26 show the estimated scaling parameters of infiltration processes from the three sets of experiments. The following conclusions are drawn from the figures:

i) There is a weak to moderate correspondence between C_{1R} and α_i. The two parameters are positively correlated for the most part.

ii) Parameter C_{1R} has a moderate impact on C_{1i}. The latter is proportional to the former although the correlation becomes weak as C_{1R} becomes large.

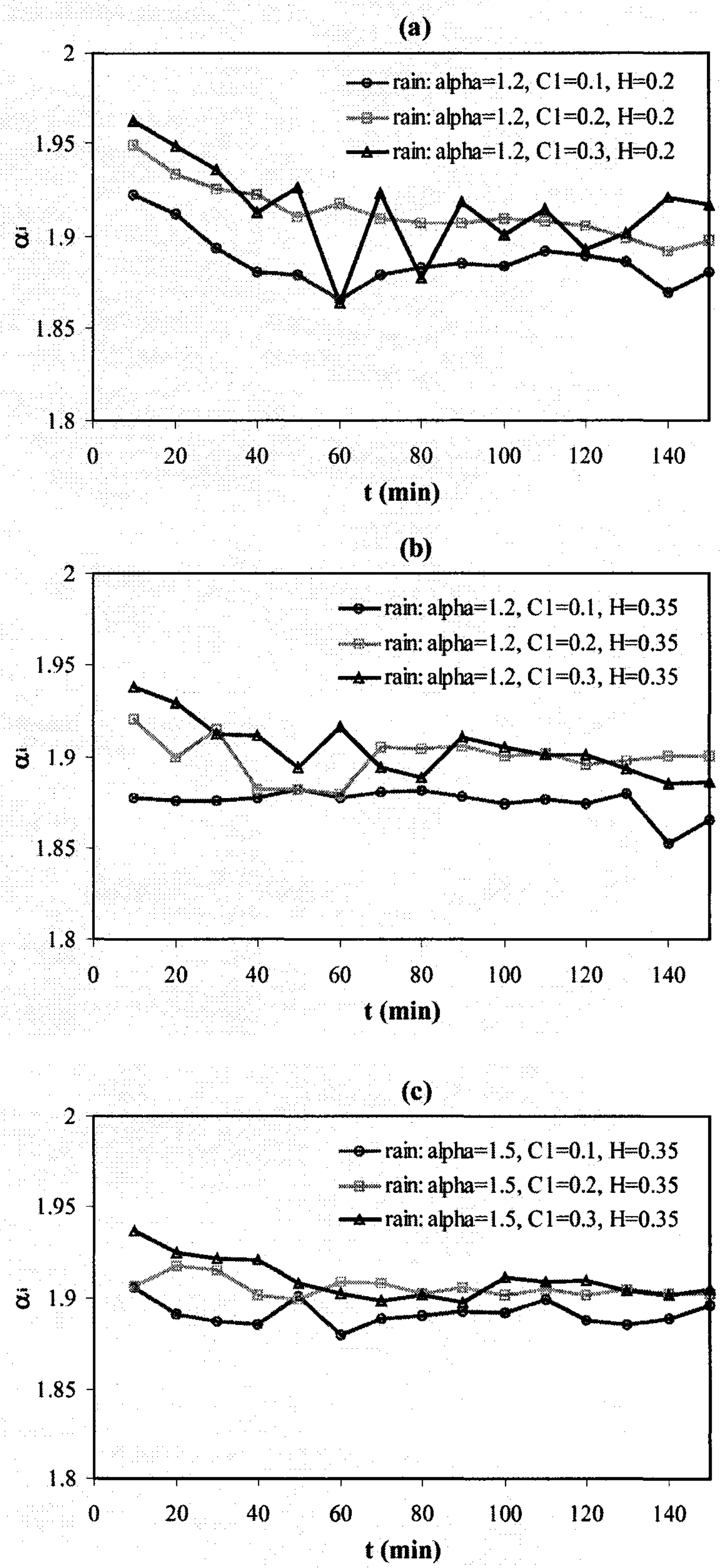

Figure 5.24 Effect of C_{1R} on α_i under scaling K_s field: $\alpha_{Ks} = 2.0$, $C_{1Ks} = 0.01$, and $H_{Ks} = 0.2$; and steady scaling rain fields with $C_{1R} = 0.1/0.2/0.3$ and (a) $\alpha_R = 1.2$, $H_R = 0.2$; (b) $\alpha_R = 1.2$, $H_R = 0.35$; and (c) $\alpha_R = 1.5$, $H_R = 0.35$.

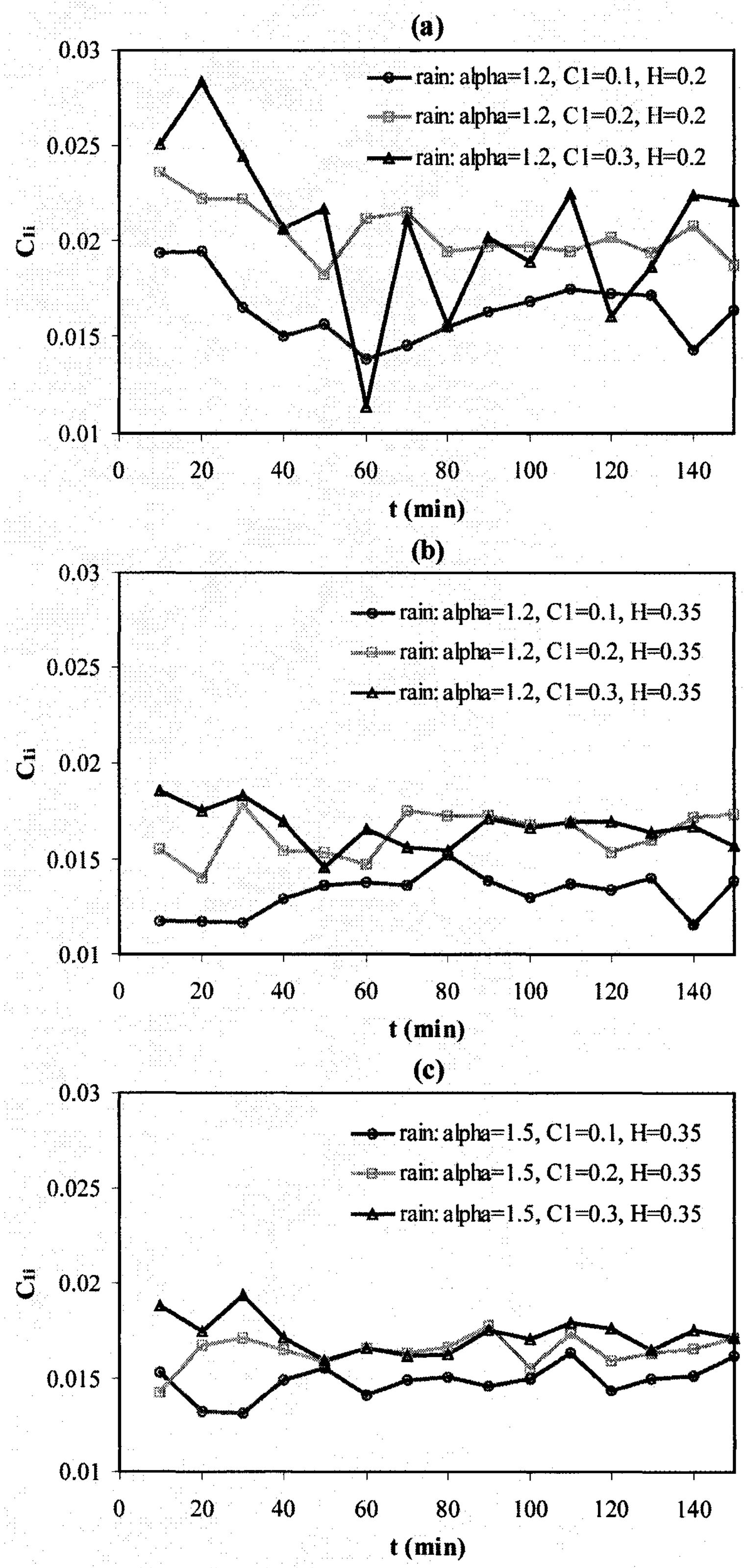

Figure 5.25 Effect of C_{1R} on C_{1i} under scaling K_s field: $\alpha_{Ks} = 2.0$, $C_{1Ks} = 0.01$, and $H_{Ks} = 0.2$; and steady scaling rain fields with $C_{1R} = 0.1/0.2/0.3$ and (a) $\alpha_R = 1.2$, $H_R = 0.2$; (b) $\alpha_R = 1.2$, $H_R = 0.35$; and (c) $\alpha_R = 1.5$, $H_R = 0.35$.

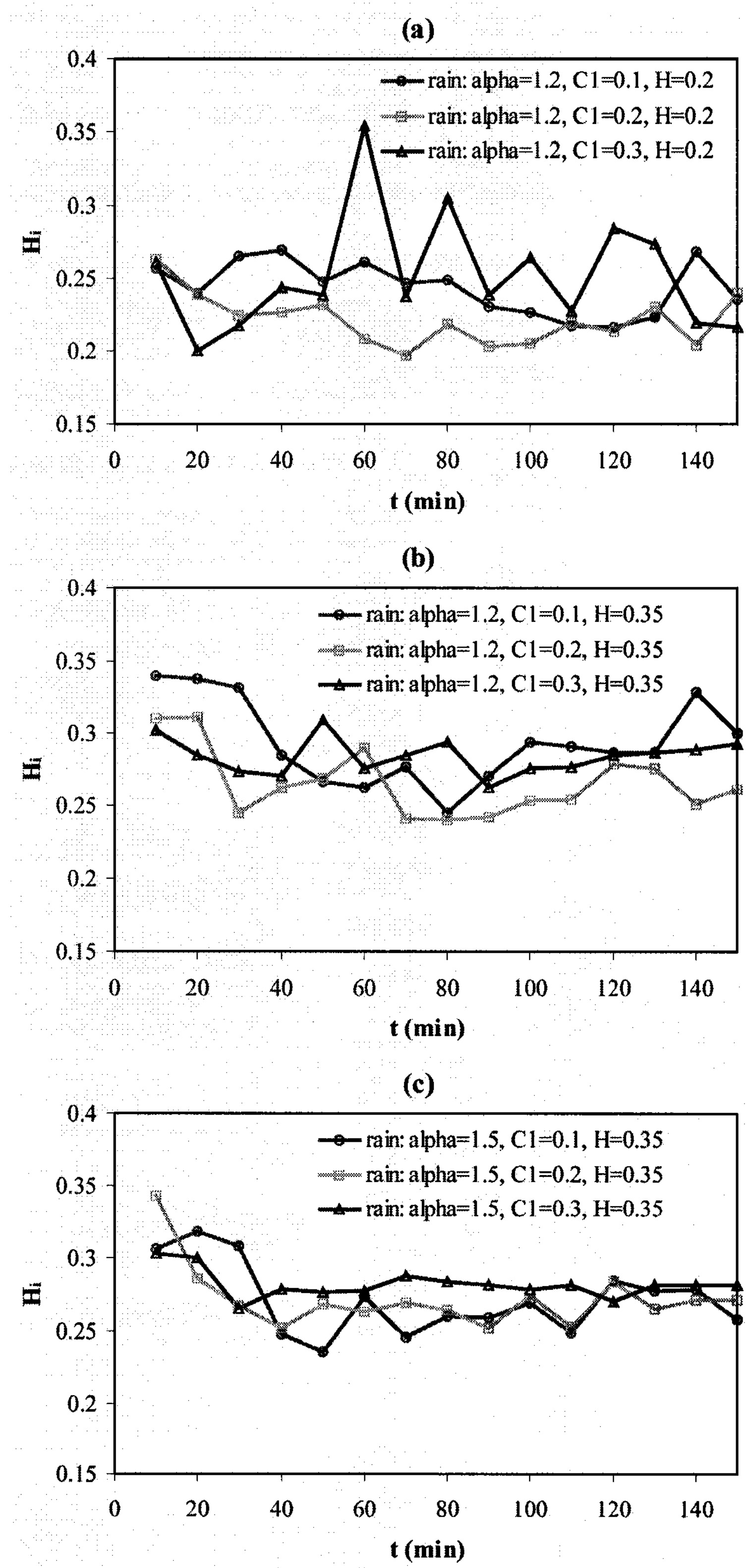

Figure 5.26 Effect of C_{1R} on H_i under scaling K_s field: $\alpha_{Ks} = 2.0$, $C_{1Ks} = 0.01$, and $H_{Ks} = 0.2$; and steady scaling rain fields with $C_{1R} = 0.1/0.2/0.3$ and (a) $\alpha_R = 1.2$, $H_R = 0.2$; (b) $\alpha_R = 1.2$, $H_R = 0.35$; and (c) $\alpha_R = 1.5$, $H_R = 0.35$.

iii) The impact of C_{1R} on H_i is weak. The association between the two parameters is strongly non-linear.

The influence of C_{1R} on infiltration parameters is weak to moderate.

5.3.4.3 Effects of Rain H

Three sets of experiments are carried out for the study of the impact of H_R on infiltration. They have the following rain parameters: $H_R = 0.0, 0.1, 0.2$, and 0.5; and

$$\text{Set 1: } \alpha_R = 1.2,\ C_{1R} = 0.1$$

$$\text{Set 2: } \alpha_R = 1.5,\ C_{1R} = 0.1$$

$$\text{Set 3: } \alpha_R = 1.5,\ C_{1R} = 0.3$$

It is noted that a zero H_R means that the rain field is conservative or homogeneous. Figure 5.27 compares the relative frequencies of the rain fields from Set 3. Some of the corresponding rain fields are shown in Figure 5.28.

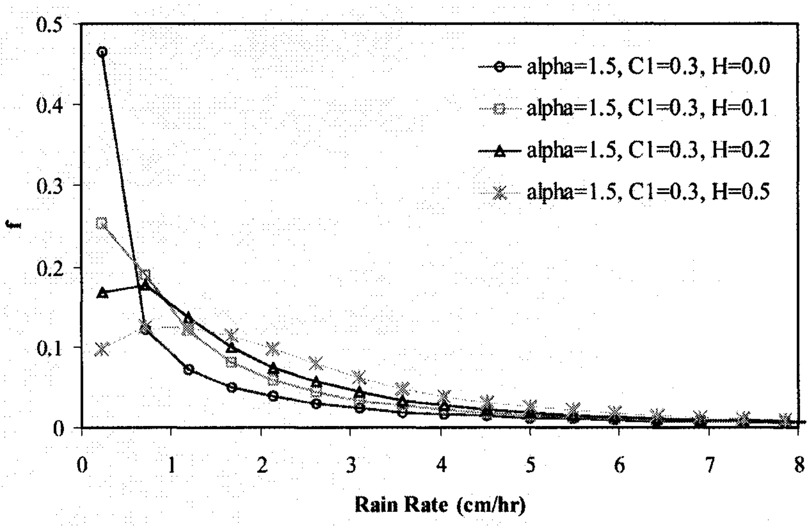

Figure 5.27 Average relative frequency of steady rain fields

Figures 5.27 and 5.28 reveal that larger H_R leads to more area with high intensity rainfall than smaller H_R, and hence gives rise to more developed infiltration field as shown in Figure 5.29.

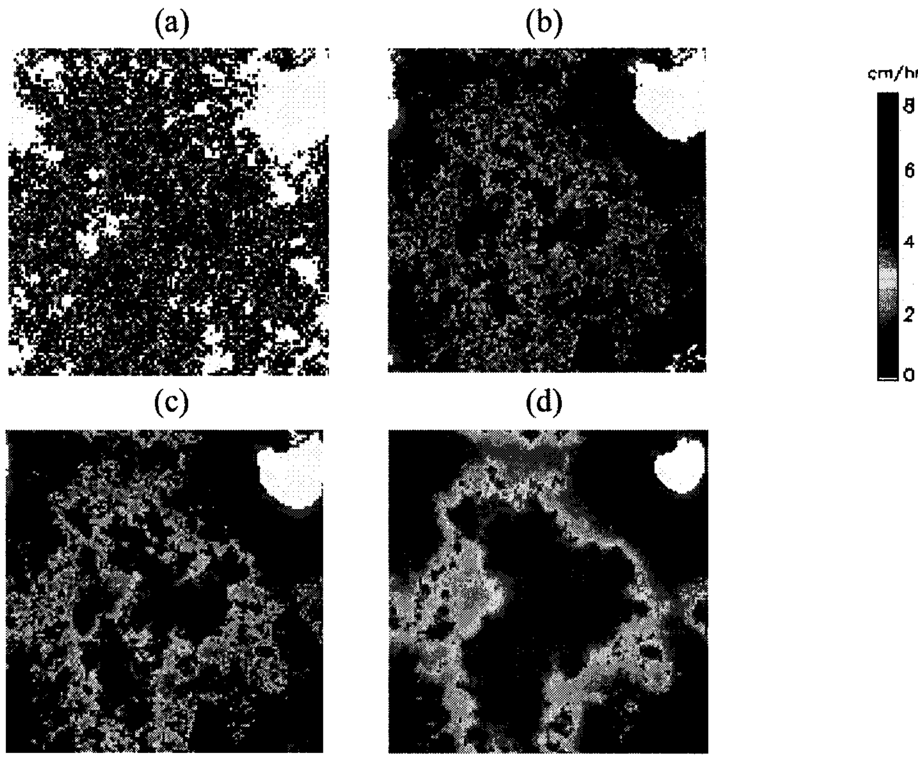

Figure 5.28 Steady rain fields with parameters (a) $\alpha_R = 1.5$, $C_{1R} = 0.3$, and $H_R = 0.0$; (b) $\alpha_R = 1.5$, $C_{1R} = 0.3$, and $H_R = 0.1$; (c) $\alpha_R = 1.5$, $C_{1R} = 0.3$, and $H_R = 0.2$; and (d) $\alpha_R = 1.5$, $C_{1R} = 0.3$, and $H_R = 0.5$.

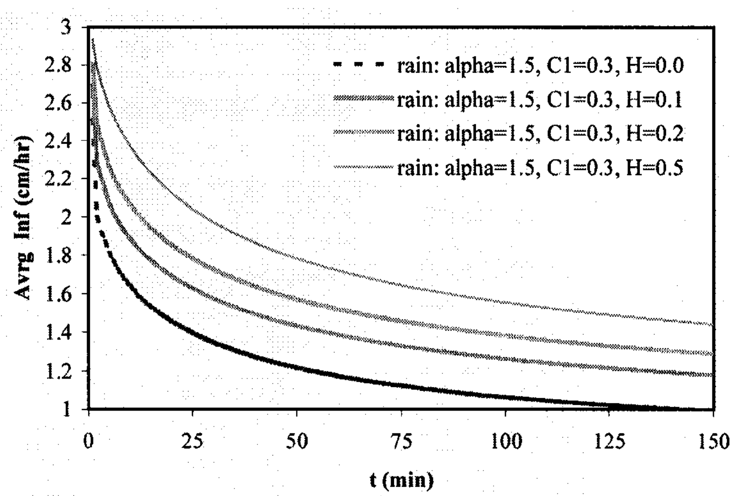

Figure 5.29 Effect of H_R on the field average surface infiltration rates under steady scaling rain and scaling K_s ($\alpha_{Ks} = 2.0$, $C_{1Ks} = 0.01$, and $H_{Ks} = 0.2$)

Figure 5.30 presents the average R_i^2 time series of the infiltration processes from Set 3. Majority of the infiltration fields have R_i^2 greater than 0.9 and thus are strongly scaling. The same conclusion applies to the other two sets of experiments. Only the infiltration fields at the very early stage in the cases where $H_R = 0.5$ are shown to be weakly scaling. The β_i time series of the infiltration processes are displayed in Figure 5.31 along with the values of the rmse_β_i. The rmse_β_i of the three sets of infiltration processes are: 0.40, 0.18, 0.16, and 0.09; 0.39, 0.26, 0.16, and 0.08; 0.45, 0.30, 0.18, and 0.13. Figure 5.31 also shows that 1) larger H_R leads to larger β_i; and 2) β_i increases in time. Therefore, an infiltration field will have smaller α_i, C_{1i}, and/or larger H_i if it is subject to a rain field with larger H_R or lasting for prolonged period of time. Figure 5.32 – 5.34 show the estimated infiltration parameters from the three sets of experiments. They lead to the following conclusions:

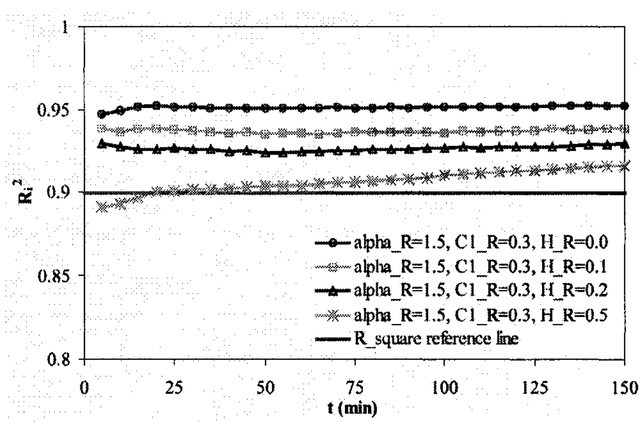

Figure 5.30 Effect of H_R on R_i^2 of the infiltration fields under steady scaling rain and scaling K_s fields ($\alpha_{Ks} = 2.0$, $C_{1Ks} = 0.01$, and $H_{Ks} = 0.2$)

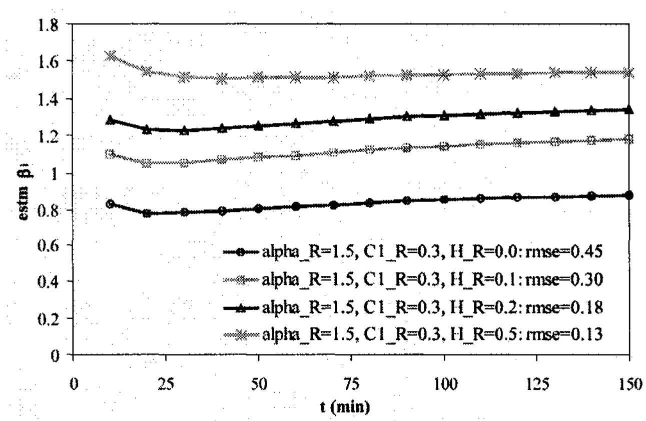

Figure 5.31 Effect of H_R on β_i of the infiltration processes under steady scaling rain and scaling K_s fields ($\alpha_{Ks} = 2.0$, $C_{1Ks} = 0.01$, and $H_{Ks} = 0.2$)

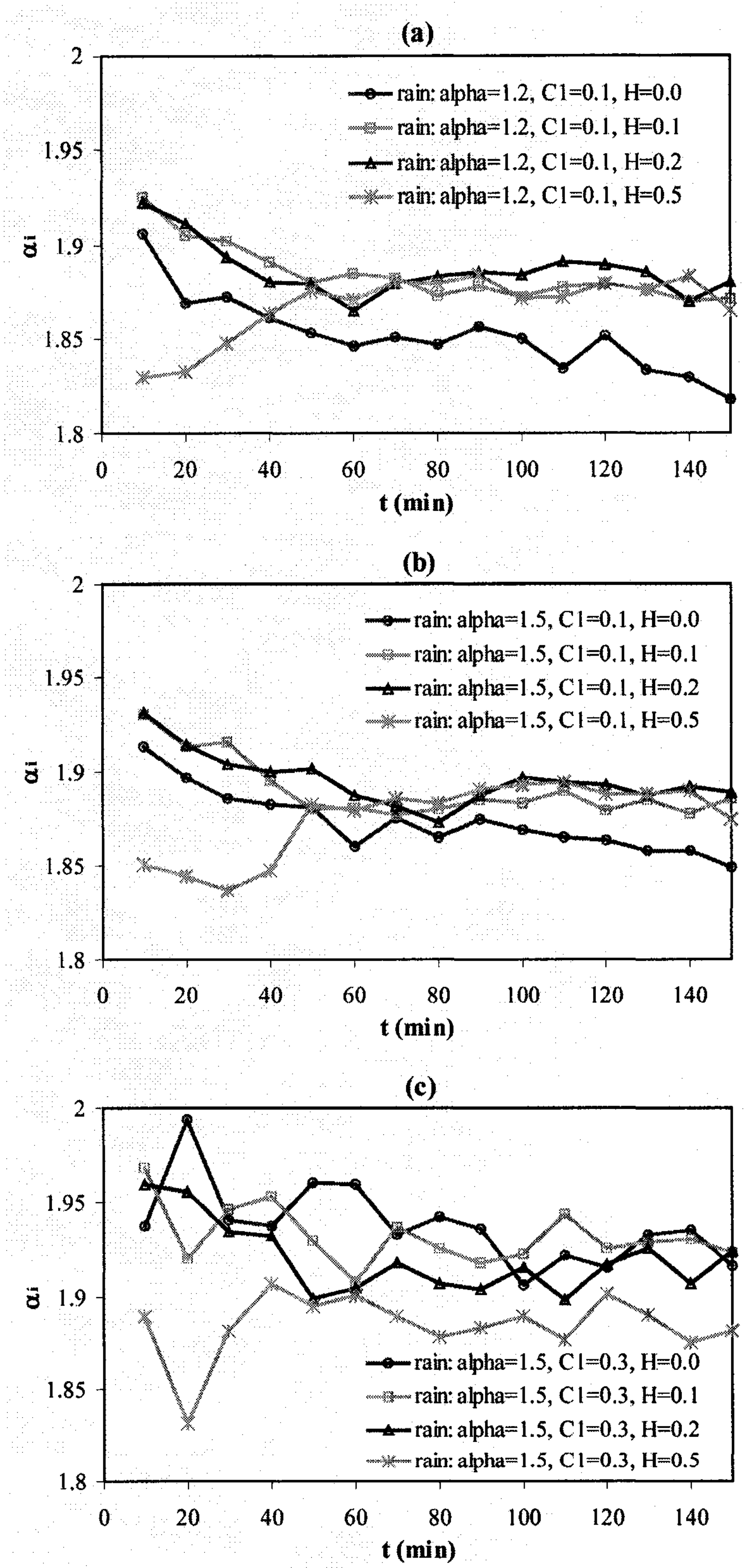

Figure 5.32 Effect of H_R on α_i under scaling K_s field: $\alpha_{Ks} = 2.0$, $C_{1Ks} = 0.01$, and $H_{Ks} = 0.2$; and steady scaling rain fields with $H_R = 0.0/0.1/0.2/0.5$ and (a) $\alpha_R = 1.2$, $C_{1R} = 0.1$; (b) $\alpha_R = 1.5$, $C_{1R} = 0.1$; and (c) $\alpha_R = 1.5$, $C_{1R} = 0.3$.

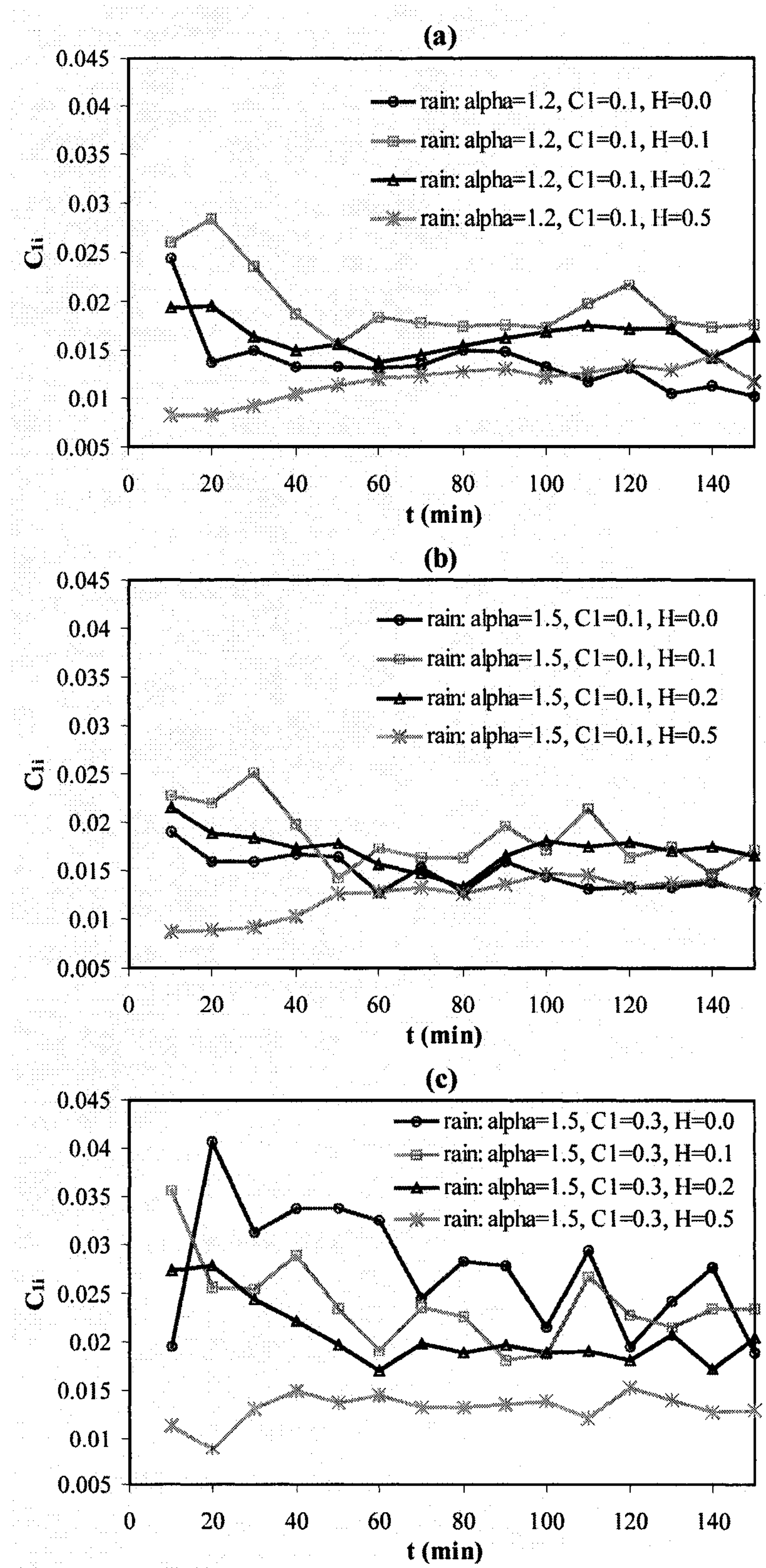

Figure 5.33 Effect of H_R on C_{1i} under scaling K_s field: $\alpha_{Ks} = 2.0$, $C_{1Ks} = 0.01$, and $H_{Ks} = 0.2$; and steady scaling rain fields with $H_R = 0.0/0.1/0.2/0.5$ and (a) $\alpha_R = 1.2$, $C_{1R} = 0.1$; (b) $\alpha_R = 1.5$, $C_{1R} = 0.1$; and (c) $\alpha_R = 1.5$, $C_{1R} = 0.3$.

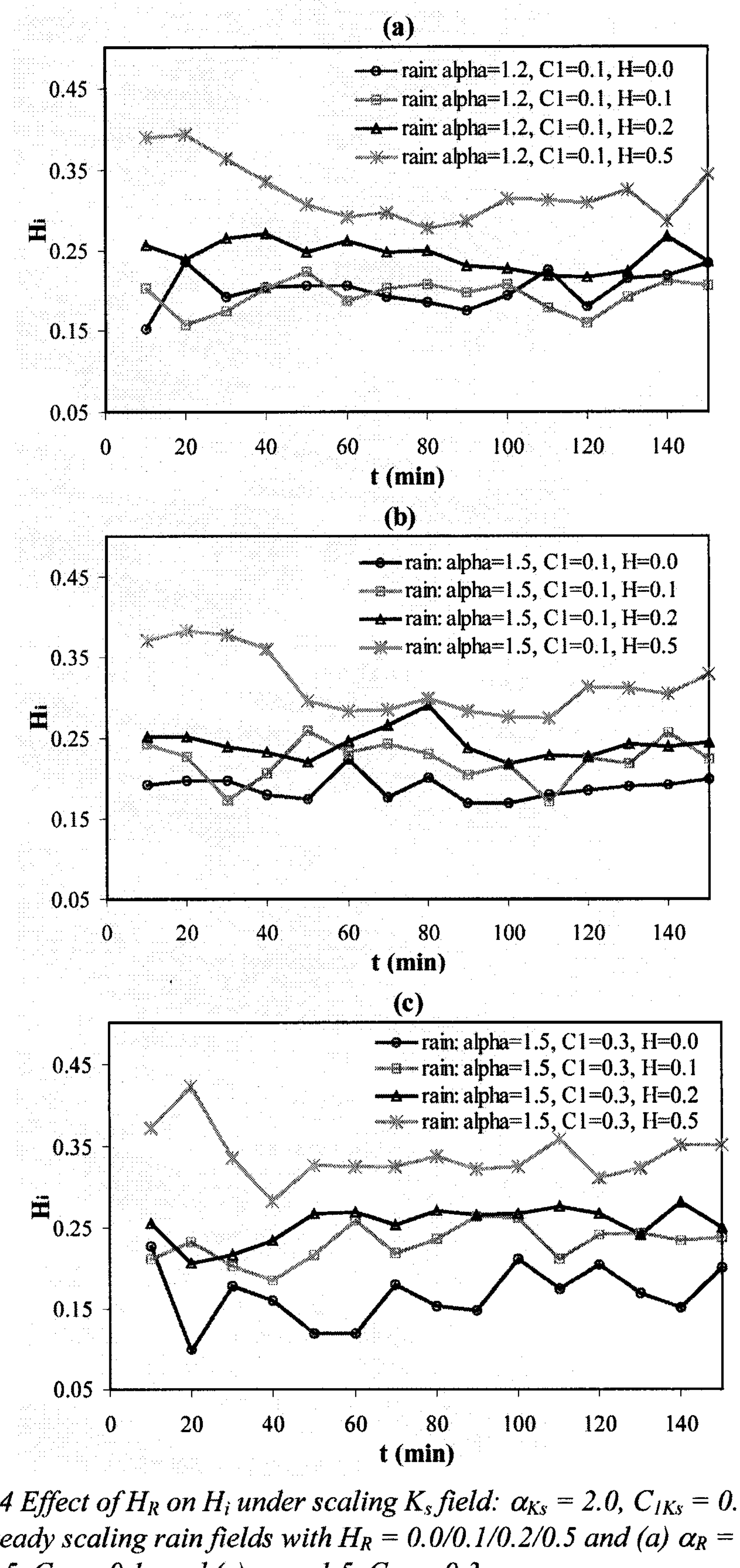

Figure 5.34 Effect of H_R on H_i under scaling K_s field: $\alpha_{Ks} = 2.0$, $C_{1Ks} = 0.01$, and $H_{Ks} = 0.2$; and steady scaling rain fields with $H_R = 0.0/0.1/0.2/0.5$ and (a) $\alpha_R = 1.2$, $C_{1R} = 0.1$; (b) $\alpha_R = 1.5$, $C_{1R} = 0.1$; and (c) $\alpha_R = 1.5$, $C_{1R} = 0.3$.

i) Homogeneous ($H_R = 0$) and close to homogeneous (H_R is close to 0) rain fields prove to be a special class of rain which is characterized by quite different behavior from non-homogeneous rain with larger H_R. The threshold H_R value is a function of both the infiltration parameter being analyzed and the values of α_R and C_{1R}. The differences between the two types of rain are discussed in the following context.

ii) H_R has a moderate to strong impact on α_i. In the small H_R range including $H_R = 0$, α_i increases with H_R. As H_R gets larger, α_i will become inversely proportional to H_R.

iii) The impact of H_R on C_{1i} appears to be proportional to C_{1R}. In a small range of H_R close to $H_R = 0$, C_{1i} is positively proportional to H_R and becomes inversely proportional to H_R as H_R moves out of this range. However, C_{1i} is inversely proportional to H_R throughout the range of H_R tested if C_{1R} is large.

iv) While the values of H_i are small when H_R is zero, they are nonetheless non-zero and hence show that homogeneous rain field does not lead to homogeneous infiltration fields.

v) The impact of H_R on H_i is strong. The two parameters are positively correlated.

In summary, H_R has a moderate to strong impact on infiltration parameters.

5.3.5 Effects of Scaling K_s on Infiltration under Steady Rain

Besides rainfall, saturated hydraulic conductivity, K_s, is another variable that plays a very important role in determining surface infiltration. It is not only an explicit part of the equation that is used to compute infiltration capacity (eq. 4.6), it also determines some other variables that are related to infiltration, such as wetting front suction, through empirical regression relations (eqs. 4.38 – 4.40) in this study. This section is devoted to the study of the impact of scaling K_s field on surface infiltration.

5.3.5.1 Effects of K_s α

Three K_s fields are generated and supplied to the DIMBRR model for the study of the effect of K_s α (α_{Ks}) on infiltration. The three fields have the same average value (1.32 cm/hr), C_{1Ks} (0.01), and H_{Ks} (0.2) but different α_{Ks} (α_{Ks} = 1.5, 1.75, or 2.0). The fields are presented in Figure 5.35. The same scaling rain fields are used in all three cases with α_R = 1.2, C_{1R} = 0.2, and H_R = 0.3. Twenty-five experiments are conducted for each combination of K_s parameters.

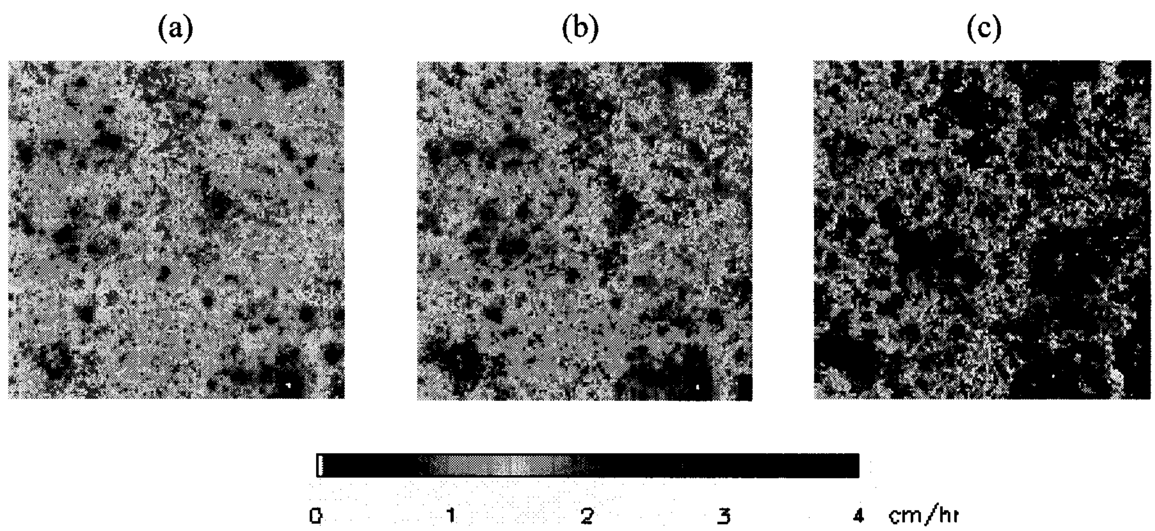

Figure 5.35 K_s fields with parameters (a) α_{Ks} = 1.5, C_{1Ks} = 0.01, H_{Ks} = 0.2; (b) α_{Ks} = 1.75, C_{1Ks} = 0.01, H_{Ks} = 0.2; and (c) α_{Ks} = 2.0, C_{1Ks} = 0.01, H_{Ks} = 0.2.

As shown in Figure 5.35, K_s field with larger α_{Ks} has more concentrated areas with large K_s, *i.e.* stronger singularity, than field with smaller α_{Ks}. Similar to the case with rain α_R, a field with high α_{Ks} does not have an efficient structure for generating large field average infiltration. Rather, K_s field with smaller α_{Ks} will yield more developed infiltration fields than field with larger α_{Ks}. Figure 5.36 illustrates this point with a plot comparing the time series of the average infiltration rates of the three cases. It is seen in Figure 5.36 that this effect is more obvious when α_{Ks} becomes larger ($\rightarrow$ 2.0). The average R_i^2 time series are shown in Figure 5.37. The infiltration fields are strongly scaling from the highest α_{Ks} and weakly scaling from the other two K_s fields. Figure 5.38 shows the β_i time series along with the rmse_β_i values. The following inequality holds for most infiltration fields: $\beta_i(\alpha_{Ks}=2.0) < \beta_i(\alpha_{Ks}=1.5) < \beta_i(\alpha_{Ks}=1.75)$. This shows that β_i is connected to α_{Ks} through a non-linear relationship. All β_i time series in Figure 5.38 have increasing trends. The rmse_β_i of the three infiltration processes are 0.1, 0.09, and 0.07.

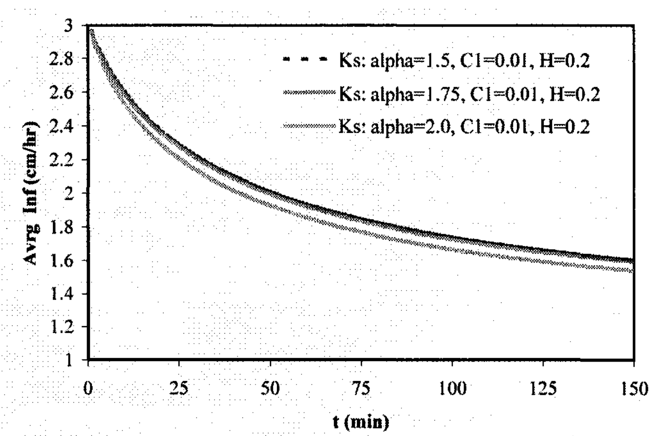

Figure 5.36 Effect of α_{Ks} on the field average surface infiltration rates under steady scaling rain (α_R = 1.2, C_{1R} = 0.2, and H_R = 0.3) and scaling K_s fields

Figure 5.39 shows the scaling parameters of the infiltration processes from the above-mentioned K_s and rain fields. The following discoveries are made from Figure 5.39.

i) The effect of α_{Ks} on α_i is weak in the early stage of the infiltration process (30 min. or so). The former also has little impact on the latter throughout the process if α_{Ks} is less than 1.75. However, α_i is strongly influenced by α_{Ks} as the latter becomes larger ($\rightarrow$ 2.0). Parameter α_i increases monotonically with α_{Ks}.

ii) Similar conclusions as i) apply to the relation between C_{1i} and α_{Ks}; namely, larger α_{Ks} brings about larger C_{1i} if α_{Ks} is large. The effect of α_{Ks} on C_{1i} is weak for smaller α_{Ks} and for the early part of the infiltration process. The variation of C_{1i} with α_{Ks} is unidirectional (Figure 5.39 (b)).

iii) The impact of α_{Ks} on H_i is weak to moderate. It is perceived that H_i is inversely correlated to α_{Ks} especially as the latter becomes large (Figure 5.39 (c)).

Overall, the impact of α_{Ks} on infiltration is moderate to strong for large α_{Ks}, and the variations of the infiltration parameters with α_{Ks} are usually unidirectional

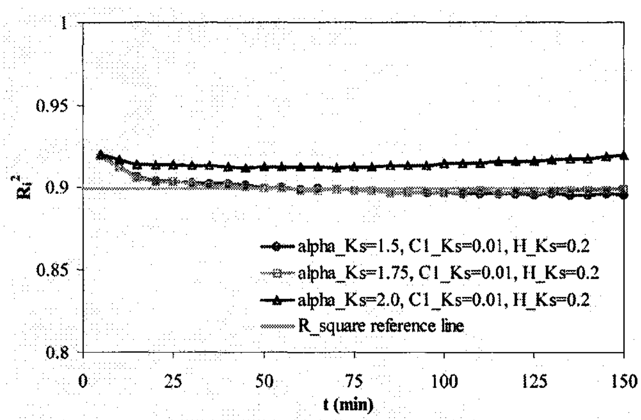

Figure 5.37 Effect of α_{Ks} on R_i^2 of the infiltration fields under steady scaling rain (α_R = 1.2, C_{1R} = 0.2, and H_R = 0.3) and scaling K_s fields

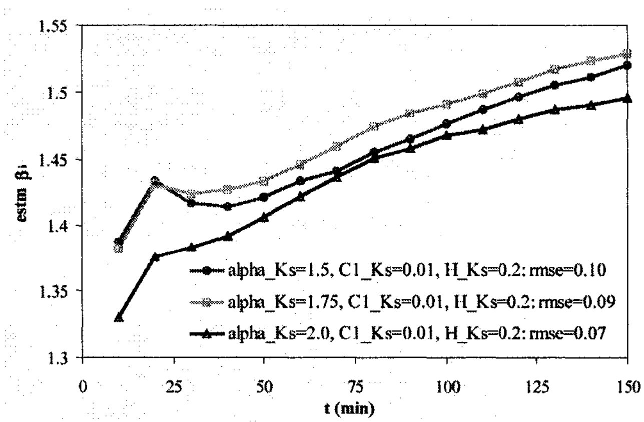

Figure 5.38 Effect of α_{Ks} on β_i of the infiltration fields under steady scaling rain (α_R = 1.2, C_{1R} = 0.2, and H_R = 0.3) and scaling K_s fields

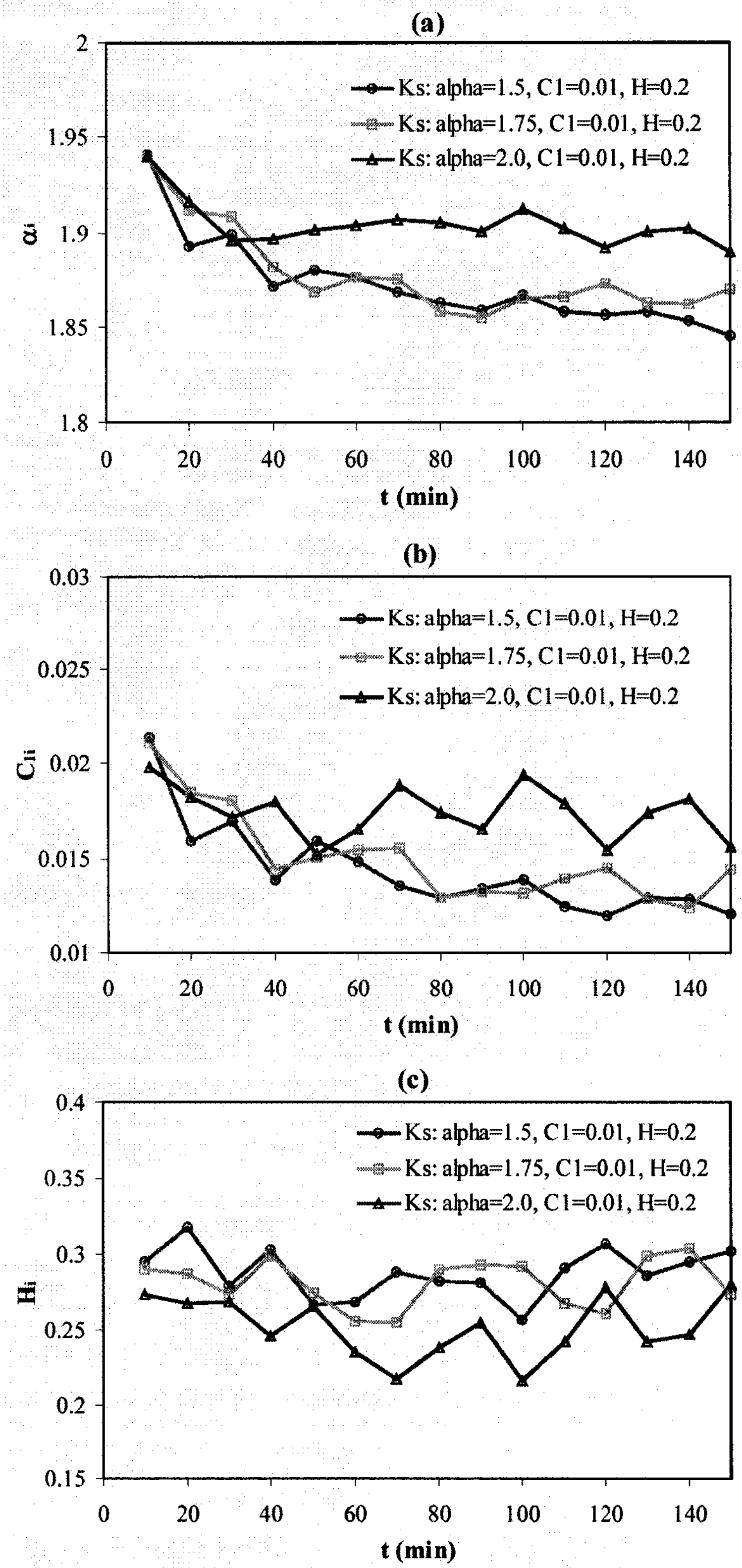

Figure 5.39 Effect of α_{Ks} on the estimated infiltration parameters (a) α_i, (b) C_{1i}, and (c) H_i, under steady scaling rain field ($\alpha_R = 1.2$, $C_{1R} = 0.2$, and $H_R = 0.3$) and scaling K_s fields.

5.3.5.2 Effects of K_s C_1

Three scaling K_s fields are used for this study, each with different C_{1Ks} (0.01, 0.05, or 0.1) but the same α_{Ks} (2.0) and H_{Ks} (0.2). Twenty-five experiments are conducted for each combination of the K_s parameters. Figure 5.40 shows the time series of the field average infiltration rates resulting from the three K_s fields. Smaller C_{1Ks} clearly leads to more infiltration on average.

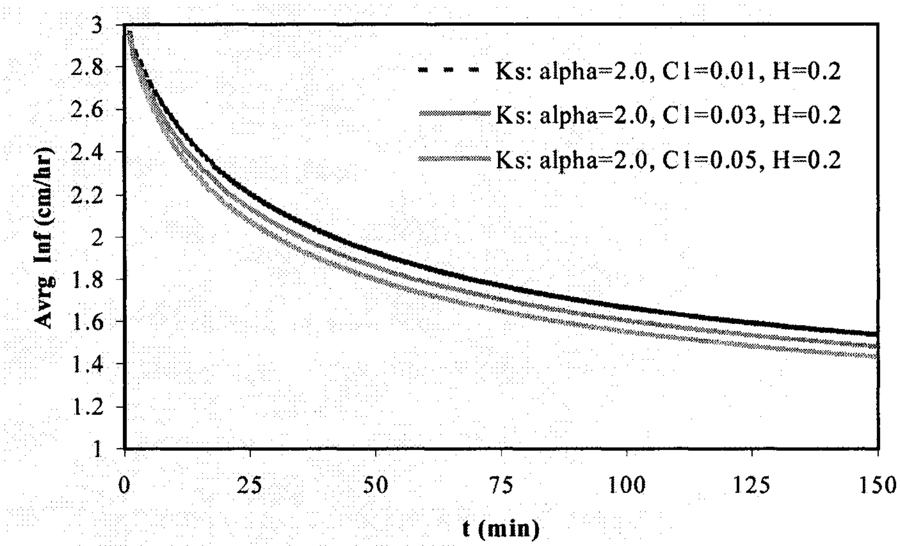

Figure 5.40 Effect of C_{1Ks} on the field average surface infiltration rates under steady scaling rain (α_R = 1.2, C_{1R} = 0.2, and H_R = 0.3) and scaling K_s fields

The R_i^2 time series are plotted in Figure 5.41. The figure shows that all infiltration fields are strongly scaling. The β_i time series shown in Figure 5.42 reveal that smaller C_{1Ks} produces larger β_i. Being consistent with all the infiltration processes studied so far, the three β_i time series also have an increasing trend. Hence, smoother infiltration fields will result from K_s field with smaller C_{1Ks} and/or prolonged rainfall. Figure 5.43 presents the estimated scaling parameters of the infiltration processes corresponding to the three K_s fields. The findings from the figure are:

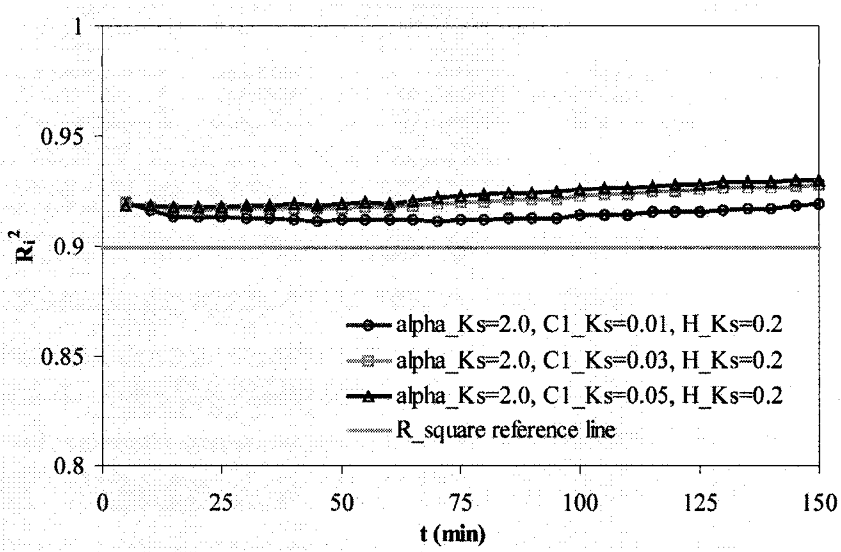

Figure 5.41 Effect of C_{1Ks} on R_i^2 of the infiltration fields under steady scaling rain (α_R = 1.2, C_{1R} = 0.2, and H_R = 0.3) and scaling K_s fields

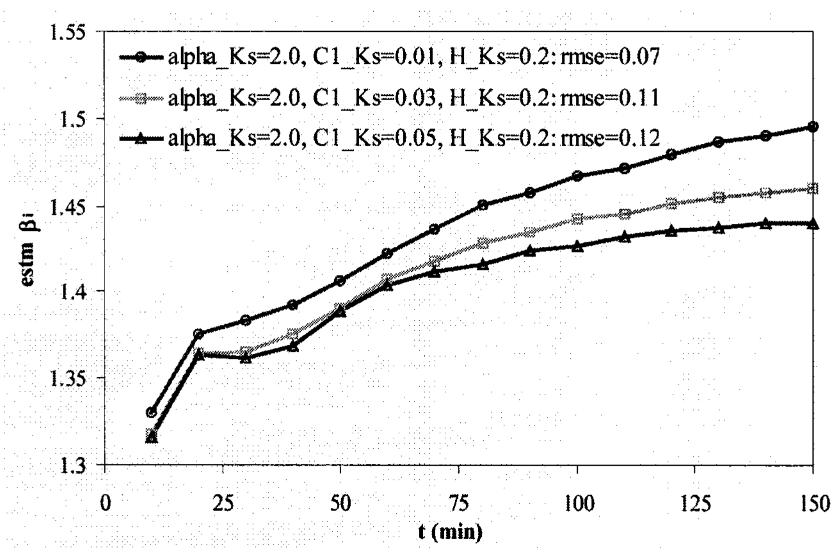

Figure 5.42 Effect of C_{1Ks} on β_i of the infiltration fields under steady scaling rain (α_R = 1.2, C_{1R} = 0.2, and H_R = 0.3) and scaling K_s fields

i) Parameter C_{1Ks} has a weak impact on α_i (Figure 5.43 (a)). While it is obvious that α_i decreases as C_{1Ks} increases from 0.01 to 0.03 and 0.05, the trend is rather obscure as C_{1Ks} becomes larger than 0.03.

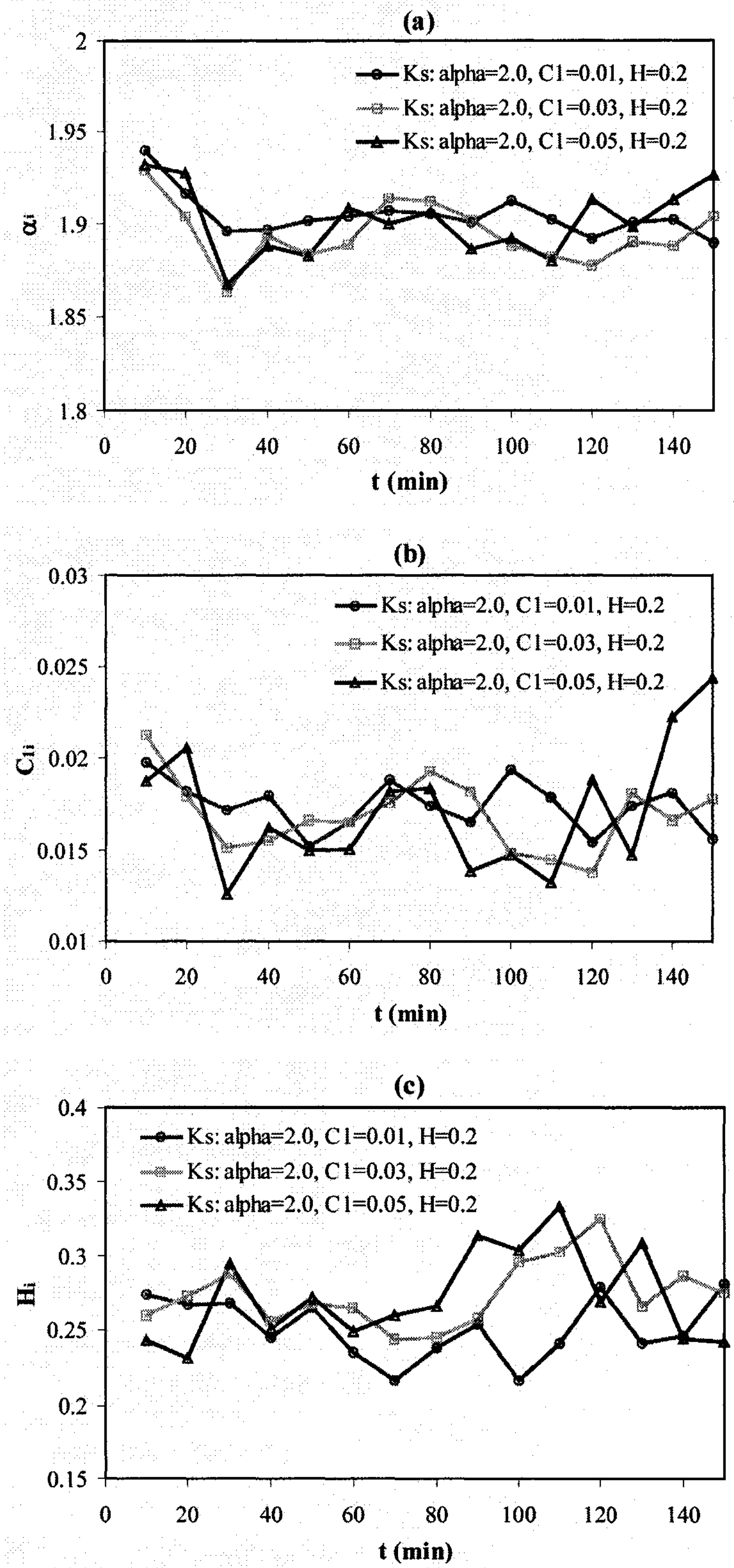

Figure 5.43 Effect of C_{1Ks} on the estimated infiltration parameters (a) α_i, (b) C_{1i}, and (c) H_i, under steady scaling rain field (α_R = 1.2, C_{1R} = 0.2, and H_R = 0.3) and scaling K_s fields.

ii) Parameter C_{1Ks} also has a weak impact on C_{1i} (Figure 5.43 (b)). Even though the variation of C_{1i} with C_{1Ks} is not very clear, it is discernable that the two parameters are inversely correlated.

iii) The influence of C_{1Ks} on H_i is weak as shown in Figure 5.43 (c). H_i increases with C_{1Ks} as the latter shifts from 0.01 to 0.03 and 0.05 even though the trend is ambiguous in the C_{1Ks} range of 0.03 and 0.05.

In summary, C_{1Ks} has a weak impact on the scaling parameters of infiltration process.

5.3.5.3 Effects of K_s H

Four K_s fields are employed for analyzing the impact of K_s H (H_{Ks}) on infiltration. Parameter α_{Ks} and C_{1Ks} for all the four fields are 2.0 and 0.01, respectively. Parameter H_{Ks} is 0.0, 0.1, 0.3, or 0.4 for each of the K_s field. It is noted here that $H_{Ks} = 0$ yields a conservative or homogeneous field. Twenty-five experiments are performed for each combination of the K_s parameters. The time series of the field average infiltration rates resulting from the four K_s fields are shown in Figure 5.44. Essentially, no difference is observed in all the time series of the field average infiltration. This demonstrates that H_{Ks} has very minor impact on the field average infiltration. Figure 5.45 displays the R_i^2 time series of the infiltration processes. Infiltration fields from the first three K_s fields are shown to be strongly scaling. Most part of the R_i^2 time series from the highest H_{Ks} (0.4) is lower than the R^2 reference line. However, the R_i^2 values are stable and fairly close to the reference line. Therefore, the infiltration process from this case is considered weakly scaling. The time series of β_i are presented in Figure 5.46 along with their rmse_β_i values. It is observed that β_i increases with H_{Ks} except for the first 100 min. or so in the case of homogeneous K_s field ($H_{Ks} = 0$). The time series of β_i also have increasing trend in all cases. The rmse_βi values for the four infiltration processes are 0.06, 0.09, 0.08, and 0.09, respectively.

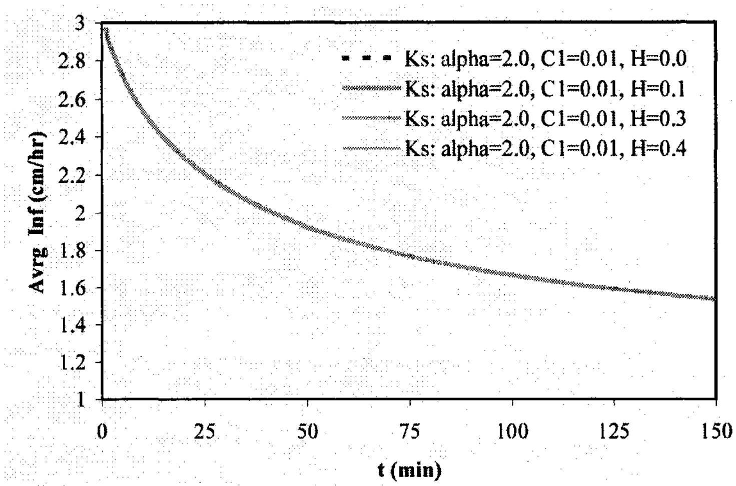

Figure 5.44 Effect of H_{Ks} on the field average surface infiltration rates under steady scaling rain (α_R = 1.2, C_{1R} = 0.2, and H_R = 0.3) and scaling K_s fields

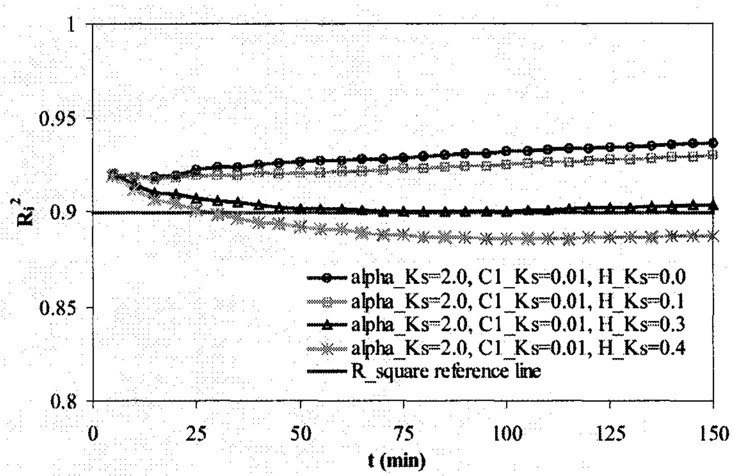

Figure 5.45 Effect of H_{Ks} on R_i^2 of the infiltration fields under steady scaling rain (α_R = 1.2, C_{1R} = 0.2, and H_R = 0.3) and scaling K_s fields

Figure 5.47 compares the estimated infiltration parameters from the four K_s fields. The results are:

i) There is an adjusting period of about 20 to 30 min. at the beginning of the infiltration processes. The variations of the infiltration parameters with the rain parameters behave differently inside and outside this period. The same adjusting (transition) period is also observed in Figures 5.12 and 5.39.

ii) A special zone develops close to $H_{Ks} = 0$ (homogeneous K_s field) in the second part of the infiltration process where α_i increases with H_{Ks}. Otherwise α_i is inversely proportional to H_{Ks} after the initial adjusting period. The impact of H_{Ks} on the singularity of the infiltration field is moderate.

iii) H_{Ks} has a weak impact on C_{1i}. The latter increases with H_{Ks} in the vicinity of $H_{Ks} = 0$, and decreases with H_{Ks} outside the small zone.

iv) Infiltration parameter H_i is moderately influenced by H_{Ks}. It decreases with the latter in the vicinity of $H_{Ks} = 0$, and monotonically increases with H_{Ks} outside the small zone.

v) Homogeneous K_s field ($H_{Ks} = 0$) does not lead to homogeneous infiltration field.

Overall, H_{Ks} has a weak to moderate impact on the scaling parameters of infiltration process.

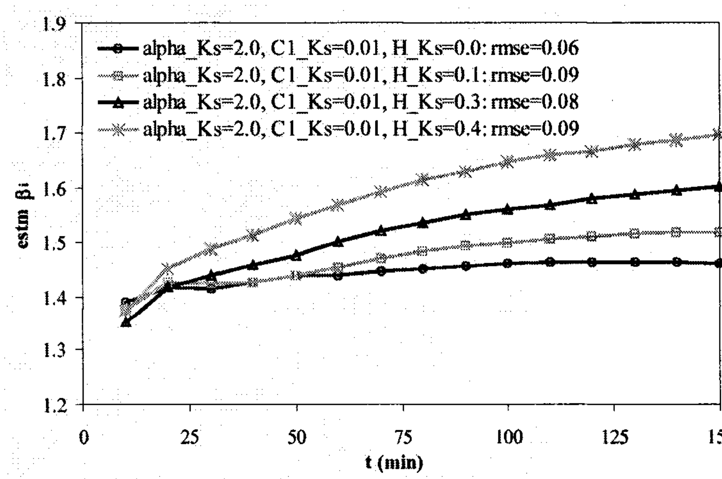

Figure 5.46 Effect of H_{Ks} on β_i of the infiltration fields under steady scaling rain (α_R = 1.2, C_{1R} = 0.2, and H_R = 0.3) and scaling K_s fields

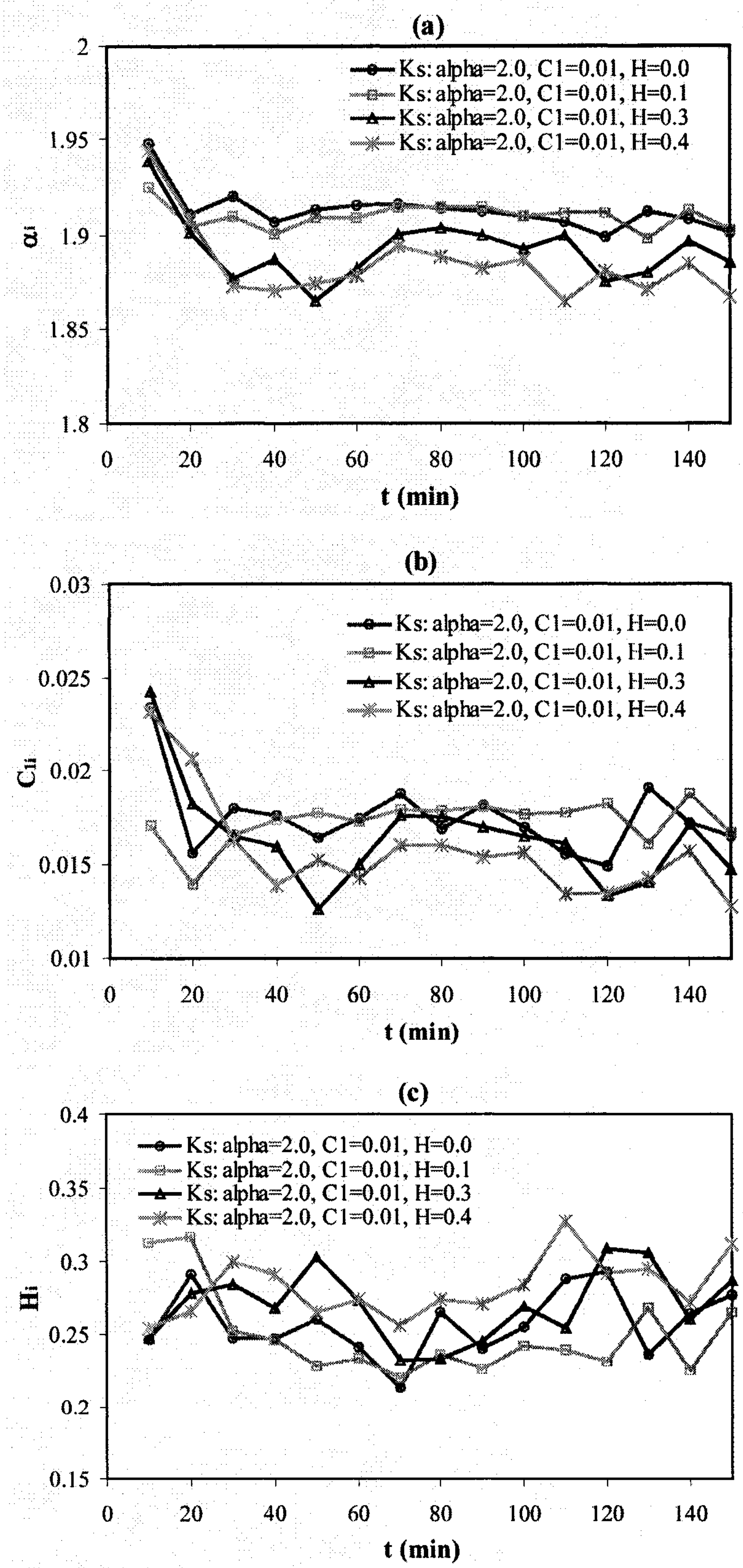

Figure 5.47 Effect of H_{Ks} on the estimated infiltration parameters (a) α_i, (b) C_{1i}, and (c) H_i, under steady scaling rain field ($\alpha_R = 1.2$, $C_{1R} = 0.2$, and $H_R = 0.3$) and scaling K_s fields.

The analyses performed so far have shown that the scaling properties of infiltration processes under the condition of steady rain are a combined result of rain and soil scaling (or non-scaling) properties and the interactions between rain and soil, among other factors. It is concluded that infiltration process will eventually become scaling as long as the embedded K_s field is scaling. All the infiltration fields examined in this section are shown to be scaling. Figure 5.48 shows the rmse_β_i of the 33 scaling infiltration processes used in this part of the study, and Table 5.1 lists the input scaling parameters of the corresponding rain and K_s fields. It is observed that the majority of the rmse_β_i are less than 0.2 – indicating that the UM model fits in the infiltration data with reasonable accuracy. The infiltration processes corresponding to the large rmse_β_i (> 0.2) are the results of homogeneous or close to homogeneous rain fields (Table 5.1). In summary, rain parameter H_R tends to be an important factor in determining the scaling parameters of infiltration process while α of K_s only plays a significant role if the parameter is large ($\rightarrow$ 2.0). A more complete description of the findings from this section is provided in Chapter 7.

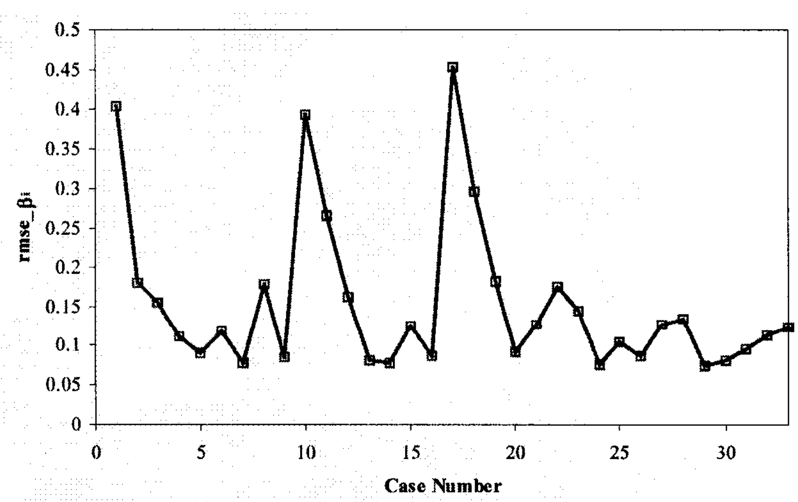

Figure 5.48 The rmse_β_i of all the scaling infiltration processes under steady scaling rain and scaling K_s fields.

Table 5.1 Scaling Parameters of Steady Rain and K_s Fields from Section 5.3.4

Case #	α_R	C_{1R}	H_R	α_{Ks}	C_{1Ks}	H_{Ks}
1	1.2	0.1	0.0	2.0	0.01	0.2
2	1.2	0.1	0.1	2.0	0.01	0.2
3	1.2	0.1	0.2	2.0	0.01	0.2
4	1.2	0.1	0.35	2.0	0.01	0.2
5	1.2	0.1	0.5	2.0	0.01	0.2
6	1.2	0.2	0.2	2.0	0.01	0.2
7	1.2	0.2	0.35	2.0	0.01	0.2
8	1.2	0.3	0.2	2.0	0.01	0.2
9	1.2	0.3	0.35	2.0	0.01	0.2
10	1.5	0.1	0.0	2.0	0.01	0.2
11	1.5	0.1	0.1	2.0	0.01	0.2
12	1.5	0.1	0.2	2.0	0.01	0.2
13	1.5	0.1	0.35	2.0	0.01	0.2
14	1.5	0.1	0.5	2.0	0.01	0.2
15	1.5	0.2	0.2	2.0	0.01	0.2
16	1.5	0.2	0.35	2.0	0.01	0.2
17	1.5	0.3	0.0	2.0	0.01	0.2
18	1.5	0.3	0.1	2.0	0.01	0.2
19	1.5	0.3	0.2	2.0	0.01	0.2
20	1.5	0.3	0.35	2.0	0.01	0.2
21	1.5	0.3	0.5	2.0	0.01	0.2
22	1.8	0.1	0.2	2.0	0.01	0.2
23	1.8	0.2	0.2	2.0	0.01	0.2
24	1.8	0.2	0.35	2.0	0.01	0.2
25	1.2	0.2	0.3	1.5	0.01	0.2
26	1.2	0.2	0.3	1.75	0.01	0.2
27	1.2	0.2	0.3	2.0	0.01	0.0
28	1.2	0.2	0.3	2.0	0.01	0.1
29	1.2	0.2	0.3	2.0	0.01	0.2
30	1.2	0.2	0.3	2.0	0.01	0.3
31	1.2	0.2	0.3	2.0	0.01	0.4
32	1.2	0.2	0.3	2.0	0.03	0.2
33	1.2	0.2	0.3	2.0	0.05	0.2

5.4 Analysis of Infiltration under Space-Time Rain

Rainfall in the real world is characterized by variations both in space and in time. Thus, it is essential to add the temporal dynamics in rain field in the study of infiltration process. In the absence of a practical space-time rain model that fits into the framework of universal multifractal, a series of "space-time" rain fields is generated using the UM model as explained below.

First, a large rain field with 2048 x 2048 pixels – the largest scaling field that can be generated with the available computer resources – is generated using the UM model. Then consecutive cutouts from this large field with the size of 128 x 128 pixels are taken as 'space-time' rain fields at one pixel apart. This in effect adds advection to a steady rain field. If advection is assumed to be 10 m/s, moving one pixel at a time translates to a time step of 3 s, and a total of 96 min rainfall can be extracted from the large rain field. Figure 5.49 shows 6 such "space-time" rain fields at 6 min apart with some overlapping on the edges of the images. They compose a strip of the large rain field from which these rain fields are cut out.

5.4.1 Experimental Set-up

Unless otherwise noted, the following set-ups are employed in the experiments carried out in this section.

i) Average rain rate for the rain fields with 2048 x 2048 pixel is 3 cm/hr.

ii) Average K_s is 1.32 cm/hr.

iii) Rain duration is 90 min.

iv) Twenty-five experiments are conducted for the analysis on space-time rain impact on infiltration and ten experiments for the study on the influence of K_s on infiltration. The average statistics (field average, scaling parameters, *etc.*) are used in the analysis.

5.4.2 Effects of Space-Time Scaling Rain on Infiltration

5.4.2.1 Effects of Rain α

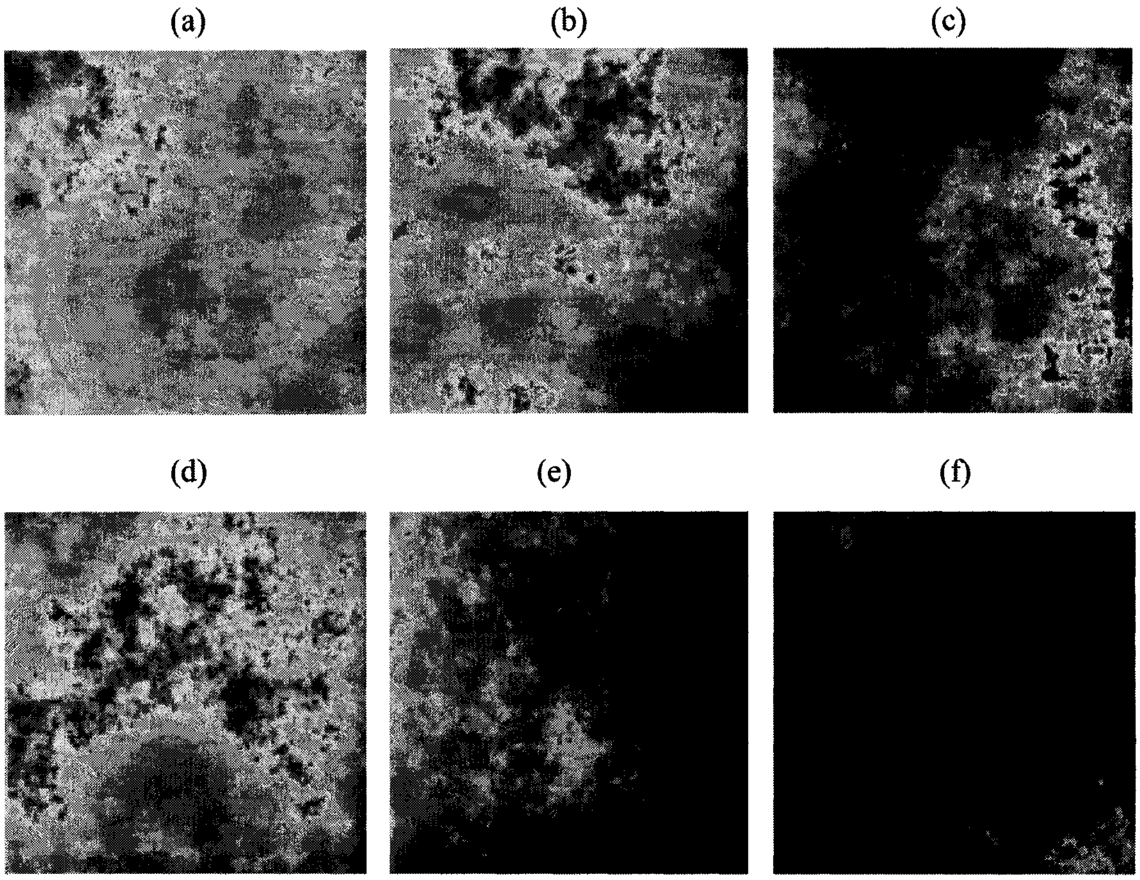

Figure 5.49 Space-time rain fields at (a) 7 min, (b) 13 min, (c) 19 min, (d) 25 min, (e) 31 min, and (f) 37 min.

Three types of rain fields are used for the study on the impact of α_R on infiltration. The rain parameters are

Rain field 1: $\alpha_R = 1.2$, $C_{1R} = 0.2$, $H_R = 0.5$

Rain field 2: $\alpha_R = 1.5$, $C_{1R} = 0.2$, $H_R = 0.5$

Rain field 3: $\alpha_R = 1.8$, $C_{1R} = 0.2$, $H_R = 0.5$

Figure 5.50 compares the average rain relative frequencies from the three rain types. It is shown that smaller α_R corresponds to more area with high rain intensity and thus produces a larger average infiltration rate (Figure 5.51). This is consistent with the findings from the steady rain. Figure 5.52 shows the R_i^2 time series resulted from the three rain fields. The R_i^2 series are shown to be above the R^2 reference line and indicate that the infiltration fields subject to space-time scaling rain and scaling K_s fields are strongly scaling. Figure 5.53 presents the three β_i time series along with their respective rmse_β_i values.

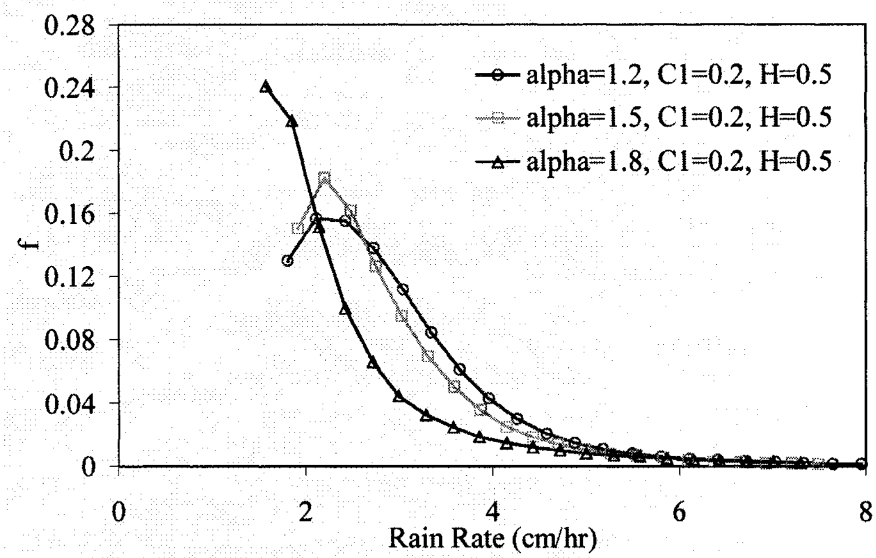

Figure 5.50 Average relative frequency of space-time rain fields

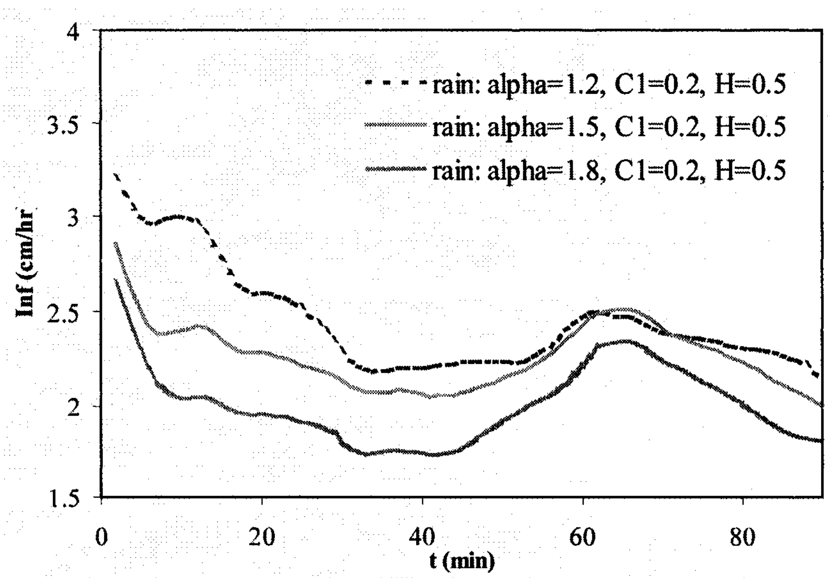

Figure 5.51 Effect of α_R on the field average surface infiltration rates under space-time scaling rain and scaling K_s fields (α_{Ks} = 2.0, C_{1Ks} = 0.01, and H_{Ks} = 0.2)

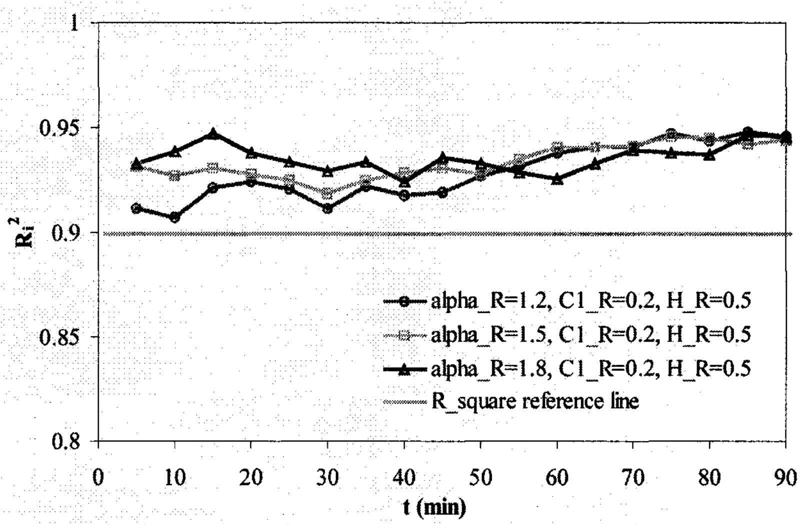

Figure 5.52 Effect of α_R on the R_i^2 of the infiltration fields under space-time scaling rain and scaling K_s fields (α_{Ks} = 2.0, C_{1Ks} = 0.01, and H_{Ks} = 0.2)

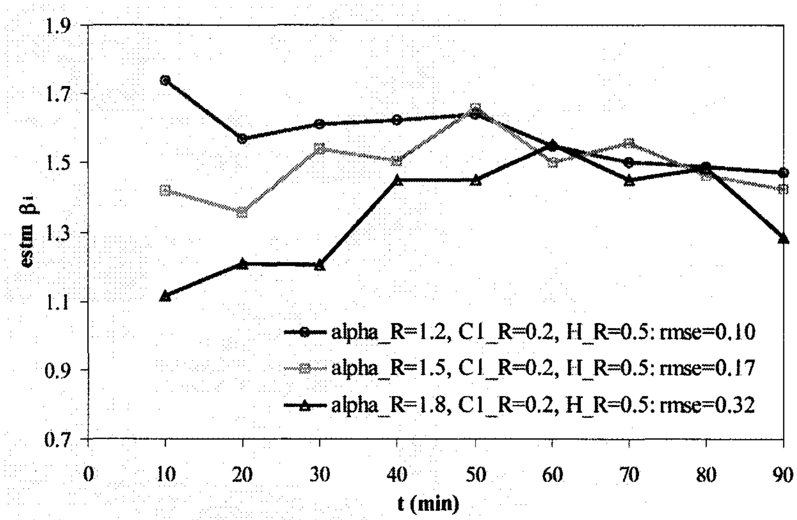

Figure 5.53 Effect of α_R on the β_i of the infiltration fields under space-time scaling rain and scaling K_s fields (α_{Ks} = 2.0, C_{1Ks} = 0.01, and H_{Ks} = 0.2)

A common trend found in the three time series in Figure 5.53 is that β_i of the infiltration processes decrease after a certain period of time – indicating that infiltration fields become more singular, more sparse in its mean process, and/or more homogeneous in time under the condition of scaling space-time rainfall and scaling K_s fields. Although higher α_R leads to smaller β_i in the first part of the infiltration process, all rain fields yield similar β_i after a certain time. It is speculated that the reason for the observed phenomenon is the transition from rain-dominated to soil-dominated infiltration process. The rmse_β_i of the three processes are respectively 0.10, 0.17, and 0.32.

Figure 5.54 presents the estimated scaling parameters of the infiltration processes from the three space-time rain scenarios. The following conclusions are derived from the figure:

i) Rain parameter α_R has little effect on α_i.

ii) Rain parameter α_R also has little effect on C_{1i}.

iii) Rain parameter α_R has a weak and non-linear impact on H_i.

iv) Both α_i and C_{1i} generally increase in time while H_i does not have a clear trend. These trends state that under the rain fields as given, infiltration fields become more singular in time and have increased sparseness in their mean processes. Their homogeneity, on the other hand, does not change monotonically in time.

Overall, the impact of α_R on the scaling parameters of infiltration is weak.

5.4.2.2 Effects of Rain C_1

Three groups of rain fields are used for this study with the following parameters.

Rain field 1: $\alpha_R = 1.2$, $C_{1R} = 0.2$, $H_R = 0.5$

Rain field 2: $\alpha_R = 1.2$, $C_{1R} = 0.3$, $H_R = 0.5$

Rain field 3: $\alpha_R = 1.2$, $C_{1R} = 0.4$, $H_R = 0.5$

Figure 5.55 shows the time series of the field average of the infiltration processes resulting from the three rain fields. Smaller C_{1R} is seen to lead to more infiltration on average – a finding consistent with the steady rain case. The three time series of R_i^2 are displayed in Figure 5.56. The high R_i^2 values reveal that the infiltration fields are strongly scaling.

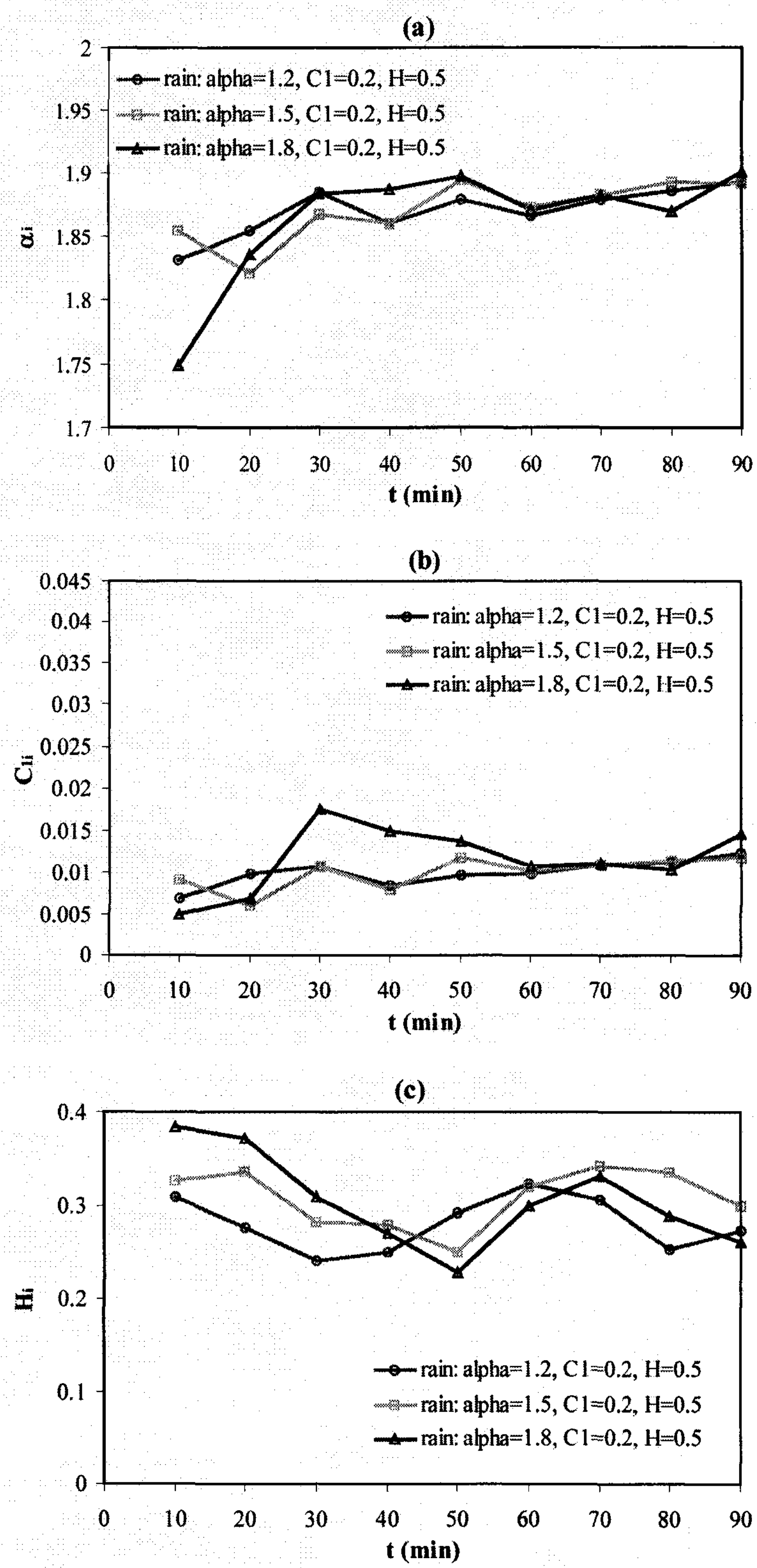

Figure 5.54 Effect of α_R on the estimated infiltration parameters (a) α_i, (b) C_{1i}, and (c) H_i, under space-time scaling rain field and scaling K_s fields (α_{Ks} = 2.0, C_{1Ks} = 0.01, and H_{Ks} = 0.2).

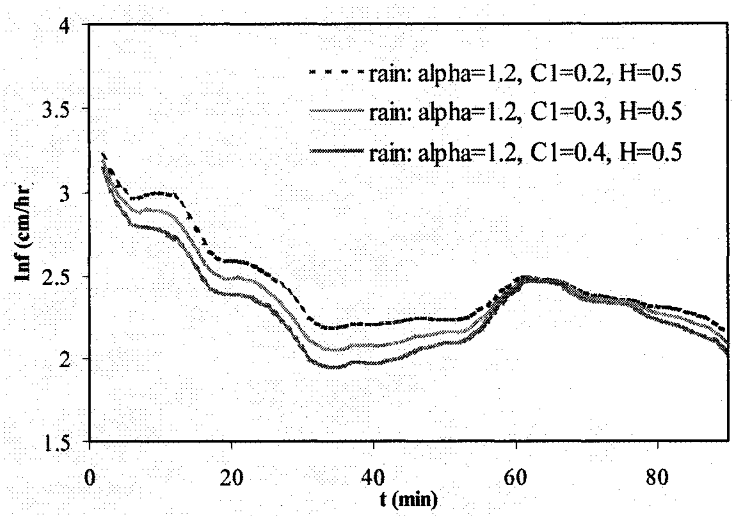

Figure 5.55 Effect of C_{1R} on the field average surface infiltration rates under space-time scaling rain and scaling K_s fields (α_{Ks} = 2.0, C_{1Ks} = 0.01, and H_{Ks} = 0.2)

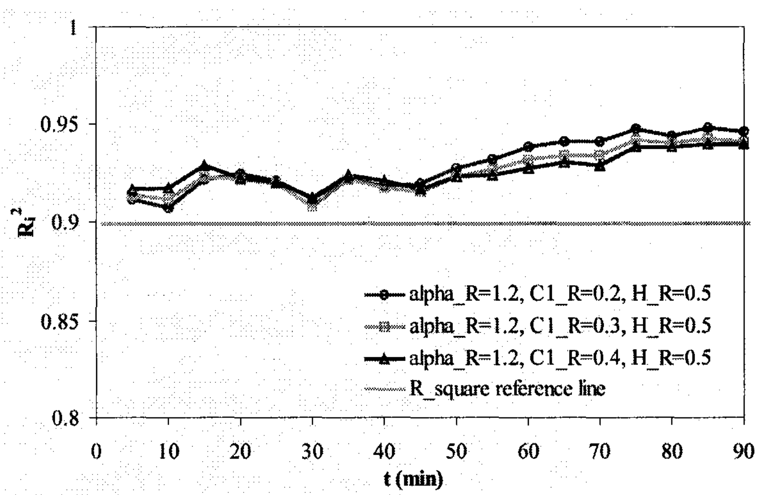

Figure 5.56 Effect of C_{1R} on the R_i^2 of the infiltration fields under space-time scaling rain and scaling K_s fields (α_{Ks} = 2.0, C_{1Ks} = 0.01, and H_{Ks} = 0.2)

Figure 5.57 shows the β_i time series and their rmse_β_i values. Smaller C_{1R} corresponds to larger β_i in the early stage of the infiltration process. However, little difference is observed in β_i from the three time series after a certain time length (about 60 min). All series show a decreasing trend from this point on. Hence, larger C_{1R} and prolonged rainfall will produce more singularity, more sparseness, and/or more homogeneity in the infiltration fields under the space-time rainfalls and the scaling K_s fields used.

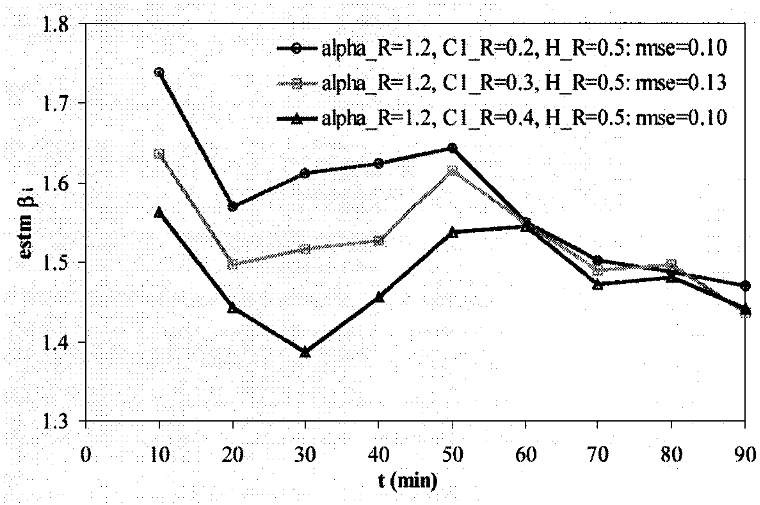

Figure 5.57 Effect of C_{1R} on the β_i of the infiltration fields under space-time scaling rain and scaling K_s fields (α_{Ks} = 2.0, C_{1Ks} = 0.01, and H_{Ks} = 0.2)

Figure 5.58 shows the time series of the estimated infiltration parameters. The observations from the figure are summarized below.

i) Parameter C_{1R} has a weak to moderate impact on α_i depending on the developing stage of the infiltration process.

ii) Parameter C_{1R} has a weak impact on C_i.

iii) Parameter C_{1R} has a weak and non-unidirectional impact on H_i.

iv) Both α_i and C_{1i} show generally monotonically increasing trend under the three rain fields used in this study and indicate increased singularity and sparseness with time. No universal conclusions can be drawn for H_i from the cases run here.

In general, C_{1R} has a weak influence on the scaling parameters of infiltration process.

5.4.2.3 Effects of Rain H

Four types of rain fields are generated for this study. Their model parameters are

Rain field 1: $\alpha_R = 1.2$, $C_{1R} = 0.2$, $H_R = 0.0$

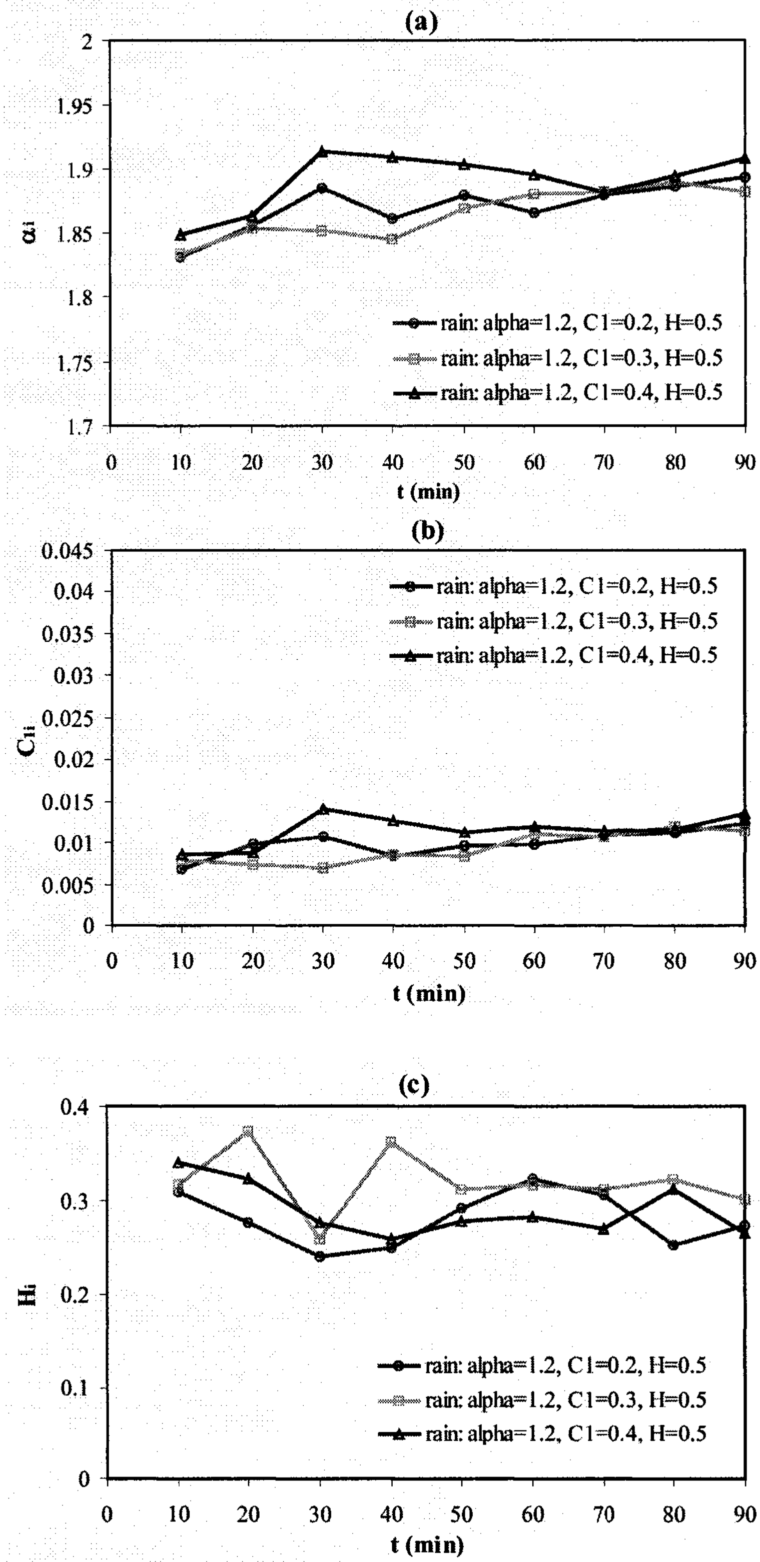

Figure 5.58 Effect of C_{1R} on the estimated infiltration parameters (a) α_i, (b) C_{1i}, and (c) H_i, under space-time scaling rain field and scaling K_s fields (α_{Ks} = 2.0, C_{1Ks} = 0.01, and

Rain field 2: $\alpha_R = 1.2$, $C_{1R} = 0.2$, $H_R = 0.1$

Rain field 3: $\alpha_R = 1.2$, $C_{1R} = 0.2$, $H_R = 0.3$

Rain field 4: $\alpha_R = 1.2$, $C_{1R} = 0.2$, $H_R = 0.5$

Figure 5.59 compares the field average infiltration rates from the four rain cases. It is observed that the higher average infiltration rates correspond to the smaller H_R at the beginning of the process but to the larger H_R afterwards. Recall that the average infiltration rate is universally proportional to H_R under steady rainfall (Figure 5.29). The difference between the two cases is obviously caused by the added rain dynamics in the former case. Increased H_R effectively 'smoothes out' a scaling rain field by (non-linearly) increasing smaller values of the rain field and decreasing larger values. Therefore, a small H_R (including $H_R = 0$) corresponds to a rain field with significant rain intensities over a small area, but very low rain intensities over the majority of the field (Figure 5.27). Since infiltration capacity decreases over time if there is enough rainfall, steady rain fields with small H_R offers an inefficient water supply field where little water is available for infiltration over most area and rapidly diminished infiltration capacity at the points with high rain intensities would prevent high infiltration rates from lasting very long. In the case of space-time rain, however, the points with high rain rates move through the study area and lead to much infiltration along their paths. This effect is most clearly seen at the early stage of the infiltration process when the infiltration capacity is high. As the soil absorbs more water, infiltration capacity reduces and so will the effective infiltration. This process accelerates for smaller H_R and is responsible for the phenomenon observed in the later part of the infiltration process in Figure 5.59.

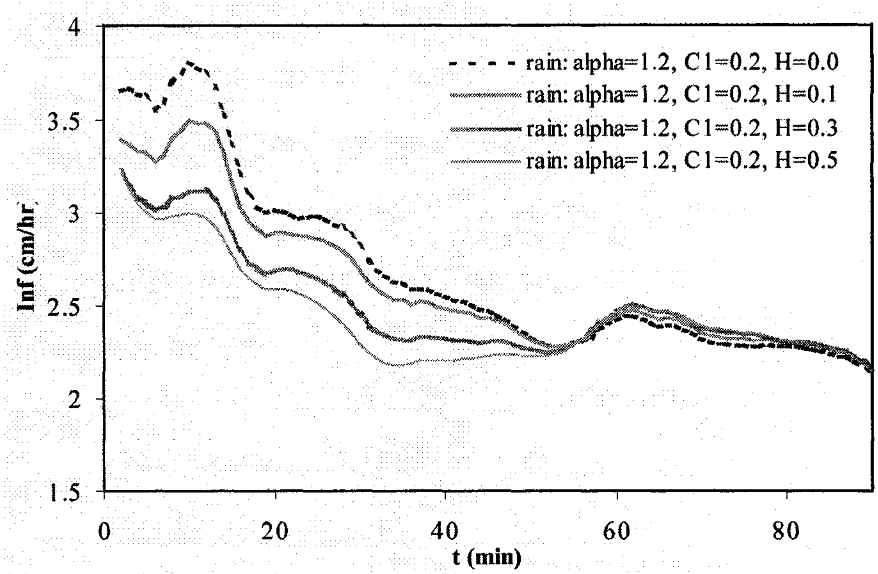

Figure 5.59 Effect of H_R on the field average surface infiltration rates under space-time scaling rain and scaling K_s fields ($\alpha_{Ks} = 2.0$, $C_{1Ks} = 0.01$, and $H_{Ks} = 0.2$)

Figure 5.60 shows the time series of the R_i^2 of the four infiltration processes. The larger H_R's are shown to produce strongly scaling infiltration fields. The infiltration fields from the smaller H_R's tend to be weakly scaling at the beginning and gradually become strongly scaling. The rmse_β_i values shown in Figure 5.61 further show that the UM model fits to the infiltration fields. Figure 5.61 also presents the four β_i time series. It is shown that β_i increases with H_R. This is the consequence of the decreased α_i, C_{1i}, and increased H_i as H_R becomes larger (Figure 5.62). The rmse_β_i values for the four infiltration processes are 0.08, 0.23, 0.10, and 0.08, respectively.

Figure 5.62 presents the estimated infiltration parameters from the four rain fields. The conclusions derived from the figure are:

i) H_R has a strong and non-unidirectional impact on α_i. Similar to steady rain, a special zone exists close to $H_R = 0$ (homogeneous rain field) where α_i is proportional to H_R. The two parameters become inversely correlated as H_R becomes larger.

ii) H_R has a strong and non-unidirectional influence on C_{1i}. Similar to the case of α_i, there is a special zone close to $H_R = 0$ where C_{1i} increases with H_R and becomes monotonically decreasing with H_R as the latter increases.

iii) H_i takes heavy influence from H_R. The former decreases with the latter in a small range of H_R close to zero, and increases unidirectionally with the latter outside this range. The same behavior is observed in the steady rain case.

iv) Homogeneous space-time rain did not produce homogeneous infiltration fields in the cases examined.

v) Both α_i and C_{1i} decrease in time if H_R is smaller than about 0.3. Otherwise, the two parameters will reverse the trend and increase in time. The latter case is what was observed in the study on the impact of α_R and C_{1R}.

vi) Opposite to the changing trend of α_i and C_{1i}, H_i increases in time if H_R is smaller than about 0.3. The trend is unclear if H_R is larger than 0.3.

The influence of H_R of space-time rain field on the scaling parameters of infiltration process is very strong.

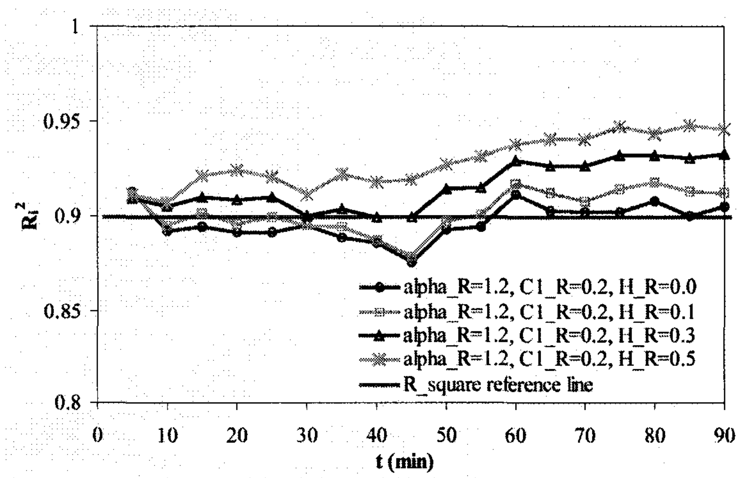

Figure 5.60 Effect of H_R on the R_i^2 of the infiltration fields under space-time scaling rain and scaling K_s fields ($\alpha_{Ks} = 2.0$, $C_{1Ks} = 0.01$, and $H_{Ks} = 0.2$)

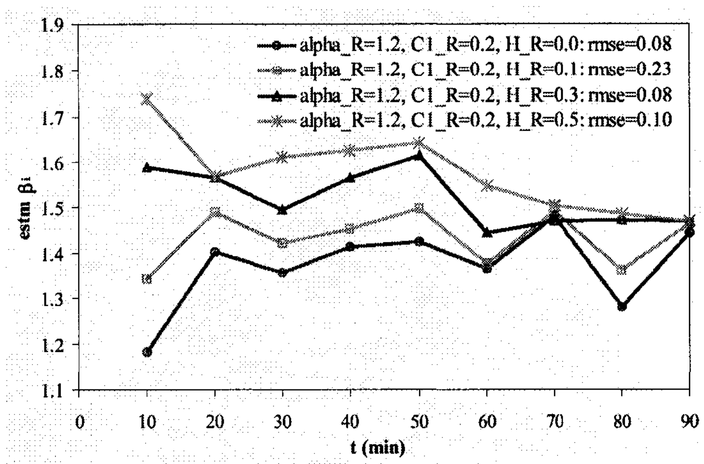

Figure 5.61 Effect of H_R on the β_i of the infiltration fields under space-time scaling rain and scaling K_s fields ($\alpha_{Ks} = 2.0$, $C_{1Ks} = 0.01$, and $H_{Ks} = 0.2$)

5.4.3 Effects of Scaling K_s on Infiltration under Space-Time Rain

5.4.3.1 Effects of K_s α

Three types of K_s fields are employed for this study. Their scaling parameters are

K_s field 1: $\alpha_{Ks} = 1.5$, $C_{1Ks} = 0.01$, $H_{Ks} = 0.2$

K_s field 2: $\alpha_{Ks} = 1.75$, $C_{1Ks} = 0.01$, $H_{Ks} = 0.2$

K_s field 3: $\alpha_{Ks} = 2.0$, $C_{1Ks} = 0.01$, $H_{Ks} = 0.2$

The UM model parameters of the space-time rain fields used are $\alpha_R = 1.2$, $C_{1R} = 0.2$, $H_R = 0.3$. The studies of the infiltration processes produced from the above K_s and rain fields yield the following results (figures are not included): 1) smaller α_{Ks} leads to more field average infiltration throughout the infiltration process; 2) R_i^2 values indicate that the infiltration fields are generally strongly scaling with a brief period of weak scaling at about half-way of the infiltration processes; 3) the estimated β_i is proportional to parameter α_{Ks}; and 4) the rmse_β_i of the three infiltration processes are 0.22, 0.14, and 0.08 which shows that larger α_{Ks} produces infiltration fields that can be better described by the UM model. Figure 5.63 shows the estimated scaling parameters of the three infiltration processes. The following conclusions are drawn from the figure.

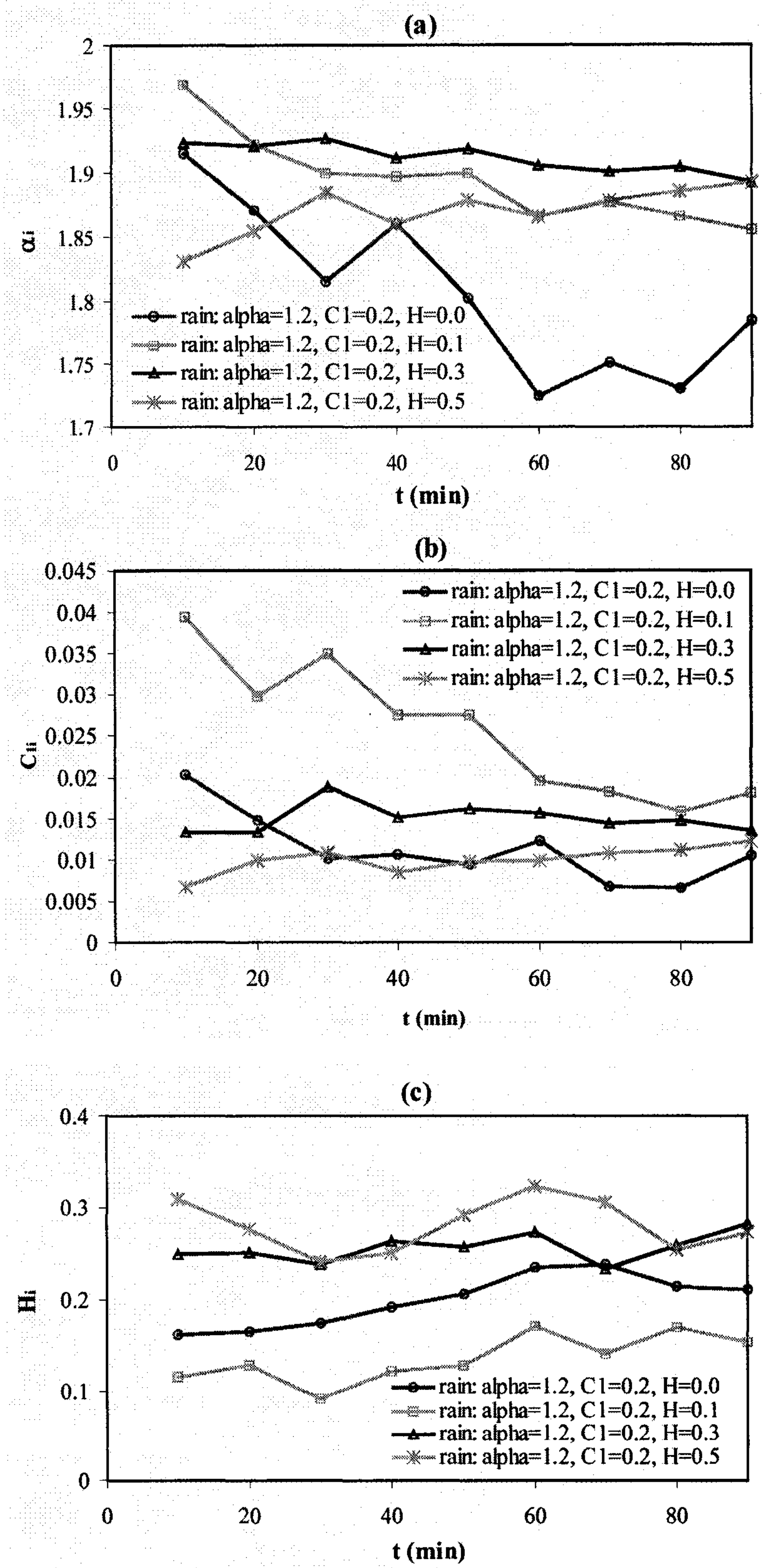

Figure 5.62 Effect of H_R on the estimated infiltration parameters (a) α_i, (b) C_{1i}, and (c) H_i, under space-time scaling rain field and scaling K_s fields (α_{Ks} = 2.0, C_{1Ks} = 0.01, and H_{Ks} = 0.2).

i) The impact of α_{Ks} on α_i becomes stronger with time. The two parameters are positively correlated.

ii) Parameter α_{Ks} has a moderate influence on C_{1i} in the later part of the process, and the two parameters are positively correlated at this stage.

iii) The influence of α_{Ks} on H_i is weak and generally unidirectional.

iv) Both α_i and C_{1i} generally decrease in time for the range of K_s tested. The change is more rapid with smaller α_{Ks}. This means that infiltration rate becomes more evenly distributed in time over the field with less sparseness on average.

The effect of α_{Ks} on infiltration is mixed from a strong influence on α_i to a weak influence on H_i.

5.4.3.2 Effects of K_s C_1

The scaling parameters of the three sets of K_s fields used for this part of the study are listed below.

K_s field 1: $\alpha_{Ks} = 2.0$, $C_{1Ks} = 0.01$, $H_{Ks} = 0.2$

K_s field 2: $\alpha_{Ks} = 2.0$, $C_{1Ks} = 0.02$, $H_{Ks} = 0.2$

K_s field 3: $\alpha_{Ks} = 2.0$, $C_{1Ks} = 0.03$, $H_{Ks} = 0.2$

The parameters of the space-time rain fields used are $\alpha_R = 1.2$, $C_{1R} = 0.2$, $H_R = 0.3$. The studies performed in this part show (figures are not included) that: 1) smaller C_{1Ks} corresponds to larger field average infiltration; 2) R_i^2 values for all the infiltration processes are above 0.9, indicating that the infiltration fields are strongly scaling; 3) different C_{1Ks} makes little difference to the estimated β_i time series; and 4) the RMSE of the β_i time series are 0.08, 0.11, and 0.12, respectively. Figure 5.64 shows the estimated

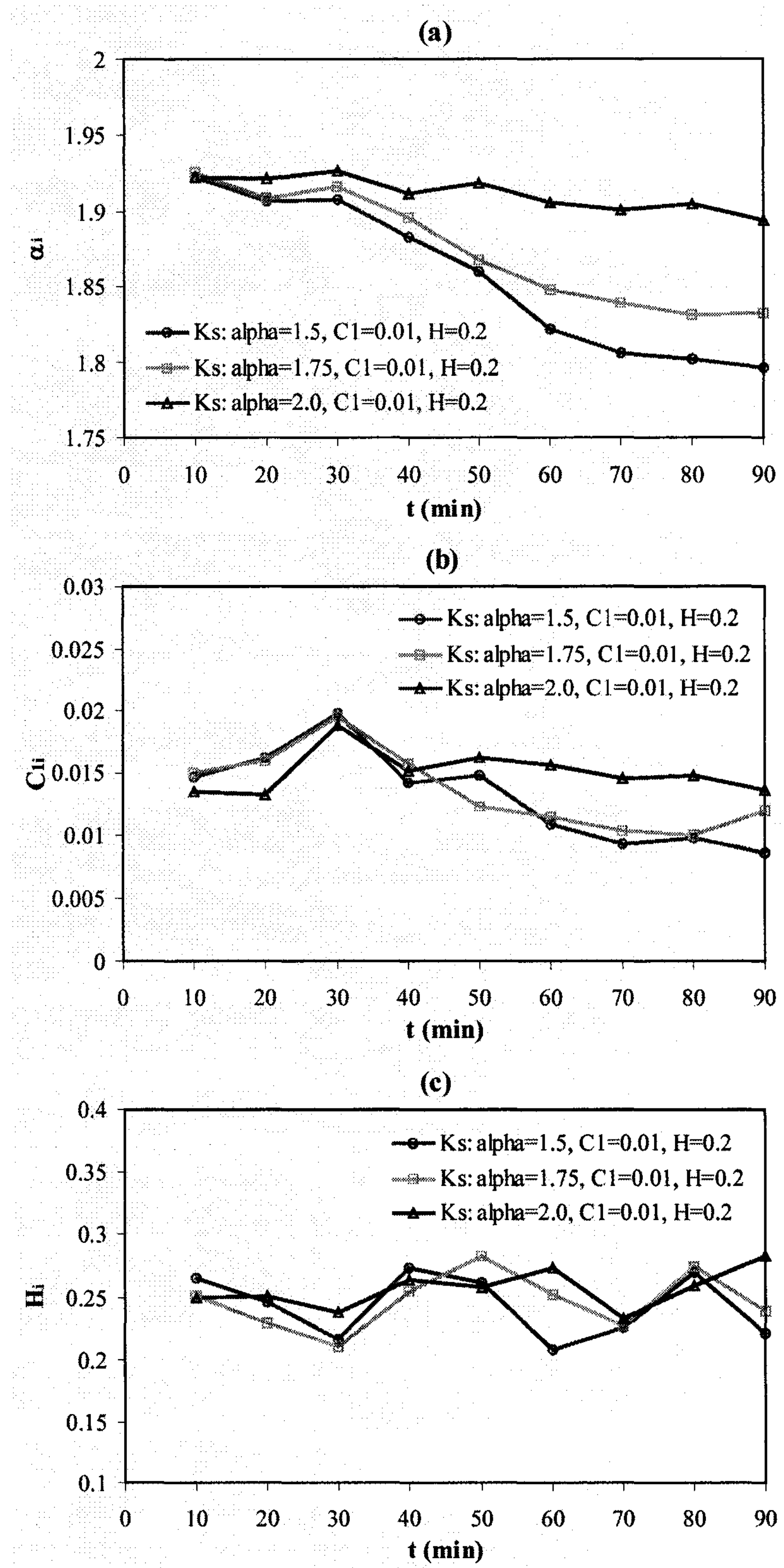

Figure 5.63 Effect of α_{Ks} on the estimated infiltration parameters (a) α_i, (b) C_{1i}, and (c) H_i, under space-time scaling rain field ($\alpha_R = 1.2$, $C_{1R} = 0.2$, and $H_R = 0.3$) and scaling K_s fields.

infiltration parameters. The results are summarized below.

i) Parameter C_{1Ks} has a weak to moderate impact on α_i considering the small range of C_{1Ks} used. The two parameters are positively correlated.

ii) C_{1Ks} has a strong and unidirectional impact on C_{1i}.

iii) The impact of C_{1Ks} on H_i is weak and unidirectional.

iv) Parameter α_i decreases in time in all cases. No temporal trend is detected in C_{1i} and H_i except a decreasing trend for C_{1i} in the case of $C_{1Ks} = 0.01$.

In summary, C_{1Ks} has a mixed impact on infiltration parameters from a strong impact on C_{1i} to a weak impact on H_i.

5.4.3.3 Effects of K_s H

The scaling parameters of the four types of K_s fields used for this study are

K_s field 1: $\alpha_{Ks} = 2.0$, $C_{1Ks} = 0.01$, $H_{Ks} = 0.0$

K_s field 2: $\alpha_{Ks} = 2.0$, $C_{1Ks} = 0.01$, $H_{Ks} = 0.1$

K_s field 3: $\alpha_{Ks} = 2.0$, $C_{1Ks} = 0.01$, $H_{Ks} = 0.3$

K_s field 4: $\alpha_{Ks} = 2.0$, $C_{1Ks} = 0.01$, $H_{Ks} = 0.4$

where the first type of K_s field is homogeneous with $H_{Ks} = 0$.

The studies of the infiltration fields from the four K_s fields result in the following findings (figures are not included): 1) H_{Ks} essentially makes no difference to the field average infiltration; 2) the highest H_{Ks} (0.4) leads to weakly scaling infiltration fields while the other three K_s fields produce mostly strongly scaling infiltration processes; 3) the estimated β_i is proportional to H_{Ks}; and 4) the rmse_β_i of the four infiltration processes are respectively 0.22, 0.14, 0.16, and 0.26.

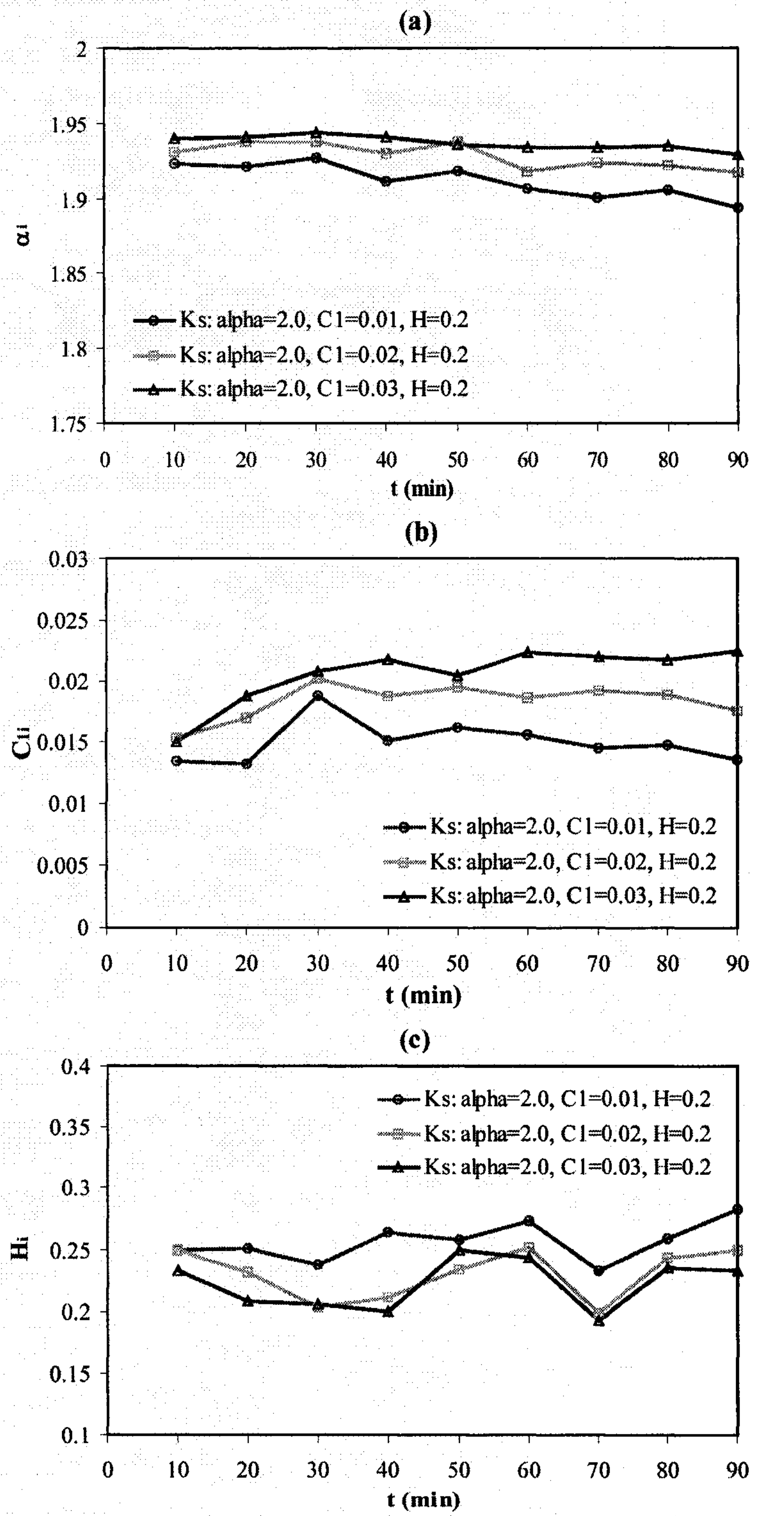

Figure 5.64 Effect of C_{1Ks} on the estimated infiltration parameters (a) α_i, (b) C_{1i}, and (c) H_i, under space-time scaling rain field ($\alpha_R = 1.2$, $C_{1R} = 0.2$, and $H_R = 0.3$) and scaling K_s fields.

Figure 5.66 shows the estimated scaling parameters of the infiltration processes from the four K_s fields. The conclusions are as follow:

i) The influence of H_{Ks} on α_i is weak.

ii) H_{Ks} also has a weak impact on C_{1i}.

iii) The impact of H_{Ks} on H_i is weak. Although the correlation of the two parameters is rather obscure, it is discernable that they are proportional to each other.

iv) Homogeneous K_s field will not produce homogeneous infiltration field.

v) There is a decreasing temporal trend in α_i in most cases tested while no clear trend can be detected in the other two infiltration parameters.

vi) Overall, the impact of H_{Ks} on infiltration is weak.

Table 5.2 lists the 16 sets of UM model parameters of the rain and K_s fields used in this part of the study, and Figure 5.66 shows their corresponding rmse_β_i. Most cases have relatively small rmse_β_i (< 0.2) and indicate good fit of the UM model to the infiltration fields. The infiltration processes with large rmse_β_i values correspond to the following cases: large α_R, small α_{Ks}, large H_{Ks}, or homogeneous K_s field.

Because of the dynamics introduced to the rain fields, the infiltration processes under space-time rainfalls exhibit some different characteristics from the steady rain cases while retaining some other properties. Two findings are worth mentioning here. One is the temporal trend associated with the infiltration parameters under space-time rainfall. The directions of the trend for the three infiltration parameters are determined by rain parameter H_R. The experiments performed on the effect of rain field parameters showed that both α_i and C_{1i} decrease and H_i increases in time if H_R is small (about 0.3), which

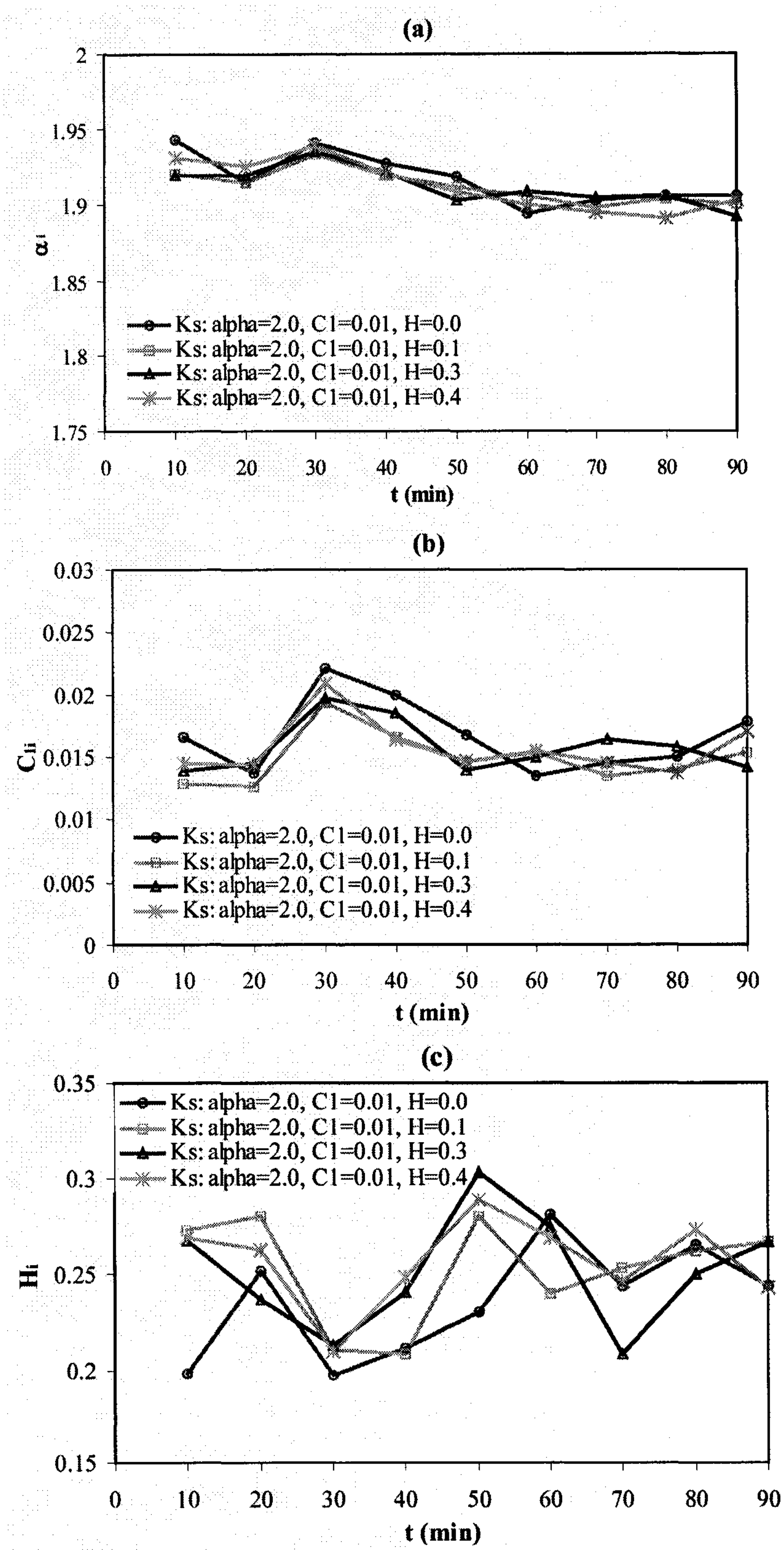

Figure 5.65 Effect of H_{Ks} on the estimated infiltration parameters (a) α_i, (b) C_{1i}, and (c) H_i, under space-time scaling rain field ($\alpha_R = 1.2$, $C_{1R} = 0.2$, and $H_R = 0.3$) and scaling K_s fields.

Table 5.2 Scaling Paramters of Space-Time Rain and Ks fields from Section 5.4

Case #	α_R	C_{1R}	H_R	α_{Ks}	C_{1Ks}	H_{Ks}
1	1.2	0.2	0.0	2.0	0.01	0.2
2	1.2	0.2	0.1	2.0	0.01	0.2
3	1.2	0.2	0.5	2.0	0.01	0.2
4	1.2	0.3	0.5	2.0	0.01	0.2
5	1.2	0.4	0.5	2.0	0.01	0.2
6	1.5	0.2	0.5	2.0	0.01	0.2
7	1.8	0.2	0.5	2.0	0.01	0.2
8	1.2	0.2	0.3	1.5	0.01	0.2
9	1.2	0.2	0.3	1.75	0.01	0.2
10	1.2	0.2	0.3	2.0	0.01	0.2
11	1.2	0.2	0.3	2.0	0.02	0.2
12	1.2	0.2	0.3	2.0	0.03	0.2
13	1.2	0.2	0.3	2.0	0.01	0.0
14	1.2	0.2	0.3	2.0	0.01	0.1
15	1.2	0.2	0.3	2.0	0.01	0.3
16	1.2	0.2	0.3	2.0	0.01	0.4

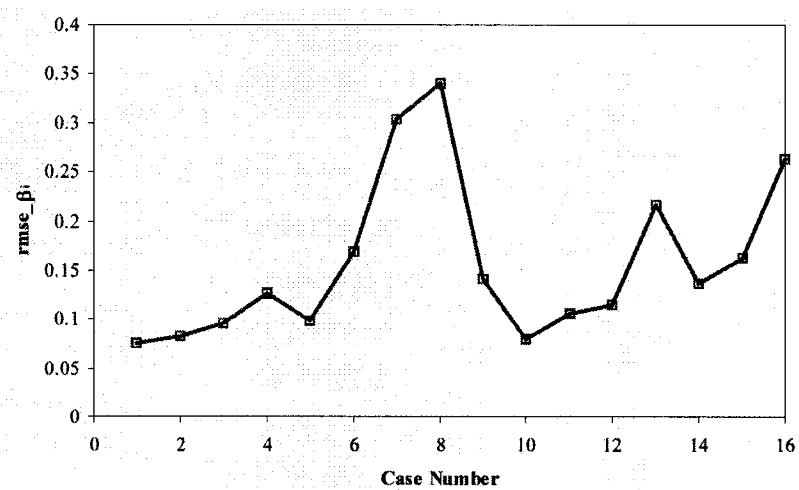

Figure 5.66 The rmse_β_i of all the scaling infiltration processes under space-time scaling rain and scaling K_s fields.

causes the infiltration field to be less singular, more space filling and less homogeneous. As H_R increases, the above trends in α_i and C_{1i} reverse and the resulting infiltration field becomes more singular and sparse even though H_i does not have clear temporal trend in this case. The studies of the impact of the K_s parameters support the above findings.

The second finding is the difference between infiltration processes produced by homogeneous and non-homogeneous rainfalls and K_s fields. Inside a small range of H_R and H_{Ks} close to zero (homogeneous field), the scaling parameters of infiltration process are often observed to behave differently from outside the range (non-homogeneous) such as varying with H_R or H_{Ks} in opposite directions. This fact shows that homogeneous forcing is a special case for infiltration process. More detailed conclusions derived in this section are summarized in Chapter 7.

5.5 Effects of Average Rain Rate

Three sets of 10 experiments are designed to examine the effect of average rain rate on the scaling properties of infiltration under the condition of space-time rainfall. The rain fields have the same scaling parameters but different average rain rate as follow.

Rain field 1: average RR = 3 cm/hr, $\alpha_R = 1.2$, $C_{1R} = 0.2$, $H_R = 0.5$

Rain field 2: average RR = 2 cm/hr, $\alpha_R = 1.2$, $C_{1R} = 0.2$, $H_R = 0.5$

Rain field 3: average RR = 1 cm/hr, $\alpha_R = 1.2$, $C_{1R} = 0.2$, $H_R = 0.5$

where RR stands for rain rate. The rain duration is 90 min. The same scaling K_s field is applied in all the experiments with parameters $\alpha_{Ks} = 2.0$, $C_{1Ks} = 0.01$, $H_{Ks} = 0.2$, and average $K_s = 1.32$ cm/hr. It is noted that the average rain rate of the third group of rain fields is lower than the average K_s.

Figure 5.67 presents the R_i^2 of the infiltration processes resulted from the three rain fields. All R_i^2 time series are above the reference R^2 line and indicate that the infiltration processes are strongly scaling including the infiltration fields resulted from the lowest rain intensity fields. Figure 5.68 shows the β_i time series of the three scaling infiltration processes. The three time series show similar variations, although the magnitude of the variations is larger in the β_i time series corresponding to the rainfalls with lower average rain rates. The rmse_β_i of the three time series are 0.28 for average rain rate equals 1 cm/hr, 0.09 for average rain rate equals 2 cm/hr, and 0.11 for average rain rate equals 3 cm/hr. The large value from the first case shows that the UM model does not fit the infiltration fields from low rain intensity (lower than K_s) as well as the infiltration fields resulting from high rain intensity.

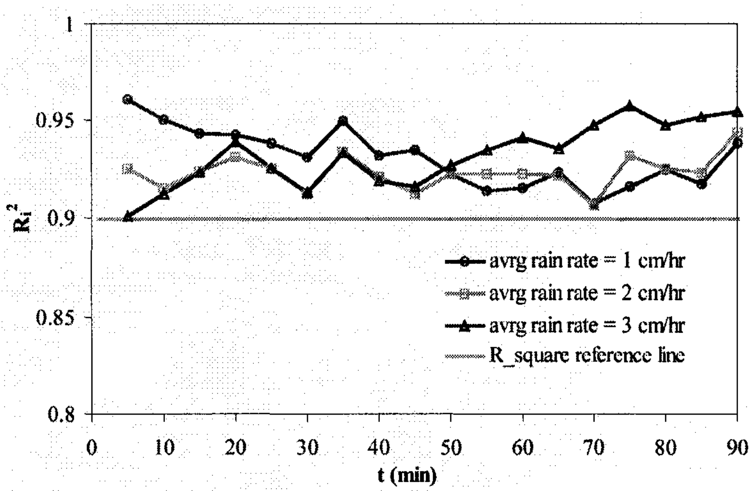

Figure 5.67 Effect of rain intensity on the R_i^2 of the infiltration fields under space-time scaling rain (α_R = 1.2, C_R = 0.2, and H_R = 0.5) and scaling K_s fields (α_{Ks} = 2.0, C_{1Ks} = 0.01, and H_{Ks} = 0.2)

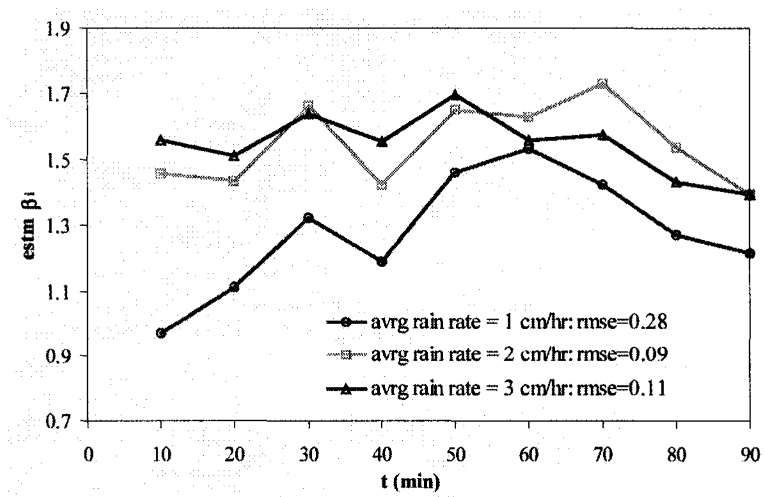

Figure 5.68 Effect of rain intensity on the estimated β_i of the infiltration fields under space-time scaling rain (α_R = 1.2, C_R = 0.2, and H_R = 0.5) and scaling K_s fields (α_{Ks} = 2.0, C_{1Ks} = 0.01, and H_{Ks} = 0.2)

Figure 5.69 displays the estimated scaling parameters of the infiltration processes produced from the three groups of rain fields. It is concluded that the scaling parameters of the infiltration processes from the different rain intensities are comparable. However, higher average rain rates will lead to smoother time series of the infiltration scaling parameters – indicating more stable infiltration fields.

As discussed in Section 5.2.3, the same set of initial soil moisture content values are used for all the experiments in this study. However, it is expected that the choice of initial soil moisture content will have an impact on the scaling behavior of the infiltration

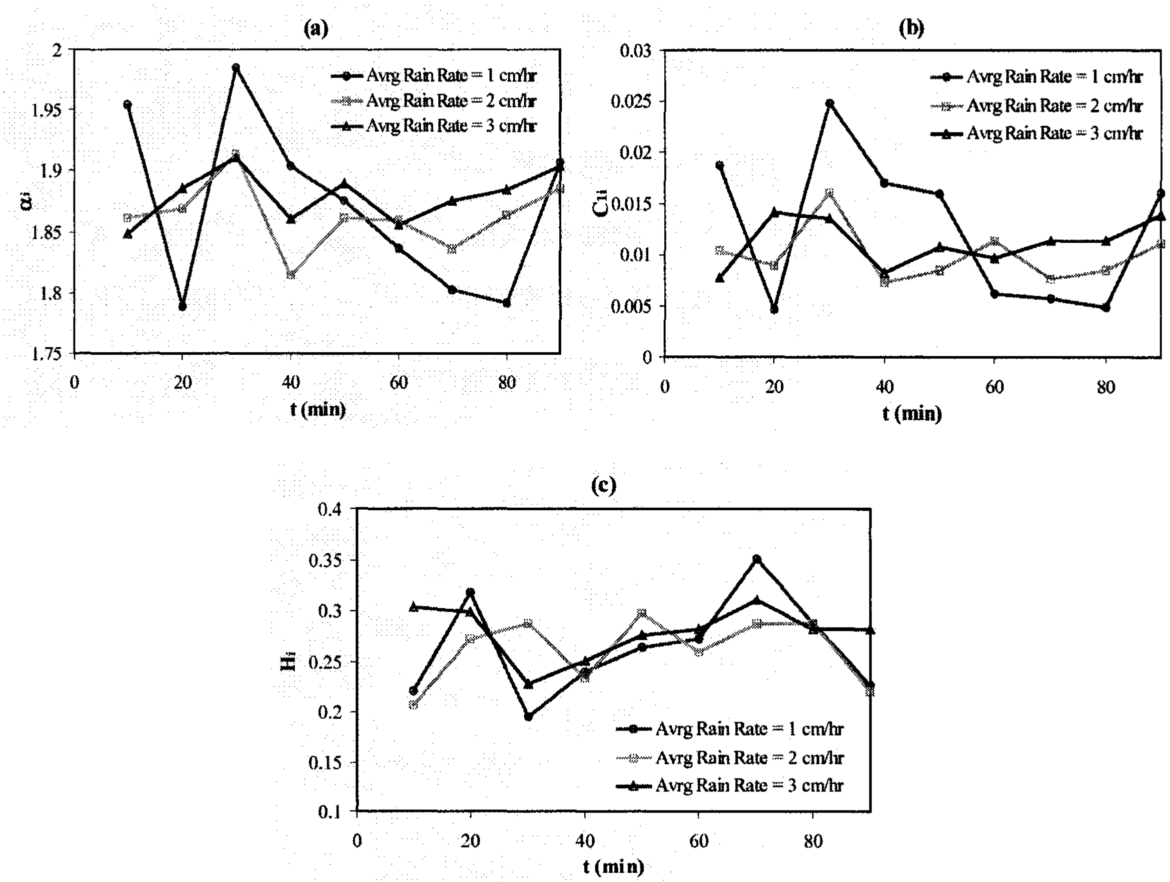

Figure 5.69 Effect of rain intensity on the estimated infiltration parameters (a) α_i, (b) C_{1i}, and (c) H_i, under space-time scaling rain field ($\alpha_R = 1.2$, $C_{1R} = 0.2$, and $H_R = 0.5$) and scaling K_s field ($\alpha_{Ks} = 2.0$, $C_{1Ks} = 0.01$, and $H_{Ks} = 0.2$)

processes. With a set of initial soil moisture content values that are smaller than the set used in this study, rain will be in control of the infiltration field for longer period of time before the influence from soil becomes the dominant factor. It will also take longer time for the infiltration fields to develop to the same stage than the infiltration fields shown in this chapter. For instance, the infiltration field under space-time rain will likely be more singular, less space filling and more homogeneous in a drier field if the rain field has a low degree of heterogeneity (refer to Figure 5.62). If the initial soil moisture contents are higher than what were used in this study, it is predicted that the infiltration field is more developed at the beginning of the rainfall-runoff process than its counterpart infiltration field in this chapter. Hence, the scaling parameters of the infiltration field will start at more advanced points in their respective time series (refer to Figure 5.62). Using the same example as above, a more saturated field under space-time rain will likely be less singular, less sparse, and more heterogeneous if the rain field has a low degree of heterogeneity.

Topography is also expected to have an impact on the infiltration process. For instance, a steep hillside field will receive less infiltration than a flat plane in the same area under the same rainfall due to faster runoff on the hillside. Thus, it is speculated that the infiltration field will be more developed in the latter case. Channels also play a role in the scaling characteristics of infiltration field. Since the infiltration rate in channels tends to be high, channels usually represent singularity in infiltration field. Hence, the infiltration field on a topography with many major channels will likely be more singular than an infiltration field on a more homogenized topography.

Much more work can be devoted to the study of the connections between infiltration and other hydrological fields and processes in the framework of scaling. This research serves as a humble first step in that direction.

Chapter 6

Effects of Multifractal Rainfall and Saturated Hydraulic Conductivity on Surface Runoff and Channel Streamflow

This chapter focuses on the study of surface runoff and channel streamflow in the framework of universal multifractal. Runoff and infiltration are the only two mechanisms in the DIMBRR model available for dispersing water from rainfall. Excess rainfall becomes surface runoff and is routed to its downslope pixels. The water mass eventually feeds to streamflow in the channel network if it is not infiltrated along the way. The runoff field being analyzed in this chapter is the instantaneous flow rate in the form of surface runoff on the overland and streamflow in the channels.

The same K_s fields and steady rain fields are used for the study of runoff as for infiltration in Chapter 5. The analytical tools employed in Chapter 5 are also used in this chapter such as modified R^2 and the methods for estimating scaling parameters.

6.1 Effects of Non-Scaling Rain and Scaling K_s on Runoff

A set of 25 steady non-scaling rain fields is generated as described in Section 5.3.2. The steady rain lasts 500 min. and the DIMBRR model runs for 600 min. Figure 6.1 displays the power spectrums of the runoff fields at a few points in time. The slope and the modified R^2 of the power spectrum (hereafter denoted as R_Q^2) are shown in Figure 6.2. The slope stays negative and the R_Q^2 is above the R^2 threshold throughout the rain period, indicating that the runoff field is strongly scaling during the rainfall. Both the slope and the R_Q^2 time series have an adjusting period of about 60 min. at the beginning of the rainfall-runoff process. They are stable after the period until rainfall stops at 500 min. For about 60 min. after rain stops, R_Q^2 decreases and slope increases and yet they both still meet the scaling criteria. A close examination of the runoff fields reveals that only a handful of major channels still sustain some water at 560 min., and the maximum runoff is less than 0.6 m^3/s. The slope and R_Q^2 time series loose the consistency in their variations after 560 min. and the spectrum becomes smooth and flat – revealing a runoff field that is physically trivial and no longer scaling.

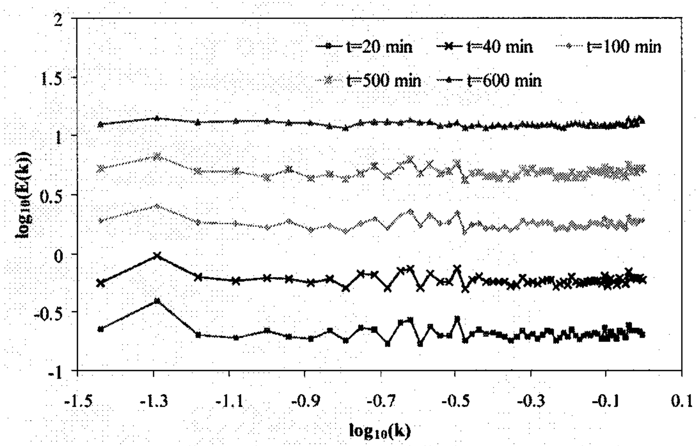

Figure 6.1 Average power spectrums of runoff fields under non-scaling rainfall and scaling K_s field (the lines have been offset for clarity)

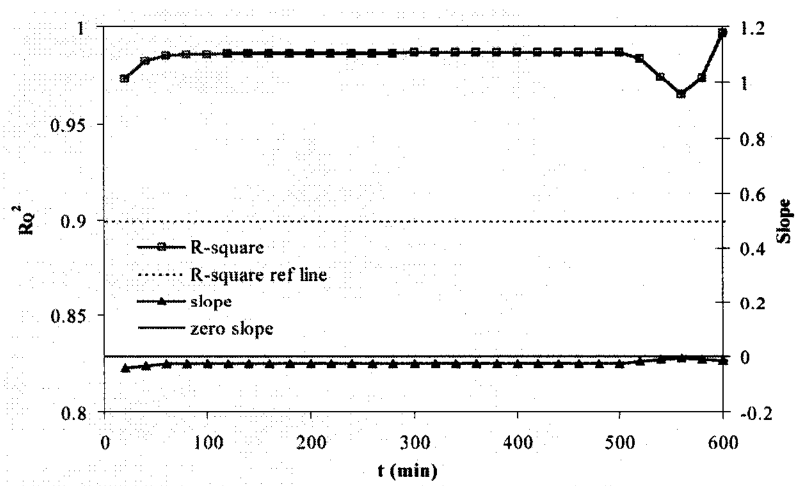

Figure 6.2 Slope and R_Q^2 of the average power spectrums of runoff fields under non-scaling rainfall and scaling K_s field

6.2 Effects of Scaling Rain and Non-Scaling K_s on Runoff

The same lognormal K_s and scaling rain fields are used for this study as for the study on infiltration with non-scaling K_s field (Section 5.3.3). Figure 6.3 shows the power spectrum of the runoff fields, and Figure 6.4 presents the slope and the R_Q^2 time series. Figure 6.4 shows that the slope of the runoff power spectrum stays negative and the R_Q^2 time series is above the R^2 reference line throughout the process, *i.e.* the runoff process is strongly scaling despite a non-scaling K_s field.

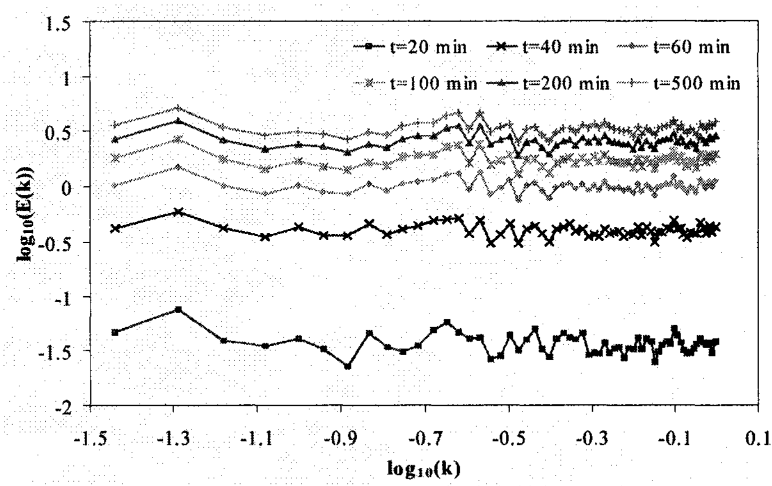

Figure 6.3 Average power spectrums of runoff fields under scaling rainfall and non-scaling K_s field

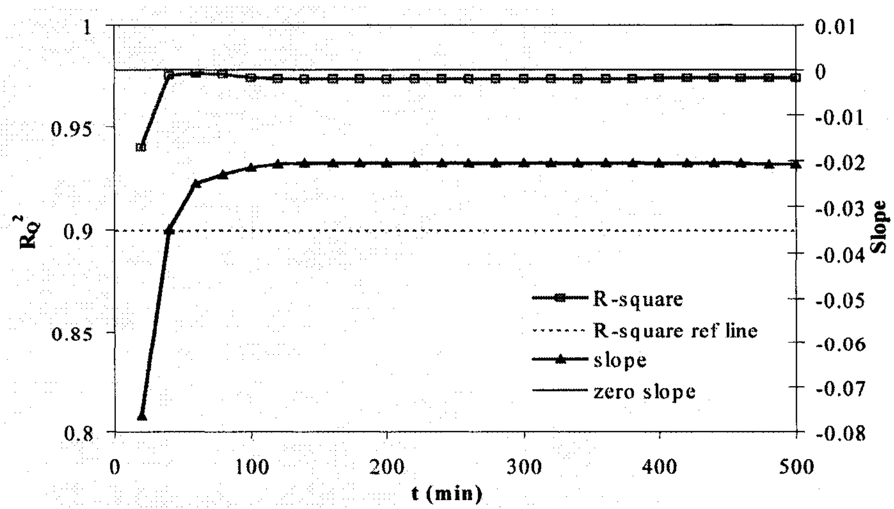

Figure 6.4 Slope and R_Q^2 of the average power spectrums of runoff fields under scaling rainfall and non-scaling K_s field

6.3 Effects of Steady Scaling Rain on Runoff

Steady rainfalls are employed for the analysis of the effect of multifractal rainfall on runoff. The experimental set-ups are basically the same as for the study on infiltration and are briefly reviewed here again. The average rain rate in all the experiments is 3 cm/hr with 150-minute rainfall duration. Scaling K_s fields have an average of 1.32 cm/hr. Ten instead of twenty-five experiments are conducted for each set of combinations of rain scaling parameters because little difference is observed among the experiments.

Analysis performed in this study reveal that the initial estimates of runoff parameter H (hereafter denoted as H_Q) are close to zero in all combinations of rain scaling parameters that are tested. Figure 6.5 shows the initial H_Q time series from some of the rain fields. The experiments performed in Section 3.3.4 demonstrated that the initial H_Q's are greater than the true H_Q's in the majority cases, and the only cases where the initial H_Q's underestimate the true H_Q's are when the latter are large. Thus, the low initial H_Q values

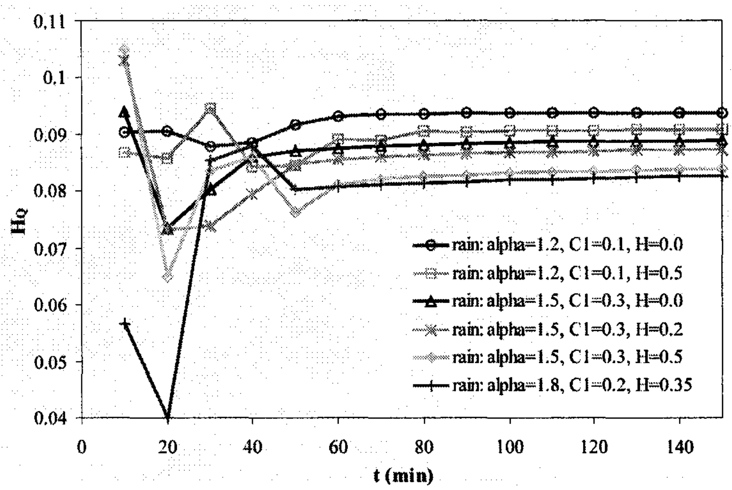

Figure 6.5 Time series of initial estimates of runoff parameter H.

observed in Figure 6.5 indicate low true H_Q of the runoff fields. Since H_Q is small in all the cases regardless of the non-homogeneity of the rainfall and K_s fields applied, all runoff fields are taken as homogeneous, and only α and C_1 of the runoff processes (hereafter denoted as α_Q and C_{1Q}, respectively) will be estimated in the rest of this chapter.

6.3.1 Effects of Rain α

Three sets of rain fields are used for this study. Their parameters are

Set 1: $C_{1R} = 0.1$, $H_R = 0.2$

Set 2: $C_{1R} = 0.2$, $H_R = 0.2$

Set 3: $C_{1R} = 0.2$, $H_R = 0.35$

Parameter α_R values for these sets are 1.2, 1.5, and 1.8. K_s parameters are $\alpha_{Ks} = 2.0$, $C_{1Ks} = 0.01$, and $H_{Ks} = 0.2$. Runoff fields at two different times from one of the experiment are displayed in Figure 6.6. As can be seen in the figures, channel flow dominates the runoff field in magnitude. Since higher values will make more of a contribution to moments than lower values, it is expected that the space-time structures of channel streamflow are the main cause of results obtained from moment based analysis such as the estimation of the UM model parameters.

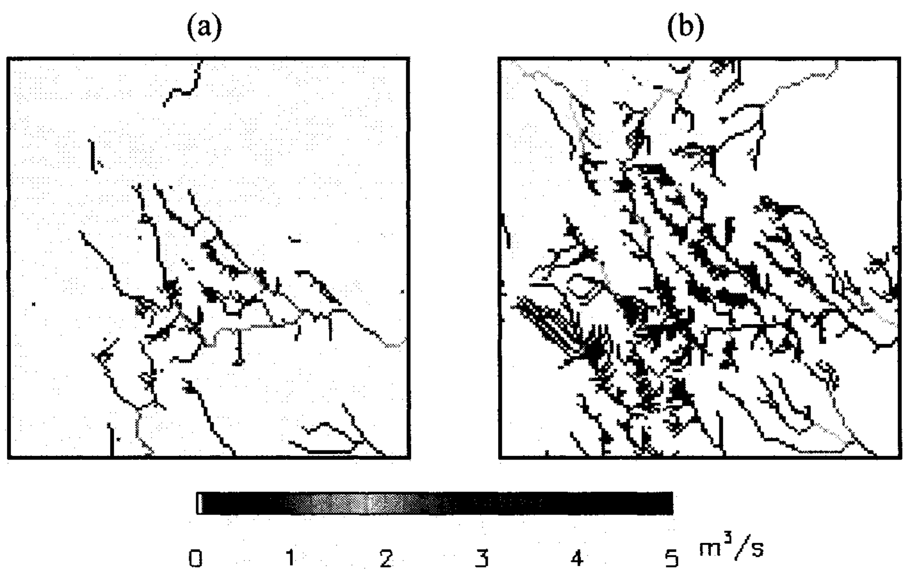

Figure 6.6 Runoff fields at (a) 20 min, and (b) 150 min. after rain starts. The scaling parameters of the steady rain field are $a_R = 1.2$, $C_{1R} = 0.1$, and $H_R = 0.2$, and the scaling parameters of the K_s field are $\alpha_{Ks} = 2.0$, $C_{1Ks} = 0.01$, and $H_{Ks} = 0.2$.

The R_Q^2 time series of the runoff processes from the second set of rain fields are displayed in Figure 6.7. The corresponding estimated β_Q time series are presented in Figure 6.8 along with their respective rmse_β_Q (the RMSE of the β_Q time series). The runoff fields are shown to be strongly scaling in all cases. The rmse_β_Q of the three sets of runoff processes are: 0.07, 0.09, 0.11; 0.05, 0.10, 0.14; and 0.06, 0.11, 0.15, respectively. Judging from the rmse_β_Q values, the runoff fields fit to the UM model reasonably well. Figure 6.9 compares the average hydrographs of the second set of rainfall-runoff events at the outlet of the subwatershed inside the study area (Figure 5.2).

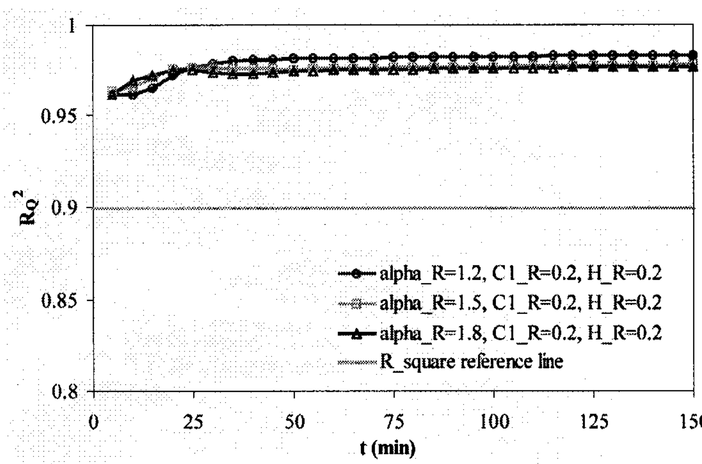

Figure 6.7 Effect of α_R on R_Q^2 of the runoff fields under steady scaling rain and scaling K_s fields (α_{Ks} = 2.0, C_{1Ks} = 0.01, and H_{Ks} = 0.2)

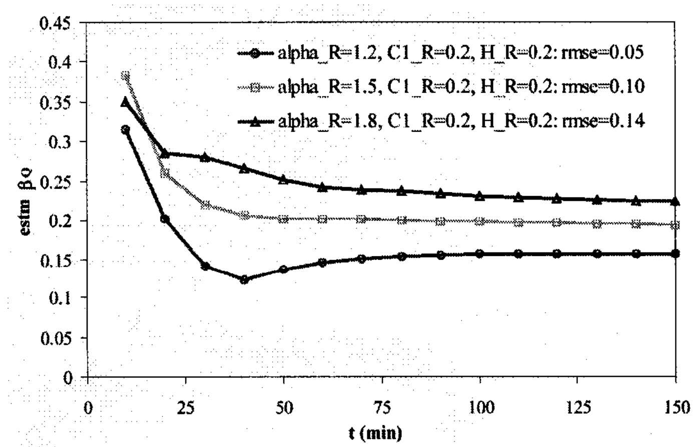

Figure 6.8 Effect of α_R on β_Q of the runoff fields under steady scaling rain and scaling K_s fields (α_{Ks} = 2.0, C_{1Ks} = 0.01, and H_{Ks} = 0.2)

The hydrographs are indicative of the development of the runoff process over the whole study area. As expected, higher α_R leads to larger runoff. All rain fields deposit the same amount of water into the study area because of the equal average rain rate. DIMBRR model assumes that any rainfall water that does not infiltrate will become runoff. It was learned from Chapter 5 that higher α_R corresponds to lower average infiltration (Figure 5.11). Hence, what is shown in Figure 6.9 is an expected result.

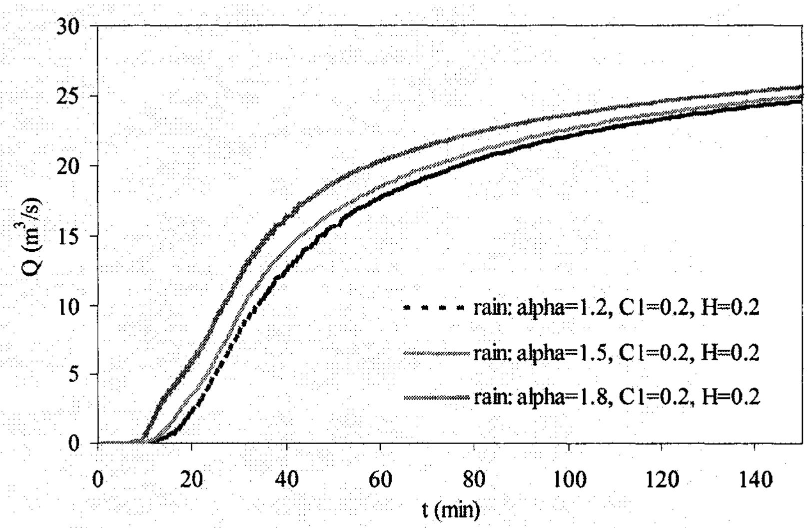

Figure 6.9 Impact of rainfall parameter α_R on average hydrograph

The estimated runoff parameters from the three sets of rain fields are shown in Figures 6.10 and 6.11. The behavior of the parameters is consistent in all three cases. Parameter α_Q appears to decrease monotonically with α_R, *i.e.* strong singularity in rain field translates to weak singularity in runoff field. Another finding from Figure 6.10 is that α_Q increases monotonically with time. Thus, runoff process becomes more singular as it progresses. On the other hand, parameter C_{1Q} is positively correlated with α_R. It has a decreasing trend in time. Thus, large singularity in rain field brings about large sparseness in the mean runoff process while the sparseness decreases as the runoff process develops. Larger α_R also leads to larger runoff.

(a)

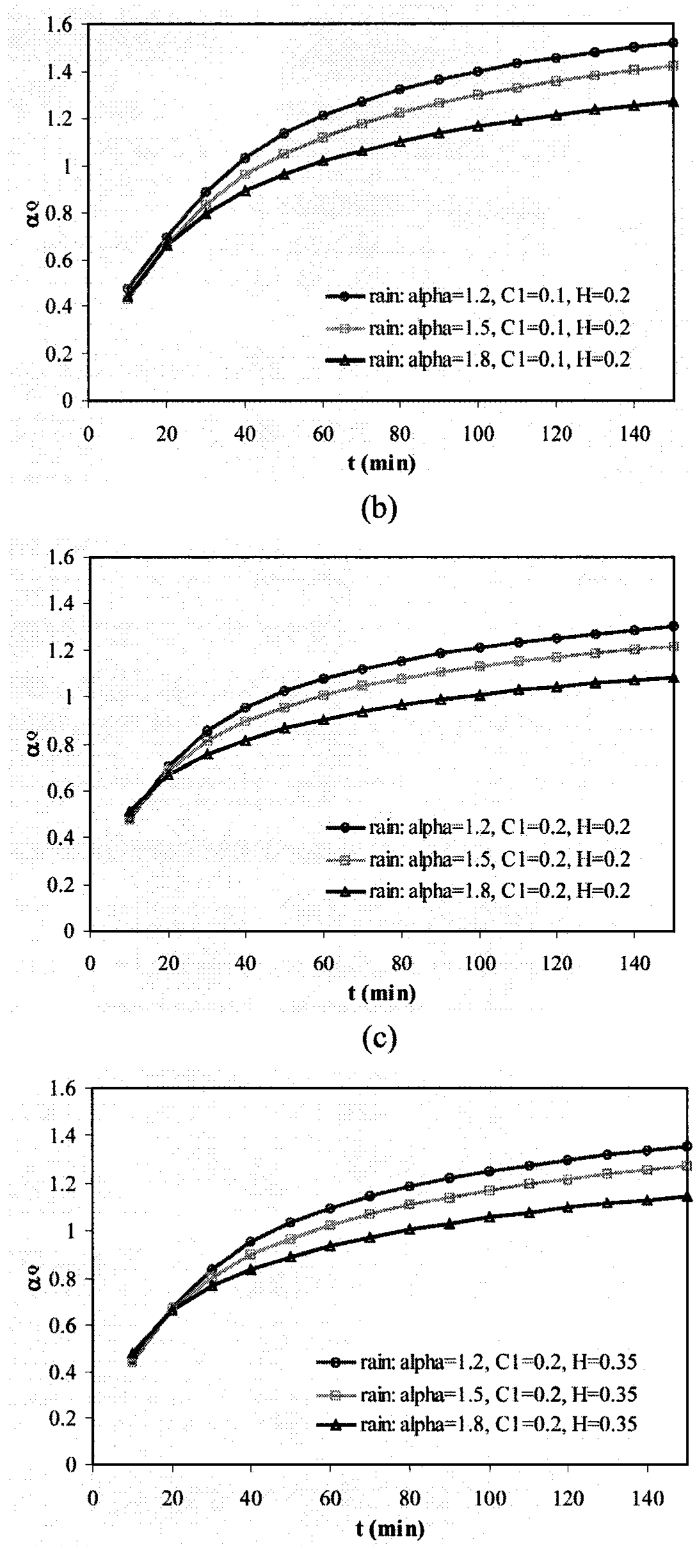

Figure 6.10 Effect of α_R on α_Q under scaling K_s field: $\alpha_{Ks} = 2.0$, $C_{1Ks} = 0.01$, and $H_{Ks} = 0.2$; and steady scaling rain fields with $\alpha_R = 1.2/1.5/1.8$ and (a) $C_{1R} = 0.1$, $H_R = 0.2$; (b) $C_{1R} = 0.2$, $H_R = 0.2$; and (c) $C_{1R} = 0.2$, $H_R = 0.35$.

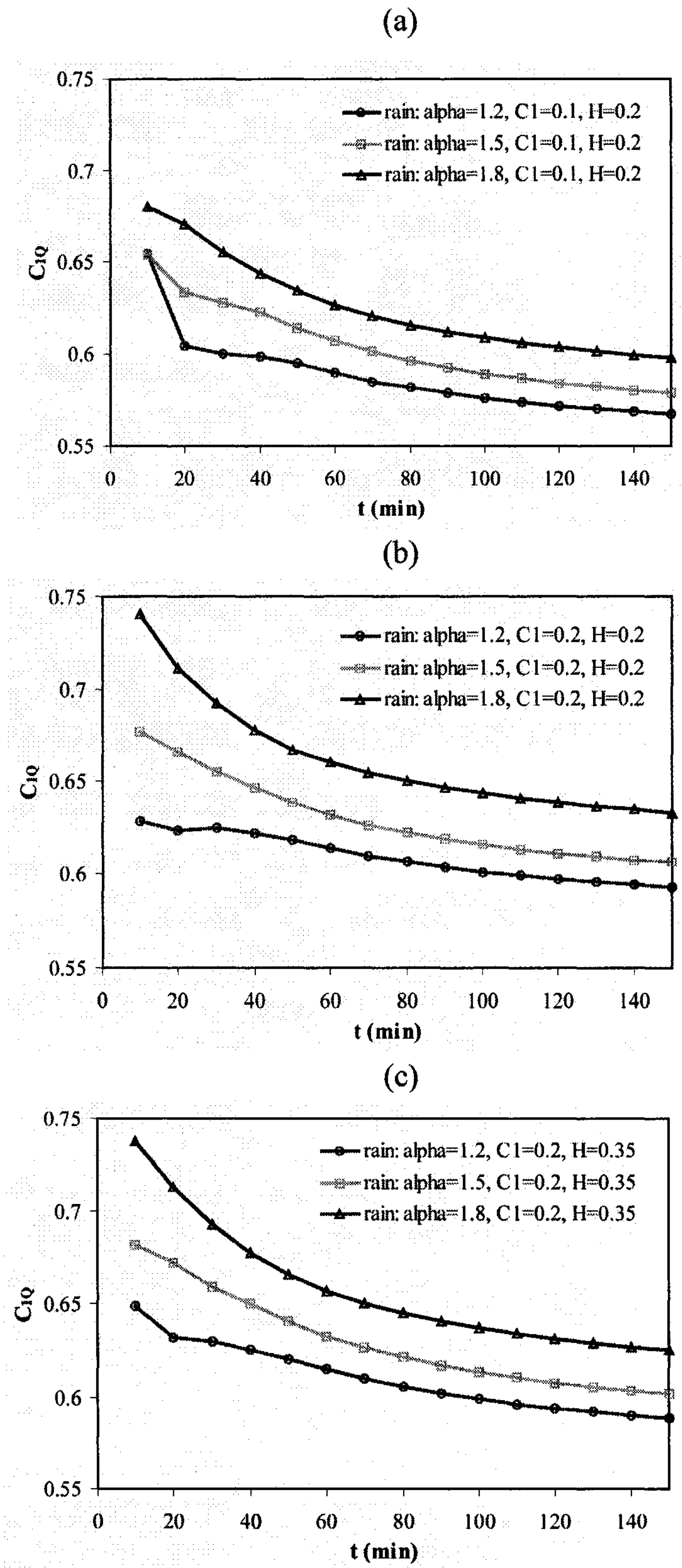

Figure 6.11 Effect of α_R on C_{1Q} under scaling K_s field: $\alpha_{Ks} = 2.0$, $C_{1Ks} = 0.01$, and $H_{Ks} = 0.2$; and steady scaling rain fields with $\alpha_R = 1.2/1.5/1.8$ and (a) $C_{1R} = 0.1$, $H_R = 0.2$; (b) $C_{1R} = 0.2$, $H_R = 0.2$; and (c) $C_{1R} = 0.2$, $H_R = 0.35$.

6.3.2 Effects of Rain C_1

Three sets of experiments are carried out for this study. Rain parameter C_{1R} are 0.1, 0.2, and 0.3 for all sets. The other two parameters are as below.

Set 1: $\alpha = 1.2$, $H = 0.2$

Set 2: $\alpha = 1.2$, $H = 0.35$

Set 3: $\alpha = 1.5$, $H = 0.35$

Since the three sets of experiments have similar results, only one set of experiments is discussed here. Figure 6.12 displays the average hydrographs of the rainfall-runoff events from the first set. As the complement of infiltration (Figure 5.22), runoff shows positive correlation with C_{1R}.

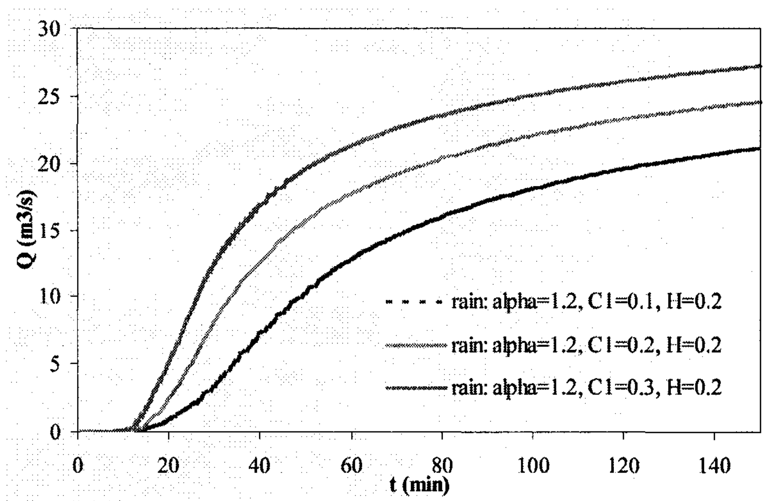

Figure 6.12 Impact of rainfall parameter C_1 on average hydrograph

Without showing the figures, the study on the power spectrums of the runoff processes reveal the following: 1) the runoff fields are strongly scaling in all cases; 2) the runoff fields fit into the UM model reasonably well with the rmse_β_Q for the three sets being 0.07, 0.05, 0.04; 0.08, 0.06, 0.05; and 0.10, 0.11, 0.12, respectively. The estimated scaling parameters of runoff process are shown in Figure 6.13. Parameter α_Q is inversely proportional to C_{1R} while C_{1Q} is positively correlated to C_{1R}, *i.e.* increased sparseness in the mean of the rain field leads to less singularity and more sparseness in the mean of the runoff process. Such change in the rain scaling parameter also corresponds to increased runoff both in flow rate and volume. Parameter α_Q increases and parameter C_{1Q} decreases in time.

(a)

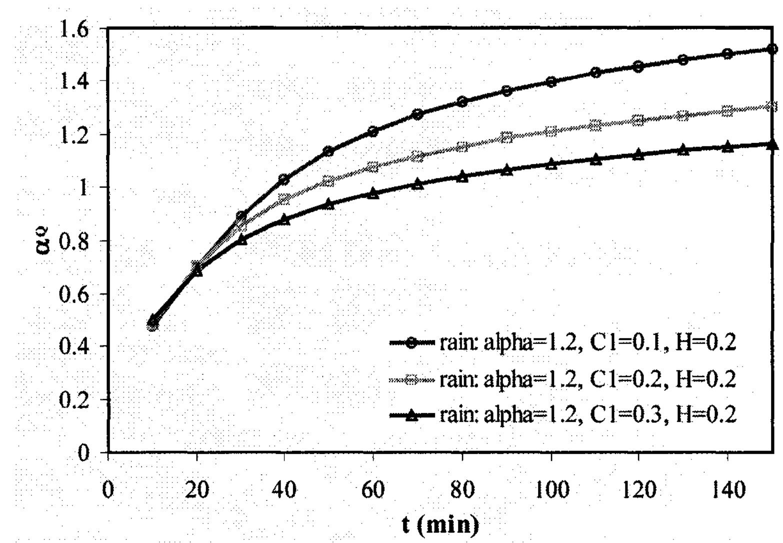

(b)

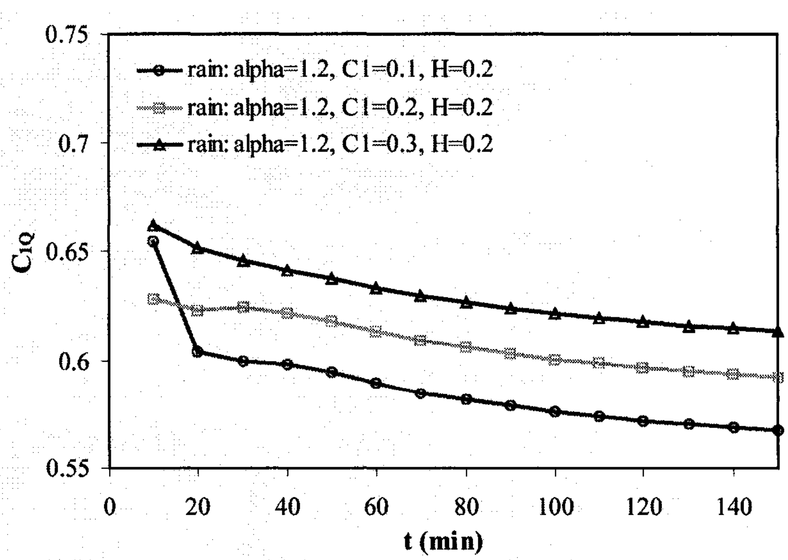

Figure 6.13 Effect of C_{1R} on runoff scaling parameters (a) α_Q, and (b) C_{1Q} under steady scaling rain and scaling K_s fields ($\alpha_{Ks} = 2.0$, $C_{1Ks} = 0.01$, and $H_{Ks} = 0.2$)

6.3.3 Effects of Rain H

Three sets of rain fields are employed for this study. Parameter values for H_R used in all sets are 0.0, 0.2, 0.35, and 0.5. The other two rain parameters are given below.

Set 1: $\alpha = 1.2$, $C_1 = 0.1$

Set 2: $\alpha = 1.5$, $C_1 = 0.1$

Set 3: $\alpha = 1.5$, $C_1 = 0.3$

Figure 6.14 compares the average hydrographs from the rain fields in the third set. The figure shows that larger H_R induces less runoff.

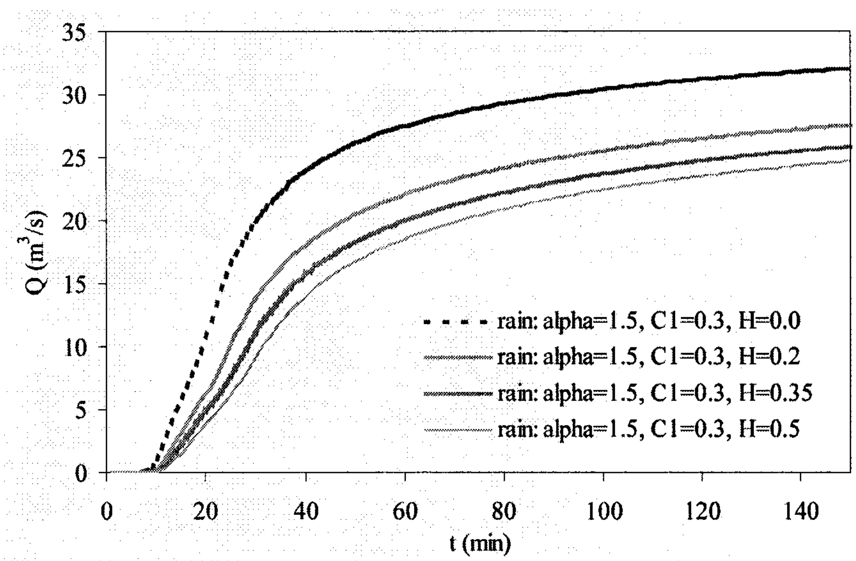

Figure 6.14 Effect of rainfall parameter H_R on average hydrograph

Study of the power spectrums of the runoff process shows (figures are not included) that: 1) the runoff fields from the three sets of rain fields are strongly scaling; and 2) the runoff fields fit into the UM model reasonably well with the following rmse_β_Q: 0.06, 0.07, 0.08, 0.08; 0.08, 0.09, 0.10, 0.09; and 0.08, 0.11, 0.12, 0.13. Figures 6.15 and 6.16 present the estimated runoff parameters from the three sets of rain fields. Figure 6.15 shows that there is a period at the beginning of the runoff process when α_Q is inversely proportional to H_R. After this time period, α_Q becomes positively correlated to H_R. The time when this transition occurs appears to be more of a function of C_{1R} than of α_R. The larger the C_{1R}, the earlier the transition will occur. Parameter α_Q increases monotonically in time. Larger H_R corresponds to more rapid change in α_Q. For the time period tested, H_R has less impact on the infiltration parameters when C_{1R} is small. Parameter C_{1Q} has similar behavior but with a reversed trend for the most part. It increases with H_R early on and decreases with the parameter after some time. The transition time is also mainly dependent of C_{1R}. A monotonically decreasing temporal trend can be seen in C_{1Q}. Larger H_R leads to more rapid change in C_{1Q} in time. Compared to α_R and C_{1R}, H_R clearly has less impact on runoff parameters even though such impact is more complex.

6.4 Effects of Scaling K_s on Runoff

It was demonstrated in Chapter 5 that K_s has a significant impact on surface infiltration. This section is devoted to the study on the influences of K_s field on runoff process. The basic set-ups of the experiments are the same as in the last section, *i.e.* the steady scaling rains have an average rain rate of 3 cm/hr with 150 min. rainfall duration and the following scaling parameters: $\alpha_R = 1.2$, $C_{1R} = 0.2$, and $H_R = 0.3$; average K_s is 1.32 cm/hr; and ten experiments are conducted for each set of combinations of K_s scaling parameters.

6.4.1 Effects of K_s α

Three K_s fields are employed for this study. Parameter α_{Ks} used in all cases are 1.5, 1.75, and 2.0. The other two parameters are $C_{1Ks} = 0.01$, and $H_{Ks} = 0.2$. Figure 6.17 compares the average hydrographs resulting from each K_s field. The figure reveals that α_{Ks} has a positive correlation with runoff especially if α_{Ks} is larger than at least 1.75.

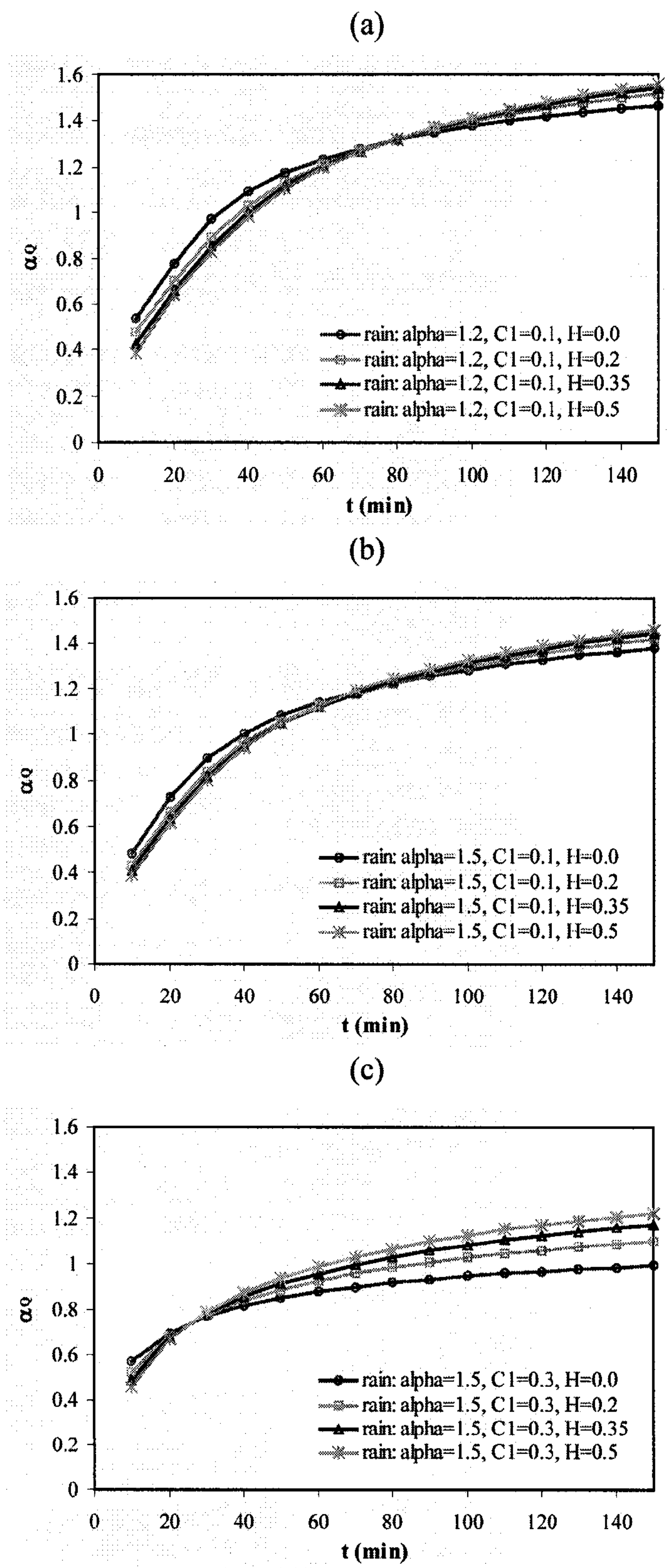

Figure 6.15 Effect of H_R on α_Q under scaling K_s field: $\alpha_{Ks} = 2.0$, $C_{1Ks} = 0.01$, and $H_{Ks} = 0.2$; and steady scaling rain fields with $H_R = 0.0/0.2/0.35/0.5$ and (a) $\alpha_R = 1.2$, $C_{1R} = 0.1$; (b) $\alpha_R = 1.5$, $C_{1R} = 0.1$; and (c) $\alpha_R = 1.5$, $C_{1R} = 0.3$.

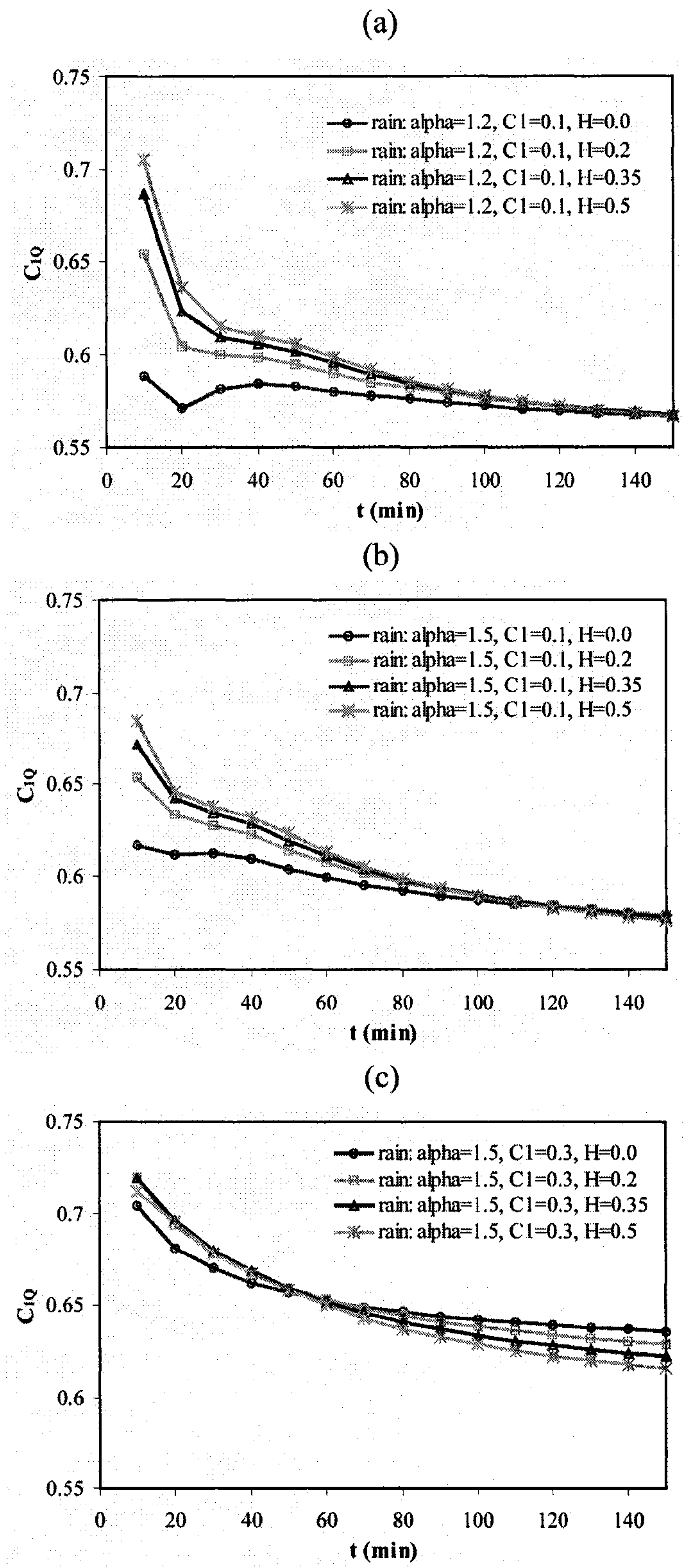

Figure 6.16 Effect of H_R on C_{1Q} under scaling K_s field: $\alpha_{Ks} = 2.0$, $C_{1Ks} = 0.01$, and $H_{Ks} = 0.2$; and steady scaling rain fields with $H_R = 0.0/0.2/0.35/0.5$ and (a) $\alpha_R = 1.2$, $C_{1R} = 0.1$; (b) $\alpha_R = 1.5$, $C_{1R} = 0.1$; and (c) $\alpha_R = 1.5$, $C_{1R} = 0.3$.

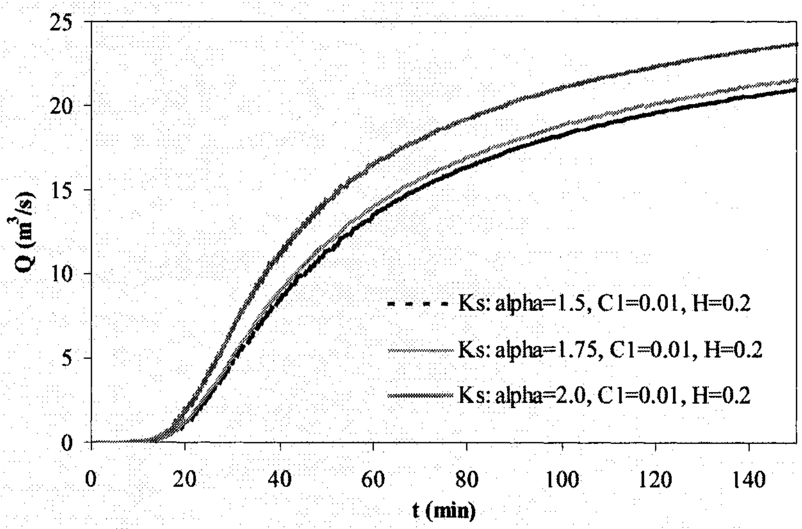

Figure 6.17 Effect of α_{Ks} on average hydrograph

The studies of the power spectrum of the three runoff processes show (figures not included) that: 1) the runoff fields are strongly scaling throughout the processes with R_Q^2 values well above the R^2 reference threshold; and 2) the runoff fields fit to the UM model with the following rmse_β_Q: 0.03, 0.03, and 0.05. Figure 6.18 shows the estimated scaling parameters of the runoff processes. The fact that only larger α_{Ks} has some appreciable effect on runoff also manifests itself in Figure 6.18 (a), the effect of α_{Ks} on α_Q. The two parameters are positively correlated. Compared to the effect of rainfall on runoff (Section 6.3), it is clear that α_{Ks} has a very minor influence on runoff parameters. As in all the other cases shown so far, α_Q has an increasing trend and C_{1Q} has a decreasing trend in time.

6.4.2 Effects of K_s C_1

Three C_{1Ks} are used for this study: 0.01, 0.03, and 0.05. The other two parameters are α_{Ks} = 2.0, and H_{Ks} = 0.2. Figure 6.19 compares the average hydrographs resulted from the three K_s fields. It shows that larger C_{1Ks} leads to larger runoff both in flow rate and volume. Studies of the power spectrums of the runoff processes show (figures not included) that 1) the runoff fields are strongly scaling throughout the processes; and 2) the runoff fields conform to the UM model with the following rmse_β_Q: 0.05, 0.06, and 0.07.

(a)

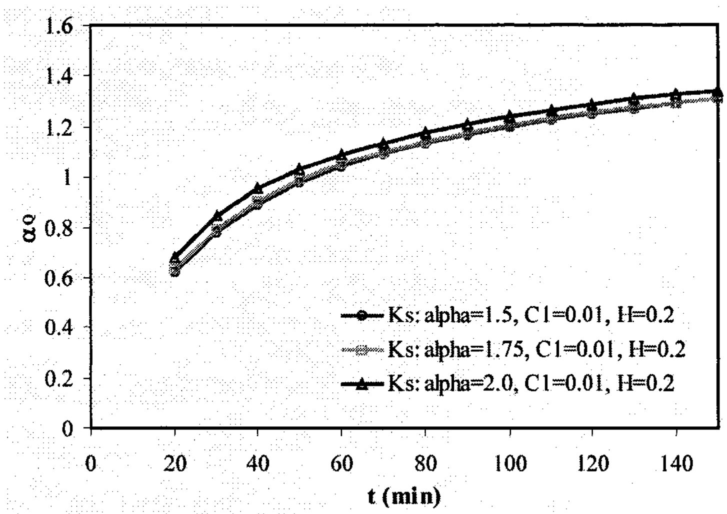

(b)

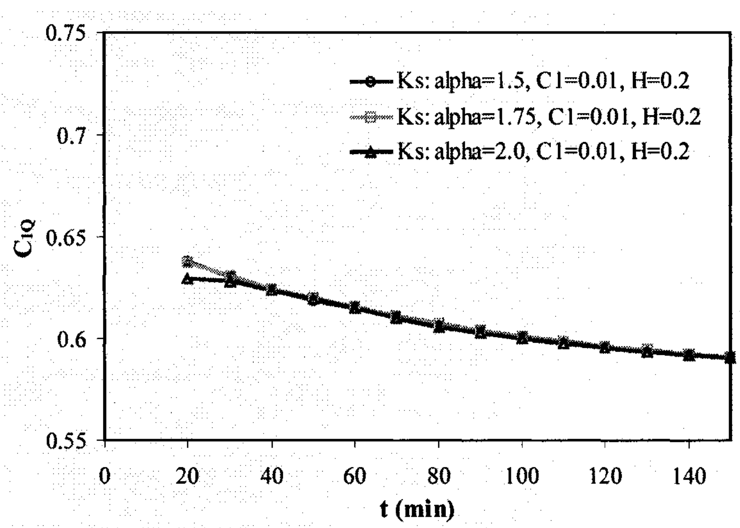

Figure 6.18 Effect of α_{Ks} on (a) α_Q, and (b) C_{1Q} under steady scaling rain field (α_R = 2.0, C_{1R} = 0.01, and H_R = 0.2) and scaling K_s fields

Figure 6.20 presents the estimated runoff parameters from the three K_s fields. Parameter α_Q appears to be positively correlated to α_{Ks}. The impact of α_{Ks} on C_{1Q}, however, is rather weak. The temporal trends in α_Q and C_{1Q} are consistent with previous findings, *i.e.* the former increases in time and the latter decreases in time.

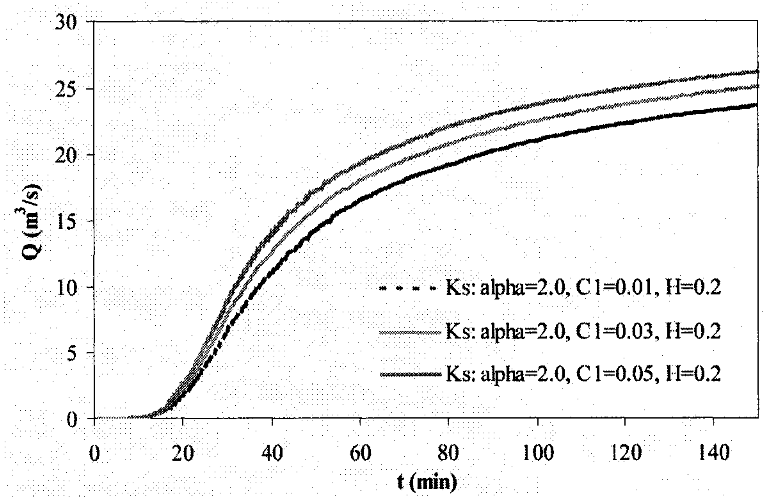

Figure 6.19 Effect of C_{1Ks} on average hydrograph

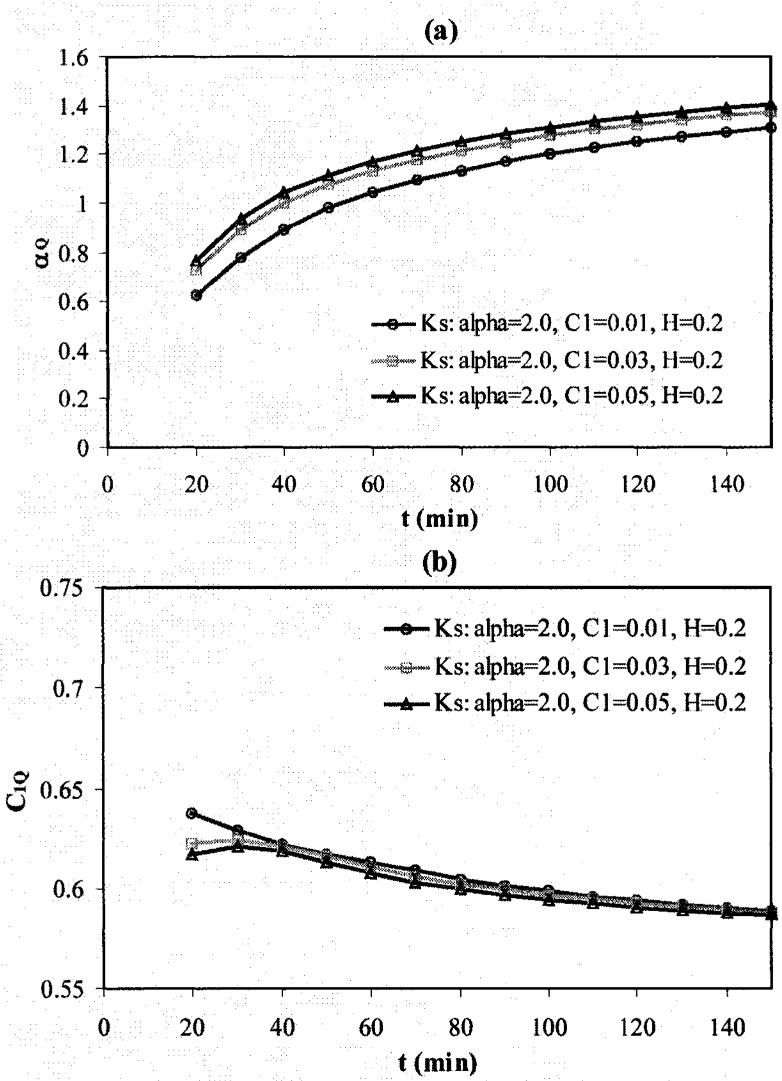

Figure 6.20 Effect of C_{1Ks} on the estimated runoff parameters (a) α_Q, and (b) C_{1Q} under space-time scaling rain field (α_R = 1.2, C_{1R} = 0.2, and H_R = 0.3) and scaling K_s fields.

6.4.3 Effects of K_s H

Four types of K_s fields are examined for this study. They have the common parameters $\alpha_{Ks} = 2.0$, and $C_{1Ks} = 0.01$, and different H_{Ks} with values of 0.0, 0.1, 0.3, and 0.4. Figure 6.21 demonstrates the impact of H_{Ks} on runoff in the form of a hydrograph. Larger H_{Ks} is shown to produce more runoff. However, the effect is rather weak. The runoff power spectrum studies show (figures not included) that: 1) the runoff fields are strongly scaling throughout the processes; and 2) the runoff fields fit to the UM model with the following rmse_β_Q: 0.05, 0.05, 0.05, and 0.06.

Figure 6.22 presents the estimated scaling parameters of runoff processes from the four types of K_s fields. It is concluded from the figure that H_{Ks} has little impact on the scaling parameters of runoff processes.

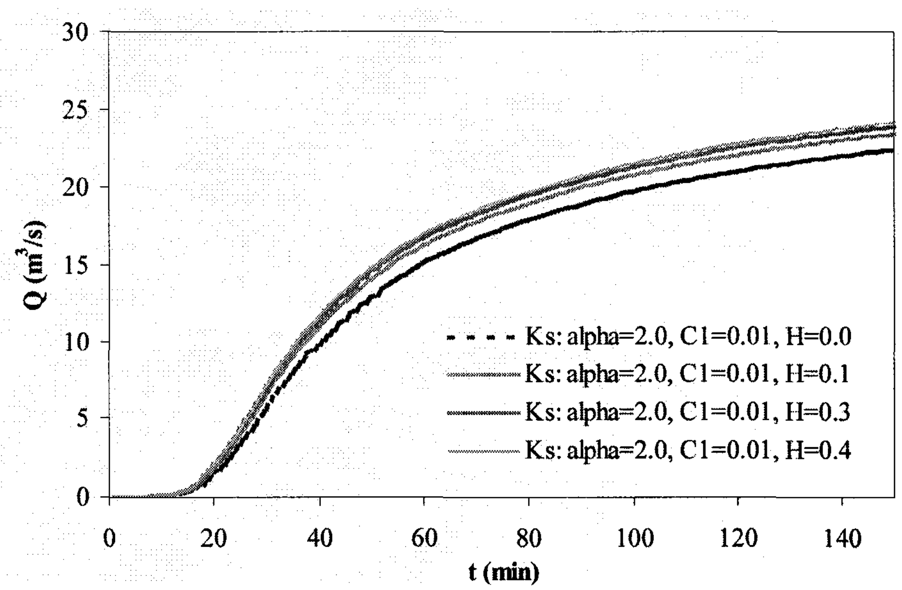

Figure 6.21 Effect of H_{Ks} on average hydrograph

(a)

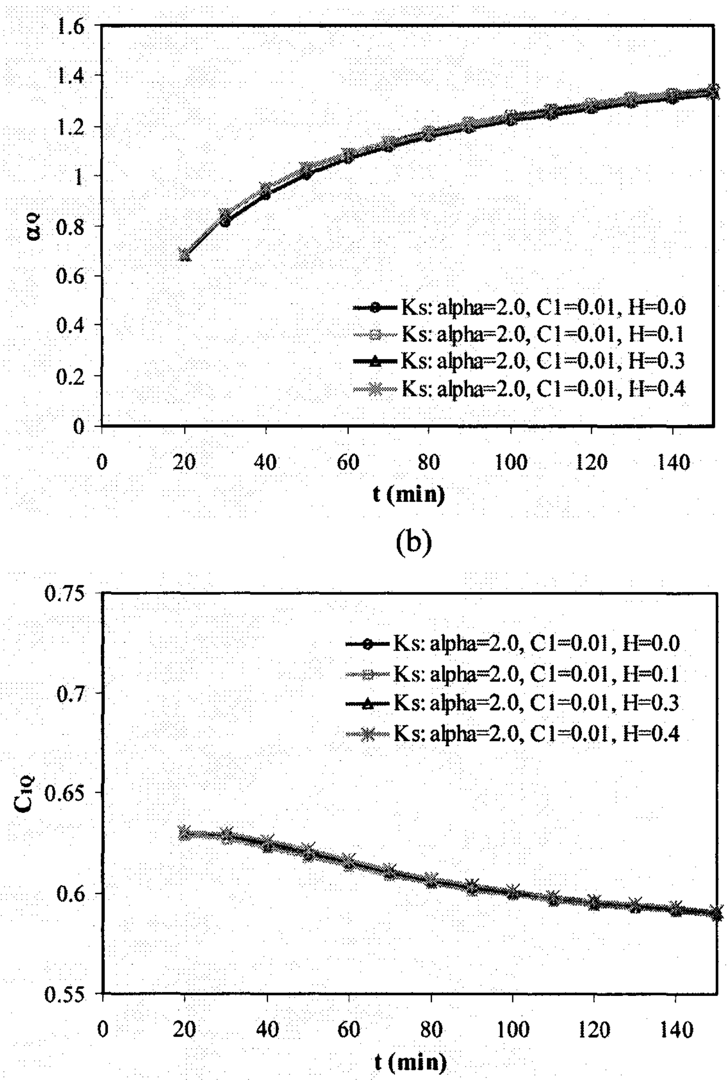

Figure 6.22 Effect of H_{Ks} on the estimated runoff parameters (a) α_Q, and (b) C_{1Q} under space-time scaling rain field (α_R = 1.2, C_{1R} = 0.2, and H_R = 0.3) and scaling K_s fields.

6.5 Scaling of Contributing Area

Since the runoff field is closely related to the contributing area field (a field whose value is the contributing area at each pixel), the scaling properties of the contributing area field are analyzed herein to explore the link between this field and the runoff field.

Figure 6.23 shows the contributing area field of the study area. The power spectrum of the field is displayed in Figure 6.24. The slope of the logarithm of the power spectrum is less than zero and the R^2 is 0.99 – indicating that the contributing area is scaling. Further analysis shows that the initial H parameter is 0.096, *i.e.*, the contributing area is homogeneous or close to homogeneous. The other two UM model parameters are estimated and the result is $\alpha = 1.35$, and $C_1 = 0.54$. These values are comparable to the values of the corresponding runoff parameters after the runoff field is well developed. This finding reveals that the scaling properties of the contributing area field are good indicators of the scaling behavior of the runoff field after it is well developed, *i.e.*, the dominant channel streamflow is established within the channel network.

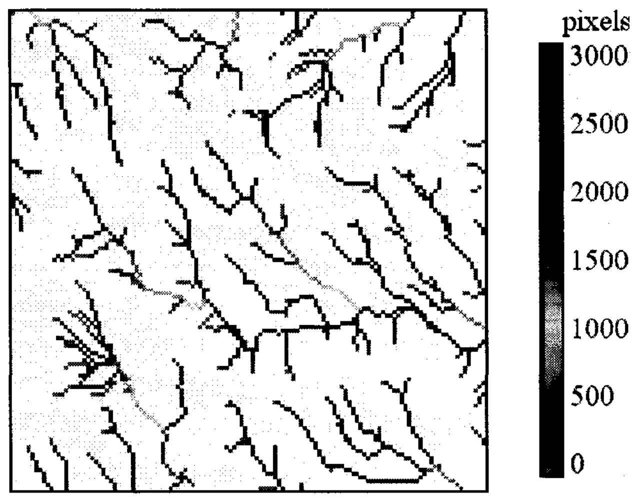

Figure 6.23 Contributing area field of the study area

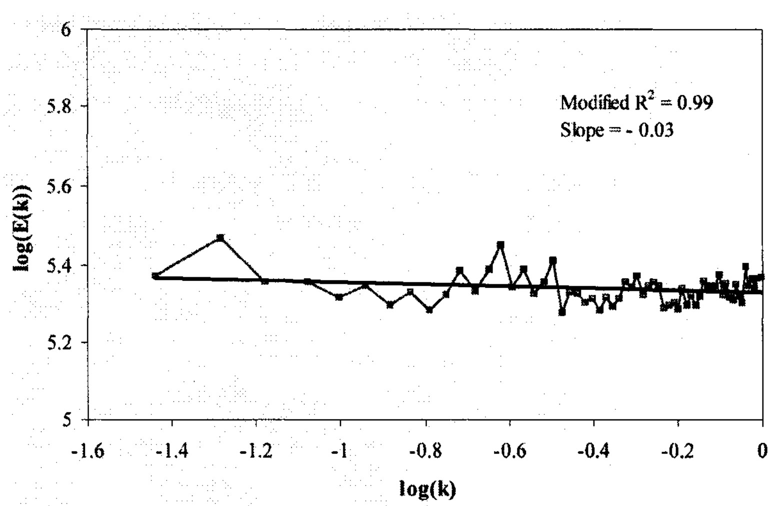

Figure 6.24 Power spectrum of the contributing area field of the study area

In summary, runoff field is homogeneous and scaling after an adjusting period even if rain rate and K_s fields are not scaling. However, the length of the adjusting period is dependant on the rain and K_s fields. The scaling properties of steady rainfall field have much stronger influence on runoff than K_s field does. Runoff parameters α and C_1 tend to change in opposite directions, both in their variations with the scaling parameters of rain and K_s, and in their temporal trends. This means that a runoff process always becomes more singular and yet more space filling in time; this is shown clearly in Figure 6.6. Finally, the scaling properties of the contributing area and the well-developed runoff field are closely related. Chapter 7 includes a more in-depth review of the findings from this chapter.

For a field that is drier than what was used in this research, there will be more infiltration hence less rainfall excess for runoff, leading to a longer time for streamflow to develop in the channels. Therefore, the time it takes for the runoff field to become scaling is expected to be longer than the corresponding runoff field in this study. Moreover, the scaling parameters of the runoff field in the drier case are likely to start at an early point in their respective temporal trends (for example, refer to Figures 6.10 and 6.11), that is, the runoff field will be less singular and less space filling in a drier field than a wetter one. For a field that has higher initial soil moisture content values than what were used in this study, the reverse conclusions from the drier case can be expected. The runoff field will become scaling faster and is more singular and less sparse than in the latter case.

Section 6.5 shows that runoff field is also under strong influence of topography. Besides the effect of contributing area (determined by topography) on runoff, channel network also plays an important role in determining the scaling properties of runoff field.

Channels are not only responsible for the upward temporal trend in the singularity of runoff field, but also for the large sparseness observed in runoff fields in this chapter. Thus it is speculated that a topography with distinguished channels will lead to runoff fields that are more singular and sparser than a runoff field on a more homogenized field. Another example of the possible effect of topography on runoff is that a steeper field will result in more runoff, yielding a more developed runoff field that becomes scaling earlier and is more singular and less sparse.

The above discussions touch on just two important watershed properties that could have strong influences on runoff field, but which were not included herein. More thorough studies on the effect of various fields and processes on runoff could be interesting topics for future research.

Chapter 7

SUMMARY AND CONCLUSIONS

The stated objective of this research is to study the space-time properties of surface infiltration and runoff and the effect of rainfall and saturated hydraulic conductivity (K_s) on these watershed processes within the framework of universal multifractal model. There are two core components of this study: 1) models for generating rainfall and K_s fields, which act as driving forces to watershed processes; 2) a rainfall-runoff model to derive space-time infiltration and runoff processes, which are the watershed responses to the driving forces.

A universal multifractal (UM) model (Chapter 3) is chosen for the generation of multifractal rainfall and K_s fields. This model completely characterizes a multifractal field using only three parameters (α, C_1, and H). By varying the three parameters within their respective ranges, which are predefined based on physical considerations, rainfall and hydraulic conductivity fields with various characteristics are obtained. After an introduction to the UM model, a detailed analysis is conducted in this chapter to define the criteria for scaling field in general, and for fitting the UM model in particular. The criteria are based on the radial power spectrum of the field being examined. Specifically, a field has to have linear log-power spectrum with negative regression angle for it to be a scaling field. The linearity is measured by a modified R^2 value of the power spectrum. The criteria for a field to fit to the UM model are the agreement between the (negative) regression angle of the power spectrum and its theoretical prediction obtained from the three UM model parameters (In reality, the theoretical prediction of β is also an estimate itself because it is computed from the estimated UM model parameters (Section 5.3.4.1). The double trace moment technique is employed in this study to estimate the UM model parameters of a conservative (or homogeneous) field. An approach was developed in this study for more accurately estimating the parameters of non-conservative (or non-homogeneous) fields. It was found that if the underlying conservative field of a non-conservative field is derived by fractional differentiation of order H, where H is initially determined in this study using structure function, then parameter α of the conservative field is highly sensitive to the value of H when the H estimate falls into a very narrow range that encloses the true H. This finding was taken advantage of, and a trial-and-error approach was taken to find more accurate values of the three parameters of a non-conservative field. The estimation approaches are evaluated in the last part of Chapter 3, and it is concluded from the results that the UM model parameters of conservative fields can be reproduced and estimated with significant accuracy. Additionally, the approach developed in Chapter 3 can estimate the UM model parameters of the non-conservative fields that are in either good or excellent agreement with the true parameters.

The second component of this research, a physically based, distributed rainfall-runoff model, named DIMBRR model, was developed in Chapter 4. This model employs the D-infinity model to determine flow path at each pixel. A routing hierarchy is then defined throughout all the pixels of the watershed under study. A model that can handle variable rainfall intensity is used to compute ponding time. Infiltration is calculated using the Green-Ampt model. The kinematic wave model is used to route Hortonian runoff and channel flow. Finally, an implicit finite difference scheme is applied for solving all the relevant equations numerically. As a fully distributed model, it can handle input rainfall, soil parameters, and other watershed properties that vary in space and/or time down to pixel scale (in this case, 30 m^2). DIMBRR model was first verified against theoretical solutions for idealized overland plane with satisfactory results. It was then calibrated using rainfall and channel streamflow data collected from USDA-ARS Walnut Gulch experimental watershed. A sensitivity study was carried out to identify the most significant parameters in terms of their sensitivities to runoff volume, peak flow, and time to peak flow (in order of significance). Two variables, porosity and K_s, were chosen as calibration parameters based on the results of the sensitivity analysis. A set of porosity and hydraulic conductivity values were first determined from soil textures and vegetation conditions recorded at the watershed. Retaining the relative magnitudes of the values in the sub-regions within the watershed, two multipliers are applied to porosity and $K_{s,}$ respectively, throughout the watershed during calibration. By systematically varying the multipliers within their practical ranges, a pair of multipliers was found to be able to reasonably reproduce the runoff volume, peak flow, and time to peak flow of five rainfall-runoff events used for calibration. The duel multipliers were then applied to nine rainfall-runoff events from the same watershed for verification. The final results indicate that DIMBRR model is an acceptable rainfall-runoff model to use for the study on the effects of rainfall and K_s on watershed processes.

Chapter 5 is devoted to the study on surface infiltration. Rainfall and K_s fields with various characteristics are generated and inputted to the DIMBRR model to produce space-time infiltration processes. The scaling properties of the infiltration processes are then analyzed to find the impact from the input fields. Non-scaling rainfall and hydraulic conductivity fields were first tested for their general influences on infiltration. The experiments were then followed by an in-depth analysis of the effect of scaling input fields on infiltration. Two types of scaling rain fields are applied in this study: steady rain, and space-time rain. In both cases, a quasi-Monte Carlo technique was used where a series of experiments were conducted for every combination of rain and K_s parameters and the average values were used for examination. Various analyses were carried out on the experiment results such as traditional statistics, power spectrum, and scaling analysis in terms of the three scaling parameters. The effect of rainfall field on infiltration was broken down to three parts: the impact of rain α, C_1, and H. The same approach was taken for the study on the effect of K_s. The space-time rain fields were created from large-size steady rainfall fields, which are essentially steady rain fields with advection. The quasi-Monte Carlo approach was also taken in this part of the study. Similar analyses were performed for the infiltration data as in the case of steady rainfall.

Chapter 6 reported the research on the effect of steady rainfall and K_s on surface runoff and channel streamflow. By design, infiltration and runoff are the only two mechanisms in the DIMBRR model that disperse water from rainfall. Rainfall in excess of infiltration becomes surface runoff and eventually feeds into streamflow in the channel network. The runoff field being analyzed in this study is the instantaneous flow rate in the form of surface runoff overland and streamflow in the channels. Similar to the work on infiltration, non-scaling rainfall and K_s fields were analyzed first, followed by more detailed study on the effect of scaling rainfall and K_s fields on runoff. The analytical tools used for examining infiltration fields were also applied to the runoff processes.

The analyses performed on infiltration and runoff processes yielded some interesting results. The conclusions from the study on infiltration are given below, followed by the conclusions about runoff. Unless otherwise noted, the conclusions apply to both steady rain and space-time rain.

1. As a result of the complex interactions of the underlying processes of watershed, surface infiltration rate shows the effects of the scaling properties of both rain and soil.
2. If rain field is non-scaling, but K_s field is scaling, the infiltration process will eventually become scaling. The infiltration field becomes non-scaling after rain stops.
3. If K_s field is non-scaling, infiltration process will be non-scaling for the most part even if the rainfall field is scaling.
4. The infiltration processes are found to be either strongly scaling or weakly scaling for all the experiments where both rain fields and K_s fields are scaling.
5. The heterogeneity of rain, H_R, is the most important rain parameter to determine the strongly or weakly scaling nature of the infiltration field. More homogeneous steady rain and more heterogeneous space-time rain tend to produce stronger scaling behavior in infiltration.
6. The UM model can be fitted to the majority of the infiltration processes with a high degree of agreement. The largest fitting error stems from homogeneous or close to homogeneous steady rain and from one of the following possible causes

in the case of space-time rain: large rain singularity, small K_s singularity, large K_s heterogeneity, or homogeneous K_s field.

7. Less singular and less sparse scaling rain field lead to more field average infiltration. Larger heterogeneity from steady rain field and from space-time rain field in the later part of the infiltration process also give rise to more field average infiltration. The added rain dynamics in the space-time rain causes the inverse correlation between field average infiltration and rain heterogeneity in a certain period of time in the early stage of the infiltration process.
8. Among the three rainfall parameters, rain heterogeneity has the strongest influence on the infiltration scaling parameters. Away from a small range in the vicinity of $H_R = 0$ (homogeneous rain), more heterogeneous (*i.e.* less homogeneous) rain field leads to more heterogeneous, less singular, and more space-filling infiltration field.
9. Homogeneous and close-to-homogeneous rain fields form a special class of rain, which is responsible for different (usually just the opposite) behavior of infiltration scaling parameters from non-homogeneous rain in their variations with the rain field parameters.
10. Homogeneous space-time rain did not produce homogeneous infiltration fields in the cases examined.
11. Because of the dynamics of the space-time rainfalls, infiltration field has some different characteristics from the case of steady rainfall. One such example is the clear temporal trends manifested in the infiltration parameters in the space-time rainfall cases. The trends are largely missing under steady rainfall. The

directions of the trends are determined by rain heterogeneity. With more homogeneous rain ($H_R < 0.3$), both the singularity and the sparseness of the infiltration field decrease and the degree of heterogeneity of the infiltration field increases in time. As the rain heterogeneity increases, the above trends in the singularity and the sparseness of infiltration field reverse even though the infiltration heterogeneity does not have clear temporal trend in this case.

12. The degree of heterogeneity is the most important K_s parameter to determine the strongly or weakly scaling nature of the infiltration field. Less heterogeneous K_s field will lead to stronger scaling behavior in infiltration.
13. Less singular and less sparse K_s field leads to more field average infiltration while H_{Ks} essentially has no effect.
14. Under steady rain, large K_s singularity has the most significant influence on the infiltration field. Large singularity in the K_s field will induce large singularity and sparseness and more homogeneity in the infiltration field.
15. Under space-time rain, the singularity of K_s has a positive and progressively stronger influence on the singularity of infiltration while the sparseness of K_s shows a positive and strong impact on the sparseness of infiltration.
16. Homogeneous K_s field did not produce homogeneous infiltration field in the cases examined.
17. Homogeneous K_s field is also a special case mainly with steady rainfall. The scaling parameters of infiltration field from homogeneous K_s field and its vicinity behave differently from non-homogeneous K_s fields.

18. The singularity and the sparseness of infiltration field usually have the same changing trend while the heterogeneity of infiltration field changes in the opposite direction. This means that if an infiltration field becomes less singular in time, it most likely also becomes less sparse (or more space-filling) and more heterogeneous, and *vice versa*. This finding reveals the internal connections among the scaling parameters of infiltration process.
19. Rain fields with the same scaling parameters but different average rain rates will lead to infiltration processes that are scaling and comparable in their scaling parameters. However, high intensity rains will produce more stable infiltration fields and thus smoother time series of the infiltration scaling parameters than weak rain fields do.
20. Surface runoff field is strongly scaling and homogeneous ($H_Q = 0$) after an adjusting period even if rain rate and K_s fields are not scaling. However, the length of the adjusting period is dependant on the rain and K_s fields. Hence the runoff field might not become scaling if the adjusting period is longer than the duration of the rain.
21. If a runoff field becomes scaling before rain ends, it will still be scaling for a certain period of time after rain stops.
22. Channel streamflow dominates surface runoff field and is thus expected to be mostly responsible for conclusions about runoff process.
23. The scaling properties of the contributing area field are good indicators of the scaling properties of the well-developed runoff field.

24. As the complement of infiltration, runoff shows some opposite behavior from that of infiltration. One example is that more singular, sparser, and/or more homogeneous steady rain field lead to more runoff.
25. The scaling properties of steady rainfall field have strong influence on runoff process. Runoff singularity decreases with rain singularity and rain sparseness, and runoff sparseness increases with the two rain properties. A transition phase exists for the singularity and the sparseness of runoff in their variations with rain heterogeneity. The singularity of runoff decreases and the sparseness of runoff increases with the rain heterogeneity before the transition phase, and the changing trends reverse after the transition phase. The sparseness of rain appears to be mostly responsible for when the transition occurs.
26. Under steady rainfall, more runoff results from more singular, sparser, and/or more heterogeneous K_s field.
27. The scaling properties of runoff processes receive minor impact from K_s field compared to rainfall field, especially in its sparseness. The singularity of runoff field increases slightly with the singularity and sparseness of K_s field.
28. Contrary to infiltration field, whose singularity and sparseness have the same changing trend, the singularity and sparseness of a runoff field tend to change in the opposite directions both in their variations with the scaling parameters of rain and K_s and in their temporal trends. The singularity of a runoff field always increases in time while its sparseness constantly decreases.
29. By definition, a scaling process is scale invariant. Therefore, the above conclusions regarding the scaling infiltration and runoff processes can be applied

to a range of scales, although more work is needed to define the ranges quantitatively.

REFERENCES

ASCE Task Committee on Geostatistical Techniques in Geohydrology of the Ground Water Hydrology Committee of the ASCE Hydraulics Division, Review of geostatistics in geohydrology, I: basic concepts, *J. of Hydraulic Eng.*, 116, 612-632, 1990.

Broadbridge, P., and I. White, Time-to-ponding: Comparison of analytic, quasi-analytic and approximate predictions, *Water Resour. Res.*, 23, 2302-2310, 1987.

Canton, Y., F. Domingo, A. Sole-Benet, J. Puigdefabregas, Influence of soil-surface types on the overall runoff of the Tabernas badlands (south-east Spain): field data and model approaches, *Hydrol. Process.*, 16, 2621 – 2643, 2002.

Chambers, J.M., C.L. Mallows, and B.W. Stuck, A method for simulating stable random variables, *Journal of the American Statistical Association*, 71, 340, 1976.

Chow, V.T., D.R. Maidment, and L. W. Mays, *Applied Hydrology*, McGraw-Hill, New York, 1988.

Costa-Cabral, M., and S. J. Burges, Digital elevation model networks (DEMON): A model of flow over hillslopes for computation of contributing and dispersal areas, *Water Resour. Res.*, 30, 1681-1692, 1994.

Dagan, G., and E. Bresler, Unsaturated flow in spatially variable fields 1. derivative of models of infiltration and redistribution, *Water Resour. Res.*, 19, 413-420, 1983.

Eagleson, P. S., *Dynamic Hydrology*, McGraw-Hill, New York, 1970.

Falco, T., F. Francis, S. Lovejoy, D. Schertzer, B. Kerman, and M. Drinkwater, Universal multifractal scaling of synthetic aperture radar images of sea-ice, *IEEE Trans. Geosci. and Remote Sensing*, 34, 906 – 914, 1996.

Feder, J., *Fractals*, Plenum Press, New York, 1988.

Feller, W., *An Introduction to Probability Theory and its Applications*, 2nd Ed., John Wiley & Sons, New York, 1971.

Freeman, T. G., Calculating catchment area with divergent flow based on a regular grid, *Comput. Geosci.*, 17, 413-422, 1991.

Goodrich, D.C., *Basin Scale and Runoff Model Complexity*, Technical Report No. HWR 91-010, June 1990.

Govindaraju, R.S., R. Morbidelli, C. Corradini, Areal infiltration modeling over soils with spatially correlated hydraulic conductivities, *J. Hydrol. Eng.*, 6, 150 – 158, 2001.

Grassberger, P., Generalized dimensions of strange attractors, *Phys. Lett.*, 97A, 227-230, 1983.

Green, T., R.H. Erskine, A. Martinez, M.R. Murphy, L. Ahuja, J.D. Salas, and J.A. Ramirez, Spatial crop yield and soil water content: measurement, scaling and topographic analyses, *Proc. Intl. Congress on Modelling and Simulation, MODSIM 2001*, Ghassemi, F. (ed.), 7-11 Dec. 2001.

Gupta, V.K., S.L. Castro, T.M. Over, On scaling exponents of spatial peak flows from rainfall and river network geometry, *Fractals, Scaling and Nonlinear Variability in Hydrology*, 81 – 104, 1996.

Gupta, V.K., D.R. Dawdy, Physical interpretations of regional variations in the scaling exponents of flood quantiles, *Scale Issues in Hydrological/Environmental Modelling*, 347 – 361, 1995.

Gupta, V.K., and E.C. Waymire, Multiscaling properties of spatial rainfall and river

distributions, *J. Geophys. Res.*, 95(D3), 1999-2009, 1990.
—, and —, A statistical analysis of mesoscale rainfall as a random cascade, *J. Appl. Meteorol.*, 32, 251-267, 1993.
Harris, D., M. Menabde, A. Seed, G. Austin, Multifractal characterization of rain fields with a strong orographic influence, *J. Geophy. Res.*, 101, 26405-26414, 1996.
Hentschel, H. G. E., and I. Procaccia, The infinite number of generalized dimensions of fractals and strange attractors, *Physica*, 8D, 435-444, 1983.
James, W.P., and K.W. Kim, a distributed dynamic watershed model, *Water Resour. Bulletin*, 26, 587-596, 1990.
Joel, A, I. Messing, O. Seguel, M. Casanova, Measurement of surface water runoff from plots of two different sizes, *Hydrol. Process.*, 16, 1467 – 1478, 2002.
Kolmogorov, A. N., The local structure of turbulence in incompressible viscous fluid for very large Reynolds numbers., *C. R. Russ. Acad. Sci.*, 30, 301-303, 1941.
Lamperti, Semi-stable stochastic processes, *Trans. Am. Math. Soc.*, 104, 62-78, 1962.
Lavallée, D., *Multifractal Techniques: Analysis and Simulations of Turbulents Fields*, Ph.D. Dissertation, McGill University, Montréal, Canada, 1991.
Lavallée, D., S. Lovejoy, D. Schertzer, and P. Ladoy, Nonlinear variability of landscape topography: multifractal analysis and simulation, *Fractal in Geography*, L. De Cola and N. Lam, Eds., 158-192, 1993.
Lea, N. L., An aspect driven kinematic routing algorithm, in *Overland Flow: Hydraulics and Erosion Mechanics*, edited by A. J. Parsons and A. D. Abrahams, Chapman & Hall, New York, 1992.
Liu, H. H., and F. J. Molz, Multifractal analyses of hydraulic conductivity distributions, *Water Resour. Res.*, 33, 2483-2488, 1997.
Lovejoy, S., The statistical characterization of rain areas in terms of fractals, *Proc. 20th Conference on Radar Meteorology*, Boston: American Meteorological Society, 476-483, 1981.
Lovejoy, S., D. Schertzer, Multifractals, universality classes and satellite and radar measurements of cloud and rain fields, *J. Geophy. Res.*, 95, 2021 – 2034, 1990.
Maidment, D.R., *Handbook of Hydrology*, McGraw-Hill, Inc., 1992.
Maller, R. A., and M. L. Sharma, An analysis of areal infiltration considering spatial variability, *J. Hydrol.*, 52, 25-37, 1981.
Mandelbrot, B. B., Intermittent turbulence in self-similar cascades: Divergence of high moments and dimension of the carrier, *J. Fluid Mech.*, 62, 331-358, 1974.
Mantoglou, A., and L. W. Gelhar, Stochastic modeling of large-scale transient unsaturated flow systems, *Water Resour. Res.*, 20, 37-46, 1987.
Marsan, D., and D. Schertzer, Causal space-time multifractal processes: predictability and forecasting of rain fields, *J. Geophy. Res.*, 101, 26333-26346, 1996.
Marsily, G., *Quantitative Hydrogeology: Groundwater Hydrology for Engineers*, Academic Press, Inc., Orlando, FL, 1986.
Menabde, M., A. Seed, D. Harris, and G. Austin, Self-similar random fields and rainfall simulations, *J. Geophy. Res.*, 102, 13,509 – 13,515, 1997.
Merz, B., A. Bardossy, Effects of spatial variability on the rainfall runoff process in a small loess catchment, *J. Hydrol.*, 212 – 213, 304-317, 1998.
Monin, A.S., and A.M. Yaglom, *Statistical Fluid Mechanics*, vol. 2, MIT Press, Cambridge, Mass., 1975.

Nash, J.E., and J.V. Sutcliffe, River flow forecasting through conceptual models, I. A discussion of principles, *Journal of Hydrology*, 10, 282-290, 1970.

O'Callaghan, J. F., and D. M. Mark, The extraction of drainage networks from digital elevation data, *Comput. Vision Graphics Image Process.*, 28, 328-344, 1984.

Ogden, F. L., and P. Y. Julien, CASC2D: A two-dimensional, physically-based, Hortonian hydrologic model, *Mathematical Models of Small Watershed Hydrology and Applications*, V. P. Singh and D. Frevert, Eds., 69 – 112, 2002.

Olsson, J, M. Persson, J. Albergel, R. Berndtsson, P. Zante, P. Oehrstroem, S. Nasri, Multiscaling analysis and random cascade modeling of dye infiltration, *Water Resour. Res.*, 38, 2002.

Over, T. M., and V. K. Gupta, Statistical analysis of mesoscale rainfall: Dependence of a random cascade generator on large-scale forcing, *J. Appl. Meteorol.*, 33, 1526-1542, 1994.

—, and —, A space-time theory of mesoscale rainfall using random cascades, *J. Geophys. Res.*, 101, 26319-26331, 1996.

Pandey, G., S. Lovejoy, D. Schertzer, Multifractal analysis of daily river flows including extremes for basins of five to two million square kilometers, one day to 75 years, *J. Hydrol.*, 208, 62 – 81, 1998.

Parisi, G., and U. Frisch, A multifractal model of intermittency, *Turbulence and Predictability in Geophysical Fluid Dynamics and Climate Dynamics*, Ghil, Benzi, and Parisi, Eds., North-Holland, 84 – 88, 1985.

Pecknold, S., S. Lovejoy, D. Schertzer, C. Hooge, and J. F. Malouin, The simulation of universal multifractals, *Cellular Automata: Prospects in Astrophysical Applications*, J. M. Perdand and A. Lejeune, Eds., 228-267, 1993.

Peters-Lidard, C.D., F. Pan, and E. F. Wood, A re-examination of modeled and measured soil moisture spatial variability and its implications for land surface modeling, *Advances in Water Resources*, 24, 1069 – 1083, 2001.

Quinn, P. F., K. J. Beven, and P. Chevallier, and O. Planchon, The prediction of hillslope flow paths for distributed hydrological modeling using digital terrain models, *Hydrol. Proc.*, 5, 59-80, 1991.

Rawls, W.J., D.L. Brakensiek, A procedure to predict Green Ampt infiltration parameters, *Adv. Infiltration, Am. Soc. Agric. Eng.*, pp. 102-112, 1983.

Rawls, W.J., D.L. Brakensiek, Prediction of soil water properties for hydrologic modeling, *Watershed Management in the Eighties*, ASCE, pp. 293-299, 1985.

Renard, K.G., et al., Agricultural impacts in an arid environment: Walnut Gulch Studies. *Proc. Sec. US/CIS Joint Conf. On Environ. Hydrology and Hydrogeology*, Arlington, VA, May 16-20, 1993.

Rodriguez-Iturbe, I., G. K. Vogel, R. Rigon, D. Entekhabi, F. Castelli, and A. Rinaldo, On the spatial organization of soil moisture fields, *Geophys. Res. Letters*, 22, 2757-2760, 1995.

Salas, J.D., R.A. Smith, G.Q. Tabios III, J. Heo, *Statistical Computer Techniques in Hydrology and Water Resources*, Dept. of Civil Eng., Colorado State University, 1993.

Samorodnitsky, G., M.S. Taqqu, *Stable Non-Gaussian Random Processes*, Chapman & Hall, New York, 1994.

Scoging, H., Modelling overland-flow hydrology for dynamic hydraulics, *Overland Flow*, A.J. Parsons and A.D. Abrahams, Ed., Chapman & Hall, New York, NY, 1993.

Schertzer, D., and S. Lovejoy, Physical modeling and analysis of rain and clouds by anisotropic, scaling multiplicative processes, *J. Geophys. Res.*, 92, 9693-9714, 1987.

Schertzer, D., S. Lovejoy, D. Lavallee, and F. Schmitt, Generic multifractal phase transitions and self-organized criticality, *Cellular Automata: Prospects in Astrophysical Applications*, J. M. Perdand and A. Lejeune, Eds., 216-227, 1993.

Schmitt, F., S. Lovejoy, and D. Schertzer, Multifractal analysis of the Greenland ice-core project climate data, *Geophys. Res. Lett.*, 22, 1689-1692, 1995.

Sivapalan, M., and E. F. Wood, Spatial heterogeneity and scale in the infiltration response of catchments, *Scale Problems in Hydrology*, edited by V. K. Gupta, I. Rodriguez-Iturbe, and E. F. Wood, 81-106, Reidel Publishing Company, 1986.

Smith, R. E., and J. Y. Parlange, A parameter-efficient hydrologic infiltration model, *Water Resour. Res.*, 14, 533 – 538, 1978.

Smith, R.E., D.C. Goodrich, D.A. Woolhiser, and C.L. Unkrich, KINEROS, A KINematic runoff and EROSion model, *Computer Models of Watershed Hydrology*, V.P. Singh, Ed., Water Resour. Pubs., Highlands Ranch, Colorado, 697-731, 1995.

Smith, R.E., and J.-Y. Parlange., A parameter-efficient hydrologic infiltration model, *Water Resour. Res.*, 14, 533-538, 1978.

SWRC (Southwest Watershed Research Center), *Documentation for Selected Precipitation/Runoff Event Data Sets*, USDA-ARS, 1993.

Tarboton, D. G., A new method for the determination of flow directions and upslope areas in grid digital elevation models, *Water Resour. Res.*, 33, 309 – 319, 1997.

Tennekoon, L., M.C. Boufadel, D. Lavallee, J. Weaver, Multifractal anisotropic scaling of the hydraulic conductivity, *Water Resour. Res.*, 39, 1193, 2003.

Tessier, Y., S. Lovejoy, P. Hubert, D. Schertzer, S. Pecknold, Multifractal analysis and modeling of rainfall and river flows and scaling, causal transfer functions, *J. Geophys. Res.*, 101, 26427 – 26440, 1996.

Tessier, Y., S. Lovejoy, and D. Schertzer, Universal multifractals: theory and observations for rain and clouds, *J. Appl. Meteor.*, 32, 223 – 250, 1993.

USDA Soil Conservation Service, Soil Survey of Logan County, Colorado, 1974.

Wilson, J., D. Schertzer, S. Lovejoy, Continuous multiplicative cascade models of rain and clouds, *Non-linear Variability in Geophysics Scaling and Fractals*, D. Schertzer and S. Lovejoy, Eds., Klumer Academic Publishers, 1991.

Woolhiser, D.A., R.E. Smith, and D.C. Goodrich, *KINEROS, a Kinematic Runoff and Erosion Model, Documentation and User Manual*, USDA-ARS, 1990.

Yaglom, A. M., The influence of fluctuations in energy dissipation on the shape of turbulence characteristics in the inertial interval, *Sov. Phys. Dokl.*, 11, 26-29, 1966. *Geophys. Res.*, 101, 26427-26440, 1996.

Yoo, D.H, Numerical model of surface runoff, infiltration, river discharge and groundwater flow – SIRG, *Mathematical Models of Small Watershed Hydrology and Applications*, V. P. Singh and D. Frevert, Eds., 69 – 112, 2002.

Appendix 3.1

PROOF OF UNIVERSAL MULTIFRACTAL GENERATOR BEING 1/F NOISE

The materials in this appendix are taken from Wilson *et al.* (1991). According to probability theory, if random variable g and function $\varphi_g(q)$ are related as follows

$$E[e^{qg}] = e^{\varphi_g(q)} \tag{A3.1}$$

then $\varphi_g(q)$ is called the second Laplacian characteristic function of g. It is the logarithm of the Laplace transform of the probability density. It has the following property

$$\varphi_{\sum g_i}(q) = \sum_i^n \varphi_{g_i}(q) \tag{A3.2}$$

Next, we will use Gaussian generator for the following demonstration. Lévy generators can follow the same path. Suppose g is a sinusoid with wavenumber $\underline{k}$, amplitude $f(\underline{k})u_k$ and phase $\phi_{\underline{k}}$, where $u_k \sim N(0, \sigma^2)$ and $\phi_{\underline{k}}$ is a uniformly distributed random variable over $[0, 2\pi]$, *i.e.* $g_{\underline{k}} = f(\underline{k})u_{\underline{k}}e^{i\phi k}$, then

$$\varphi_{\int g_{\underline{k}} d\underline{k}}(q) = -\frac{\sigma^2}{2} q^2 \int |f(\underline{k})|^2 d\underline{k} \tag{A3.3}$$

Let ε_λ (λ is resolution) be a multifractal field, then

$$E[\varepsilon_\lambda{}^q] = \lambda^{K(q)} \tag{A3.4}$$

where K(q) is the scaling exponent of the q-th moment. Rewrite this equation as

$$E[e^{q\ln\varepsilon_\lambda}] = e^{K_u(q)\ln\lambda} = e^{\varphi_{\varepsilon_\lambda}(q)} \tag{A3.5}$$

It is therefore obvious that $\varphi_{\varepsilon\lambda}(q) = K_u(q) \ln\lambda$ is the second Laplacian characteristic function of $\ln(\varepsilon_\lambda)$, where $K_u(q)$ is unnormalized moment function. Since $K_u(q) = -\sigma^2 q^2/2$, one can use the addition property of the second Laplacian characteristic function and add random sinusoids with wavenumbers between 1 and λ with $f(\underline{k})$ chosen so that

$$\int_1^\lambda | f(\underline{k}) |^2 \, d\underline{k} = 2\pi \int_1^\lambda | f(\underline{k}) |^2 | \underline{k} | \, d | \underline{k} | = \ln \lambda \qquad \text{(A3.6)}$$

Since $2\pi|f(\underline{k})|^2 |\underline{k}|$ is simply the spectral energy E(k), the above equation can be written as

$$\int_1^\lambda E(k) d | \underline{k} | = \int_1^\lambda \frac{1}{| k |} d | \underline{k} | = \ln \lambda \qquad \text{(A3.7)}$$

i.e. the energy spectrum of the logarithm of a multifractal field must be a "1/f noise" (have a wavenumber spectrum $E(k) \propto |\underline{k}|^{-1}$).

Appendix 3.2

UNIVERSAL MULTIFRACTAL FORMULA AND DERIVATIONS

The materials in this appendix are primarily taken from the following papers: Schertzer and Lovejoy (1987, 1991), Lovejoy and Schertzer (1990), Lavallée (1991), Lavallée *et al.* (1993), Wilson *et al.* (1991), and Tessier *et al.* (1993).

In discrete cascade models, the scale ratio is $\Lambda = \lambda_0^N$, where $\Lambda > 0$; λ_0 ($\lambda_0 > 0$) is the fixed scale ratio for one step; and N (N is a positive integer) is the number of steps. As Λ goes to infinity, singularities are observed: at some points, the generated scaling field goes to infinity (a singularity) whereas over most of the space, it goes to zero (regularity). The resulting multifractal behavior of the scaling field ε_λ at any intermediate scale ratio λ ($\lambda \leq \Lambda$; in the discrete case, $\lambda = \lambda_0^n$; $n \leq N$) can be determined either by the scaling of its probability distribution, whose exponent is the codimension $c(\gamma)$ of the corresponding singularity γ, as

$$\Pr(\varepsilon_\lambda > \lambda^\gamma) \approx \lambda^{-c(\gamma)} \tag{A3.8}$$

or equivalently, by the scaling of its different moments, with corresponding moment scaling function K(q), as

$$E[\varepsilon_\lambda{}^q] \approx \lambda^{K(q)} \tag{A3.9}$$

where $c(\gamma)$ and K(q) are linked by a Legendre transform. For a multifractal field, there is an infinite hierarchy of $c(\gamma)$ and K(q). The difficulty of computing $c(\gamma)$ and K(q), however, can be overcome easily in the framework of the universal multifractal by linking the codimension and the moment scaling function with the three universal multifractal parameters (H, C_1, α) as described below.

As shown in eq. (A3.5), $\varphi_{\varepsilon\lambda}(q) = K_u(q) \ln\lambda$ is the second Laplacian characteristic function of Gaussian ($\alpha = 2$) or Lévy ($0 < \alpha < 2$) generator Γ_λ ($= \ln\varepsilon_\lambda$), where $K_u(q)$ (different from $K(q)$) is the unnormalized moment function. This means that $\varphi_{\varepsilon\lambda}(q)$ should have logarithm divergence in order for the ε_λ field to be multifractal, *i.e.* to satisfy eq. (A3.9). Define generator $\Gamma_{\alpha\lambda}(\underline{k})$ in the Fourier space as

$$\Gamma_{\alpha\lambda}(\underline{k}) = f(\underline{k}) u_\alpha(\underline{k}) \tag{A3.10}$$

where $f(\underline{k})$ is a non-random weighting function to be determined later, and $u_\alpha(\underline{k})$ is a Gaussian or Lévy white noise. In the case of a Gaussian generator, weighting function $f(\underline{k})$ can be derived from eq. (A3.6) as

$$f(\underline{k})|_{\alpha=2} \propto |\underline{k}|^{-d/2} \tag{A3.11}$$

and the second Laplacian characteristic function $\varphi_{\varepsilon\lambda}(q)$ be derived from eq. (A3.5) as

$$\varphi_{\varepsilon\lambda}(q)|_{\alpha=2} = -\frac{C_1}{\alpha-1} q^\alpha \int |f(\underline{k})|^\alpha \, d\underline{k} \qquad \alpha \neq 1 \tag{A3.12}$$

because $C_1 = \sigma^2/2$ and $\alpha = 2$. The generalized form of $f(\underline{k})$ and $\varphi_{\varepsilon\lambda}(q)$ for the Lévy subgenerators are

$$f(\underline{k}) \propto |\underline{k}|^{-d/\alpha'} \tag{A3.13}$$

and

$$\varphi_{\varepsilon\lambda}(q) = -\frac{C_1}{\alpha-1} q^\alpha \int |f(\underline{k})|^{\alpha'} \, d\underline{k} \tag{A3.14}$$

where

$$\frac{1}{\alpha}+\frac{1}{\alpha'}=1 \tag{A3.15}$$

From the definition of $\varphi_{\varepsilon\lambda}(q)$ and eq. (A3.6), the unnormalized moment scaling function, $K_u(q)$, is derived as

$$K_u(q)=\frac{C_1}{\alpha-1}q^{\alpha} \tag{A3.16}$$

To ensure the conservation of the mean of the scaling field at varying scales, a field $\underline{\varepsilon}_\lambda$ produced from a cascade model needs to be normalized by its expected value $E[\underline{\varepsilon}_\lambda] = \lambda^{K_u(1)}$. This leads to a normalized field ε_λ whose scaling exponent is

$$K(q)=K_u(q)-qK_u(1)=\frac{C_1}{\alpha-1}(q^{\alpha}-q) \qquad \alpha\neq 1 \tag{A3.17}$$

From this equation, the codimension function can be obtained *via* a Legendre transform

$$c(\gamma)=C_1\left(\frac{\gamma}{C_1\alpha'}+\frac{1}{\alpha}\right)^{\alpha'} \qquad \alpha\neq 1 \tag{A3.18}$$

By taking the limit as $\alpha \to 1$ of eq. (A3.17) and (A3.18), the following formula can be derived for the case $\alpha = 1$

$$K(q)=C_1 q\log q \qquad \alpha=1 \tag{A3.19}$$

$$c(\gamma)=C_1\exp\left(\frac{\gamma}{C_1}-1\right) \qquad \alpha=1 \tag{A3.20}$$

The above formulas of $K(q)$ and $c(\gamma)$ are for conservative multifractal fields for which the exponent of power law filter, H, is 0. Next, the formulas are derived for the computation of H, followed by the new forms of $K(q)$ and $c(\gamma)$ with non-zero H.

For a nonconservative multifractal field, ΔR

$$\Delta R=\varepsilon_\lambda \lambda^{-H} \tag{A3.21}$$

where ε_λ is the underlying conservative field, the energy spectrum of the field has a power-law relationship with wavenumber, *i.e.*

$$E(k) \sim k^{-\beta} \tag{A3.22}$$

Since E(k) is the Fourier transform of the autocorrelation function which is a second order moment, the following equation can be obtained from eqs. (A3.9), (A3.21), (A3.22) and (3.17) from Chapter 3.

$$\beta = 1 - K(2) + 2H \tag{A3.23}$$

Thus from eq. (A3.17)

$$H = \frac{\beta - 1 + K(2)}{2} = \frac{\beta - 1}{2} + \frac{C_1(2^\alpha - 2)}{2(\alpha - 1)} \tag{A3.24}$$

If $H \neq 0$, the following relations can be derived from eqs. (A3.8), (A3.9), and (A3.21)

$$K(q) \to K(q) - qH \tag{A3.25}$$

and

$$\gamma \to \gamma - H \tag{A3.26}$$

Thus the following formulas for K(q) and c(γ) can be obtained

$$K(q) - qH = \begin{cases} \dfrac{C_1}{\alpha - 1}(q^\alpha - q), & \alpha \neq 1 \\ C_1 q \log(q), & \alpha = 1 \end{cases} \tag{A3.27}$$

and

$$c(\gamma - H) = \begin{cases} C_1\left(\dfrac{\gamma}{C_1\alpha'} + \dfrac{1}{\alpha}\right)^{\alpha'}, & \alpha \neq 1 \\ C_1 \exp\left(\dfrac{\gamma}{C_1} - 1\right), & \alpha = 1 \end{cases} \tag{A3.28}$$

Appendix 3.3

ESTIMATION OF UNIVERSAL MULTIFRACTAL PARAMETER H

The materials in this appendix are primarily taken from the following papers: Schmitt et al. (1995), and Liu and Molz (1997).

The universal multifractal parameter H can be estimated from structure function analysis. The following equation defines the q^{th} order structure function

$$E[(\Delta\varepsilon_h)^q] = E[|\varepsilon(z+h) - \varepsilon(z)|^q] \tag{A3.29}$$

where E[ ] is moment, ε is a multifractal process, z is distance, and h is lag. If q = 2, the above equation defines variogram. For scaling processes, the scale invariant structure function exponent, ξ(q), (Monin and Yaglom, 1975) is defined by

$$E[(\Delta\varepsilon_h)^q] = Ah^{\xi(q)} \tag{A3.30}$$

where A may be a function of q but not h. The structure function exponent has the following form

$$\xi(q) = qH - \frac{C_1}{\alpha - 1}(q^\alpha - q), \qquad \alpha \neq 1 \tag{A3.31}$$

Thus Thus H = ξ(1).

Appendix 4.1 FLOWCHART - OVERLAND FLOW ROUTING

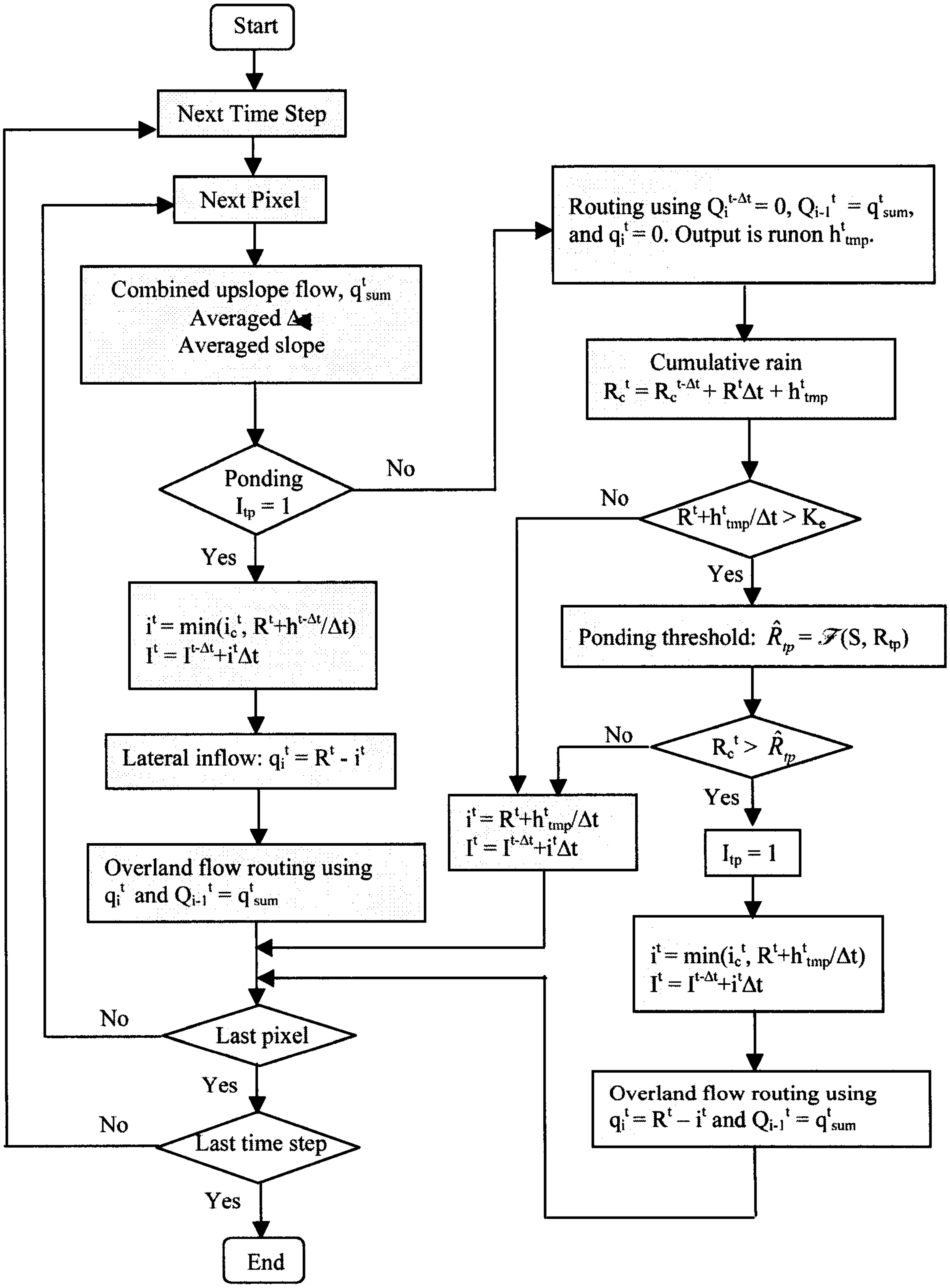

Appendix 4.2 FLOWCHART - CHANNEL FLOW ROUTING

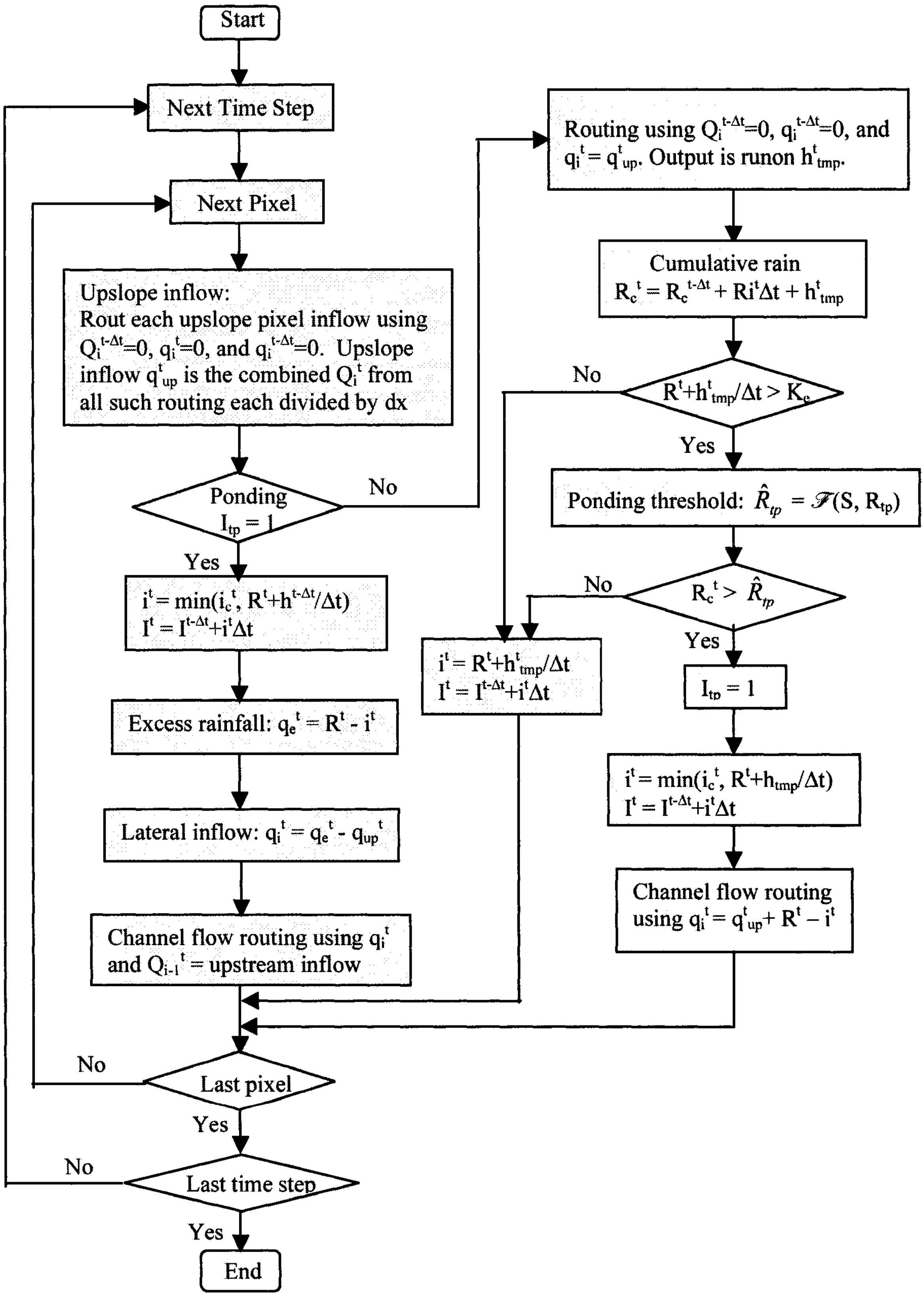

Appendix 4.3

FORMULAS FOR THEORETICAL HYDROGRAPH

All formulas in this appendix are taken from Eagleson (1970, Chapter 15).

Discharge in kinematic wave model can be written as

$$Q(x,t) = \alpha h^m(x,t) \tag{A4.1}$$

where h is flow depth. Time of concentration is

$$t_c = \left(\frac{L R_*^{1-m}}{\alpha} \right)^{1/m} \tag{A4.2}$$

L is the length of the overland plane, and R_* is rainfall excess, *i.e.*

$$R_* = R - i \tag{A4.3}$$

where R is rain rate and i is infiltration rate.

Runoff without infiltration

It is assumed that rain rate is constant and there is no infiltration. Denote t_r as the duration of rainfall excess and t_c as the time of concentration. The following formulas can be derived for flow depth at catchment outlet, h_L.

Case $t_c \le t_r < \infty$:

$$h_L = \begin{cases} R_* t & 0 \le t \le t_c \le t_r \\ \left(\frac{L R_*}{\alpha} \right)^{1/m} & t_c \le t \le t_r \end{cases} \tag{A4.4}$$

and

$$L = \alpha h_L^{m-1}[h_L R_*^{-1} + m(t - t_r)] \qquad t_c \le t_r < t \tag{A4.5}$$

<u>Case $t_r < t_c$:</u>

$$h_L = \begin{cases} R_* t & 0 \le t \le t_r < t_c \\ R_* t_r & t_r < t \le t_p \end{cases} \tag{A4.6}$$

and

$$L = \alpha h_L^{m-1}[h_L R_*^{-1} + m(t - t_r)] \qquad t_p < t \tag{A4.7}$$

where

$$t_p = t_r + \frac{t_c^* - t_r}{m} \tag{A4.8}$$

and

$$t_c^* = \frac{L}{\alpha (R_* t_r)^{m-1}} \tag{A4.9}$$

Runoff with infiltration

It is assumed that both rain rate and infiltration rate are constants. The following formulas exist for $m = 2$.

<u>Case $t_r \ge t_c$:</u>

$$h_L = \begin{cases} (R - i)t & 0 \le t \le t_c \le t_r \\ (R - i)t_c & t_c < t \le t_r \end{cases} \tag{A4.10}$$

$$h_L = (R - i)^{\frac{1}{2}}[R(t - t_r)^2 + t_c^2 (R - i)]^{\frac{1}{2}} - R(t - t_r) \qquad t_r \le t \le t_i \tag{A4.11}$$

and

$$h_L = 0 \qquad t_i \le t \tag{A4.12}$$

where

$$t_i = t_r + \frac{t_c(R-i)}{(iR)^{1/2}} \tag{A4.13}$$

<u>Case $t_r < t_c$</u>

There are three possible situations: (1) $t_i > t_p$, (2) $t_i < t_p$, or (3) $t_i = t_p$.

(1) $t_i = t_p$

$$h_L = (R-i)t_r \tag{A4.14}$$

$$t_r = \left(\frac{i}{R}\right)^{\frac{1}{2}} t_c \qquad for\ t_i = t_p \tag{A4.15}$$

(2) $t_i > t_p$

This is equivalent to $t_r > (i/R)^{1/2} t_c$.

$$h_L = \begin{cases} (R-i)t & 0 \le t \le t_r \\ Rt_r - it & t_r < t < t_p \end{cases} \tag{A4.16}$$

$$h_L = (R-i)^{\frac{1}{2}}[R(t-t_r)^2 + t_c^{\,2}(R-i)]^{\frac{1}{2}} - R(t-t_r) \qquad t_p \le t \le t_i \tag{A4.17}$$

and

$$h_L = 0 \qquad t_i < t \tag{A4.18}$$

(3) $t_i < t_p$

This is equivalent to $t_r < (i/R)^{1/2} t_c$.

$$h_L = \begin{cases} (R-i)t & 0 \le t \le t_r \\ Rt_r - it & t_r < t < t_i \\ 0 & t_i < t \end{cases} \tag{A4.19}$$

The above formulas are used to generate the theoretical hydrographs shown in Section 4.2.

Appendix 4.4

HYDROLOGICAL PROPERTIES CLASSIFIED BY USDA SOIL TEXTURE*

Texture Class	Saturated hydraulic conductivity cm/hr	Water retained at –33 kPa cm^3/cm^3	Water retained at –1500 kPa cm^3/cm^3	Wetting front soil suction head cm
Sand	23.56	0.091	0.033	4.95
Loamy sand	5.98	0.125	0.055	6.13
Sandy loam	2.18	0.207	0.095	11.01
Loam	1.32	0.270	0.117	8.89
Silt loam	0.68	0.330	0.133	16.68
Sandy clay loam	0.30	0.255	0.148	21.85
Clay loam	0.20	0.318	0.197	20.88
Silty clay loam	0.20	0.366	0.208	27.30
Sandy clay	0.12	0.339	0.239	23.90
Silty clay	0.10	0.387	0.250	29.22
Clay	0.06	0.396	0.272	31.63

* Taken after Rawl and Brakensiek (1983, 1985)

Appendix 4.5

RAIN DATA FROM EVENT 8/12/1973*

Month	Day	Hour	Minute	Cumulative Rain from last recording (in)
Rain Gage 27				
8	12	20	46	0.000000E+00
8	12	20	53	1.500000E-01
8	12	21	7	5.000000E-02
8	12	21	15	9.000000E-02
8	12	21	23	1.800000E-01
8	12	21	28	2.600000E-01
8	12	21	33	1.900000E-01
8	12	21	43	6.000000E-02
8	12	21	50	7.000000E-02
8	12	22	6	2.000000E-02
8	12	22	25	1.000000E-02
8	12	23	6	3.000000E-02
8	12	23	26	1.000000E-02
Rain Gage 28				
8	12	20	50	0.000000E+00
8	12	20	53	6.000000E-02
8	12	20	57	1.300000E-01
8	12	21	8	9.000000E-02
8	12	21	16	1.300000E-01
8	12	21	26	1.100000E-01
8	12	21	31	2.700000E-01
8	12	21	38	1.800000E-01
8	12	21	49	4.000000E-02
8	12	21	56	6.000000E-02
8	12	23	3	3.000000E-02
8	12	23	48	5.000000E-02
Rain Gage 31				
8	12	21	0	0.000000E+00
8	12	21	8	9.000000E-02
8	12	21	22	6.000000E-02
8	12	21	28	1.900000E-01
8	12	21	33	2.200000E-01
8	12	21	43	1.300000E-01
8	12	21	50	1.000000E-01
8	12	22	4	6.000000E-02
8	12	22	53	1.000000E-02
8	12	23	30	3.000000E-02

* Data source: (ftp://hydrolab.arsusda.gov/pub/arswater/l63/)

Rain Gage 32

8	12	21	0	0.000000E+00
8	12	21	11	7.000000E-02
8	12	21	26	3.000000E-02
8	12	21	36	3.000000E-01
8	12	21	44	6.000000E-02
8	12	21	56	1.100000E-01
8	12	22	28	2.000000E-02
8	12	22	59	6.000000E-02

Rain Gage 33

8	12	20	46	0.000000E+00
8	12	20	54	7.000000E-02
8	12	21	6	7.000000E-02
8	12	21	18	5.000000E-02
8	12	21	29	3.300000E-01
8	12	21	37	6.000000E-02
8	12	21	45	9.000000E-02
8	12	22	43	3.000000E-02
8	12	23	9	3.000000E-02
8	12	23	43	2.000000E-02

Rain Gage 38

8	12	21	15	0.000000E+00
8	12	21	20	1.800000E-01
8	12	21	32	2.000000E-01
8	12	21	43	1.200000E-01
8	12	22	45	4.000000E-02
8	12	23	31	3.000000E-02

Rain Gage 39

8	12	20	45	0.000000E+00
8	12	21	8	6.000000E-02
8	12	21	22	2.000000E-02
8	12	21	33	2.200000E-01
8	12	21	54	1.700000E-01
8	12	22	21	2.000000E-02
8	12	23	21	4.000000E-02

Rain Gage 40

8	12	20	30	0.000000E+00
8	12	20	59	4.000000E-02
8	12	21	16	2.000000E-02
8	12	21	29	6.000000E-02
8	12	21	39	2.000000E-01
8	12	21	50	1.000000E-01
8	12	22	1	5.000000E-02
8	12	22	24	1.000000E-02
8	12	22	48	2.000000E-02
8	12	23	7	2.000000E-02
8	12	23	26	2.000000E-02

Rain Gage 43

8	12	20	55	0.000000E+00
8	12	21	19	4.000000E-02
8	12	21	29	3.900000E-01
8	12	21	37	2.100000E-01
8	12	21	49	1.300000E-01
8	12	22	35	6.000000E-02
8	12	23	48	3.000000E-02

Rain Gage 44

8	12	20	30	0.000000E+00
8	12	21	9	4.000000E-02
8	12	21	27	3.000000E-02
8	12	21	31	2.400000E-01
8	12	21	39	2.500000E-01
8	12	21	49	1.100000E-01
8	12	22	7	6.000000E-02
8	12	22	47	2.000000E-02
8	12	24	0	1.000000E-02
8	13	24	18	0.000000E+00
Rain Gage 45				
8	12	20	30	0.000000E+00
8	12	20	37	1.600000E-01
8	12	20	57	5.000000E-02
8	12	21	9	3.000000E-02
8	12	21	24	5.000000E-02
8	12	21	32	3.900000E-01
8	12	21	43	1.200000E-01
8	12	21	57	7.000000E-02
8	12	22	16	4.000000E-02
8	12	23	6	1.000000E-02
8	12	23	42	3.000000E-02
Rain Gage 51				
8	12	20	23	0.000000E+00
8	12	20	56	4.000000E-02
8	12	21	6	2.000000E-02
8	12	21	21	2.000000E-02
8	12	21	28	3.300000E-01
8	12	21	38	2.600000E-01
8	12	21	50	2.000000E-01
8	12	22	45	0.000000E+00
8	12	23	46	2.000000E-02
Rain Gage 52				
8	12	20	25	0.000000E+00
8	12	20	36	1.200000E-01
8	12	20	58	2.000000E-02
8	12	21	22	2.000000E-02
8	12	21	28	2.700000E-01
8	12	21	34	1.700000E-01
8	12	21	44	1.100000E-01
8	12	22	1	7.000000E-02
8	12	22	48	1.000000E-02
8	12	23	41	5.000000E-02
Rain Gage 54				
8	12	21	15	0.000000E+00
8	12	21	20	5.000000E-02
8	12	21	26	3.300000E-01
8	12	21	32	1.200000E-01
8	12	21	42	1.100000E-01
8	12	22	0	4.000000E-02
8	12	22	46	4.000000E-02
8	12	22	59	2.000000E-02
8	12	23	52	3.000000E-02
Rain Gage 55				
8	12	21	18	0.000000E+00
8	12	21	24	1.300000E-01

8	12	21	29	2.600000E-01
8	12	21	37	7.000000E-02
8	12	22	27	5.000000E-02
8	12	23	4	6.000000E-02
8	12	23	47	3.000000E-02
Rain Gage 56				
8	12	20	28	0.000000E+00
8	12	21	1	4.000000E-02
8	12	21	26	8.000000E-02
8	12	21	33	2.200000E-01
8	12	21	42	8.000000E-02
8	12	21	58	4.000000E-02
8	12	22	25	3.000000E-02
8	12	22	50	4.000000E-02
8	12	23	15	2.000000E-02
8	12	23	29	0.000000E+00
8	12	23	48	2.000000E-02
Rain Gage 57				
8	12	20	30	0.000000E+00
8	12	20	38	1.400000E-01
8	12	21	9	6.000000E-02
8	12	21	26	4.000000E-02
8	12	21	30	2.400000E-01
8	12	21	36	2.800000E-01
8	12	21	49	1.300000E-01
8	12	22	5	2.000000E-02
8	12	22	29	4.000000E-02
8	12	22	59	1.000000E-02
8	12	23	26	2.000000E-02
8	12	23	39	1.000000E-02
Rain Gage 60				
8	12	21	25	0.000000E+00
8	12	21	32	1.100000E-01
8	12	21	38	1.400000E-01
8	12	21	51	8.000000E-02
8	12	22	46	4.000000E-02
8	12	23	48	5.000000E-02
Rain Gage 62				
8	12	21	35	0.000000E+00
8	12	21	44	1.200000E-01
8	12	22	17	5.000000E-02
8	12	22	59	2.000000E-02
8	12	23	33	6.000000E-02
Rain Gage 71				
8	12	20	45	0.000000E+00
8	12	20	49	1.600000E-01
8	12	20	59	6.000000E-02
8	12	21	14	6.000000E-02
8	12	21	22	3.200000E-01
8	12	21	29	3.100000E-01
8	12	21	39	1.000000E-01
8	12	21	45	1.300000E-01
8	12	22	47	2.000000E-02
8	12	23	27	4.000000E-02
Rain Gage 72				
8	12	20	25	0.000000E+00

8	12	20	34	2.600000E-01
8	12	21	22	1.000000E-01
8	12	21	31	7.000000E-02
8	12	21	40	1.900000E-01
8	12	22	11	1.000000E-02
8	12	22	52	5.000000E-02
8	12	23	52	1.000000E-02
Rain Gage 73				
8	12	20	50	0.000000E+00
8	12	20	58	4.000000E-02
8	12	21	15	2.000000E-02
8	12	21	22	3.200000E-01
8	12	21	28	1.700000E-01
8	12	21	45	1.800000E-01
8	12	22	46	4.000000E-02
8	12	23	38	2.000000E-02
Rain Gage 74				
8	12	20	48	0.000000E+00
8	12	21	7	1.100000E-01
8	12	21	20	3.900000E-01
8	12	21	29	3.900000E-01
8	12	21	40	1.500000E-01
8	12	21	50	1.100000E-01
8	12	22	14	3.000000E-02
8	12	22	48	3.000000E-02
8	12	23	19	0.000000E+00
8	12	23	33	2.000000E-02
Rain Gage 80				
8	12	20	45	0.000000E+00
8	12	20	54	1.700000E-01
8	12	21	1	1.500000E-01
8	12	21	16	6.000000E-02
8	12	21	25	1.400000E-01
8	12	21	35	4.300000E-01
8	12	21	45	1.100000E-01
8	12	21	56	8.000000E-02
8	12	22	29	2.000000E-02
8	12	23	3	3.000000E-02
8	12	23	19	2.000000E-02
8	12	23	35	1.000000E-02
Rain Gage 82				
8	12	21	30	0.000000E+00
8	12	21	37	3.000000E-02
8	12	21	45	1.500000E-01
8	12	22	7	5.000000E-02
8	12	23	13	6.000000E-02
8	12	23	53	4.000000E-02
Rain Gage 87				
8	12	20	55	0.000000E+00
8	12	21	5	7.000000E-02
8	12	21	20	3.000000E-02
8	12	21	26	1.600000E-01
8	12	21	33	1.200000E-01
8	12	21	42	8.000000E-02
8	12	21	54	7.000000E-02
8	12	22	52	2.000000E-02

8	12	23	36	3.000000E-02
Rain Gage 88				
8	12	20	15	0.000000E+00
8	12	20	24	3.000000E-02
8	12	21	17	7.000000E-02
8	12	21	21	3.000000E-01
8	12	21	29	1.700000E-01
8	12	21	42	1.000000E-01
8	12	22	3	4.000000E-02
8	12	22	24	3.000000E-02
8	12	23	2	1.000000E-02
8	12	23	22	2.000000E-02
Rain Gage 89				
8	12	20	47	0.000000E+00
8	12	21	13	1.100000E-01
8	12	21	22	5.500000E-01
8	12	21	35	2.900000E-01
8	12	22	2	6.000000E-02
8	12	23	12	3.000000E-02
Rain Gage 90				
8	12	20	29	0.000000E+00
8	12	20	40	5.000000E-02
8	12	21	2	1.000000E-02
8	12	21	24	3.000000E-02
8	12	21	30	2.900000E-01
8	12	21	35	2.100000E-01
8	12	21	41	9.000000E-02
8	12	21	49	1.100000E-01
8	12	22	6	6.000000E-02
8	12	23	2	6.000000E-02
8	12	23	47	1.000000E-02
Rain Gage 91				
8	12	21	25	0.000000E+00
8	12	21	34	3.400000E-01
8	12	21	50	1.200000E-01
8	12	22	10	5.000000E-02
8	12	22	46	2.000000E-02
8	12	23	17	2.000000E-02
8	12	23	43	3.000000E-02
Rain Gage 94				
8	12	21	22	0.000000E+00
8	12	21	28	2.000000E-01
8	12	21	40	1.800000E-01
8	12	21	58	4.000000E-02
8	12	22	30	4.000000E-02
8	12	22	53	4.000000E-02
8	12	23	19	1.000000E-02
8	12	23	44	3.000000E-02

Appendix 4.6

PARAMETER ω FOR RAIN FIELDS FROM RAIN EVENT 8/12/1971

Time (min.)	ω	Time (min.)	ω	Time (min.)	ω
1	.1772E-01	46	.3104E+00	91	.8264E+00
2	.1799E-01	47	.1815E+00	92	.8241E+00
3	.1800E-01	48	.1776E+00	93	.8241E+00
4	.1800E-01	49	.1775E+00	94	.8241E+00
5	.1772E-01	50	.1748E+00	95	.6471E+00
6	.1799E-01	51	.1528E+00	96	.2217E+00
7	.1800E-01	52	.1493E+00	97	.1936E+00
8	.1800E-01	53	.3926E+00	98	.1901E+00
9	.1875E-01	54	.4216E+00	99	.1931E+00
10	.4299E-02	55	.4148E+00	100	.1490E+00
11	.1308E+01	56	.4212E+00	101	.1514E+00
12	.1328E+01	57	.4366E+00	102	.7086E-01
13	.1328E+01	58	.4369E+00	103	.6350E-01
14	.1320E+01	59	.5258E+01	104	.6477E-01
15	.1277E+01	60	.6329E+01	105	.6377E-01
16	.1635E+01	61	.8265E+01	106	.6668E-01
17	.1641E+01	62	.8181E+01	107	.4964E-01
18	.1641E+01	63	.1596E+02	108	.4943E-01
19	.1641E+01	64	.1604E+02	109	.4841E-01
20	.7244E+00	65	.1515E+02	110	.3351E-01
21	.7357E+00	66	.1672E+02	111	.3403E-01
22	.6888E+00	67	.1139E+02	112	.2353E-01
23	.3278E+00	68	.8872E+01	113	.1106E-01
24	.4757E-01	69	.9468E+01	114	.1086E-01
25	.4250E-01	70	.1280E+02	115	.1069E-01
26	.1581E-01	71	.1218E+02	116	.8336E-02
27	.1540E-01	72	.9835E+01	117	.7563E-02
28	.1539E-01	73	.9602E+01	118	.7552E-02
29	.1539E-01	74	.9996E+01	119	.7552E-02
30	.1515E-01	75	.8978E+01	120	.7171E-02
31	.1687E+01	76	.7963E+01	121	.7284E-02
32	.1675E+01	77	.5649E+01	122	.5568E-02
33	.1692E+01	78	.6097E+01	123	.5410E-02
34	.1589E+01	79	.5318E+01	124	.5408E-02
35	.4500E+00	80	.4569E+01	125	.5323E-02
36	.4484E+00	81	.3321E+01	126	.5407E-02
37	.4483E+00	82	.2162E+01	127	.5379E-02
38	.4483E+00	83	.2029E+01	128	.5379E-02
39	.6114E+00	84	.1527E+01	129	.5379E-02
40	.6367E+00	85	.8398E+00	130	.5234E-02
41	.6808E+00	86	.8532E+00	131	.6361E-02
42	.6793E+00	87	.8276E+00	132	.6379E-02
43	.3053E+00	88	.9549E+00	133	.7074E-02
44	.2933E+00	89	.1096E+01	134	.1048E-01
45	.2944E+00	90	.9609E+00	135	.9145E-02

Time (min.)	ω	Time (min.)	ω
136	.9705E-02	181	.6416E-02
137	.9712E-02	182	.6431E-02
138	.9712E-02	183	.6724E-02
139	.9712E-02	184	.6729E-02
140	.9561E-02	185	.6313E-02
141	.9052E-02	186	.6411E-02
142	.9043E-02	187	.7075E-02
143	.9043E-02	188	.7098E-02
144	.9044E-02	189	.7099E-02
145	.8903E-02	190	.6988E-02
146	.9041E-02	191	.7097E-02
147	.9044E-02	192	.7421E-02
148	.9044E-02	193	.7503E-02
149	.9048E-02	194	.7504E-02
150	.8907E-02	195	.6890E-02
151	.8790E-02	196	.7105E-02
152	.9043E-02	197	.7061E-02
153	.9234E-02	198	.6950E-02
154	.9152E-02	199	.5726E-02
155	.9009E-02	200	.5617E-02
156	.8368E-02	201	.5684E-02
157	.8358E-02	202	.5256E-02
158	.8154E-02	203	.5249E-02
159	.7887E-02	204	.5196E-02
160	.7760E-02	205	.4997E-02
161	.7881E-02	206	.5076E-02
162	.7883E-02	207	.4642E-02
163	.7883E-02	208	.4022E-02
164	.7883E-02	209	.3645E-02
165	.5968E-02	210	.3411E-02
166	.6062E-02	211	.3464E-02
167	.6063E-02	212	.3380E-02
168	.5508E-02	213	.3580E-02
169	.5775E-02	214	.1290E-02
170	.5238E-02	215	.1234E-02
171	.5320E-02	216	.1254E-02
172	.5278E-02	217	.1254E-02
173	.5277E-02	218	.8467E-03
174	.5277E-02	219	.0000E+00
175	.5070E-02		
176	.5149E-02		
177	.5150E-02		
178	.5540E-02		
179	.5577E-02		
180	.5490E-02		